

Original Article

Cite this article: Jarvis I, Atar E, Gröcke DR, Herringshaw LG, and Trabucho-Alexandre JP. A global reference for black shale geochemistry and the T-OAE revisited: upper Pliensbachian – middle Toarcian (Lower Jurassic) chemostratigraphy in the Cleveland Basin, England. *Geological Magazine* 161(e13): 1–77. <https://doi.org/10.1017/S0016756824000244>

Received: 20 November 2023

Revised: 18 June 2024

Accepted: 9 July 2024






Keywords:

Oceanic anoxic event; carbonaceous mudstone; carbon isotopes; trace metals; palaeoredox proxies; anoxia; extinction

Corresponding author:

Ian Jarvis; Email: i.jarvis@kingston.ac.uk

A global reference for black shale geochemistry and the T-OAE revisited: upper Pliensbachian – middle Toarcian (Lower Jurassic) chemostratigraphy in the Cleveland Basin, England

Ian Jarvis¹ , Elizabeth Atar² , Darren R. Gröcke² , Liam G. Herringshaw³  and João P. Trabucho-Alexandre^{2,4} 

¹Department of Geography, Geology and the Environment, Kingston University London, Kingston upon Thames, UK;

²Department of Earth Sciences, Durham University, Durham, UK; ³Centre for Lifelong Learning, University of York, York, UK and ⁴Department of Earth Sciences, Universiteit Utrecht, Utrecht, The Netherlands

Abstract

The Pliensbachian–Toarcian succession of North Yorkshire provides a global reference for the interval incorporating the Toarcian Oceanic Anoxic Event (T-OAE, ~183 Ma). Major and trace element, carbon stable-isotope ($\delta^{13}\text{C}_{\text{org}}$) and total organic carbon (TOC) data for the Dove's Nest core, drilled close to the classic outcrop sections of the Yorkshire coast, demonstrate geochemical, mineralogical and grain-size trends linked to sea level and climate change in the Cleveland Basin. High-resolution correlation between the core and outcrop enables the integration of data to generate a comprehensive chemostratigraphic record. Palaeoredox proxies (Mo, U, V, TOC/P, DOP and Fe speciation) show a progressive shift from oxic bottom waters in the late Pliensbachian through dysoxic–anoxic conditions in the earliest Toarcian to euxinia during the T-OAE. Anoxia–dysoxia persisted into the middle Toarcian. Elemental and isotope data (Re, Re/Mo, $\delta^{34}\text{S}_{\text{CAS}}$, $\delta^{98}\text{Mo}$ and $\epsilon^{205}\text{Tl}$) from the coastal sections evidence global expansion of anoxic and euxinic seafloor area driving drawdown of redox-sensitive metals and sulfate from seawater leading to severe depletion in early Toarcian ocean water. The record of anoxia–euxinia in the Cleveland Basin largely reflects global-scale changes in ocean oxygenation, although metal depletion was temporarily enhanced by periods of local basin restriction. Osmium and Sr isotopes demonstrate a pulse of accelerated weathering accompanying the early Toarcian hyperthermal, coincident with the T-OAE. The combined core and outcrop records evidence local and global environmental change accompanying one of the largest perturbations in the global carbon cycle during the last 200 Ma and a period of major biotic turnover.

1. Introduction

The early Toarcian (183.73 – 181.17 Ma; Gradstein *et al.*, 2020; Al-Suwaidi *et al.*, 2022) was a period of dramatic global palaeoenvironmental change and biotic turnover associated with one of the largest perturbations in the global carbon cycle of the last 200 Ma, evidenced by a large (~3 – 7‰ Vienna Peedee Belemnite, VPDB) negative carbon isotope excursion (CIE) in marine carbonate ($\delta^{13}\text{C}_{\text{carb}}$) and marine and terrestrial organic carbon ($\delta^{13}\text{C}_{\text{org}}$) records (Küspert, 1982; Jenkyns & Clayton, 1997; Hesselbo *et al.*, 2000, 2007; Suan *et al.*, 2015; Them *et al.*, 2017a; Fantasia *et al.*, 2018a; Cramer & Jarvis, 2020; Jin *et al.*, 2020; Kemp *et al.*, 2020; Ruebsam & Al-Husseini, 2020; Nie *et al.*, 2023; Richey *et al.*, 2023; Gambacorta *et al.*, 2024) and commonly referred to as the Toarcian Oceanic Anoxic Event (T-OAE). The T-OAE was associated with widespread deposition of carbonaceous (typically ~5 – 10% total organic carbon, TOC) marine mudstones ('black shales') (Jenkyns, 1985, 1988; Kemp *et al.*, 2022b), linked to the development of regional bottom-water anoxia – euxinia. These conditions are typified by the basins of NW Europe where major black shale successions include the Jet Rock (England), Posidonia Shale (Posidonienschiefer; Germany, Netherlands and North Sea) and Schistes carton (France), but anoxia is now known to have extended more widely, including parts of the deep Panthalassa Ocean (Kemp *et al.*, 2022a; Chen *et al.*, 2023).

The CIE has been ascribed to the release of large volumes of isotopically light carbon from the Karoo, Ferrar and Chon Aike Large Igneous Provinces (LIPs; Pálffy & Smith, 2000; Percival *et al.*, 2015; Guex *et al.*, 2016; Ramirez & Algeo, 2020; Bergman *et al.*, 2021; Heimdal *et al.*, 2021; Al-Suwaidi *et al.*, 2022; Fleischmann *et al.*, 2022; Jiang *et al.*, 2023). The acceleration of Karoo–Ferrar LIPs activity and subsequent peak magmatism agree closely with the onset of early

© The Author(s), 2024. Published by Cambridge University Press. This is an Open Access article, distributed under the terms of the Creative Commons Attribution licence (<https://creativecommons.org/licenses/by/4.0/>), which permits unrestricted re-use, distribution and reproduction, provided the original article is properly cited.



Toarcian warming and the T-OAE (Greber *et al.*, 2020; Gaynor *et al.*, 2022; Luttinen *et al.*, 2022; Jiang *et al.*, 2023; Ware *et al.*, 2023; Fendley *et al.*, 2024). It is argued that the release of volcanic CO₂ drove global warming (cf. Jenkyns, 1999), with the rise in surface temperature (Gómez *et al.*, 2016) causing dissociation of terrestrial and seafloor methane clathrates (cf. Dickens *et al.*, 1995; Hesselbo *et al.*, 2000; DB Kemp *et al.*, 2005), CH₄ release and further warming (Suan *et al.*, 2011), an enhanced hydrological cycle (Chen *et al.*, 2021), increased rates of continental weathering and soil erosion (Brazier *et al.*, 2015; Ruebsam *et al.*, 2018, 2020a; Kemp *et al.*, 2020), permafrost and glacier destabilization (Krencker *et al.*, 2019; Ruebsam *et al.*, 2019), increased wetland methanogenesis (Them *et al.*, 2017a), eustatic sea-level rise and marine transgression (Suan *et al.*, 2010; Remirez & Algeo, 2020; Reolid *et al.*, 2021). Thermogenic methane release from coals in the Karoo–Ferrar LIPs has also been postulated (McElwain *et al.*, 2005; Heimdal *et al.*, 2021), although the viability of this process to generate the observed negative δ¹³C excursion has been contested (Gröcke *et al.*, 2009; Rahman *et al.*, 2018).

The combined effects of these extensive palaeoenvironmental changes led to a marine biotic crisis and global second-order mass extinction affecting multiple groups including ammonites, belemnites, brachiopods, corals, ostracods, benthic foraminifera and calcareous nannofossils (Hallam, 1986; Little & Benton, 1995; Wignall *et al.*, 2005; Dera *et al.*, 2010; Caruthers *et al.*, 2013; Danise *et al.*, 2015; Jiang *et al.*, 2020; Piazza *et al.*, 2020; Caswell & Herringshaw, 2023) and also significantly impacted terrestrial ecosystems (Slater *et al.*, 2019; Danise *et al.*, 2022; Galasso *et al.*, 2022; Jin *et al.*, 2022; Baranyi *et al.*, 2023, 2024).

In this paper, we present new geochemical results for the upper Pliensbachian – middle Toarcian of the Dove's Nest borehole in North Yorkshire, England, that was drilled in the Cleveland Basin, close to the classic coastal exposures that provide a global Lower Jurassic reference section. Despite the importance of the area, controversy continues regarding the interpretation of palaeoenvironmental conditions in the basin before, during and after the T-OAE (e.g. Hesselbo *et al.*, 2020a; Remirez & Algeo, 2020), the significance of geochemical elemental and isotopic proxies obtained from the sections as indicators of global processes (van de Schootbrugge *et al.*, 2005; McArthur *et al.*, 2008; Pearce *et al.*, 2008; Dickson *et al.*, 2017; Thibault *et al.*, 2018; Hesselbo *et al.*, 2020a; Chen *et al.*, 2023) and even the identification of the early Toarcian perturbations as an OAE (McArthur, 2019; Them *et al.*, 2022).

New data from the Dove's Nest core, combined with a review of extensive published literature, offer an improved understanding of palaeoenvironmental change in the Cleveland Basin during the Early Jurassic and confirm the global significance of the Yorkshire succession as a reference for defining the causes and consequences of the T-OAE.

2. North Yorkshire coast – a global reference for the Lower Jurassic

With a history of more than 200 years of geological research, including the seminal papers of Young & Bird (1822), Phillips (1829) and Tate & Blake (1876), and subsequent detailed mapping by the Geological Survey (Fox-Strangways, 1892), the Lower Jurassic exposed along the North Yorkshire coast between Redcar and Ravenscar (Fig. 1) is one of the most extensively studied marine sedimentary rocks globally (Hemingway, 1974; Cope *et al.*, 1980; Rawson & Wright, 1995; Powell, 2010; Rawson & Wright,

2018). It includes the Global Boundary Stratotype Section and Point (GSSP) for the Pliensbachian Stage (Meister *et al.*, 2006) and is the type section for the Lias Group (Cox *et al.*, 1999).

Detailed lithostratigraphic descriptions accompanied by a precise ammonite biostratigraphy (Buckman, 1915; Howarth, 1955, 1962, 1973, 1992; Howarth in Cope *et al.*, 1980; Powell, 1984; Howard, 1985; Hesselbo & Jenkyns, 1995; Hesselbo & King, 2019) have provided a framework for extensive palaeontological (e.g. Little & Benton, 1995; Harries & Little, 1999; Caruthers *et al.*, 2013; Danise *et al.*, 2013, 2019; Ullmann *et al.*, 2014; Lord, 2019; De Baets *et al.*, 2021; Ferrari *et al.*, 2021; Atkinson *et al.*, 2023; Caswell & Herringshaw, 2023) and geochemical studies (e.g. Jenkyns & Clayton, 1997; Hesselbo *et al.*, 2000; Cohen *et al.*, 2004; DB Kemp *et al.*, 2005, 2011; McArthur *et al.*, 2008; Pearce *et al.*, 2008; Bond *et al.*, 2010; Littler *et al.*, 2010; Gill *et al.*, 2011; French *et al.*, 2014; Ruvalcaba Baroni *et al.*, 2018; Thibault *et al.*, 2018; McArthur, 2019; Houben *et al.*, 2021; Q Li *et al.*, 2021; Wang, 2022; Kovács *et al.*, 2024) that have focussed particularly on the interval spanning the Pliensbachian – Toarcian stage boundary and the T-OAE, and the associated environmental change and biotic turnover.

The upper Pliensbachian – middle Toarcian interval that constitutes the focus of the present study comprises a neritic – epeiric mudstone-dominated succession that accumulated in the Cleveland Basin (Fig. 1), a small, largely onshore, extension of the Sole Pit Basin of the Southern North Sea (Powell, 2010). North Yorkshire was at that time located at ~44° N on the western margin of a shallow epeiric sea bordering the Pennine–Caledonian High (Scottish) landmass. The Mid North Sea High, a Palaeozoic ridge north of the Cleveland Basin, and the Pennine High to the west were the likely sources of coarser siliciclastic sediment (Wright, 2022), particularly during periods of sea-level lowstand such as in the late Pliensbachian (Bradshaw *et al.*, 1992; Hesselbo, 2008).

For biostratigraphic reference, we adopt the regional ammonite stratigraphy (Hesselbo & Jenkyns, 1995; Rawson & Wright, 2018). Following wider stratigraphic convention (cf. Hesselbo *et al.*, 2020b), we employ the ammonite zones and subzones as traditional biozones and not chronozones as promoted for the Jurassic (Page, 2017). The Toarcian lacks a standardized ammonite zonal and subzonal scheme, and significant differences exist in the index taxa and the stratigraphic placement of Pliensbachian – Toarcian ammonite zones on a regional to global scale. Compare, for example, the Yorkshire ammonite stratigraphy (Fig. 2) with that applied in the SW German Basin (e.g. Ruebsam *et al.*, 2023), the Lusitanian Basin Portugal and the Neuquén Basin Argentina (cf. Al-Suwaidi *et al.*, 2022), noting the differences in marker species and boundary positions relative to the reference carbon isotope curves. This challenges the view that the Yorkshire zones and subzones can be regarded as reliable chronostratigraphic units.

The upper Pliensbachian (*Amaltheus margaritatus* and *Pleuroceras spinatum* zones) comprises silty mudstones with hummocky cross-stratified fine sandstones and thin sideritic and berthierine (chamosite)-rich ooidal ironstones (Fig. 2; uppermost Staithes Sandstone and Cleveland Ironstone formations). The overlying lower – middle Toarcian mudstones (Whitby Mudstone Formation) include an interval (upper *Dactyloceras semicelatum* and *Cleviceras exaratum* subzones) that is characterized by very dark brown carbonaceous mudstones (terminology of Lazar *et al.*, 2015; traditionally referred to as 'black shales') of the uppermost Grey Shale and lower Mulgrave Shale (Jet Rock), which contain the large negative carbon-isotope excursion that accompanies the T-OAE (Hesselbo *et al.*, 2000; DB Kemp *et al.*, 2005). Fissile, dark

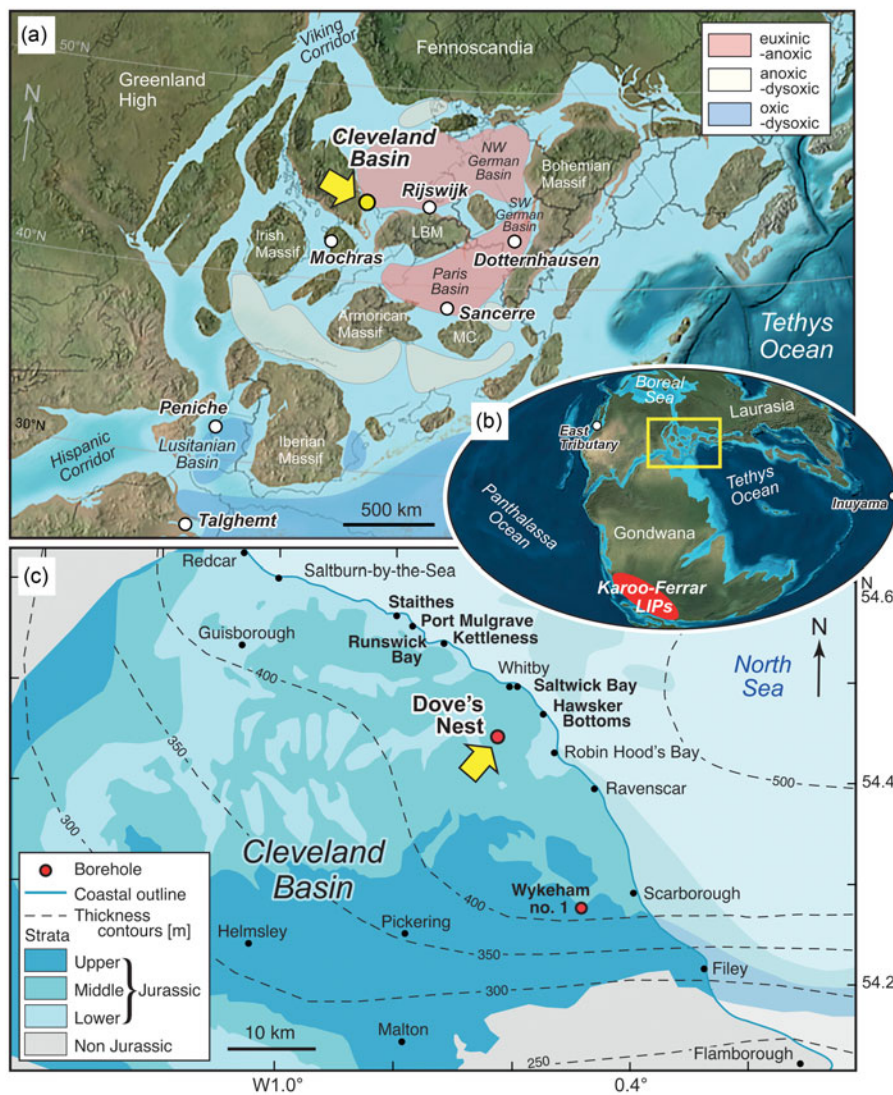


Figure 1. Early Jurassic palaeogeography, regional setting and location of the Dove's Nest study core in the Cleveland Basin. (a) Palaeogeographic reconstruction of Europe showing the location of the basin on the European epicontinental shelf; interpreted bottom-water redox conditions associated with the T-OAE are based on geological data and ocean circulation modelling (Ruvalcaba Baroni *et al.*, 2018). (b) Global palaeogeography of the Early Jurassic showing continent configuration, major ocean basins and location of the Karoo–Ferrar Large Igneous Provinces (LIPs) that were emplaced during the early–middle Toarcian (Heimdal *et al.*, 2021; Gaynor *et al.*, 2022). Yellow box shows the location of the Europe map. Palaeogeographic base maps in (a) and (b) modified from Blakey (2012, 2016); palaeolatitude in (a) revised based on the online palaeolatitude calculator of van Hinsbergen *et al.* (2015) at 183 Ma (<https://paleolatitu.de.org>) with the palaeomagnetic reference frame of Vaes *et al.* (2023). (c) Map of eastern North Yorkshire showing the geographic distribution of Jurassic sediments in the Cleveland Basin, isopachs for the Lias and location of the Dove's Nest borehole. Redrawn after Kent (1980) and Rawson & Wright (2000).

grey carbonaceous mudstones (Bituminous Shales *Harpoceras falciferum* Subzone) and then paler-coloured silty mudstones (Alum Shale Member *Hildoceras bifrons* Zone) cap the study succession. The higher part of the Alum Shale (post *Dactyloceras commune* Subzone) and the uppermost members of the Whitby Mudstone (Peak Mudstone and Fox Cliff Siltstone) are not considered here.

Correlation of the coastal sections (Fig. 1), at a decimetre scale over distances of tens of km, has been demonstrated using numbered and/or named lithostratigraphic marker 'beds', principally layers of ironstone, sideritic concretions and other calcareous concretions with distinctive shapes, sizes and mineralization, constrained by ammonite biostratigraphy (e.g. Hesselbo & Jenkyns, 1995; Rawson & Wright, 2018). However, understanding of these correlations is hampered by the retention of unique 'bed' numbering schemes for different reference sections (Howarth, 1955, 1962, 1973, 1992). A correlation of these schemes was provided by Cope *et al.* (1980) and a graphical correlation of key sections has been presented by Caswell & Herringshaw (2023, fig. 2).

Additionally, as noted by Trabucho-Alexandre *et al.* (2022), although the numbered 'beds' are the finest published stratigraphic

subdivisions of the middle and upper Lias of Yorkshire and have been used by most authors studying the succession, the 'beds' are neither genetic beds *sensu* Campbell (1967) nor geometric beds *sensu* McKee & Weir (1953). Beds may be defined, relative to laminae, based on their thickness (cf. McKee and Weir, 1953; Tucker, 2011). However, the key limitation of this descriptive approach is that it does not distinguish between strata that are 'separated from adjacent strata by surfaces of erosion, non-deposition, or abrupt change in character' (McKee and Weir, 1953, p. 382) and strata, whatever their thickness may be, that were formed by accretion of sediment onto surfaces of net sedimentation without intervening episodes of non-deposition, which is often accompanied by erosion (Campbell, 1967). For this reason, beds in a sedimentological sense (i.e. *sensu* Campbell, 1967) have no limiting thickness. Stratification within a bed should be called lamination 'whatever the thickness of the individual layers' (Kuenen 1966, p. 527).

'Beds' in the Lower Jurassic of northeast England were defined by Howarth (1955, 1962, 1973) based principally on the presence of calcareous concretions at regular intervals. The concretionary horizons coincide with horizons of faunal change, which were used to subdivide the succession into ammonite zones and subzones.

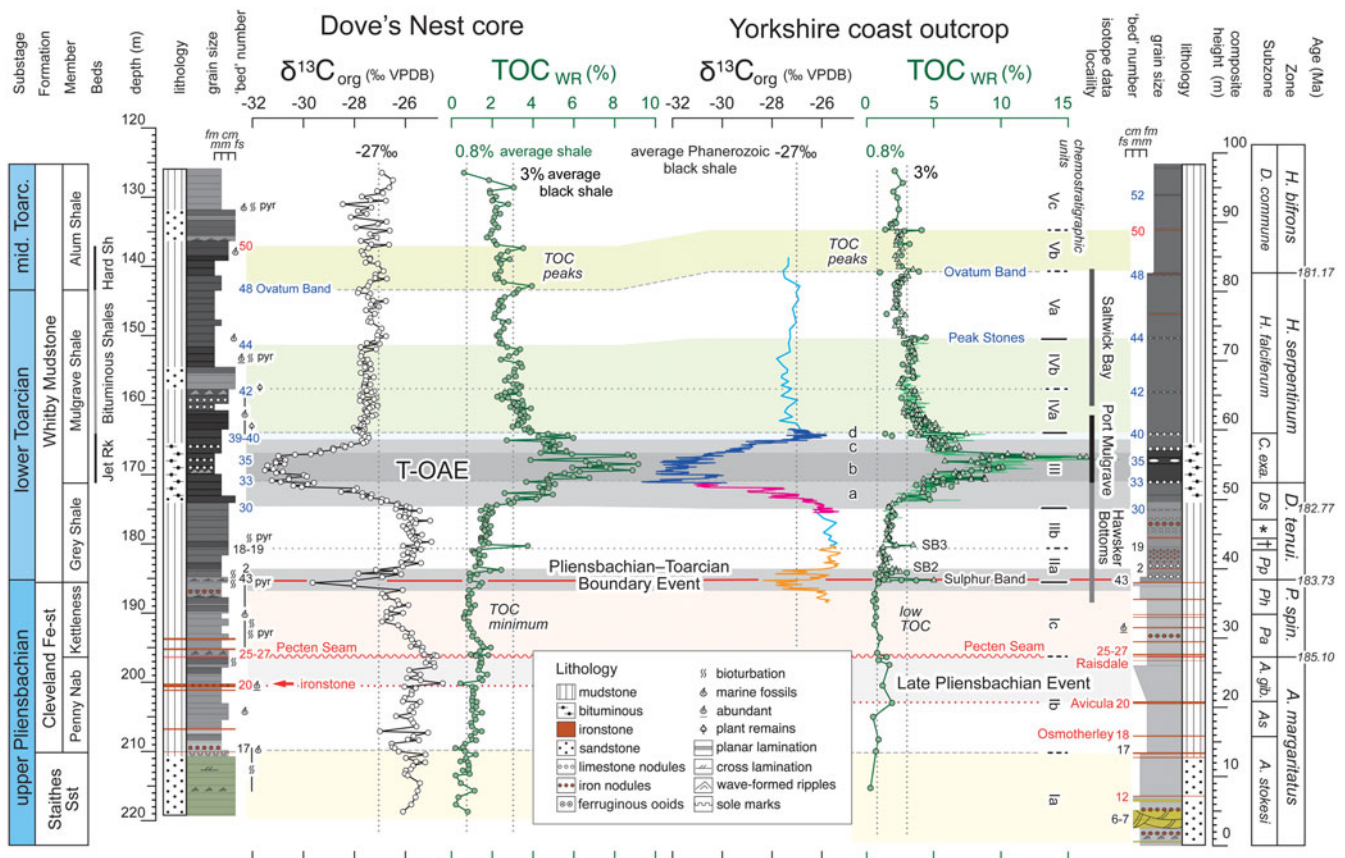


Figure 2. Stratigraphic log of the studied section of the Dove's Nest core and correlation to a composite outcrop section along the North Yorkshire coast between Hawsker Bottoms and Port Mulgrave. Organic carbon isotopes ($\delta^{13}\text{C}_{\text{org}}$) and whole-rock total organic carbon (TOC_{WR}) profiles are shown with their correlation (modified from Trabucho-Alexandre et al., 2022). Organic-rich facies associated with the large negative $\delta^{13}\text{C}_{\text{org}}$ excursion of the Toarcian Oceanic Anoxic Event (T-OAE; Jenkyns, 1985) together with the negative $\delta^{13}\text{C}_{\text{org}}$ excursion defining the Pliensbachian – Toarcian Boundary Event (Little et al., 2010) provide prominent tie points. The $\delta^{13}\text{C}_{\text{org}}$ maximum of the *A. gibbosus* Subzone is equated to the Late Pliensbachian Event positive excursion of Korte & Hesselbo (2011), De Lena et al. (2019) and Hollaar et al. (2023). Grain size scale: fm, fine mudstone; mm, medium mudstone; cm, coarse mudstone; and fs, very fine sandstone. Yorkshire coast 'bed' numbers and named marker beds from Hawsker Bottoms (Fig. 1) for the Pliensbachian (Howarth, 1955) and Whitby composite section for the Toarcian (Howarth, 1962, 1973, 1992). Dove's Nest data from Trabucho-Alexandre et al. (2022) and this study. Yorkshire coast $\delta^{13}\text{C}_{\text{org}}$ data from Hawsker Bottoms: orange, Little et al. (2010); turquoise, Cohen et al. (2004); and pink, DB Kemp et al. (2005). Port Mulgrave: dark blue, DB Kemp et al. (2005); turquoise, Cohen et al. (2004). Saltwick Bay: turquoise, Cohen et al. (2004). TOC data for the Yorkshire coast are composite section values from Kemp et al. (2011; thin green high-resolution curve), Ruvalcaba Baroni et al. (2018; green-filled triangles) and McArthur (2019; green-filled circles). Thick green line shows the trend of the two low-resolution datasets. Vertical dotted lines and numbers are the $\delta^{13}\text{C}_{\text{org}}$ reference value for average Phanerozoic black shale (Meyers, 2014) and the TOC_{WR} content of average shale (Law, 1999) and average black shale (Vine & Tourtelot, 1970). SB2 and SB3 are the middle and upper Sulphur Bands of the basal lower Toarcian (Salem, 2013; McArthur, 2019). Abbreviations of biostratigraphic zonation: *H. bifrons* = *Hildoceras bifrons*; *H. serpentinum* = *Harpoceras serpentinum*; *D. tenui.* = *Dactyloceras tenuicostatum*; *P. spin.* = *Pleuroceras spinatum*; *A. margaritatus* = *Amaltheus margaritatus*; *D. commune* = *Dactyloceras commune*; *H. falciferum* = *Harpoceras falciferum*; *C. exa.* = *Cleviceras exaratum*; *Ds* = *Dactyloceras semicelatum*; * = *Dactyloceras tenuicostatum*; † = *Dactyloceras clevelandicum*; *Pp* = *Protogrammoceras paltum*; *Ph* = *Pleuroceras hawskerense*; *Pa* = *Pleuroceras apyrenum*; *A. gib.* = *Amaltheus gibbosus*; *As* = *Amaltheus subnodosus*; *A. stokesi* = *Amaltheus stokesi*. Ages after GTS2020 (Gradstein et al., 2020) with revisions of Al-Suwaidi et al. (2022). Chemostratigraphic units modified from Remirez & Algeo (2020) and defined by multi-element proxies (see text); note that a – d, to the left of the TOC_{WR} profile for the Yorkshire coast, are subunits of Unit III, the T-OAE.

Many of these 'beds' are in the order of metres thick and thus three orders of magnitude larger than bedding in the succession (Trabucho-Alexandre, 2015). They are, therefore, bedsets comprising thin beds of mudstone, which may constitute parasequence-scale successions (Macquaker and Taylor, 1996). Such 'beds' represent longer timescales (and processes) of sedimentation.

As illustrated by Caswell & Herringshaw (2023, fig. 2), an individual marker level may have been attributed to several 'bed' numbers and may lie within 'beds' that have boundaries defined using different criteria in different places; a single 'bed' at one site may be equivalent to multiple differently numbered 'beds' elsewhere. It is essential therefore to always refer to the specific locality numbering scheme being applied when describing the stratigraphy.

The GSSP of the Toarcian Stage is located at the Peniche section in the Lusitanian Basin of Portugal (Fig. 1; da Rocha et al., 2016).

There are no formally designated auxiliary sections, but the correlation between the Peniche and Almonacid de la Cuba section in the Iberian Range (Spain) provides additional ammonite records and a magnetostratigraphy across the boundary interval that offer additional criteria for supraregional correlation (Comas-Rengifo et al., 2010; de la Rocha et al., 2016). However, both successions have a strong Tethyan influence and were characterized throughout the early Toarcian by generally low primary productivity and deposition in oxic – dysoxic bottom waters. This is in stark contrast to the Boreal higher productivity and anoxic – euxinic environment that developed progressively in the Cleveland Basin and more widely in northern European basins during the earliest Toarcian, reaching a peak during the T-OAE but commonly extending into the middle Toarcian. Chemostratigraphy and macrofossil biostratigraphy provide a basis for correlation between the two areas at high stratigraphic resolution enabling the extensive geochemical data

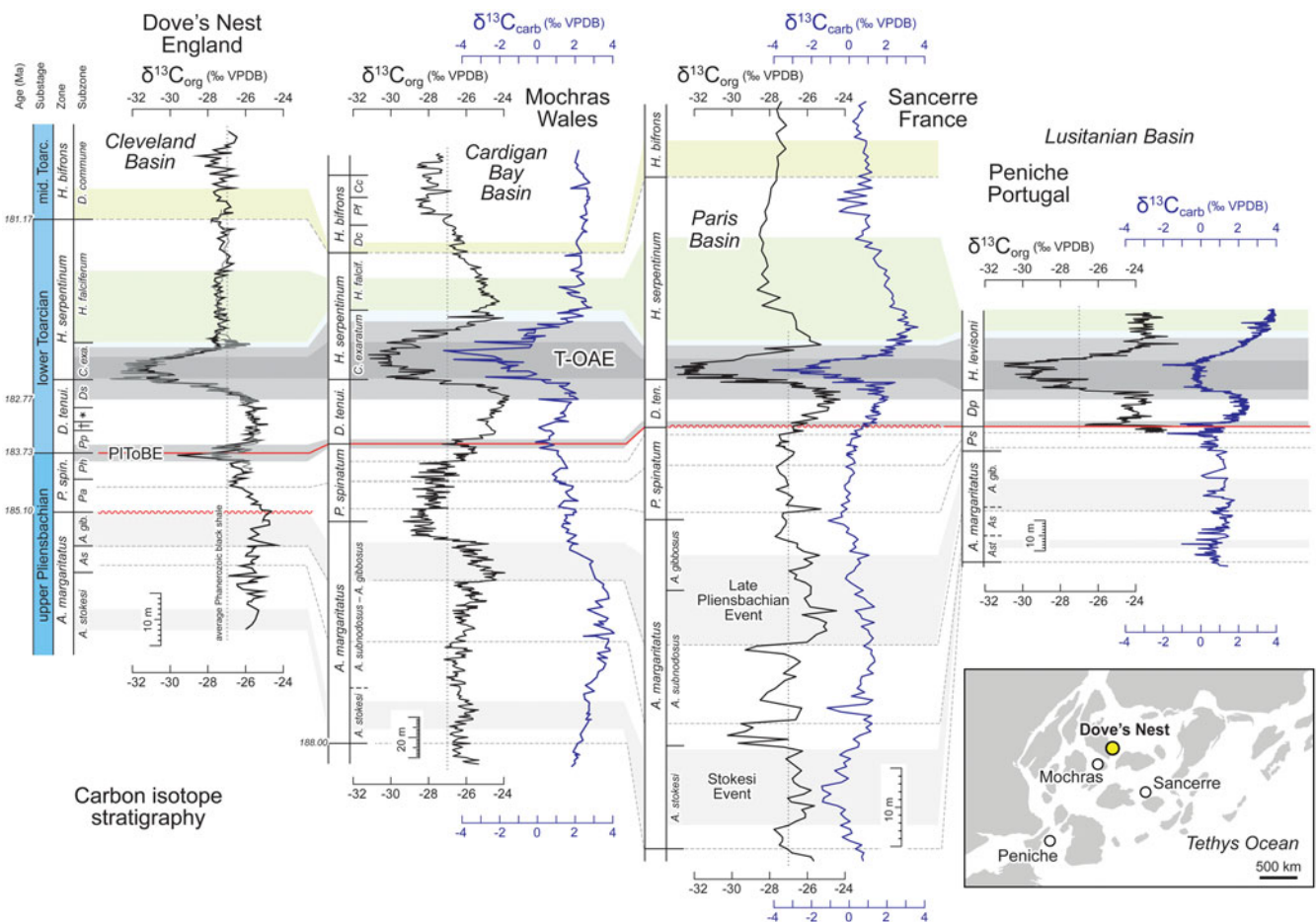


Figure 3. Carbon isotope correlation of selected European Pliensbachian – Toarcian successions. The map (bottom right) shows the palaeogeographic location of the sites (see Fig. 1 for details). Cleveland Basin $\delta^{13}\text{C}_{\text{org}}$ profiles from this study (Dove's Nest = black, coast composite = grey; see Fig. 2 for sources). The top of the *D. commune* Subzone lies ~16 m above the top of the Hard Shales on the Yorkshire coast (Hesselbo & Jenkyns, 1995). Mochras $\delta^{13}\text{C}_{\text{org}}$ data from Xu *et al.* (2018) and Storm *et al.* (2020); $\delta^{13}\text{C}_{\text{carb}}$ after Ullmann *et al.* (2022). CIEs as Figure 2 with Stokesi Event of Peti *et al.* (2017) and Storm *et al.* (2020). Sancerre $\delta^{13}\text{C}_{\text{org}}$ data from Hermoso *et al.* (2013) and Peti *et al.* (2021); $\delta^{13}\text{C}_{\text{carb}}$ after Hermoso *et al.* (2009a, 2009b; 2013) and Peti *et al.* (2021). Pliensbachian biostratigraphy follows Peti *et al.* (2017, 2021) and Zhang *et al.* (2023). Peniche $\delta^{13}\text{C}_{\text{org}}$ profile from Fantasia *et al.* (2019). Peniche Pliensbachian $\delta^{13}\text{C}_{\text{carb}}$ values after Oliveira *et al.* (2006) with stratigraphic revisions and additional data from Silva *et al.* (2011); Pliensbachian – Toarcian boundary and Toarcian $\delta^{13}\text{C}_{\text{carb}}$ after Hesselbo *et al.* (2007). Yorkshire stratigraphy follows Figure 2. Other abbreviations: PIToBE = Pliensbachian – Toarcian Boundary Event; *H. falcif.* = *Harporoceras falciferum*; *Dc* = *Dactyloceras commune*; *Pf* = *Peronoceras fibulatum*; *Cc* = *Catacoeloceras crissum*; *D. ten.* = *Dactyloceras tenuicostatum*; *Ast.* = *Amaltheus stokesi*; *Ps* = *Pleuroceras spinatum*; *Dp* = *Dactyloceras polymorphum*; *H. levisoni* = *Hildaites levisoni*.

from Yorkshire to be tied to the GSSP (e.g. Ait-Itto *et al.*, 2018; Fantasia *et al.*, 2019).

The Pliensbachian – Toarcian boundary is well exposed at Hawsker Bottoms in Yorkshire (Fig. 1; Littler *et al.*, 2010), which offers a candidate for a Standard Auxiliary Boundary Stratotype (Head *et al.*, 2023) to represent the Boreal sections of northern Europe.

3. Carbon isotopes, TOC and the T-OAE

Studies by Küspert (1982), Jenkyns & Clayton (1997) and Hesselbo *et al.* (2000) established the Yorkshire coast Toarcian succession as a global reference section for the large negative CIE associated with carbonaceous mudstones that comprise the T-OAE. As originally described, the isotopic expression of the T-OAE was considered to be the positive CIE observed in Tethyan pelagic carbonates ($\delta^{13}\text{C}_{\text{carb}}$) of the *H. falciferum* Zone (= *H. serpentinum* Zone of this study) and its equivalents (Jenkyns, 1985, 1988) rather than the immediately underlying negative excursion, which was regarded as being of potential diagenetic origin (Jenkyns & Clayton, 1997).

Subsequent work demonstrated that a positive $\delta^{13}\text{C}_{\text{org}}$ excursion is weakly developed or absent in many curves derived from the analysis of bulk organic matter (e.g. Hesselbo *et al.*, 2000). However, a large negative $\delta^{13}\text{C}$ excursion (typically 5 – 7‰ $\delta^{13}\text{C}_{\text{org}}$ in NW Europe) is observed globally in marine carbonate, terrestrial and marine bulk organic matter and individual biomarkers (e.g. Suan *et al.*, 2011; Caruthers *et al.*, 2014; Ikeda *et al.*, 2018; Ramirez & Algeo, 2020; Ruebsam & Al-Husseini, 2020; Richey *et al.*, 2023; Huang *et al.*, 2024), situated immediately below or superposed on the positive excursion, where developed (Fig. 3). The interval of the negative excursion alone is now commonly considered to represent the T-OAE (e.g. Cohen *et al.*, 2004; Them *et al.*, 2018; Ramirez & Algeo, 2020; Bodin *et al.*, 2023).

Recently, it has been proposed that the interval of the negative CIE would be better termed the Jenkyns Event and the use of T-OAE should be expanded to include intervals of higher $\delta^{13}\text{C}$ values in the underlying upper *D. tenuicostatum* Zone and overlying lower *H. falciferum* Subzone (Erba *et al.*, 2022), closer to the original concept of the T-OAE (Jenkyns, 1985, 1988) as a positive $\delta^{13}\text{C}$ event. However, views differ widely on the use of the

two terms (compare Müller *et al.*, 2017; Jin *et al.*, 2020; Reolid *et al.*, 2020; Erba *et al.*, 2022; Gambacorta *et al.*, 2023, 2024). Spatio-temporal variability in the deposition of organic-rich strata during the early Toarcian and their relationship to marine anoxia and the negative $\delta^{13}\text{C}$ excursion have been reviewed by Ruebsam & Schwark (2024). In the absence of a consensus, we follow Trabucho-Alexandre *et al.* (2022) in applying the term T-OAE to the interval of the negative $\delta^{13}\text{C}$ excursion (Figs 2, 3).

The carbon isotope profile for the upper Pliensbachian – middle Toarcian of the Yorkshire coast (Fig. 2), one of the highest resolution global organic carbon ($\delta^{13}\text{C}_{\text{org}}$) records, comprises a composite of separate datasets derived from bulk organic matter sampled from different coastal sections (Cohen *et al.*, 2004; DB Kemp *et al.*, 2005; Littler *et al.*, 2010). Cohen *et al.* (2004) analysed samples from the *Dactyloceras tenuicostatum* to lowermost *H. bifrons* zones; their data are a composite from Hawsker Bottoms, Port Mulgrave and Saltwick Bay (Figs 1, 2). DB Kemp *et al.* (2005) analysed samples from the *D. tenuicostatum* and lower *Harpoceras serpentinum* zones; their data are a composite from Hawsker Bottoms and Port Mulgrave spliced at ‘bed’ 33 (Fig. 2). Littler *et al.* (2010) presented data from the *P. spinatum* and *D. tenuicostatum* zones (Pliensbachian–Toarcian boundary) at Hawsker Bottoms.

Thibault *et al.* (2018) included some additional $\delta^{13}\text{C}_{\text{org}}$ data for the *H. serpentinum* and *H. bifrons* zones in their summary curve compiled from the above sources. We have not included these data in our reference profile (Fig. 2) due to uncertainties in the sample positions and splicing. Van de Schootbrugge *et al.* (2020) used published data to construct a Yorkshire coast composite record and incorporated new low-resolution $\delta^{13}\text{C}_{\text{org}}$ results from below and above previously published curves. Their curve extends below and above our study interval, including values from the lower and upper Pliensbachian (*Prodactyloceras davoei* – *A. margaritatus* zones) and from the middle Toarcian (*H. bifrons* Zone to above the *Grammoceras thouarsense* Zone) but lacks stratigraphic resolution comparable to this study.

Low-resolution terrestrial wood ($\delta^{13}\text{C}_{\text{wood}}$) and compound-specific $\delta^{13}\text{C}$ records across the T-OAE interval at Hawsker Bottoms show negative CIEs that are smaller in magnitude (~1.5 – 5‰ in Yorkshire) compared to the associated bulk organic $\delta^{13}\text{C}$ records (Hesselbo *et al.*, 2000; French *et al.*, 2014). Nonetheless, coincident negative excursions in biomarkers from both marine and terrestrial plants demonstrate a carbon cycle perturbation that affected both the atmospheric and marine systems.

In strong contrast to the $\delta^{13}\text{C}_{\text{org}}$ data, bulk carbonate carbon isotopes ($\delta^{13}\text{C}_{\text{carb}}$) show no clear stratigraphic pattern in the Yorkshire succession due to a pervasive and highly variable diagenetic overprint in both limestones and organic-rich siliciclastic rocks (Jenkyns & Clayton, 1997). However, a small negative shift below a marked positive $\delta^{13}\text{C}_{\text{carb}}$ excursion at the top of the *C. exaratum* Zone is identifiable in scattered isotope data obtained from belemnite rostra (McArthur *et al.*, 2000; Bailey *et al.*, 2003; Gill *et al.*, 2011; Ullmann *et al.*, 2014; compilation of Korte *et al.*, 2015). A change in life habits has been proposed to explain the subdued nature of the $\delta^{13}\text{C}_{\text{carb}}$ signal recorded in belemnites which, nonetheless, preserve a strong negative $\delta^{13}\text{C}_{\text{org}}$ excursion of ~4‰ in the organic matrix of their rostra (Ullmann *et al.*, 2014).

Whole-rock Total Organic Carbon (TOC_{WR}) data for the upper Pliensbachian – middle Toarcian in Yorkshire have been published by several authors, including Jenkyns & Clayton (1997), Hesselbo *et al.* (2000), McArthur *et al.* (2008), Kemp *et al.* (2011), Ruvalcaba

Baroni *et al.* (2018) and McArthur (2019). The Yorkshire data presented by the last three of these sources are plotted in Figure 2. A TOC_{WR} maximum, with some values exceeding 10%, coincides with the T-OAE interval, a characteristic of many other NW European sections, although organic matter enrichment is not universal across Europe (Ruvalcaba Baroni *et al.*, 2018, fig. 3; Ramirez & Algeo, 2020, fig. 3; Kemp *et al.*, 2022b, fig. 2).

4. Pliensbachian – Toarcian boundary

Following Howarth (1973, 1992), the base of the Toarcian in North Yorkshire is placed at the bottom of the ‘Sulphur Band’ of Chownes (1968), which lies between the stratigraphically highest *Pleuroceras* and the stratigraphically lowest *Dactyloceras* (Howarth in Cope *et al.*, 1980; Hesselbo & Jenkyns, 1995; Littler *et al.*, 2010; Hesselbo & King, 2019), marking the base of the *D. tenuicostatum* Zone, *Protogrammoceras paltum* Subzone (Fig. 2). The Sulphur Band is a 15-cm-thick bed of pyrite-rich finely laminated carbonaceous mudstone (‘black shale’) with very low-angle cross-lamination and broad scour-and-fill structures towards the top (Salem, 2013). The bed displays a symmetrical grain-size variation from silt to planar laminated mud and back to silt. Sedimentary structures in the upper two-thirds of the bed have been partially destroyed by *Chondrites* and *Diplocraterion* burrows penetrating down from the overlying bioturbated siltstones. The Sulphur Band lies in the middle of ‘bed’ 43 of Hawsker Bottoms but is recognized as a discrete ‘bed’ 26 at Kettleless (Howarth, 1955). Subaerial weathering of pyrite in the mudstone generates the distinctive yellow ‘sulphur’ colour of the bed when exposed in outcrops.

Howarth (1973; in Cope *et al.*, 1980) and Powell (1984) assigned Hawsker Bottoms ‘beds’ 43 and 44 to the Cleveland Ironstone Formation. According to this placement, the Pliensbachian – Toarcian boundary falls within the Kettleless Member, and many authors have followed this convention (e.g. McArthur *et al.*, 2008; Littler *et al.*, 2010; Thibault *et al.*, 2018; Hesselbo & King, 2019; McArthur, 2019). However, these two ‘beds’ consist of carbonaceous mudstone interbedded with coarse mudstone and calcareous nodules, which are characteristic of the overlying Grey Shale Member of the Whitby Mudstone. For this reason, Howard (1985) and Trabucho-Alexandre *et al.* (2022) assigned these ‘beds’ to the Grey Shales and placed the base of the member at the top of ‘bed’ 42, a thin (13 cm) red ironstone. This is underlain by a 45-cm-thick calcareous sandstone (‘bed’ 41) at Hawsker Bottoms. We follow this definition (Fig. 2): ‘bed’ 43 contains the base of the Toarcian Stage at the base of the Sulphur Band, 33 cm above the base of the Grey Shale.

The Sulphur Band (also referred to as the ‘Lower Sulphur Band’ or ‘Sulphur Band 1’; Salem, 2013; Agbi *et al.*, 2015; McArthur, 2019) constitutes a carbon isotope minimum (< -28‰ $\delta^{13}\text{C}_{\text{org}}$) and TOC_{WR} maximum (up to 6.8%) at the top of the first trough within a broad double negative $\delta^{13}\text{C}_{\text{org}}$ excursion (Pliensbachian – Toarcian Boundary Event, Fig. 2) that spans Hawsker Bottoms ‘bed’ 40 to Port Mulgrave ‘bed’ 4 at Hawsker Bottoms (Littler *et al.*, 2010, fig. 2). The amplitude of the negative CIE spanning the stage boundary approaches 2.5‰ (Fig. 2). A second $\delta^{13}\text{C}_{\text{org}}$ minimum of similar magnitude occurs 1 m above, in a higher interval of pyritic laminated black shale (Port Mulgrave ‘beds’ 2 – 3) in the lower *P. paltum* Subzone; this ‘Middle Sulphur Band’ (Salem, 2013; Agbi *et al.*, 2015) or ‘Sulphur Band 2’ (McArthur, 2019) contains up to 4% TOC_{WR} .

A negative $\delta^{13}\text{C}$ excursion, with a double peak resolved in higher-resolution records, spans the stage boundary in many other

high-resolution carbonate and organic carbon records, including the Llanbedr (Mochras Farm) borehole (Wales; subsequently referred to as Mochras); the Lorraine Sub-basin (Luxembourg); Sancerre (France); Peniche (Portugal); Brasa and Cima Benon (Italy); Es Cosconar (Spain); Talghemt and Fom Tillicht (Morocco); Chacay Melehue (Argentina); and Inuyama (Japan) (Fig. 3; Caruthers *et al.*, 2014; Martinez *et al.*, 2017; Ikeda *et al.*, 2018; Rosales *et al.*, 2018; Boulila *et al.*, 2019; Ruebsam *et al.*, 2019; Ruebsam & Al-Husseini, 2020; Menini *et al.*, 2021; Al-Suwaidi *et al.*, 2022; Fleischmann *et al.*, 2022). This confirms the Pliensbachian – Toarcian Boundary Event (PIToBE) as being a key global chemostratigraphic marker, estimated to have had a duration of ~ 200 ka (Ruebsam *et al.*, 2014; Martinez *et al.*, 2017; Al-Suwaidi *et al.*, 2022).

5. Elemental chemostratigraphy – previous studies

Several authors reported partial geochemical analyses of Yorkshire upper Pliensbachian – middle Toarcian iron ores during the mid-nineteen to mid-twentieth centuries, as summarized by Whitehead *et al.* (1952) and Gad (1966). The compositions of three mudstone samples from the Jet Rock and Alum Shales were published by Dunham (1961). A more detailed geochemical study of the Yorkshire Lias was undertaken by Gad (1966) using wet chemical techniques, the main results of which were presented by Gad *et al.* (1969) and Catt *et al.* (1971). Major-element and semi-quantitative trace-element data were provided for 28 mudstones from upper Pliensbachian – middle Toarcian sections. Selected data were also included for a range of ironstones (Gad, 1966; Catt *et al.*, 1971).

Subsequently, Pye & Krinsley (1986) published major- and trace-element data, determined by X-ray fluorescence (XRF), for 26 mudstone samples from 15 beds through the Grey Shale – Alum Shales; these data were plotted stratigraphically by Imber *et al.* (2014). Maynard (1986) and Aggett (1990) reported microprobe analyses of berthierine and siderite from the Cleveland Ironstone at Staithes. Myers & Wignall (1987), Myers (1989) and Parkinson (1996) employed portable spectral gamma-ray spectrometry to generate U, K and Th profiles at 0.5 – 1 m resolution for the Grey Shale and Jet Rock, the Cleveland Ironstone Formation and the entire Pliensbachian – Toarcian of the Yorkshire coast, respectively. Young *et al.* (1990) plotted some whole-rock and electron microprobe mineral data from the Cleveland Ironstone, and Mücke & Farshad (2005) published XRF whole-rock and electron microprobe mineral data from the five main ironstone seams. Worden *et al.* (2020) presented QEMSCAN® scanning electron microscope – energy-dispersive X-ray spectroscopy (SEM-EDX) data demonstrating a predominance of ‘granular’ siderite and minor pore-filling Fe-rich clay, identified by X-ray diffraction (XRD) as berthierine, in a Cleveland Ironstone sample from an unspecified horizon.

Recent geochemical work, despite employing more sensitive instrumental methods and much higher sampling resolutions, has generally focused on limited suites of elements considered to provide palaeoenvironmental information, principally redox-sensitive trace metals (McArthur *et al.*, 2008; Harding in Ruvalcaba Baroni *et al.*, 2018; Thibault *et al.*, 2018; McArthur, 2019; Remírez & Algeo, 2020; Houben *et al.*, 2021) or isotopes (Jenkyns *et al.*, 2001; Cohen *et al.*, 2004; Pearce *et al.*, 2008; Nielsen *et al.*, 2011; Q Li *et al.*, 2021) but has included some major-element studies (Thibault *et al.*, 2018; Wang, 2022). Most recently, Kovács

et al. (2024) compiled the elemental data of Percival *et al.* (2015) and Thibault *et al.* (2018) and supplemented these with new Hg, TOC, carbon isotope and XRF data for 24 samples from the Pliensbachian–Toarcian boundary interval at Staithes and Port Mulgrave.

Remírez & Algeo (2020) subdivided the upper Pliensbachian – middle Toarcian (upper Staithes Sandstone to lower Alum Shale, *A. margaritatus* – *H. bifrons* zones) of the coast into five chemostratigraphic units: I – V (Fig. 2). These were loosely defined as being based on a ‘similar patterns of variation in multiple proxies’, derived from data published by McArthur *et al.* (2008), with new boron and gallium determinations. However, samples were characterized for a restricted number of constituents, generally those judged to have significance for the reconstruction of bottom-water and sediment redox conditions, palaeoproductivity and/or palaeosalinity. Comprehensive major and trace-element data were lacking.

Unit I of Remírez & Algeo (2020) comprises the Staithes Sandstone and Cleveland Ironstone formations, incorporating upper Pliensbachian strata (*A. margaritatus* and *P. spinatum* zones) and the lowest *P. paltum* Subzone of the basal Toarcian (Fig. 2). Unit II represents the lower part of the Grey Shale Member of the Whitby Mudstone Formation, comprising most of the *D. tenuicostatum* Zone, including the *P. paltum*, *D. clevelandicum*, *D. tenuicostatum* and mid-*D. semicelatum* subzones. Unit III contains the upper Grey Shale and the highly pyritic carbonaceous mudstones of the Jet Rock at the base of the Mulgrave Shale Member and extends from the mid-*D. semicelatum* Subzone to the top of the *C. exaratum* Subzone. It incorporates the large negative $\delta^{13}\text{C}_{\text{org}}$ excursion in the Jet Rock that defines the T-OAE. Unit IV comprises the lower half of the Bituminous Shales in the middle Mulgrave Shale, representing the lower *H. falciferum* Subzone. Unit V constitutes the upper Bituminous Shales and overlying Alum Shale Member, comprising the upper *H. falciferum* Subzone and most of the overlying *H. bifrons* Zone (*D. commune* Subzone).

Units I – V of Remírez & Algeo (2020) equate to Zones 1 – 4 of McArthur (2019): Units I, II = Zone 1; Unit III = Zone 2; Unit IV = Zone 3; and Unit V = Zone 4. These schemes show limited similarity to the geochemical ‘units’ derived by cluster analysis of hand-held XRF elemental data, TOC and $\delta^{13}\text{C}_{\text{org}}$ values, in a study of the coastal sections by Thibault *et al.* (2018), despite near-identical stratigraphic trends being apparent for constituents that are in common.

Below, we present a suite of elemental geochemical data derived from the upper Pliensbachian – middle Toarcian of the Dove’s Nest borehole and correlate these to published data derived from the classic Yorkshire coastal sections (Fig. 1c). The core provides a single vertical section through rocks that are directly comparable in facies and thickness to the adjacent outcrops (Trabucho-Alexandre *et al.*, 2022; Caswell & Herringshaw, 2023). Our study provides the first comprehensive elemental data suite for an extended Staithes Sandstone – Whitby Mudstone (Alum Shale) succession in North Yorkshire.

Major-element and selected trace-element data, combined with lithostratigraphy and carbon-isotope stratigraphy, provide the basis for the high-resolution correlation of the Dove’s Nest core to the coastal sections. The resulting integrated chemostratigraphic framework offers increased stratigraphic coverage and additional geochemical parameters to previous studies and provides new constraints on the environmental changes that occurred before, during and after the T-OAE in the Cleveland Basin.

6. Material and methods

6.a. Dove's Nest core

The Dove's Nest Farm North Shaft NS1 borehole (Fig. 1), located ~5.5 km south of Whitby, North Yorkshire (NZ 89297 05434; 0.62480° W, 54.43650° N), was drilled in February 2013 by Fugro Geoservices UK for the AngloAmerican Woodsmith Project (formerly Sirius Minerals). The drill site is now situated in Woodsmith Mine (<https://uk.angloamerican.com/the-woodsmith-project>). The cored vertical 251 m borehole sampled a representative Lower – Middle Jurassic succession between 125 and 220 m with full recovery.

The stratigraphy of the upper Pliensbachian (top Staithes Sandstone Formation) to middle Toarcian (lower Alum Shale Member, Whitby Mudstone Formation) in the Dove's Nest core has been described by Trabucho-Alexandre *et al.* (2022) and the trace-fossil assemblages were logged by Caswell & Herringshaw (2023, figs 2, 7). Technical details of the studied section of the core, including core box numbers and depth intervals, were provided in the Supplementary Material of Trabucho-Alexandre *et al.* (2022). The thickness of the middle and upper Lias Group formations in the core is approximately the same as that exposed on the coast between Hawsker Bottoms and Whitby. However, unlike the rocks exposed along the coast, the core provides a single, continuous vertical section through unweathered sedimentary rocks, with no structural complexity, and so it offers optimum potential for the preservation of primary geochemical signals.

6.b. Sampling

The Dove's Nest core was logged in 2013 (Trabucho-Alexandre *et al.*, 2022) and 276 samples were collected for geochemical analysis at 20 – 50 cm intervals between 126.18 and 219.06 m depth. For this study, a chip with a mass of ~1 g from each sample was taken and ground to a fine powder (c. 10 µm) using a Retsch agate mortar grinder RM100 at Durham University.

6.c. Geochemical analysis

Sample solutions were prepared from the dried powders using the lithium-metaborate fusion method of Jarvis (2003, section 7.3.3). The elemental composition of the solutions was determined by inductively coupled plasma-atomic emission spectrometry (ICP-AES) and ICP-mass spectrometry (ICP-MS) analyses using JY Ultima 2C and Agilent 7700x spectrometers at Kingston University London.

Major elements (Si, Ti, Al, Fe, Mn, Mg, Ca, Na, K and P) and selected trace elements (Ba, Cr, Sr and Zr) were determined by ICP-AES on the full sample suite (Atar, 2015). The Ca data have been reported previously by Trabucho-Alexandre *et al.* (2022), together with carbon isotope values for bulk organic matter ($\delta^{13}\text{C}_{\text{org}}$) and TOC_{WR} for the same samples. The last of these were calculated from acid-insoluble residue TOC values using CaCO_3 values derived from ICP-AES Ca determinations, based on the assumption that most Ca resides in carbonate (referred to herein as CaCO_3^e). Elemental data are reported here as weight per cent oxides for the major elements and as ppm (parts per million; µg/g) for trace elements (Supplementary Material Table S1). Total Fe is expressed as $\text{Fe}_2\text{O}_3\text{T}$. By reference to international reference materials run with samples, accuracy and precision for major elements determined by ICP-AES were judged to be generally <3% for major elements and <5% for trace elements.

An additional trace-element suite (Cs, Rb, Sc, Th, U, V and Y) was determined by ICP-MS in a subset of 98 lithium-metaborate fusion solutions, chosen at ~1 m intervals through the study interval (Supplementary Material Table S2). Splits of powders for this smaller sample suite were additionally prepared using partial digestion with aqua regia for the determination of Mo by ICP-MS (modified after Moor *et al.*, 2001). The ICP-MS data reported here are derived from the instrument data files of Atar (2015) with results for elements yielding poor accuracy and/or reproducibility rejected and reported values (ppm, parts per million; µg/g) recalculated to correct some errors identified in the original document. Accuracy and precision for elements determined by ICP-MS were judged to be generally <10%. Results for Mo are reported as Mo^* (Table S2) to reflect the greater uncertainty of these data, where many values are close to or below the limit of quantitative determination.

6.d. Data presentation

Stratigraphic variation in elemental chemistry can be obscured by the closed-sum nature of major-element percentage datasets, particularly where there are large fluctuations in a dominant mineral fraction. Increases in carbonate (Ca) and/or quartz (Si) will generate coincident falls in the values of most other constituents. Element ratios or normalization may be used to address this problem. Primary mineralogical controls on elements commonly used in chemostratigraphy of carbonaceous mudstones and element ratio grain-size and palaeoredox proxies have been summarized by LaGrange *et al.* (2020).

Aluminium and/or Rb are generally considered to be stable conservative elements and are favoured as the divisor to better reveal geochemical variation in the aluminosilicate and heavy mineral fractions or trace metals, independent of quartz or carbonate dilution (e.g. Algeo, 2004; Hermoso *et al.*, 2013; Fantasia *et al.*, 2018a, b; Ruvalcaba Baroni *et al.*, 2018; Thibault *et al.*, 2018; Xu *et al.*, 2018; Bennett & Canfield, 2020; Houben *et al.*, 2021; Gambacorta *et al.*, 2023). Alternatively, normalization to a standard shale, typically Post-Archean Average Shale (PAAS) (Taylor & McLennan, 2001) or average upper continental crust (Rudnick & Gao, 2014) and expression of element concentrations as enrichment factors (EF), where $\text{EF}_{\text{elementX}} = [(X/\text{Al})_{\text{sample}} / (X/\text{Al})_{\text{PAAS}}]$, are commonly used for plotting redox-sensitive trace-element data (e.g. Brumsack, 2006; Thibault *et al.*, 2018; Algeo & Liu, 2020; Tribouvillard, 2020; Yano *et al.*, 2020). Both approaches are adopted here.

The Chemical Index of Alteration (CIA) of Nesbitt & Young (1982) was calculated using molecular proportions:

$$\text{CIA} = [\text{Al}_2\text{O}_3 / (\text{Al}_2\text{O}_3 + \text{CaO}^* + \text{Na}_2\text{O} + \text{K}_2\text{O})] \times 100$$

where CaO^* is the amount of CaO incorporated in the silicate fraction of the rock, with a correction made for carbonate and apatite content.

Carbonate content varies substantially in the study section and is associated with a range of carbonate minerals including calcite, dolomite and siderite. CO_2 contents were not determined, preventing direct carbonate correction. CaO^* values were calculated using the method of McLennan (1993): CaO was corrected for phosphate using the $\text{CaO}/\text{P}_2\text{O}_5$ value of 1.625 of unweathered marine carbonate fluorapatite (Jarvis *et al.*, 1994). If the remaining number of moles was less than that of Na_2O , this CaO^* value was adopted. If the number of moles was greater than

Na₂O, CaO* was assumed to be equivalent to Na₂O. Since Ca is typically lost more rapidly than Na during weathering, this is likely to yield minimum CIA values, by up to about 3 units (McLennan, 1993).

Transition metal ratios (e.g. Ni/Co, V/Cr and V/Mo) have long been applied as palaeoredox proxies (e.g. Ernst, 1970; Jones & Manning, 1994; Piper & Calvert, 2009), but Algeo & Liu (2020) have demonstrated that they perform poorly compared to single element enrichment factors for such purposes. We provide limited new transition metal data here and generally do not make use of bimetal ratios of these. By contrast, the molar ratio of TOC to total phosphorus (P_T), commonly referred to as the C_{org}/P ratio, has become established as a robust palaeoredox proxy in sediments and sedimentary rocks (e.g. Algeo & Ingall, 2007; Algeo & Li, 2020; Papadomanolaki *et al.*, 2022). Data obtained from Dove's Nest may be compared to published results from elsewhere.

For the interpretation of bottom water redox condition, we use a four-stage classification scheme for deoxygenation modified from Algeo & Liu (2020) comprising: oxic (>2 mL O₂ L⁻¹), dysoxic (2 to ~0 mL O₂ L⁻¹), anoxic (~0 mL O₂ L⁻¹, Fe²⁺ > 0, H₂S = 0; also termed 'anoxic-ferruginous' or 'suboxic') and euxinic (0 mL O₂ L⁻¹, Fe²⁺ = 0, H₂S > 0, also termed anoxic-euxinic) conditions. It is commonly difficult to unambiguously separate the redox state of bottom waters as opposed to those of the underlying surface or shallow subsurface sediments based on bulk geochemistry – particularly in the rock record. Sulfidic ('euxinic') conditions necessary for pyrite formation, for example, may occur in sediments accumulating under fully oxygenated water columns, although pyrite framboid size offers a potential criterion to identify water-column euxinia (Wilkin *et al.*, 1996; Wignall & Newton, 1998; Rickard, 2019).

The distinction between oxic and dysoxic facies in sediments is generally made based on body fossils and ichnofabric rather than geochemical criteria, but anoxic and euxinic redox facies are associated with geochemical reactions that can potentially leave diagnostic signals in the sediment. However, it is recognized that redox conditions in an area are typically subject to temporal variation on a range of time scales and of varying magnitude. This variation may generate mixed geochemical and other proxy records in the sedimentary record. Sedimentological evidence for at least weak or intermittent oxygenation in the form of fossil benthic fauna and bioturbation in conjunction with geochemical proxies indicating euxinic conditions is common (Algeo & Liu, 2020). This pattern may be due, for example, to the transient influx of oxygenated hyperpycnal flows into a basin or seasonal overturning of the water column, resulting in short-term colonization of an otherwise lifeless seafloor, or to longer term oxygenation events.

Different geochemical redox proxies respond at different thresholds to redox changes and acquire a signature characteristic of a specific redox state at different rates. It is essential therefore to combine data from multiple proxies to reliably identify the dominant redox conditions during the deposition of a bed.

6.e. Statistical analysis

Quantitative assessment of inter-element relationships was made by Pearson linear correlation and multivariate principal component analysis (PCA) of the geochemical data using Past 4.11 software (Hammer *et al.*, 2001). Constant-sum constraints of the elemental data (Aitchison, 1986) were removed using a centred log-ratio (clr) transformation prior to statistical analysis.

6.f. Elemental chemostratigraphy

Published elemental profiles for the Yorkshire coastal outcrops (McArthur *et al.*, 2008; Ruvalcaba Baroni *et al.*, 2018; Thibault *et al.*, 2018; McArthur, 2019; Remírez & Algeo, 2020; Wang, 2022) together with carbon isotopes and TOC data (Jenkyns & Clayton, 1997; Hesselbo *et al.*, 2000; Cohen *et al.*, 2004; DB Kemp *et al.*, 2005; McArthur *et al.*, 2008; Littler *et al.*, 2010; Kemp *et al.*, 2011; McArthur, 2019) provide the basis for a bed-scale correlation of the lower Whitby Mudstone Formation (lower Toarcian *Dactyloceras tenuicostatum* – lower *H. bifrons* zones) to the Dove's Nest core. However, only very limited and widely spaced geochemical data are available for the upper Pliensbachian Staithes Sandstone and Cleveland Ironstone formations on the coast (Gad, 1966; McArthur *et al.*, 2008; Thibault *et al.*, 2018; McArthur, 2019; Remírez & Algeo, 2020; Kovács *et al.*, 2024), where the Kettleless Member in particular shows significant lithological and thickness variation between sections (e.g. Howarth, 1955 pl. 13). Chemostratigraphic correlation of the lower section of Dove's Nest to the coast is only possible at member scale, but the core data offer new insights into the stratigraphy of the succession.

For consistency, we employ the five chemostratigraphic units (I – V) of Remírez & Algeo (2020) with minor modification and designate 14 subunits (including 4 subdivisions of the T-OAE interval: IIIa – d; Fig. 2) derived from the recognition of patterns in our more comprehensive and stratigraphically extended geochemical data from the Dove's Nest core (Tables S1, S2).

7. Results – δ¹³C_{org} and TOC stratigraphy of Dove's Nest

7.a. Upper Pliensbachian – lower Toarcian

Organic carbon isotope and TOC_{WR} curves for the upper Pliensbachian – middle Toarcian of the Dove's Nest core have been described by Trabucho-Alexandre *et al.* (2022, fig. 2). These data are reviewed here to provide a stratigraphic framework and context for the elemental chemostratigraphy.

Trabucho-Alexandre *et al.* (2022) demonstrated that the carbon isotope and TOC profiles, when combined with lithostratigraphy, provide a sound basis for the correlation of the Dove's Nest core with the Yorkshire coastal succession (Fig. 2). The data from the Dove's Nest core are fully compatible with previous high-resolution studies from the Yorkshire coast, confirm a consistent regional chemostratigraphy, and offer new higher-resolution reference profiles for the upper Pliensbachian *A. margaritatus* – *P. spinatum* zones and for the lower middle Toarcian *H. bifrons* Zone.

Carbon isotopes and organic carbon display large amplitude variation through the study interval at Dove's Nest: –31.5‰ to –24.5‰ δ¹³C_{org} and 0.2 – 9.2% TOC_{WR}, respectively (Fig. 2). Employing the standard Yorkshire coast lithostratigraphy and biostratigraphy (Simms *et al.*, 2004b; Hesselbo & King, 2019), key features of the long-term trends, from bottom to top, are:

- (1) The upper Staithes Sandstone Formation and Cleveland Ironstone Penny Nab Member (*A. margaritatus* Zone) show a somewhat erratic plateau in the δ¹³C_{org} profile, with values of –25.7 ± 0.5‰ (Fig. 2). Maximum values for the section of ~ –25‰ occur at the top of the Penny Nab Member in the *A. gibbosus* Subzone. This maximum corresponds to the level of the Late Pliensbachian Event (LPIE) positive CIE (Korte & Hesselbo, 2011; De Lena *et al.*, 2019; Cramer & Jarvis, 2020; Hollaar *et al.*, 2023; Zhang *et al.*, 2023), although the δ¹³C_{org} peak at Dove's Nest is small and likely

truncated by the disconformity at the base of the Pecten Seam. A much larger positive excursion of $\delta^{13}\text{C}_{\text{wood}}$ values ($>4\%$) has been recorded from the upper *A. margitatus* Zone of Robin Hood's Bay (Korte & Hesselbo, 2011). TOC_{WR} contents show a stepped rise from $0.7 \pm 0.3\%$ in the Staithes Sandstone to $1.7 \pm 0.6\%$ at the top of the Penny Nab.

- (2) Carbon isotope values decline from -24.8% to -26.9% $\delta^{13}\text{C}_{\text{org}}$ through the Kettleless Member (*P. spinatum* Zone) and a marked double negative excursion with values falling to -29.6% spans the Cleveland Ironstone – Whitby Mudstone formation boundary. This is the PIToBE negative CIE (Littler *et al.*, 2010; Fantasia *et al.*, 2019; Ruebsam *et al.*, 2019; Cramer & Jarvis, 2020; Al-Suwaidi *et al.*, 2022; Ullmann *et al.*, 2022; Bodin *et al.*, 2023). TOC_{WR} contents display a concave pattern (Fig. 2), falling from 1.8% at the base to a minimum of 0.6% in the middle of the Kettleless Member and then rising back to 1.5% at the top.
- (3) $\delta^{13}\text{C}_{\text{org}}$ values plateau at $25.8 \pm 0.3\%$ in the Grey Shale Member (upper *P. paltum* – lower *D. tenuicostatum* subzones) above the PIToBE, accompanied by a TOC_{WR} rise from 1.2% to 2.2%.
- (4) A sharp change in the geochemical profiles occurs with the appearance of black laminated carbonaceous mudstones ('black shales') in the middle of 'bed' 31 in the mid-*D. semicelatum* Subzone (Fig. 2). This marks the base of a broad large negative $\delta^{13}\text{C}_{\text{org}}$ excursion in the upper Grey Shale and Jet Rock beds of the lower Mulgrave Shale Member, with values falling to -31.5% , accompanied by a large TOC_{WR} peak and values up to 9.2% (Fig. 2). This is an expression of the T-OAE (Section 3), which terminates at the top of the *C. exaratum* Subzone.
- (5) $\delta^{13}\text{C}_{\text{org}}$ values rise and plateau at $-27.4 \pm 0.4\%$ in the Bituminous Shales (*H. falciferum* Subzone), continuing upward into the lower Alum Shale (*H. bifrons* Zone) and are accompanied by generally falling TOC_{WR} from 3.9% to 1.8%. A coincident small, stepped rise in $\delta^{13}\text{C}_{\text{org}}$ and fall in TOC_{WR} occurs in the upper Bituminous Shales above 'bed' 44 (Peak Stones) in the mid-*H. falciferum* Subzone (Fig. 2).
- (6) An interval of elevated TOC values bounded at the bottom and top by peaks of up to 4% occurs between 'beds' 48 (Ovatum Band) and 50, the interval of the Hard Shales (lower *D. commune* Subzone) at the base of the Alum Shale Member.

The most prominent features of the chemostratigraphy, therefore, are the presence of two intervals with negative $\delta^{13}\text{C}_{\text{org}}$ excursions (Fig. 2): the PIToBE and the T-OAE, the latter accompanied by a thick interval of laminated carbonaceous mudstones with high TOC contents. Additionally, a large step down to lower $\delta^{13}\text{C}_{\text{org}}$ and step up to higher TOC contents in the long-term profiles occur at the base of the T-OAE interval. It is notable that $\delta^{13}\text{C}_{\text{org}}$ values below the T-OAE are consistently $\sim 1\%$ higher than the average Phanerozoic black shale value of -27% (Meyers, 2014), while the succession above yields marginally lower values than this average.

TOC_{WR} values in the lower section lie close to an average shale value of 0.8% (Law, 1999), while those above are significantly higher, at $>2\%$ (characteristic of a very good petroleum source rock). Average black shale TOC_{WR} values of 3% (Vine & Tourtelot, 1970) are exceeded in the three laminated mudstones of the Sulphur Bands (SB1 – 3) in the Grey Shale (Fig. 2), throughout the

upper Grey Shales to mid-Mulgrave Shale, and at the bottom and top of the Hard Shales.

7.b. Pliensbachian – Toarcian boundary

The amplitude of the PIToBE negative CIE approaches 4% $\delta^{13}\text{C}_{\text{org}}$ at Dove's Nest (Fig. 2). The Sulphur Band (SB1) is not obvious in the core, probably due to the lack of weathering. However, a distinctive bioturbated layer with abundant *Chondrites* burrows at ~ 185 m is similar to that developed above the Sulphur Band in the top of 'bed' 43 at Kettleless and Runswick Bay (Trabucho-Alexandre *et al.*, 2022, fig. 4). The Pliensbachian–Toarcian boundary is therefore placed below the *Chondrites* interval, at 185.5 m in the core. This placement of the boundary is consistent with the $\delta^{13}\text{C}_{\text{org}}$ record (Fig. 2): a large negative excursion is developed below the boundary (minimum -29.6% at 185.75 m) and a second negative excursion above it (minimum -27.8% at 184.41 m).

The $\delta^{13}\text{C}_{\text{org}}$ minimum identified at Dove's Nest occurs in an Fe-rich (12% Fe_2O_3) calcareous (8.9% CaCO_3^e) sample at 185.75 m that is only moderately enriched in TOC_{WR} (1.5%). Coincident enrichment in Fe, Mg, Ca and Mn indicates the presence of siderite. Comparison to the succession at Hawsker Bottoms (Littler *et al.*, 2010, fig. 2) suggests that our sampling missed the Sulphur Band in the core, while sampling the sideritic ironstone a short distance below (Hawsker Bottoms 'bed' 42), or the successions differ.

7.c. Toarcian Oceanic Anoxic Event (T-OAE)

The thickness (9.5 m) of the lower Toarcian $\delta^{13}\text{C}_{\text{org}}$ negative excursion constituting the T-OAE in the Dove's Nest core, which occurs between 175.1 and 165.2 m with $\delta^{13}\text{C}_{\text{org}}$ values of -31.5% to -25.8% (Fig. 2), is very similar to that in the curves of Hesselbo *et al.* (2000) and DB Kemp *et al.* (2005), which were derived from the lower Toarcian outcrops at Hawsker Bottoms and Port Mulgrave (=mid-'bed' 31 to top 'bed' 38) on the Yorkshire coast. The shape of the excursion, which extends from the mid-*D. semicelatum* to upper *C. exaratum* subzones and the $\delta^{13}\text{C}_{\text{org}}$ values, are most similar to those of Hesselbo *et al.* (2000); values reported by DB Kemp *et al.* (2005) are more ^{13}C -depleted, down to -33.2% .

The Dove's Nest $\delta^{13}\text{C}_{\text{org}}$ profile is overlain on the Yorkshire coast composite curve and correlated to a compilation of published upper Pliensbachian – middle Toarcian carbon isotope data (Oliveira *et al.*, 2006; Hesselbo *et al.*, 2007; Hermoso *et al.*, 2009a, 2009b, 2012, 2013; Silva *et al.*, 2011; Peti *et al.*, 2017; Xu *et al.*, 2018; Fantasia *et al.*, 2019; Storm *et al.*, 2020; Ullmann *et al.*, 2022) for three well-characterized European sections in Figure 3. This exemplifies how the PIToBE and T-OAE offer robust tie points for correlation that complement the biostratigraphy.

The $\delta^{13}\text{C}_{\text{org}}$ excursion interval at Dove's Nest corresponds to a large TOC_{WR} peak with values of up to 9.2% (Fig. 2), which extends from the base of the T-OAE interval to the top of the Jet Rock at 164.0 m, the top calcareous beds of which (Top Jet Dogger and Millstones, 'beds' 39, 40) exhibit small $\delta^{13}\text{C}_{\text{org}}$ and TOC_{WR} peaks.

8. Elemental chemostratigraphy of Dove's Nest

Major-element and selected trace-element profiles for the upper Pliensbachian – middle Toarcian of the Dove's Nest core are plotted in Supplementary Material Figures S1 and S2 and selected data ratioed to Al or Th are plotted in Figures 4 and 5. These profiles illustrate a clear litho-geochemical differentiation of the

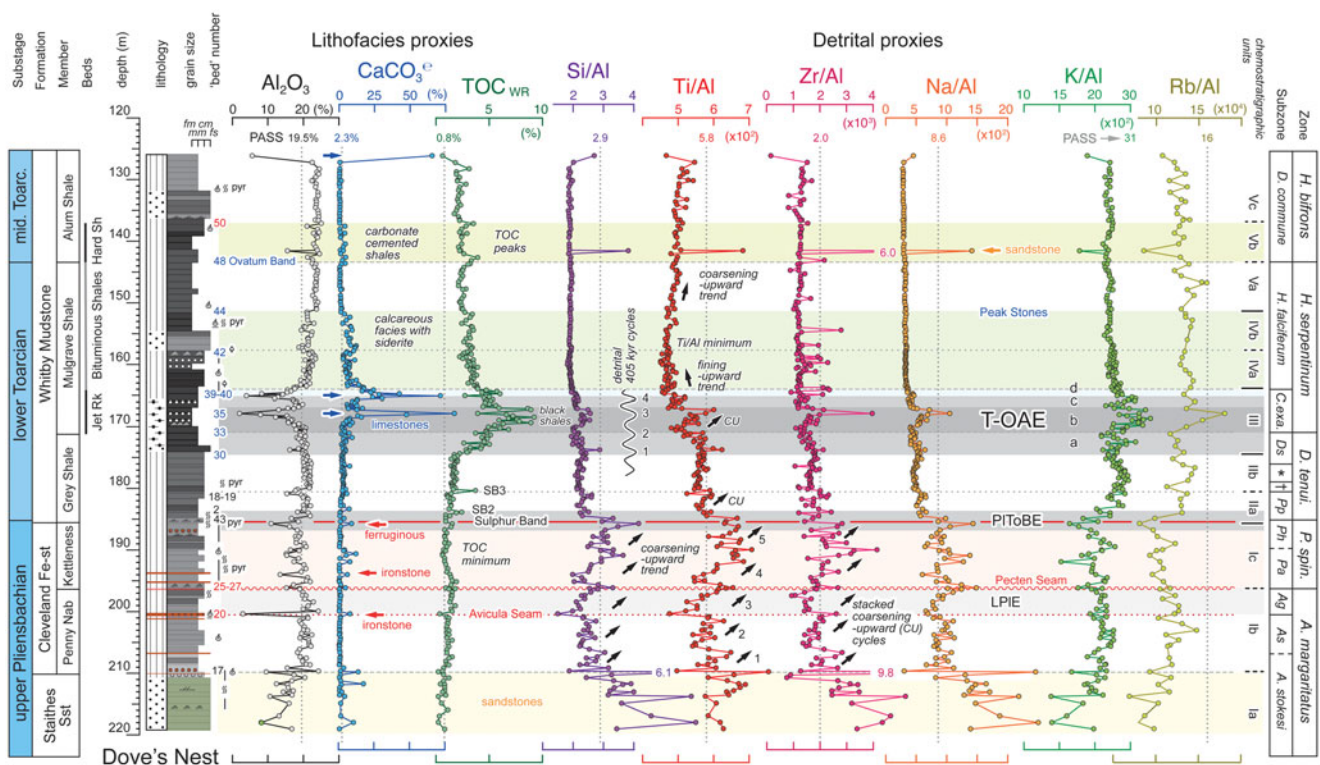


Figure 4. Geochemical profiles for lithofacies proxies Al_2O_3 (aluminosilicates, principally clay minerals), CaCO_3^e (carbonates; calcite, siderite) and TOC_{WR} (organic fraction) through the upper Pliensbachian – middle Toarcian of the Dove’s Nest core, with selected detrital proxies. ‘Bed’ numbers, names and biostratigraphy are derived from chemostratigraphic correlation to Hawsker Bottoms for the Pliensbachian (Howarth, 1955) and a Whitby composite section for the Toarcian (Howarth, 1962, 1973, 1992): red, sideritic beds; blue, limestones; and black other beds (see Fig. 2). Vertical dotted lines and numbers are reference values for Post-Archean Average Shale (PASS; = average mud of Taylor & McLennan, 2001). Prominent limestone ‘bed’ 35 (Whale Stones) and ‘beds’ 39 – 40 (Top Jet Dogger and Millstones) are clearly expressed by their high CaCO_3^e contents. Significant shifts in the elemental (Figs S1, S2) and element-ratio profiles (Figs 4, 5) combined with coincident changes in $\delta^{13}\text{C}_{\text{org}}$ and TOC (Fig. 2) are used to define the chemostratigraphic units (see text), modified from the scheme of Remírez & Algeo (2020). LPIE = Late Pliensbachian Event; other abbreviations as Figure 2. Detrital proxies show multiple stacked CU cycles superimposed on a longer-term fining-upward trend through the top Staithes Sandstone to mid-Cleveland Ironstone, followed by a marked upward increase in grain size comprising 3 stacked CU cycles (cf. Macquaker & Taylor, 1996). Cycle 3 is most prominent and coincides with an interval of high $\delta^{13}\text{C}_{\text{org}}$ and TOC_{WR} values ascribed to the LPIE. The base of the Whitby Mudstone is a sharp facies break to clay-mineral dominated sediments illustrated by a steep rise in K/Al, Rb/Al and Cs/Al (not plotted) ratios. The T-OAE is expressed by a sharp increase and peak in TOC_{WR} (maximum 9.2%), although elevated organic matter contents continue upward through the Whitby Mudstone. Upward-coarsening, 405 ka cycles in the Jet Rock (Si/Al profile) derived from cycle analysis of the coastal section by Thibault *et al.* (2018, fig. 2) are also displayed in the Dove’s Nest record.

regional lithostratigraphic units identified in the core based on sedimentological criteria, carbon isotope and TOC profiles (Trabucho-Alexandre *et al.*, 2022). The elemental chemistry offers additional criteria for the identification of marker beds. It provides evidence of significant stratigraphic changes in sediment composition that do not necessarily coincide with lithostratigraphic unit boundaries but are considered to have palaeoenvironmental significance.

The chemostratigraphic units proposed by Remírez & Algeo (2020) are readily identified in the Dove’s Nest core. The succession is further divided here, with a total of 14 chemostratigraphic intervals recognizable on the $\delta^{13}\text{C}_{\text{org}}$ and TOC_{WR} profiles (Fig. 2) but characterized by a wide range of elemental properties (Figs 4, 5, S1, S2): Unit I, which was not sampled in detail for previous geochemical studies, is divided into three subunits: Ia corresponds to the top of the Staithes Sandstone, Ib to the Penny Nab Member of the Cleveland Ironstone and Ic to the Kettlecess Member. The base of Unit II is taken immediately above the base of the Grey Shale of the Whitby Mudstone at the correlated level of the Sulphur Band. The unit comprises Subunits IIa and b; the base of IIb is placed at the step increase in TOC_{WR} associated with the laminated black shale of SB3.

Unit III, the interval of the T-OAE, which corresponds to the top of the Grey Shale and the Jet Rock at the base of the Mulgrave Shale, is divided into four subunits based primarily on the $\delta^{13}\text{C}_{\text{org}}$ curve but coincident with significant shifts in the elemental chemostratigraphy (Figs 4, 5). Subunit IIIa corresponds to the main falling limb of the negative $\delta^{13}\text{C}$ excursion, ‘phase A’ of Thibault *et al.* (2018). Subunit IIIb is the $\delta^{13}\text{C}$ minimum (‘phase B’), and IIIc is the rising limb of the CIE (‘phase C’). Subunit IIId is the small $\delta^{13}\text{C}$ peak immediately above the negative excursion interval, comprising the top Jet Rock (‘beds’ 39, 40; Top Jet Dogger and Millstones) in the coastal sections.

Unit IV constitutes the lower Bituminous Shales characterized by high TOC content and a low plateau in $\delta^{13}\text{C}$ values. It is divided into a lower subunit (IVa) with falling TOC and an upper subunit (IVb) with no long-term TOC trend. Unit V is divided into three subunits: Va corresponds to the upper Bituminous Shales, Vb to the Hard Shales at the base of the Alum Shale Member, an interval of carbonate-cemented shales with elevated TOC contents (Figs 2, 4) and Vc to the ‘Main Alum Shale’ beds.

The litho- and biostratigraphic framework, sedimentology and geochemical characteristics of the chemostratigraphic units are described below.

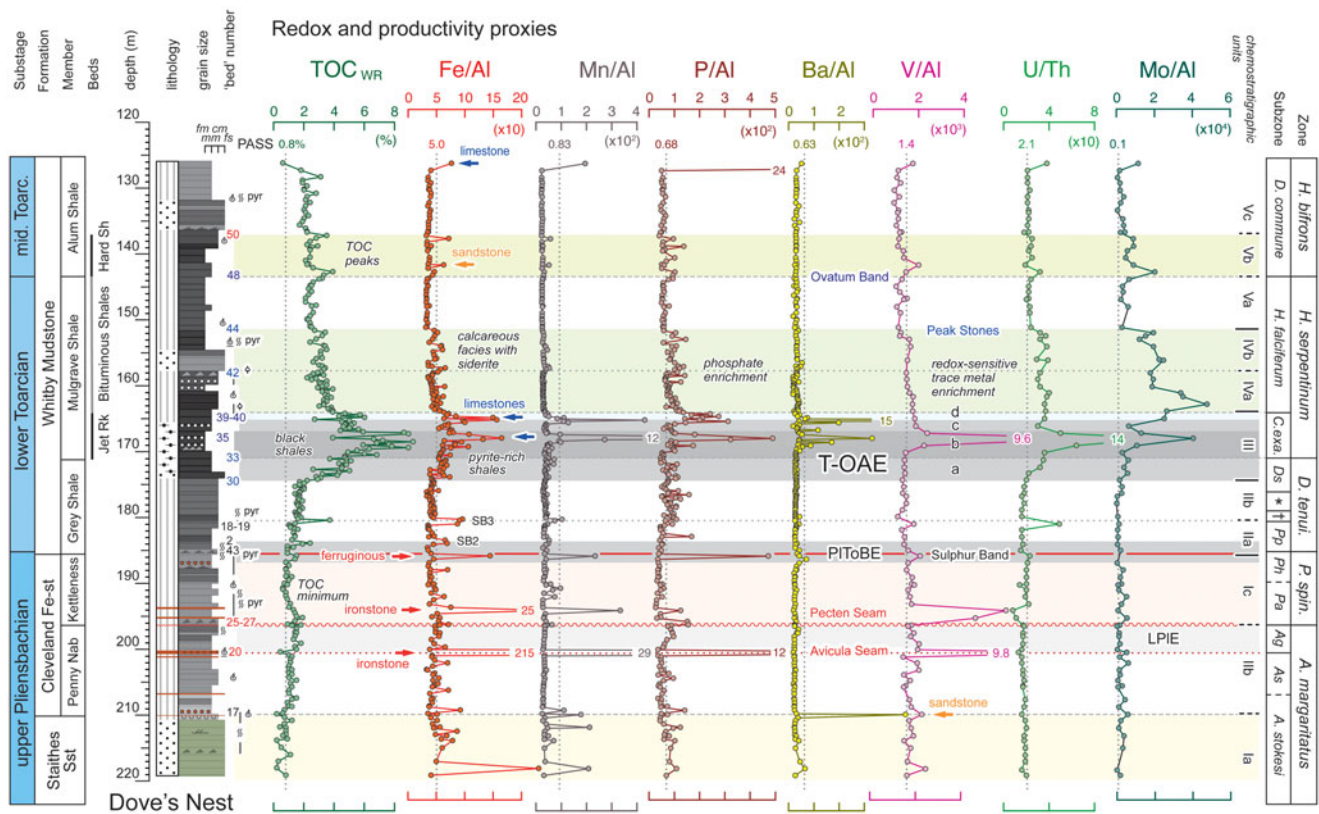


Figure 5. Geochemical profiles for redox and productivity proxies through the upper Pliensbachian – middle Toarcian of the Dove's Nest core. Stratigraphic framework as in Figure 4. SB2 – SB3 are the middle and upper Sulphur Bands, consisting of laminated pyritic carbonaceous mudstones.

8.a. Unit I Staithees Sandstone and Cleveland Ironstone

The lowest beds sampled during this study are assigned to the uppermost Staithees Sandstone Formation (*A. stokesi* Subzone, Fig. 2; Powell, 1984, 2010; Howard, 1985; Hesselbo & Jenkyns, 1995; Hesselbo & King, 2019). In the coastal sections, the formation consists of bioturbated fossiliferous, fine- to medium-grained, micaceous, calcareous sandstones and sandy siltstones. At outcrop, colours range from blue-grey when fresh to yellow-brown when weathered. Thicker sandstones are commonly cross-bedded, including hummocky cross-stratification (HCS). Thinner sandstone sheets have erosional bases and fine-upward to mudstone. Parallel lamination, low-angle cross-lamination and wave-ripple lamination are common in the sandstones where not destroyed by bioturbation. Sideritic and calcitic concretions are present in the more argillaceous beds. The sandstones were deposited from sediment-laden, storm-surge and ebb currents in inner- and mid-shelf settings (Powell, 2010). The formation is 28.6 m thick in the type section at Staithees and 25.7 m at Hawsker Bottoms (Howard, 1985).

The Staithees Sandstone is interpreted to have accumulated predominantly in a shoreface environment above storm wave-base, likely 25 – 30 m depth in an epeiric setting (Walker & Plint, 1992; Immenhauser, 2009), followed by long-term deepening through the Cleveland Ironstone, which was deposited mostly below storm wave-base (Van Buchem & Knox, 1998). Following Howard (1985), the base of the Cleveland Ironstone Formation at Hawsker Bottoms is placed at the base of 'bed' 17 of Howarth (1955), where hard ferruginous and calcareous sandstone

('bed' 16) passes up into mudstone ('bed' 17). This lies towards the summit of the *A. stokesi* Subzone (*A. margaritatus* Zone) of the lowest upper Pliensbachian (Hesselbo & Jenkyns, 1995).

Blue-grey coarse mudstones and very fine sandstones predominate from the base of the Dove's Nest core study interval at 223.64 m. Cross-lamination and lenticular bedding are common. A lithological change to very thin – thin beds of grey medium- to coarse-grained mudstone at 209.7 m is correlated to the base of 'bed' 17 at Hawsker Bottoms (Fig. 2), marking the base of the Cleveland Ironstone Formation (Howard, 1985). The Staithees Sandstone in the core contains more mud than at the coast and the sandstones are finer and thinner; the medium to thick HCS beds of the coastal exposures are absent. By comparison to the coast, the 13.5 m thick section studied at Dove's Nest represents the upper half of the formation.

8.a.1. Subunit 1a (Staithees Sandstone) 219.1 – 209.7 m

Few geochemical data are available for the Staithees Sandstone from the coast: Gad (1966) analysed one sample from Staithees ('bed' 12 of Howarth, 1955) and McArthur (2019) and Ramirez & Algeo (2020) reported a partial analysis of another sample from the same locality ('bed' 17). The formation lies within chemostratigraphic Unit I of the latter authors (Fig. 2). We distinguish the Staithees Sandstone as Subunit 1a (base not defined), which is characterized by the lowest and most erratic Al_2O_3 , TiO_2 , K_2O , Cs, Rb, Sc and Th values (typical phyllosilicate-associated elements) and low TOC and U contents (Figs S1, S2). Coarse detrital mineral proxy elements SiO_2 (quartz), Na_2O (Na-plagioclase) and Zr (zircon) are

notably enriched (Fig. S1), up to 70%, 1.8% and 320 ppm, respectively.

Very high but stratigraphically upward decreasing values of Si/Al, Zr/Al and Na/Al with rising K/Al, Cs/Al and Rb/Al (e.g. Fig. 4) are interpreted to reflect a broad fining-upward trend towards a sharp facies break at the formation top. Beds containing carbonate concretions are revealed by isolated spikes in CaO and MnO, the former representing up to 17% CaCO₃^e (Fig. 4). A weakly mineralized calcareous 'ironstone' (14% Fe₂O₃T, 5.7% CaO) was sampled at 218.02 m. Elevated MnO (0.11%) and a lack of Mg enrichment point to a likely oxide – hydroxide (e.g. goethite) mineralogy in this bed. The sampling resolution was insufficient to resolve clear bed-scale trends in this part of the succession.

8.a.2. Subunit 1b (Penny Nab Member, Cleveland Ironstone) 209.7 – 196.3 m

In the type area of the Cleveland Hills, the Cleveland Ironstone Formation contains thick ironstone beds ('seams') that were mined extensively in the nineteenth and early twentieth centuries (Hallimond *et al.*, 1925; Whitehead *et al.*, 1952; Chowns, 1968). The ironstones thin and the intervening mudstones thicken to the SE, where the formation consists dominantly of silty mudstones with interbedded thin seams of sideritic and berthierine-rich ('chamosite') oolitic ironstone (Howard, 1985; Hesselbo & Jenkyns, 1995). The latter constitute up to 33% of the stratal thickness of the formation in north Cleveland, decreasing to only 5% at Hawsker Bottoms (Chowns, 1966, 1968; Howard, 1985), immediately to the NE of Dove's Nest (Fig. 1).

Regional ironstone marker beds (Fig. 2) include the Osmotherley ('bed' 18), Avicula ('bed' 20) and Raisdale ('bed' 23) seams. A fourth marker bed, the Two Foot Seam, is absent at Hawsker Bottoms due to the disconformity at the base of the Pecten Seam ('beds' 25 – 27). The seams cap coarsening-upward cycles typically 2 – 5 m thick, with individual cycles being laterally continuous over much of the basin (Shalaby, 1980; Rawson *et al.*, 1983; Howard, 1985). The ironstones have been interpreted to represent marine flooding surfaces (Young *et al.*, 1990) with each cycle constituting an individual depositional sequence, incorporating 0.1 – 1.0 m thick parasequences (Macquaker & Taylor, 1996).

Howard (1985) defined two members in the Cleveland Ironstone, the Penny Nab (top *A. margaritatus* Zone) and Kettleless (*P. spinatum* Zone) separated by the base Pecten Seam disconformity. The base of the Penny Nab Member is formed by a transgressive lag of reworked and bored carbonate nodules, internal moulds of the ammonite *Amaltheus stokesi* (Sowerby) and eroded and bored belemnites. The Penny Nab Member consists dominantly of medium- to coarse-grained mudstone and argillaceous silty sandstone with interbedded thin seams of oolitic ironstone. The member is built up of five small-scale cycles. The lowest three coarsen upward and are capped by ironstones, while the upper two are erosionally truncated below oolitic ironstone seams (Howard, 1985; Young *et al.*, 1990).

The Kettleless Member represents the ironstone facies that dominate the upper Cleveland Ironstone in its type area: in north and west Cleveland the member consists entirely of oolitic ironstone. The base of the Kettleless Member (*P. spinatum* Zone) rests with an angular unconformity on the Penny Nab Member across the whole of the Cleveland Basin (Chowns, 1966; Howard, 1985). The top of the Penny Nab Member has been progressively removed by increasing erosion towards the south-east of the basin, with a whole parasequence missing in the Hawsker Bottoms

section. To the east and southeast, the ironstone interfingers with and undergoes a lateral facies change into coarse-grained mudstone and subordinate very fine-grained sandstone. Minor coarsening-upward cycles, 0.35 – 2.5 m thick, are capped by nodular siderite mudstone.

The number of cycles within the member decreases to the NW from a maximum of six at Hawsker Bottoms. Sedimentary facies in the two members have been interpreted to reflect the progradation of sediments from the NW during deposition of the Penny Nab followed by a switch to progradation from the SE for the Kettleless (Young *et al.*, 1990).

Trabucho-Alexandre *et al.* (2022) placed the base of the Cleveland Ironstone at 210.15 m in the Dove's Nest core. Based on our geochemical data, we place it slightly higher at 209.7 m corresponding to a level (sample 209.67) marking a sharp fall in SiO₂ and rise in Al₂O₃ (Fig. S1) indicative of a significant increase in clay mineral content and representing a lithological transition to mudstone. The immediately underlying sample at 209.81 m shows very high Si/Al, Ti/Al and Na/Al ratios (Fig. 4) with a spike of 2300 ppm Ba and elevated MnO (Fig. S1) suggesting the presence of a former redox boundary. The Cleveland Ironstone Formation is 24.2 m thick in the core, very similar to the 23.4 m thickness recorded at Hawsker Bottoms by Howard (1985). Very thin to thin beds of grey medium- to coarse-grained mudstones dominate this interval. Beds have sharp erosional bases overlain by siltstone lags and are commonly bioturbated.

Five ironstone horizons were identified visually in the lower 13.4 m of the Cleveland Ironstone at Dove's Nest by Trabucho-Alexandre *et al.* (2022) which was ascribed to the Penny Nab Member. The thickest and most prominent ironstone was sampled at 200.39 m and coincides with a minimum and subsequent step increase in TOC_{WR} values (Fig. 2) and a marked breakpoint in the Si/Al, Ti/Al, Zr/Al and Na/Al profiles (Fig. 4). This ironstone is particularly fossiliferous with a prominent oolitic texture and has been correlated to the Avicula Seam at the top of the *Amaltheus subnodosus* Subzone (Trabucho-Alexandre *et al.*, 2022).

The high 47.2% Fe₂O₃ but low SiO₂ (4.9%) and Al₂O₃ (2.9%) contents of the Avicula Seam in the core point to dominant siderite mineralogy, with no significant pyrite observed, while coincident high MgO, MnO and CaO contents (Fig. S1) are indicative of associated magnesite and rhodochrosite substitution typical of Cleveland Ironstone siderites (Maynard, 1986; Aggett, 1990). Recalculation of the Dove's Nest Avicula Seam analysis yields a total carbonate content of 89% with a composition of 76.5% FeCO₃, 13.8% MgCO₃, 8.6% CaCO₃ and 1.1% MnCO₃. This corresponds closely with electron microprobe analyses of Cleveland Ironstone siderites obtained by Aggett (1990): 77.8 – 79.7% FeCO₃, 10.8 – 13.9% MgCO₃, 7.0 – 8.9% CaCO₃ and 0.8 – 1.3% MnCO₃. Based on a revision of the carbonate content (previously reported as 7.72% CaCO₃ based solely on the Ca value; Trabucho-Alexandre *et al.*, 2022) to accommodate siderite rather than calcite, the TOC_{WR} value calculated for this sample is 0.37%.

The siderite-dominated mineralogy of the Avicula Seam at Dove's Nest is consistent with its equivalents in the coastal successions described by Chowns (1968) and Mücke & Farshad (2005), although Gad (1966) emphasized the relatively berthierine-rich (chamosite) composition of some intervals within the 'bed'. However, significant mineralogical and geochemical variation occurs within the 60 cm thick seam at Staithees (Gad, 1966; Catt *et al.*, 1971) and siderite replacement of berthierine ooids and groundmass is commonly extensive in the Cleveland Ironstone

Formation (Hallimond *et al.*, 1925; Kearsley, 1989; Aggett, 1990; Mücke & Farshad, 2005).

Elevated P and P/Al (Figs 5, S1) point to the presence of associated phosphates, as observed in the Avicula Seam elsewhere (Young *et al.*, 1990). The high V/Al ratio (Fig. 5) is consistent with the general V enrichment in the ironstones (Gad, 1966; Mücke & Farshad, 2005). A high Th/K ratio (Table S1) compared to the associated mudstones is also worth noting, as generally observed in Cleveland Basin ironstones (Parkinson, 1996), which has been attributed to the presence of Th-rich kaolinite derived from a tropically weathered source area (Myers, 1989). Despite some other samples from the Penny Nab showing limited Fe enrichment (>10% Fe₂O₃; Fig. S1), none of these display significant deviations in other constituents that characterize the Avicula Seam ironstone (Figs S1, S2).

The Avicula Seam marks the top of a 5 m thick interval of increasing upward Si/Al, Ti/Al, Zr/Al and Na/Al values that fall sharply at, or immediately above, the seam (Fig. 4). This pattern is interpreted to represent a major coarsening-upward cycle (cf. Rawson *et al.*, 1983; Howard, 1985), reflecting increasing proportions of coarser silt-size detrital minerals (e.g. quartz, Na-plagioclase, ilmenite, titanite, zircon) in the mudstones (cf. Thibault *et al.*, 2018). Comparable cycles occur below, at the base of the Penny Nab Member and above with values rising upward towards the top of the member at the disconformity at the base of the Pecten Seam (Fig. 4). A Si/Al peak immediately below the Pecten Seam has been documented previously at Staithes (Young *et al.*, 1990, fig. 4). These three stacked coarsening-upward cycles generate an asymmetric saw-tooth pattern in the geochemical profiles (Fig. 4).

The coarsening-upward cycles developed in the Penny Nab Member at Dove's Nest correspond broadly to Type 1 cycles I – III of Howard (1985) and 'parasequences' I – III of Young *et al.* (1990), considered to be of sequence scale by Macquaker & Taylor (1996). They represent the 4th-order cycles of Van Buchem & Knox (1998). Howard (1985) placed ironstones (Osmotherley, Avicula, Raiswell) at the top of each coarsening-upward cycle, while Young *et al.* (1990) interpreted the ironstones as occurring above a disconformity (marine flooding surface) at the base of each 'parasequence'. Macquaker & Taylor (1996) considered the ironstones to have formed during prolonged breaks in sediment accumulation, either as the downdip equivalents of sequence boundaries or during the deposition of forced regressive systems tracts. The finer structure within the geochemical profiles at Dove's Nest is consistent with the presence of additional smaller scale and lower amplitude cycles (parasequences), but these are inadequately resolved by the sampling resolution.

The top of the Penny Nab Member in the Dove's Nest core comprises a succession of 30 thin beds with erosional bedding planes and silt lags. Comparable structures, some of which are gutter casts, form a distinctive 2 m interval in the Lower Gibbosus Shales (Hawsker Bottoms top 'bed' 21 and 'bed' 22 of Howarth, 1955) called the 'upper striped bed' by Greensmith *et al.* (1980). This interval was considered by Trabucho-Alexandre *et al.* (2022) to represent the top of the member at Dove's Nest since the Raisdale Seam, an ironstone regionally developed between the Lower Gibbosus Shales and the Middle Gibbosus Shales (Cope *et al.*, 1980), is either indistinct or absent in the core.

8.a.3. Subunit 1c (Kettleless Member, Cleveland Ironstone) 196.3 – 185.6 m

Across most of the Cleveland Basin, the base of the Kettleless Member, marking the contact between the *A. margaritatus* and

P. spinatum zones (*A. gibbosus* and *P. apyrenum* subzones), is a disconformity that becomes more pronounced toward the south and east (Cope *et al.*, 1980; Howard, 1985), but is lithologically indistinguishable from a normal bedding plane. In the Dove's Nest core, as in the coastal outcrops, the bottom of the Kettleless Member consists of coarse mudstones with lenticular bedding formed by starved combined-flow ripples of siltstone encased in finer mudstones (Trabucho-Alexandre *et al.*, 2022). These mudstones are part of a group of beds referred to as the Pecten Seam (Marley, 1857; Chowns, 1966; Cope *et al.*, 1980; Simms *et al.*, 2004b). The Pecten Seam has been defined differently by different authors. Howarth (1955) and Cope *et al.* (1980) included Hawsker Bottoms 'beds' 25 – 31 in the Pecten Seam comprising a lower 43 cm thick Grosmont Pecten Bed ('beds' 25 – 27) at the base, overlain by the 2.6 m thick Eston Shell Beds ('beds' 28 – 31), above. Chowns (1966) additionally included 'bed' 32, the 1.1 m thick 'Black Hard' in the Seam. By contrast, Howard (1985), Young *et al.* (1990) and Hesselbo & Jenkyns (1995) restricted the Pecten Seam to 'beds' 25 – 27.

The Pecten Seam at Dove's Nest was placed between 196.36 – 193.29 m at Dove's Nest by Trabucho-Alexandre *et al.* (2022), corresponding to Hawsker Bottoms 'beds' 25 – 31 (cf. Howarth, 1955). The bottom ironstone at 196.30 m (<10 cm thick) is oolitic, fossiliferous and bioturbated, whereas the remaining ironstone horizons, picked out by a reddish hue at 195.18 m (25 cm) and 193.69 m (30 cm) in an otherwise black succession, are indistinct. The mudstones between the ironstone horizons vary between medium-grained and homogenous, with pyrite-filled small burrows, to coarser, thin-bedded and (low-angle) cross-laminated. The top of the Kettleless Member (~187 m) is characterized by *Chondrites* burrows above laminated mudstones. The Sulphur Band (SB1) is not obvious in the core, probably due to the lack of weathering, but the distinctive bioturbated layer (top 'bed' 43) above the Sulphur Band seen at Kettleless and Runswick was identified by Trabucho-Alexandre *et al.* (2022).

The Kettleless Member and the bottom of 'bed' 43 constitute chemostratigraphic Subunit 1c (top ~185.6 m). Iron profiles demonstrate that the basal and second ironstones of the Pecten Seam were not captured by our geochemical sampling (Figs 5, S1) but sample 194.02 shows the top ironstone (25.2% Fe₂O₃T) to be again dominantly sideritic (50% carbonate) with an estimated composition of 72.9% FeCO₃, 14.3% MgCO₃, 11.8% CaCO₃, 0.96% MnCO₃. A trend of stratigraphically upward decreasing, then rising, TOC_{WR} and δ¹³C_{org} values through the member at Dove's Nest (Fig. 2) is accompanied by rising detrital proxy element ratios, Si/Al, Ti/Al, Zr/Al and Na/Al (Fig. 4) that peak around the TOC minimum, decrease above and then rise upward again forming peaks at the base of the Grey Shale. These are interpreted to represent two major stacked coarsening-upward cycles above the base Kettleless disconformity (Fig. 4). The P₂O₅ peaks within the Pecten Seam (Figs 5, S1) at Dove's Nest may correspond to the francolite (carbonate fluorapatite) concentrations observed in the seam at Staithes by Young *et al.* (1990, fig. 4).

Howard (1985) distinguished seven (Pecten Seam and i – vi) Type 2 cycles (= 'parasequences' of Young *et al.*, 1990) in the Kettleless Member at Hawsker Bottoms. As in the underlying Penny Nab Member, finer structure within the profiles at Dove's Nest suggests that additional smaller scale cycles are present in addition to the two that are documented, but the sampling resolution is inadequate to capture the detail of these. The coarsest-grained interval in the middle of the Kettleless Member at Dove's Nest likely corresponds to cycle/'parasequence' iv on the coast.

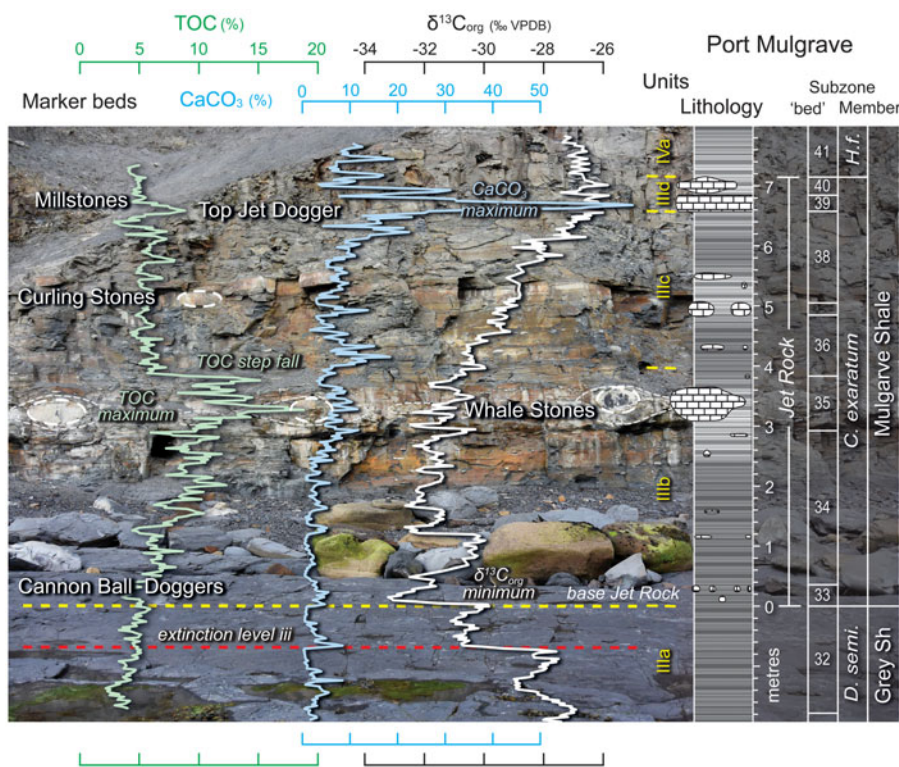


Figure 6. Field photograph of the lower cliff face immediately west of the old harbour of Port Mulgrave (Fig. 1) annotated with the TOC, CaCO₃ and δ¹³C_{org} data of DB Kemp *et al.* (2005) and Kemp *et al.* (2011) and the stratigraphic framework of Howarth (1962). The five distinctive concretionary horizons in the Jet Rock, extinction level iii of Caswell *et al.* (2009) and chemostratigraphic units (IIIa – IVa) with key intervals of change are indicated. *D. semi.* = *Dactyloceras semicelatum*; *C. exaratum* = *Cleviceras exaratum*; *H.f.* = *H. falciferum*. Chemostratigraphic correlation to Dove's Nest is illustrated in Figure 7. Note that the shore platform in the foreground occurs at the level of the base Jet Rock ('bed' 33). The sedimentary log and geochemical profiles below this ('bed' 32) represent variations in the subsurface at this site.

In total, five major coarsening-upward cycles through the Cleveland Ironstone are resolved by our data (Fig. 4). Cycle 3 is bounded by the Avicula Seam at the base and Pecten Seam at the top, cycle 5 terminates in the Pliensbachian – Toarcian boundary interval below the Sulphur Band.

8.b. Unit II Whitby Mudstone lower – middle Grey Shale

The Grey Shale (Powell, 1984) is the lowest member of the Whitby Mudstone Formation in Yorkshire (Fig. 2), which is the type area for the *D. tenuicostatum* Zone, the lowest zone of the Toarcian (Howarth, 1973; Hesselbo *et al.*, 2020b). Hawsker Bottoms 'bed' 43 contains the Pliensbachian – Toarcian boundary at the base of the Sulphur Band (SB1), 33 cm above the base of the Grey Shale (= base of Kettleless 'bed' 25). The member consists of 13.6 m of grey mudstone containing 15 rows of calcareous concretions. The lower beds include micaceous mudstones and ripple-laminated coarse-grained mudstones indicative of current activity, but these pass up into laminated mudstones in the upper part of the member. Evidence for storm-influenced deposition includes normally graded layers with silt lags interpreted as tempestites, as well as ripples, gutter casts and HCS (Kemp *et al.*, 2018), indicative of deposition above storm wave-base and likely < 30 m water depth (Section 8a; cf. Walker & Plint, 1992; Immenhauser, 2009).

The mudstones of the Grey Shale in the Dove's Nest core are similar to those of the Cleveland Ironstone Formation, but they are a much darker grey and are the least fossiliferous interval of the studied section. By contrast, the Cleveland Ironstone and the Bituminous Shales are the two most fossiliferous intervals albeit with very different assemblages.

The intervals containing the Sulphur Band marker bed (SB1) and overlying Sulphur Band 2 (SB2), with the twin δ¹³C_{org} minima of the Pliensbachian – Toarcian Boundary Event, are clearly picked out by TOC, Fe₂O₃, Fe/Al (Figs 4, 5, S1) and S (not determined

here, but well displayed in the coastal succession (e.g. Thibault *et al.*, 2018, fig. 8) peaks.

8.b.1. Subunit IIa (lower Grey Shale Member) 185.6 – 180.4 m

The base of the Whitby Mudstone, the base of Subunit IIa, marks a major long-term shift in the chemostratigraphy of the succession with coincident falls in coarser grained detrital proxies Si/Al, Ti/Al, Na/Al, Zr/Al and accompanying rises in phyllosilicate (principally clay minerals) associated element ratios K/Al, Rb/Al (Fig. 4) and Cs/Al (not plotted). The succession between Sulphur Bands 2 and 3 (SB2 – SB3, *P. paltum* Subzone) includes a distinctive 1.8 m succession of six rows of deep-red weathering sideritic nodules and interbedded decimetric grey mudstones (Port Mulgrave 'beds' 7 – 17), the Six Red Nodule beds of Howarth (1973) and Hesselbo & Jenkyns (1995).

8.b.2. Subunit IIb (middle Grey Shale Member) 180.4 – 174.5 m

A marked step increase in the TOC profile above the red nodule beds in the basal *D. clevelandicum* Subzone (Fig. 2) accompanies the laminated bituminous mudstones of Sulphur Band 3 (SB3, 'bed' 19a) at the base of Subunit IIb. Coincident peaks in Fe₂O₃, T, MgO and MnO (Fig. S1) point to a siderite component in this bed, in addition to pyrite observed in the core. Accompanying the rise in TOC, are step increases in Al₂O₃, MgO, K₂O and P₂O₅ and step falls in SiO₂, Na₂O, Si/Al, Ti/Al, Zr/Al and Na/Al (Figs 4, S1) indicating a consistently higher proportion of phyllosilicates and relatively stable, finer grain sizes throughout Subunit IIb.

8.c. Unit III (T-OAE) Whitby Mudstone, Grey Shale – Mulgrave Shale

Excellent agreement exists between the high-resolution chemostratigraphic records published for the interval of the T-OAE on the Yorkshire coast (Figs 6, 7; Hesselbo *et al.*, 2000; DB Kemp *et al.*,

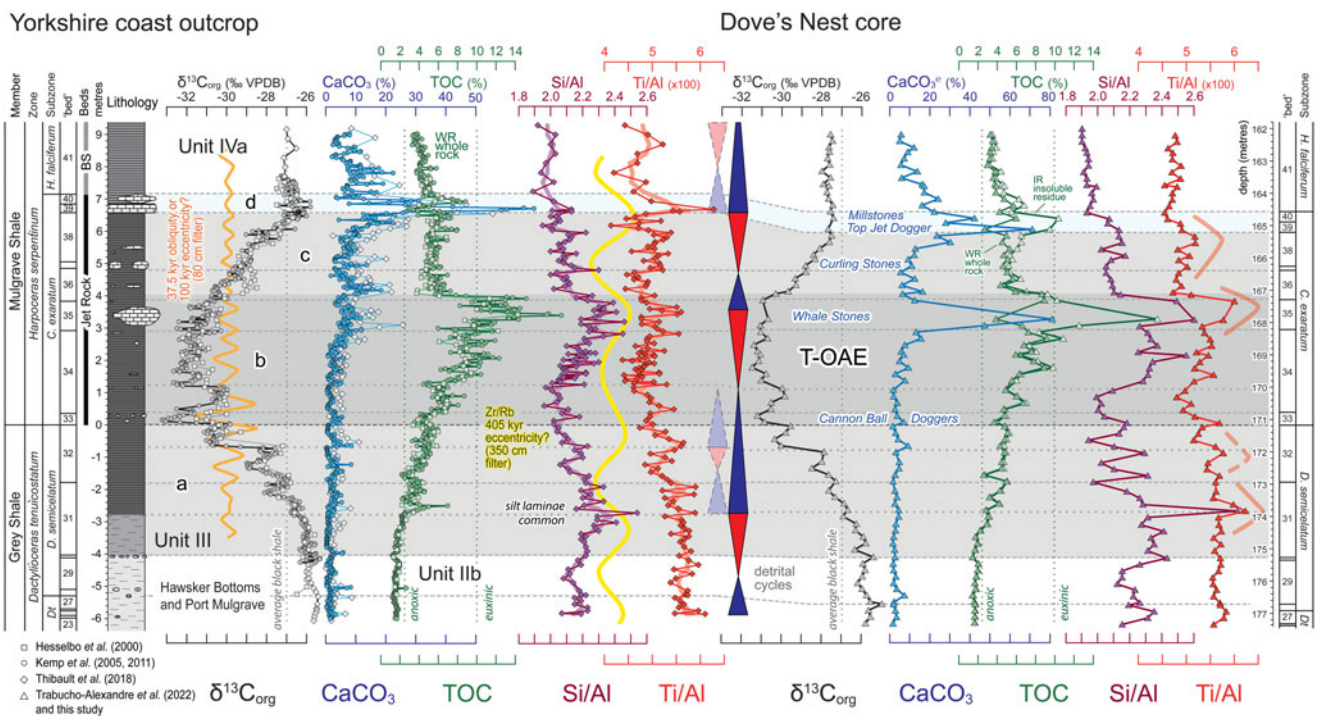


Figure 7. Chemostratigraphic correlation of the T-OAE interval in the Yorkshire coastal outcrop reference sections with the Dove's Nest core. Stratigraphy after Howarth (1962, 1973, 1992) and Howarth (in Cope *et al.*, 1980). Dt = *Dactyloceras tenuicostatum* Subzone. Lithological log is based on the Hawsker Bottoms and Port Mulgrave sections from DB Kemp *et al.* (2005); lithologies are dark-grey laminated mudrocks (dark-grey shading), medium-grey mudrocks (pale-grey shading) and carbonate bands and nodules (brick pattern). Major carbonate markers – ‘Stone’ bands and ‘Doggers’ – are indicated. Sample heights of Hesselbo *et al.* (2000, fig. 3) were recalculated based on the positions of major bed contacts. Data sources: Hesselbo *et al.* (2000); DB Kemp *et al.* (2005); Kemp *et al.* (2011); Thibault *et al.* (2018); Trabucho-Alexandre *et al.* (2022); this study. Si/Al and Ti/Al ratios for the coastal sections were recalculated by Thibault *et al.* (2018 supplementary data) after correction for analytical bias. Shaded intervals a – d represent subdivisions of chemostratigraphic Unit III. This unit corresponds to the interval displaying the large negative carbon-isotope excursion that characterizes the T-OAE. Dashed horizontal grey lines show the correlation of major bed bases; dotted horizontal grey lines correlate significant chemostratigraphic tie points. Cyclostratigraphic filtered output for carbon isotopes (orange curve) and the detrital fraction (yellow curve, derived from Zr/Rb data) are plotted after Thibault *et al.* (2018). Vertical dotted lines indicate: the $\delta^{13}\text{C}_{\text{org}}$ value of average Phanerozoic black shales (grey; Meyers, 2014); the oxic–anoxic– and anoxic–euxinic–facies boundaries defined by TOC content (green, 2.5% and 10%) proposed by Algeo & Maynard (2004).

2005, 2011; Ruvalcaba Baroni *et al.*, 2018; Thibault *et al.*, 2018; Wang, 2022) and the new data from Dove's Nest (Fig. 7).

8.c.1. Subunit IIIa (upper Grey Shale Member) 174.5 – 171.2 m

The onset of rising upward TOC values and falling $\delta^{13}\text{C}_{\text{org}}$ values occur from the base of Port Mulgrave ‘bed’ 31 in the upper Grey Shale *D. semicelatum* Subzone, with increasing rates of change starting at the transition to darker-coloured laminated sediments in the middle of ‘bed’ 31 (Fig. 7). The colour change occurs at the top of an interval containing increasing siltstone laminae, reflected by increasing Si/Al ratios (Fig. 7), with HCS recorded at Kettleless (cf. Wignall *et al.*, 2005, fig. 3). Benthic faunal diversity crashes and bioturbation disappears progressively through the lowest 1.5 m of ‘bed’ 31 (Wignall *et al.*, 2005; Caswell *et al.*, 2009; Caswell & Herringshaw, 2023). Pyrite framboid median and maximum sizes decrease above the onset of the TOC increase and mudstone lamination (Wignall *et al.*, 2005). Framboid maximum sizes fall to $<5\ \mu\text{m}$ and then remain constant upwards, indicative of sulfide precipitation in a euxinic water column (Wignall & Newton, 1998).

The base of Subunit IIIa is placed at the onset of the TOC rise which at Dove's Nest is coincident with the start of generally falling upward trends in detrital and broader aluminosilicate proxies, SiO_2 , TiO_2 , Al_2O_3 , Na_2O , Cs, Rb, Sc, Th, Zr, Si/Al, Ti/Al, Zr/Al and Na/Al (Figs 4, 5, 7, S1, S2) but increases in parameters associated with reducing organic-rich sediments Fe/Al (pyrite), P/Al (phosphate), U/Th and Mo/Al (organic matter). Subunit IIIa

extends upward to the $\delta^{13}\text{C}_{\text{org}}$ minimum (‘bed’ 33) at the base of the Jet Rock (Figs 6, 7).

The top of the Grey Shale (‘beds’ 31, 32), in addition to becoming increasingly organic-rich upwards, is characterized by the presence of widespread shell beds (Howarth, 1973) and represents an interval of significant biotic turnover (Caswell *et al.*, 2009; Caswell & Herringshaw, 2023) with a progressive fall in benthic macroinvertebrate diversity upwards, towards a minimum in the lower Jet Rock (Danise *et al.*, 2015).

8.c.2. Subunit IIIb (lower Jet Rock) 171.2 – 167.2 m

The Mulgrave Shale Member (Rawson & Wright, 1992) overlies the Grey Shale with the boundary on the coast being placed below a line of calcareous concretions, the Cannon Ball Doggers, ‘bed’ 33, at the base of the *C. exaratum* Subzone (Figs 6, 7). The Mulgrave Shale comprises the Jet Rock and Bituminous Shales beds of the *H. serpentinum* Zone (Fig. 2). The Jet Rock (Figs 6, 7) extends from ‘beds’ 33 – 40 (Millstones) inclusive (Hesselbo & Jenkyns, 1995) and is named after the occurrence of jet (compressed wood, traditionally ascribed to araucarian species but likely including a wide range of taxa; Caldwell Steele, 2020) that was previous mined from these beds (Hemingway, 1933). The interval is coincident with the *C. exaratum* Subzone (Howarth, 1992; Hesselbo & Jenkyns, 1995; Simms *et al.*, 2004a), although Howarth (1962) originally included ‘bed’ 32 (top *D. semicelatum* Zone) in the Jet Rock.

The Jet Rock, which consists of dark grey finely laminated pyritic bituminous mudstones, is 7.09 m thick on the coast at Port Mulgrave (Figs 2, 6, 7; Howarth, 1962). Laminae contain coccolith-rich pellets and organo-mineral aggregates and include normally graded layers with sharp bases that show erosional truncation. Discontinuous wavy laminae exhibit downlapping geometries. These features are consistent with deposition by advective dispersal of sediment from wave-enhanced gravity flows of fluid mud triggered by storms (Ghadeer & Macquaker, 2011).

A characteristic feature of the Jet Rock is the presence of common cm- to m-sized calcareous concretions, some with pyritic skins (Coleman & Raiswell, 1981). Key marker horizons within the Jet Rock (Figs 6, 7) are the: (1) Cannon Ball Doggers ('bed' 33), scattered 10 – 15 cm diameter spherical calcareous nodules with thick pyritic skins; (2) Whale Stones ('bed' 35), up to 45 cm thick, 1 × 3 m elongate doggers with thin pyritic skins, associated with irregular linear arrays of smaller pyritic-skinned tubular nodules (Lower Pseudovertebrae); and (3) Curling Stones ('bed' 37), 20 × 40 cm oblate spheroidal doggers with pyritic skins. The top of the Jet Rock comprises a prominent 50 cm thick interval of strongly cemented argillaceous limestone: 'bed' 39, the Top Jet Dogger, incorporating a 20 – 30 cm layer with very large (up to 4 m diameter) almost perfectly circular discoidal concretions set in its top, 'bed' 40, the Millstones (Howarth, 1962).

Significantly, although clearly of diagenetic origin, the most prominent named concretion beds in the Cleveland Basin succession exactly match the stratigraphic positions of equivalent carbonate marker horizons in the Posidonia Shale of Germany with respect to the corresponding carbon isotope curves: Whale Stones = Unterer Stein; Curling Stones = Steinplatte; Top Jet Dogger–Millstones = Oberer Stein, for example at Dotternhausen Quarry in the SW German Basin (e.g. see Röhl *et al.*, 2001; Ruebsam *et al.*, 2023), 950 km to the SE (Fig. 1). Comparable concretionary horizons are seen in the Schistes carton of the Truc de Balduc area of southern France (Riegraf, 1982) and a carbonate maximum at the top of the T-OAE interval, at a level equivalent to the Top Jet Dogger–Millstones, is developed in the Schistes carton at Sancerre in the southern Paris Basin (Hermoso *et al.*, 2012, 2013). Other less prominent carbonate beds are also seen in consistent positions in Germany, France and elsewhere, demonstrating the wider regional significance of the Yorkshire lithostratigraphy.

The Jet Rock contains the highest TOC_{WR} contents in the Pliensbachian – Toarcian boundary succession (Figs 2, 6, 7) with values typically around 6 – 10% but rising to >18% in one layer on the coast (McArthur *et al.*, 2008; Kemp *et al.*, 2011; Ruvalcaba Baroni *et al.*, 2018; Houben *et al.*, 2021). High-resolution (2.5 cm spaced) CaCO₃, TOC, S and δ¹³C_{org} profiles for the Jet Rock and immediately under- and overlying strata (DB Kemp *et al.*, 2005; Kemp *et al.*, 2011) on the coast provide a basis for the definition and precise placement of chemostratigraphic subunits, which can be correlated, refined and further interpreted using the multi-element dataset from the Dove's Nest core.

The base of the Jet Rock ('bed' 33) and of the *H. serpentinum* Zone mark a significant chemostratigraphic boundary with a sharp fall and minimum of δ¹³C_{org} that we use to define the base of Subunit IIIc (Figs 6, 7). By contrast, Thibault *et al.* (2018) placed the base of their 'phase B' ~65 cm lower at an underlying sharp δ¹³C_{org} decrease in the upper half of 'bed' 32, below. Subunit IIIb represents the δ¹³C minimum of the T-OAE, within which a change from falling to rising Si/Al and Ti/Al in the lower half of 'bed' 34 accompanies a further step increase in TOC values (Fig. 7).

These all reach a maximum in mid-'bed' 35, the Whale Stones, and remain high up into the base of 'bed' 36. These high TOC values are associated with an interval temporarily but overwhelmingly dominated by dense amorphous marine organic matter (Slater *et al.*, 2019; Houben *et al.*, 2021).

Subunit IIIb shows prominent negative excursions in many elements towards the top due to the diluting effects of the high carbonate content of the Whale Stones interval (Figs S1, S2). By contrast, Al- and Th-normalized values (Figs 4, 5) generally peak towards the top of the subunit, linked to increasing terrestrial detritus and grain size (Si, Ti, Na, Zr), changes in clay mineral composition (K, Rb) and phosphate deposition (P). High pyrite contents evidence increased sulfate reduction driven by higher organic matter contents and increasingly euxinic conditions (indicated by V, U, Mo enrichment in the shales).

8.c.3. Subunits IIIc and IIId (upper Jet Rock) 167.2 – 164.1 m

The sharp drop in TOC towards the base of 'bed' 36 coincides with the onset of rising δ¹³C_{org} towards a maximum at the top of the Jet Rock (Figs 6, 7). The interval of δ¹³C_{org} rise and lower TOC plateau is differentiated as Subunit IIIc. A δ¹³C_{org} maximum and TOC_{IR} peak occur in the limestones and calcareous shales of the Top Jet Dogger and Millstones ('beds' 39 – 40), above, which are designated as Subunit IIIc. It is observed that CaCO₃ contents increase steadily upward from the middle of 'bed' 38, forming a broad peak that reaches a maximum in the Top Jet Dogger but continues upward into the lower part of 'bed' 41 at the base of the Bituminous Shales and the *H. falciiferum* Subzone.

High MgO but low Fe₂O₃ values (Fig. S1) point to the likely presence of dolomite in addition to siderite in the Whale Stones and Top Jet Dogger – Millstones intervals, which also show Fe/Al and Mn/Al enrichment indicative of the latter mineral (Fig. 5), while high P₂O₅ and P/Al peaks evidence the presence of phosphates and high Ba and Ba/Al peaks, concentrations of barite. Erratic high MgO and Mg/Al ratios throughout the Jet Rock (Figs 8, S1) indicate the occurrence of dolomite in the black shales (cf. Pye, 1985). However, cements in the Whale Stones concretions consist almost exclusively of calcite (Hallam, 1962). Erratic high P values here and elsewhere in the succession may be associated with levels of phosphatic fish debris which, on the coast, are particularly common in the Jet Rock and lower Bituminous Shales (Caswell & Coe, 2014) Unit III – IV interval, and are also a common feature in coeval black shale successions like the Posidonia Shale of Germany (Riegraf, 1985; Burnaz *et al.*, 2024) and the Schistes carton of southern France (Bomou *et al.*, 2021).

8.d. Unit IV Whitby Mudstone, middle Mulgrave Shale

The Bituminous Shales, 'beds' 41 – 48, which constitute the middle and upper portions of the Mulgrave Shale Member, overlie the Jet Rock and are 22.9 m thick at Saltwick Nab (Howarth, 1962). These mainly laminated grey carbonaceous mudstones, contain few carbonate concretions but more abundant pyrite and crushed pyritized fossils than the underlying Jet Rock. Belemnites and fossilized wood are common, the latter including logs up to 3.7 m long at the outcrop. In the Dove's Nest core, the base of the Bituminous Shales comprises thin beds of coarser mudstone with fossiliferous bedding planes characterized by monospecific assemblages of *Pseudomytiloides dubius* (Sowerby). Cross-lamination reappears in these mudstones (Trabucho-Alexandre *et al.*, 2022), which include abrupt alternations of thin beds of fine and coarse mudstone (striped beds).

Three beds in the Bituminous Shales provide markers in the coastal sections (e.g. Rawson & Wright, 2018): 'bed' 42, a row of scattered oval doggers with pyritic skins and *Pseudomytiloides*; 'bed' 44, a row of scattered doggers with pyritic aggregates; 'bed' 46, a red-weathering sideritic mudstone (Fig. 2). A distinctive 36 cm interval comprising a double row of red-weathering pyritic doggers at the top of the *H. falciferum* Subzone ('bed' 48) yields a unique ammonite fauna that includes *Ovaticeras ovatum* (Young and Bird). Following Simms *et al.* (2004b), we place this 'bed', the Ovatum Band, at the top of the Bituminous Shales, although Howarth (1962) listed it separately and did not assign it to a specific member. The Bituminous Shales (including the Ovatum Band) lie entirely within the *H. falciferum* Subzone, *H. serpentinum* Zone (Hesselbo & Jenkyns, 1995).

Geochemical profiles (e.g. Figs 2, S1) demonstrate that a major facies change occurs at 'bed' 44. A sharp step fall in TOC_{WR} occurs above this bed, from $3.4 \pm 0.5\%$ below to $2.4 \pm 0.3\%$ above (Fig. 2), with coincident marked falls documented for redox-sensitive trace elements in the coastal sections, including total S, Cd, Co, Mo and Mn (McArthur *et al.*, 2008; McArthur, 2019). The boundary between chemostratigraphic Units IV and V based on this major redox-proxy shift (following Remírez & Algeo, 2020), is placed at the base of 'bed' 45. A more subtle compositional change occurs within the lower part of the Bituminous Shales around the level of 'bed' 42, which marks a change from falling TOC_{WR} values below, to a plateau above (Fig. 2) and coincident breakpoints occur in most redox-sensitive trace-element profiles (McArthur *et al.*, 2008; McArthur, 2019). We subdivide these beds into chemostratigraphic Subunits IVa below and IVb above.

8.d.1. Subunit IVa (lower Bituminous Shales, Mulgrave Shale Member) 164.1 – 157.4 m

Subunit IVa is characterized by relative plateaus in most major-element profiles at Dove's Nest (Fig. S1). The unique feature of the subunit is the very high levels of redox-sensitive trace metals, U, V and Mo, with the last of these peaking markedly (53 ppm Mo with 5 ppm U, 190 ppm V) towards the bottom of the subunit and remaining high above (Figs 5, S2). Strontium concentrations are also notably enriched in the lower section (Fig. S1) but display no clear correspondence to carbonate-associated elements, suggesting an association with phosphate (e.g. carbonate fluorapatite) and possibly diagenetic celestite.

8.d.2. Subunit IVb (middle Bituminous Shales, Mulgrave Shale Member) 157.4 – 151.2 m

The base of Subunit IVb is marked by small steps in all major element profiles (Fig. S1) driven largely by an increase in CaO contents accompanying a facies change to more sideritic shales. The subunit boundary coincides with a breakpoint in the long-term Ti/Al profile (Fig. 4) with a change from erratically falling values below to a generally increasing upward trend, attributed to the upward coarsening of the grain sizes towards the study section top. A significant broad Sr peak occurs at the base of the subunit (Fig. S1). Redox-sensitive trace metals U, V and Mo remain high throughout and then fall sharply with the TOC and CaCO_3^e declines above 'bed' 44 (Peak Stones) at the top of the subunit (Fig. S2). Subunit IVb is further characterized by relatively high P_2O_5 and P/Al values indicative of a higher phosphate mineral content than adjacent beds.

8.e. Unit V Whitby Mudstone, Mulgrave Shale – Alum Shale

The chemostratigraphic boundary between Units IV and V at 'bed' 44 (Peak Stones) within the Bituminous Shales previously observed on the Yorkshire coast (Thibault *et al.*, 2018; McArthur, 2019; Remírez & Algeo, 2020) is clearly developed in the Dove's Nest core above 151.9 m, which is correlated to 'bed' 44.

8.e.1. Subunit Va (upper Bituminous Shales, Mulgrave Shale Member) 151.2 – 143.7 m

Here, a coincident rise in Al_2O_3 and marked falls in CaCO_3^e (Figs 2, S1), TOC_{WR} and redox-sensitive trace-metal proxies, including Fe/Al, V/Al, U/Th and Mo/Al ratios (Fig. 5), is observed. Our new high-resolution carbon isotope profile from the core (Fig. 2; Trabuco-Alexandre *et al.*, 2022) confirms a step increase in $\delta^{13}\text{C}_{\text{org}}$ at the same level, previously hinted at by low-resolution data from the coast (Cohen *et al.*, 2004).

The geochemistry of the mudstones forming Subunit Va is uniform, with relatively flat plateaus on most elemental and Al-ratio profiles (Figs 4, 5, S1, S2) although Ti/Al displays an increasing upward trend.

8.e.2. Subunit Vb (Hard Shales, Alum Shale Member) 143.7 – 137.2 m

'Bed' 49 marks the base of the Alum Shale Member of the Whitby Mudstone on the Yorkshire coast. The basal part of the Alum Shale was termed the Hard Shales by Howarth (1962), reflecting the presence of carbonate cements in 'beds' 49 and 50. This 6.32 m thick interval displays a distinctive geochemical signature which, in addition to an elevated CaCO_3^e content compared to the immediately underlying and overlying succession, includes higher TOC_{WR} and Mo contents with peak values at the bottom and top of the unit (McArthur *et al.*, 2008, fig. 2; Ruvalcaba Baroni *et al.*, 2018, fig. 2). 'Bed' 48, the Ovatum Band and 'bed' 50, a 20 cm thick red-weathering sideritic mudstone, show associated Mn enrichment (McArthur, 2019, fig. 2).

A correlative interval of weakly carbonate-cemented mudstones ($0.6 - 4.7\% \text{CaCO}_3^e$) and increased TOC_{WR} ($2.1 - 3.9\%$) bracketed by peaks at the bottom and top is observed in the Dove's Nest core between 143.8 and 137.6 m (Figs 2, S1). This interval is assigned to the Hard Shales and constitutes the base of the middle Toarcian *H. bifrons* Zone (*D. commune* Subzone; Fig. 2). It corresponds to chemostratigraphic Subunit Vb. The high-Mn signature of the Ovatum Band on the coast is not seen in the core, but this part of the bed may not have been sampled or the high Mn content in the coast sample of McArthur (2019) may be a weathering artefact. The TOC peak at the base of Subunit Vb displays U and Mo enrichment and the interval in general is characterized by relatively elevated Mo and Mo/Al ratios (Figs 5, S2).

8.e.3. Subunit Vc ('Main Alum Shales', Alum Shale Member) 137.2 – 126.2 m

Howarth (1962) referred to the 15.47 m of mudstone overlying the Hard Shales as the 'Main Alum Shales' (beds 51 – 64) that are in turn overlain by the carbonate cemented beds of the Cement Shales at the top of the Alum Shale. The 'Main Alum Shales' are very fossiliferous with abundant thick-shelled shallow-burrowing bivalves, *Dacryomya ovum* (Sowerby) and common belemnites and ammonites (e.g. Atkinson *et al.*, 2023). 'Beds' 51 – 59 (12.24 m) lie within the *D. commune* Subzone (Fig. 2).

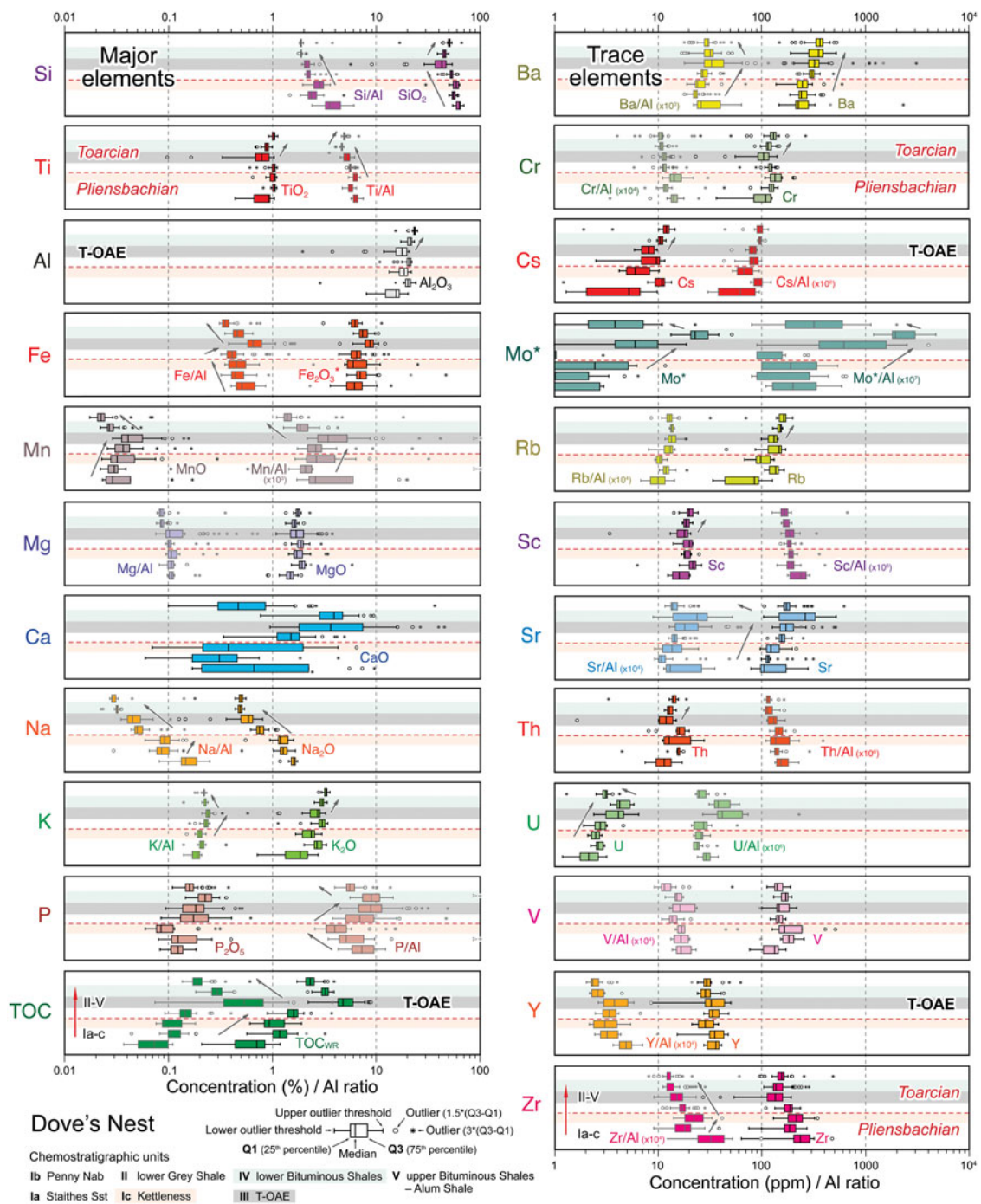


Figure 8. Box plot summary of stratigraphic trends in major- and trace-element contents and Al-ratio data of chemostratigraphic units through the upper Pliensbachian – middle Toarcian of the Dove's Nest core. Boxes represent 25–75% quartiles with median values shown by the vertical line inside the box. Whiskers are drawn from the top of the box up to the largest data point less than 1.5 times the box height from the box (the 'upper inner fence') and similarly below the box (Hammer *et al.*, 2001). Outlier values outside the inner fences are shown as circles, values further than 3 times the box height from the box (the 'outer fences') are shown as stars.

The top of our study interval in the Dove's Nest core (137.2 – 126.2 m) corresponds to the *D. commune* Subzone of the 'Main Alum Shales' and is referred to chemostratigraphic Subunit Vc. The geochemistry of these beds is very comparable to Subunit Va at the summit of the Bituminous Shales, but with higher Ti/Al ratios indicative of a higher silt content. The top of Subunit Vc is not defined.

8.f. Elemental chemostratigraphy overview

The general characteristics of the chemostratigraphic units described above are summarized in Figure 8, showing log-scaled box plots of the elemental and Al-ratio data for all major and trace elements determined in the Dove's Nest core. Elements showing an association with the coarser detrital fraction (e.g. Si, Ti, Zr) or

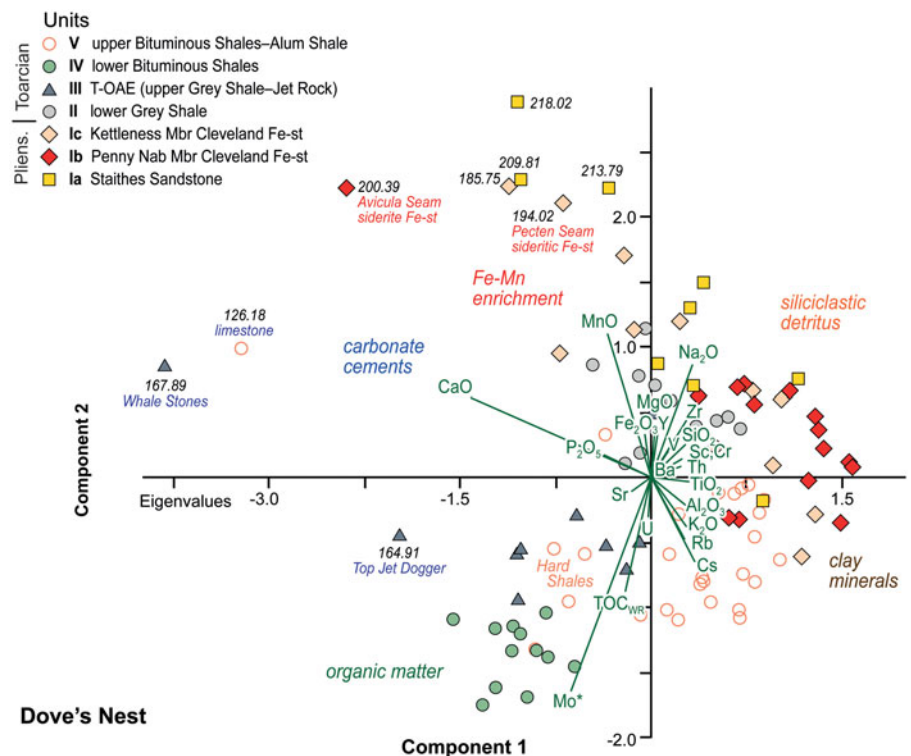


Figure 9. Principal component analysis biplot of PC1 vs PC2 for geochemical data from the upper Pliensbachian – middle Toarcian of the Dove's Nest core. Compositional data for samples ($n = 96$) having a full major- and trace-element dataset were transformed using a Centre Log-Ratio to remove closure effects prior to PCA. The first two principal components account for 48.4% and 22.9% of the variance, respectively (Table S4).

phyllosilicates (e.g. K, Rb, Sc, Th) commonly show significantly different trends for the Al-ratio data, while those associated strongly with organic matter content and sediment redox (TOC, P, Mn, Mo, U, V) are less affected by normalization. The figure illustrates the geochemical integrity of the different units.

9. Statistical analysis

9.a. Pearson r correlation

Inter-element relationships were assessed using Pearson correlation of the high-resolution sample set, and the low-resolution samples with additional trace-element data. Very similar coefficients were obtained for elements present in both sample suites. Results for the low-resolution samples are provided in Supplementary Material Table S3. Correlations between major elements are attributed to their partitioning in the dominant minerals in the rocks. Mineralogical analyses were not performed as part of the present study, but the interpretation is informed by comparison to published mineralogical data from equivalent intervals on the Yorkshire coast (e.g. Gad *et al.*, 1969; Pye & Krinsley, 1986). Quartz and clay mineral contents for 21 samples from the Dove's Nest core were provided by de Vos (2017).

High correlation coefficients ($r > 0.85$) are observed between Al_2O_3 and other aluminosilicate-associated elements TiO_2 , K_2O , Cs and Rb (Table S3). The highest correlation coefficients ($r > 0.9$) are between K_2O , Rb and Cs, typically associated with phyllosilicates, especially illite (e.g. González López *et al.*, 2005) and mica. Lower correlation coefficients for Al_2O_3 ($r = 0.5 - 0.8$) with SiO_2 , Cr, Sc and Th indicate additional mineralogical controls (e.g. quartz, heavy minerals) on these elements. SiO_2 shows the highest correlation with TiO_2 ($r = 0.8$) and lower values ($r = 0.5 - 0.8$) for Al_2O_3 , Na_2O , Cr, Sc, Th and Zr, an element suite likely associated with quartz, Na-plagioclase and heavy minerals (e.g. rutile,

ilmeneite, titanite and zircon) in a coarser-grained terrigenous clastic fraction.

CaO, principally controlled by carbonate, predictably has a high negative correlation ($r = < -0.8$) with most of the above elements (Table S3) but shows modest positive correlations with MnO and P_2O_5 ($r = 0.52$) attributable to Mn substitution in calcite and the presence of carbonate fluorapatite. Fe_2O_3 is positively correlated only with MnO and MgO ($r = \geq 0.6$) and V ($r = 0.4$) reflecting its disparate mineral associations that include siderite but also Fe–Mn oxyhydroxides, pyrite and berthierine.

9.b. PCA results

Loading coefficients of the different variables of the variance-covariance matrix for the first three principal components of the PCA for selected Dove's Nest data (96 samples with a full element suite) are listed in Supplementary Material Table S4. The first two principal components together account for 71.3% of the variance in the data. PC1 (48.4% of the variance) shows positive loadings for siliciclastic mineral-associated (quartz, feldspars, phyllosilicates, heavy minerals) elements, SiO_2 , TiO_2 , Al_2O_3 , Na_2O , K_2O , Cs, Cr, Rb, Th, Zr and a large negative loading for carbonate (CaO). This negative loading highlights the significance of carbonate impacting the geochemical composition of samples and that this is not solely an artefact of the closed-sum nature of the original dataset. Further discrimination between samples is offered by PC2 (22.9% of the variance) with large negative values for Mo^* and TOC_{WR} but positive loadings for MnO and Fe_2O_3 , amongst others. PC3 accounts for a further 9.8% of the variance and is distinguished particularly by its high positive loading for Mo^* .

A biplot of the first two principal components (Fig. 9) illustrates clear inter-element associations that can be interpreted as reflecting mineralogical controls on the bulk geochemistry of the rocks. It further demonstrates how these relate to the stratigraphic

units comprising the upper Pliensbachian – middle Toarcian succession in the Cleveland Basin.

The close proximity of vectors for individual constituents on the biplot indicates associations between (1) SiO₂, Na₂O, Zr and V, together with Cr, Sc and Th, representing siliciclastic detritus; (2) Al₂O₃, K₂O, Rb and Cs is a clay-mineral association; (3) Fe₂O₃ and Mn reflect enrichment in a Fe–Mn component – likely including siderite, goethite, other Fe–Mn oxyhydroxides and berthierine; (4) CaO and P₂O₅ represent carbonate cements and phosphate; (5) TOC_{WR}, Mo* and U are associated with organic matter. It is notable that TiO₂ falls between the main siliciclastic and clay-mineral association vectors, MgO and Y lie between the siliciclastic and Fe–Mn associations and Sr plots between carbonate cements and organic matter. This pattern indicates the presence of multiple mineralogical and/or geochemical controls on these elements.

The distribution of samples on the biplot (Fig. 9) shows good separation of the stratigraphic units, reflecting the changing proportions of mineralogical constituents and geochemical environments through the succession. Outliers are caused principally by Fe – Mn enrichment in ironstone intervals within the Staithes Sandstone and Cleveland Ironstone, and extreme carbonate cementation of individual samples in the Jet Rock (Whale Stones and Top Jet Dogger). It is worth noting that the Hard Shales (Subunit Vb) cluster with samples displaying strong organic matter enrichment (upper Grey Shales – lower Bituminous Shales, Units II and IV).

10. Discussion – Geochemistry as a grain-size proxy

In the previous text, it has been inferred that positive correlations between detrital proxy element ratios (Si/Al, Ti/Al, Zr/Al and Na/Al), and their negative correlation to typical clay-mineral-associated elements (K/Al, Rb/Al, Cs/Al), provide a grain-size proxy in the mudstone succession at Dove's Nest (Fig. 4). Limited grain-size data are available to test this interpretation. Gad *et al.* (1969) published grain-size data for 3 beds from the Whitby Mudstone at Whitby: Grey Shale 'bed' 19, 0.4% sand (>50 µm), 49.0% silt (2–50 µm), 50.6% clay (<2 µm); Jet Rock 'bed' 32, 0.01% sand, 48.0% silt, 52.0% clay; and Bituminous Shales 'bed' 43, 0.1% sand, 44.7% silt, 55.2% clay; together with results for two beds in the Alum Shale from above our study interval. These data indicate a generally fining-upward trend in the Whitby Mudstone consistent with our interpretation.

Pye & Krinsley (1986) noted a positive correlation between the silt/clay ratio and Si/Al ratio but provided no numerical data. Thibault *et al.* (2018) similarly argued that Si/Al, Zr/Al and Zr/Rb ratios offer proxies for coincident changes in fluvial transport and siliciclastic grain size in the Whitby Mudstone. However, mudstones may accumulate as coarser composite grains that reflect elevated bottom-water energy conditions (e.g. Schieber *et al.*, 2019; Z Li *et al.*, 2021), so increased grain size may not necessarily generate elevated values of detrital proxy elements.

Grain-size values determined in thin-sections of 73 samples from the Grey Shale and Jet Rock of the coastal sections at Port Mulgrave were plotted by Ghadeer (2011, fig. 8.3). These demonstrate an overall fining-upward trend (Fig. 10) with 2 – 7% fine sand and 12 – 23% silt in the basal beds of the Grey Shale Member ('beds' 1 – 6) and clay dominating (<2% silt) the top of the Jet Rock ('beds' top 36 – 40). A large peak in silt (16 – 24%), including one sample with 10% fine sand, occurs in 'bed' 31 that matches the prominent Si/Al and Ti/Al peaks observed at this level

both on the coast (Thibault *et al.*, 2018; Wang, 2022) and in the Dove's Nest core (Figs 7, 10), and the overall silt profile displays a strong similarity to the geochemical detrital proxies.

De Vos (2017) undertook quartz abundance and grain-size analyses of 21 samples from the Dove's Nest core using SEM–EDX of polished sample splits of material analysed in this study. The resulting quartz means grain-size profile closely matches the shape of the Ti/Al ratio curve (Fig. 10) and the Ti/Al ratio shows a statistically significant ($p < 0.001$) positive correlation with grain size (Fig. 11c). The coarsest grain size, mean very fine silt but incorporating fine – coarse silt fractions, characterizes the upper Penny Nab and Kettleless members of the Cleveland Ironstone. The succession then fines upward towards a minimum in the middle of the Bituminous Shales, which are fine mudstones (Figs 10, 11), before coarsening upward (CU) into coarse mudstones of the Alum Shale.

11. Mineralogical trends

Detrital minerals identified in the Whitby Mudstone of the coastal succession comprise quartz, micas (muscovite, biotite), feldspars (plagioclase, K-feldspar), illite-smectite, kaolinite and chlorite (Pye & Krinsley, 1986). Authigenic anatase and kaolinite are also present. The detrital sand and coarsest silt comprise mostly quartz, with minor feldspar and muscovite in both the Cleveland Ironstone and Whitby Mudstone (Ghadeer, 2011). Detrital Ti-bearing minerals including rutile and anatase, and their replacement product, leucosene, are a consistent accessory phase. Houben *et al.* (2016b) provided quantitative data for 4 samples from the Whitby Mudstone that yielded: 13.1 – 16.3% quartz; 0 – 1% plagioclase; 1.3 – 15.1% calcite; 0.1 – 2.8% ankerite; 0.6 – 0.9% anatase; and 8.0 – 11.0% pyrite.

11.a. Clay minerals

Gad *et al.* (1969) reported that clay fractions in the Whitby Mudstone contain approximately equal amounts of kaolinite, mica (illite) and swelling clays (vermiculite and/or smectite) with minor chlorite (<5%). The silt fraction includes clay-mineral aggregates. Houben *et al.* (2016a, b) recorded 31 – 54% illite-smectite, 17 – 27% illite, 26 – 40% kaolinite and 3 – 4% chlorite in four samples from the formation.

The clay mineralogy of the 21 samples from the Dove's Nest core was determined by de Vos (2017). Quantitative clay mineral analysis employing the XRD peak-area integration with peak-height ratio method showed kaolinite (27 ± 5%), illite (48 ± 4%) and vermiculite (25 ± 5%), with a dominance of irregularly interstratified illite-vermiculite (I/V), to be the principal components of the clay fraction (<4 µm). Muscovite and chlorite are present in minor amounts, the latter only in the lower part of the succession below 175 m (Staithes Sandstone – Grey Shale; Units I and II).

The results of de Vos (2017) are broadly consistent with earlier clay mineral studies of Pliensbachian – Toarcian sedimentary rocks in the Cleveland Basin by Morris (1980), Sellwood & Sladen (1981), Jeans (2006) and Houben *et al.* (2016a, b). Those authors emphasized the dominance of illite and kaolinite with mixed-layer clays, although they did not specify the presence of a I/V phase. Kemp & McKervey (2001) and SJ Kemp *et al.* (2005) reported illite-smectite as the interstratified species but acknowledged difficulties in the interpretation of the XRD spectra. Precise comparison between the studies is hampered by differences in analytical methodology and clay mineral terminology.

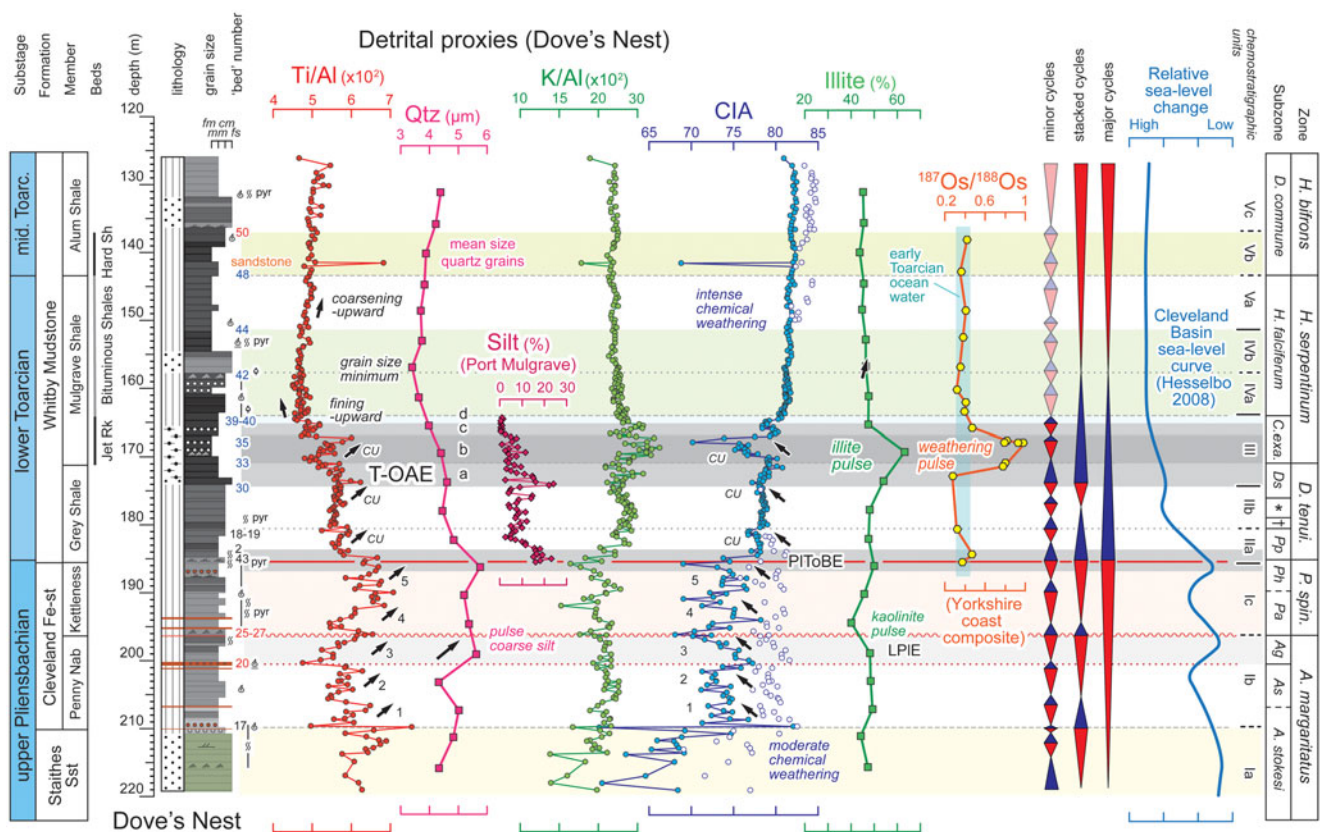


Figure 10. Ti/Al and K/Al ratio profiles from Dove's Nest compared to quartz grain size, proportion of silt, illite content, CIA, and Os isotopes. Quartz grain size and illite content (peak-area integration with height ratios method) after de Vos (2017). Silt percentage was determined from Port Mulgrave (Ghaeder, 2011). CIA = Chemical Index of Alteration (Nesbitt & Young, 1982); $CIA = [Al_2O_3 / (Al_2O_3 + CaO + Na_2O + K_2O)] \times 100$ (molecular proportions). CaO^* moles assumed to be equivalent to Na_2O (filled blue circles) with additional values derived from CaO determinations (open blue circles), where a number of moles was less than that of Na_2O (McLennan, 1993). Osmium isotope plot from Cohen *et al.* (2004, fig. 1), with composite data from 3 coastal sections: Hawsker Bottoms; Port Mulgrave; Saltwick Bay. Cleveland Basin relative sea-level curve (Hesselbo, 2008) replotted relative to biostratigraphic zones interpreted for the Dove's Nest core. $^{187}Os/^{188}Os$ ratio of early Toarcian ocean water (0.377 ± 0.065) after van Acken *et al.* (2019). Cycles are based principally on the Ti/Al profile.

Most authors have regarded the Lias Group clay mineral assemblages in the Cleveland Basin as being principally detrital (Sellwood & Sladen, 1981; Jeans, 2006; Dera *et al.*, 2009) despite a maximum burial depth of 3–4 km and temperatures of 100–120°C (SJ Kemp *et al.*, 2005), although evidence exists for the development of some authigenic kaolinite (Pye & Krinsley, 1986).

The relatively high abundance of kaolinite in the Upper Lias throughout northern Europe suggests warm temperatures and near-constant annual humid conditions on adjacent landmasses (Singer, 1984; Chamley, 1989; Fagel, 2007; Dera *et al.*, 2009). Local factors may also have played a role. For example, in Scotland, the sand and clay mineralogy of Jurassic sedimentary rocks suggests that they were derived from erosion of Devonian and Carboniferous strata (Hurst, 1985; Hall & Bishop, 2002). The high detrital kaolinite content of Rhaetian to Sinemurian mudstones in northeast Scotland has been attributed to the reworking of Carboniferous regoliths, which were uplifted and eroded at the time of formation of the Viking Graben (Hurst, 1985).

The kaolinite content in the Whitby Mudstone of the Dove's Nest core (de Vos, 2017) is lower (21–30%) than in the underlying Staithe Sandstone and Cleveland Ironstone (24–40%) which might imply a transition to cooler and dryer climate. However, this is contrary to trends elsewhere, including at Mochras in the Cardigan Bay Basin (Fig. 1a), that show widespread kaolinite enrichment in the lower Toarcian (Raucsik & Varga, 2008; Dera

et al., 2009; Brański, 2012; Hermoso & Pellenard, 2014; Xu *et al.*, 2018) and palaeotemperature records (Section 18) that indicate generally cool climate in the late Pliensbachian, a short-lived hyperthermal during the T-OAE, with persistence of warm climate conditions thereafter (Suan *et al.*, 2010; Korte *et al.*, 2015; Bougeault *et al.*, 2017; Ruebsam & Schwark, 2021).

The lower kaolinite content in the lower Toarcian at Dove's Nest may reflect clay mineral fractionation with increasing distance to shore (Gibbs, 1977; Godet *et al.*, 2008; Deconinck *et al.*, 2019), driven by relative sea-level rise accompanying the early Toarcian transgression (Hallam, 1997, 2001; Hesselbo, 2008) and the impact of extreme seasonal aridity during the T-OAE (Slater *et al.*, 2019). Similarly, a pulse of kaolinite at the base of the Kettleness Member (Fig. 10) with falling values above, may reflect nearer-shore conditions associated with the depositional hiatus that resulted in the regional disconformity at the base of the *P. spinatum* Zone, followed by sea-level rise. However, changes in sediment provenance cannot be discounted as a mechanism to explain the mineralogical trends.

Illite abundance is associated with weak weathering intensities and increased levels of mechanical weathering, implying terrestrial erosion (Singer, 1984). Illite contents at Dove's Nest, ascribed to a I/V mixed layer component (de Vos, 2017), are relatively constant throughout the succession except for the T-OAE interval (Subunits IIa, b), which shows a marked rise to 54–64% illite from an average

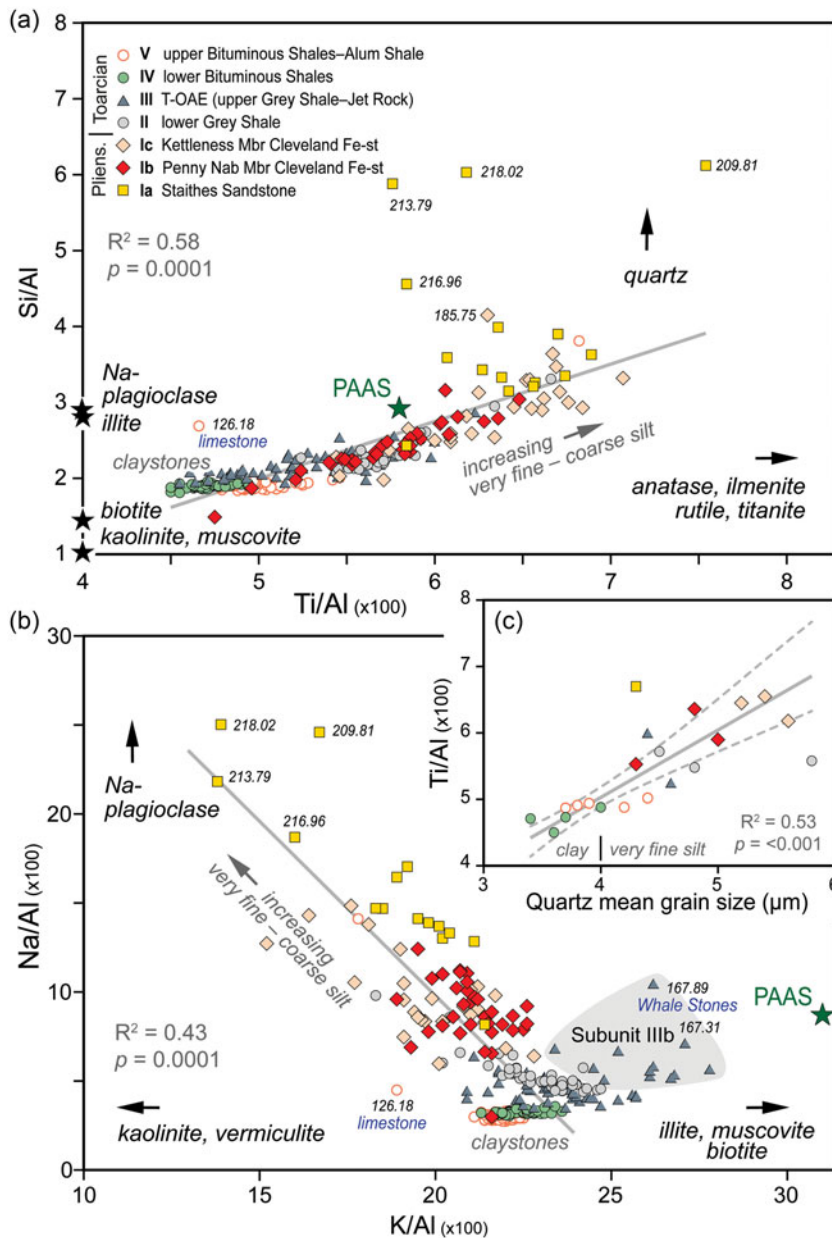


Figure 11. Geochemical cross-plots for selected detrital proxies and grain size in the Dove's Nest core. (a) Si/Al vs Ti/Al. (b) Na/Al vs K/Al. (c) Ti/Al vs quartz mean grain size (de Vos, 2017). Mineral reference compositions from webmineral.com, average shale (PAAS) after Taylor & McLennan (2001). Plotted regression lines are (a) ordinary least square and (b, c) reduced major axis, with 95% confidence envelope in (c). Grey shading in (b) represents the field of the Subunit IIIb illite and weathering pulse including Whale Stones 'bed' 35, characterized by anomalous low CIA values (Fig. 10).

of 46% below, before falling back to an average of 47% above the event (Fig. 10). The increase in illite in the I/V fraction has been ascribed to higher terrestrial erosion rates leading to deeper erosion of podzol soil profiles (de Vos, 2017). The implied elevated levels of continental erosion during the earlier phases of the T-OAE match the increase of continental weathering flux of >40% indicated by the increase in ¹⁸⁷Os/¹⁸⁸Os ratio (Section 16.b.4) from ~0.4 to ~1.0 in the top Grey Shale and Jet Rock on the coast (Fig. 10; Cohen *et al.*, 2004), and coincident increases in the Mochras borehole (Percival *et al.*, 2016), in western North America (Them *et al.*, 2017b) and in Japan (Kemp *et al.*, 2020).

11.b. Detrital proxies in the silt fraction

Mineralogical controls on bulk-rock geochemistry may be investigated using element-ratio Pearson correlations. Detrital proxy element ratios Si/Al, Ti/Al, Na/Al and Zr/Al show high

positive correlations with each other of $r \geq 0.62$ ($p = 0.0001$), most >0.75 and are negatively correlated to K/Al ($r = <-0.46$, $p = 0.0001$). Of these, Ti/Al has the highest correlation with mean grain size ($r = 0.73$) and particularly with the medium silt fraction ($r = 0.76$), although all other proxies show similar relationships.

Figure 11 shows example element-ratio cross-plots of (a) Si/Al vs Ti/Al; (b) Na/Al vs K/Al; and (c) Ti/Al vs quartz mean grain size for Dove's Nest. The geochemical units and their constituent lithostratigraphic divisions display discrete clusters. Si/Al in the Staithes Sandstone (Subunit Ia) shows the greatest scatter (Fig. 11a) attributable to large sample-to-sample differences in quartz abundance in the coarser fractions. The Cleveland Ironstone (Subunits Ib, Ic) shows a tight positive array on the Si/Al vs Ti/Al plot attributable to a close association between Ti-bearing heavy minerals (rutile, anatase) and quartz in a changing silt fraction. Claystones (Fig. 11c) of the Bituminous Shales (Unit IV, Subunit Va) display low and constant Si/Al and Na/Al ratios

(Fig. 11a, b) but significant variation in Ti/Al and K/Al reflecting variable clay mineralogy.

The remarkable similarity between the Si/Al and Na/Al profiles (Fig. 4) and a high positive correlation between Si/Al and Na/Al ($r = 0.93$) point to Na-rich plagioclase as a dominant mineralogical control, likely present as both a primary detrital fraction and as a replacement of K-feldspar (cf. Min *et al.*, 2019). The negative correlation between Na/Al and K/Al (Fig. 11b) is attributed to the presence of Na-plagioclase in the silt fractions and dominance of illite in the clay fraction, with scatter generated particularly by the presence of variable K-feldspar and micas. The large scatter and high values of K/Al in the mudstones from the T-OAE are particularly significant and are explained by pulses of illitic clay during the event (cf. Fig. 10).

Zr/Al shows the strongest correlation to Si/Al but a more irregular profile (Fig. 4) which may be explained by the nugget effect of zircon grains present in the small sample sizes analysed. The resulting element cross-plots (not shown) are like those of Si/Al.

11.c. Chemical Index of Alteration - CIA

The CIA (Nesbitt & Young, 1982; McLennan, 1993) is a widely applied chemical weathering proxy and has been used in many recent T-OAE studies (e.g. Fu *et al.*, 2017; Fantasia *et al.*, 2018a, b; Bomou *et al.*, 2021; Fu *et al.*, 2021; Alnazghah *et al.*, 2022; Liu *et al.*, 2022). A ternary plot of $\text{Al}_2\text{O}_3 - \text{CaO}^* + \text{Na}_2\text{O} - \text{K}_2\text{O}$ for the Dove's Nest data is presented in Figure 12 with the corresponding CIA values. These are plotted stratigraphically in Figure 10. Due to the large variation in carbonate content between samples, particularly in the T-OAE interval (Unit III, Fig. 7), Figure 10 plots CIA values calculated using $\text{CaO}^* = \text{Na}_2\text{O}$ (blue filled circles and blue line) for all samples and using $\text{CaO}^* = \text{phosphate corrected CaO}$ (open blue circles) for samples where the remaining number of moles was less than that of Na_2O (following McLennan, 1993). It is recognized that the CIA profile based on the former method is identical to that for $\text{Ln}(\text{Al}_2\text{O}_3/\text{Na}_2\text{O})$ in molar proportions (not plotted) which is an alternative weathering proxy applicable for moderate to high carbonate samples (Von Eynatten *et al.*, 2003; Xia & Mansour, 2022). The CIX proxy of Garzanti *et al.* (2014) that uses a modification of the CIA formula excluding CaO generates the same trend.

The CIA data for very low carbonate samples that enable the use of CaO^* values for calculation generally display higher CIA values and lower amplitude change through the succession but show the same stratigraphic trends as the Na_2O substituted values (Fig. 10). The reduced amplitude is due primarily to the high Na_2O content of the upper Pliensbachian sediments (Unit I, Figs 4, S1). The long-term trend shows increasing upwards CIA values representing weak to moderate chemical weathering of <70 (Na_2O -substituted values) in the Staithes Sandstone (Subunit Ia), moderate chemical weathering $\sim 70 - 75$ in the Cleveland Ironstone (Subunits Ib, Ic), rising to $75 - 80$ in the basal Toarcian (Units II, III) including the T-OAE, reaching high and constant values of >80 , indicative of intense chemical weathering, through the remainder of the lower Toarcian - middle Toarcian (Unit IV, V) section.

The CIA profile for the upper Pliensbachian displays a cyclicity that is inversely correlated to Si/Al, Ti/Al and Zr/Al and positively correlated to K/Al and Rb/Al (compare Figs 4 and 10), indicating a strong grain-size control. For comparison, Dinis *et al.* (2017, fig. 3) documented a 10-unit offset to lower CIX values in river sands

compared to associated river muds in their study of weathering proxies along the modern SW African margin, although parallel trends that broadly followed the regional weathering trends were observed for the two size fractions.

For Dove's Nest, coarser-grained Pliensbachian sedimentary rocks have lower CIA values due to lower clay and higher plagioclase contents that might conceivably represent cycles of chemical weathering intensity but are attributed principally to grain-size variation linked to cyclic changes in bottom energy conditions and shoreline proximity. The sequence stratigraphy (Section 8.a.2) indicates that these were driven by changes in relative sea level (Howard, 1985; Young *et al.*, 1990; Macquaker & Taylor, 1996).

The general anticorrelation of CIA with Ti/Al and the other detrital proxies continues through the Toarcian at Dove's Nest but the positive correlation to K/Al and Rb/Al is reversed in T-OAE Subunits IIIb - c where increasing K/Al ratios are linked to a pulse of illitic clay (Fig. 10). Notably, a Th/K minimum at this level is a feature of the field spectral gamma-ray stratigraphic profiles generated for the Yorkshire coast Pliensbachian - Toarcian by Myers & Wignall (1987) and Parkinson (1996). The latter considered Th/K to be a likely proxy for the kaolinite/illite ratio. The illite pulse correlates to a major global weathering event documented by a large increase in $^{187}\text{Os}/^{188}\text{Os}$ values in the coastal succession. Si/Al and K/Al profiles obtained for the T-OAE interval and adjacent beds by Thibault *et al.* (2018) and Wang (2022) on the coast display identical trends to those seen in the core (Fig. 7) but those authors were unable to calculate CIA values due to an absence of Na_2O data.

The continental weathering pulse indicated by the positive Os excursion coincides with a negative excursion in CIA values at Dove's Nest (Fig. 10). This is the opposite of what might be expected since increased chemical weathering would lead to higher CIA values. The T-OAE interval elsewhere is commonly characterized by a prominent increase in CIA values and other chemical weathering proxies (Fantasia *et al.*, 2018a, 2019; Bomou *et al.*, 2021; Wang, 2022) attributable to a warmer and wetter climate during the Toarcian hyperthermal.

In the Cleveland Basin, a pulse of detrital illite combined with a short-term upward increase in sediment grain size drove falling CIA values through the $\delta^{13}\text{C}$ minimum of the T-OAE (Subunit IIIb), despite evidence of an increasingly hot climate with extreme wet/dry seasonality based on terrestrial palynomorph assemblages (Slater *et al.*, 2019). Seasonality peaked during the later phases of the T-OAE (Subunits IIIc - d), associated with a sharp increase in CIA and lower illite content (Fig. 10). A peak of charcoal abundance at this level in the Peniche and Mochras successions (Baker *et al.*, 2017) is consistent with dryer climate conditions (increased wildfires) in the European region following a wetter phase during the initial stages of the T-OAE.

The charcoal maximum correlates to a coincident peak in the relative abundance of *Cerebropollenites*. The proliferation of *Cerebropollenites* during multiple past hyperthermal events suggests that the source plants were adapted to hot, arid climates able to survive in warm, drought-like conditions (Slater *et al.*, 2019). In the case of the Cleveland Basin, therefore, it is suggested that a wetter climate during the interval of the $\delta^{13}\text{C}$ minimum led to increased detrital input that overprinted the normal chemical weathering proxies. A change from dominantly wet to dominantly dry conditions indicated by the charcoal and palynological proxy records may reflect a temporal shift in the relative importance of dry vs wet in a strongly seasonal wet/dry cycle.

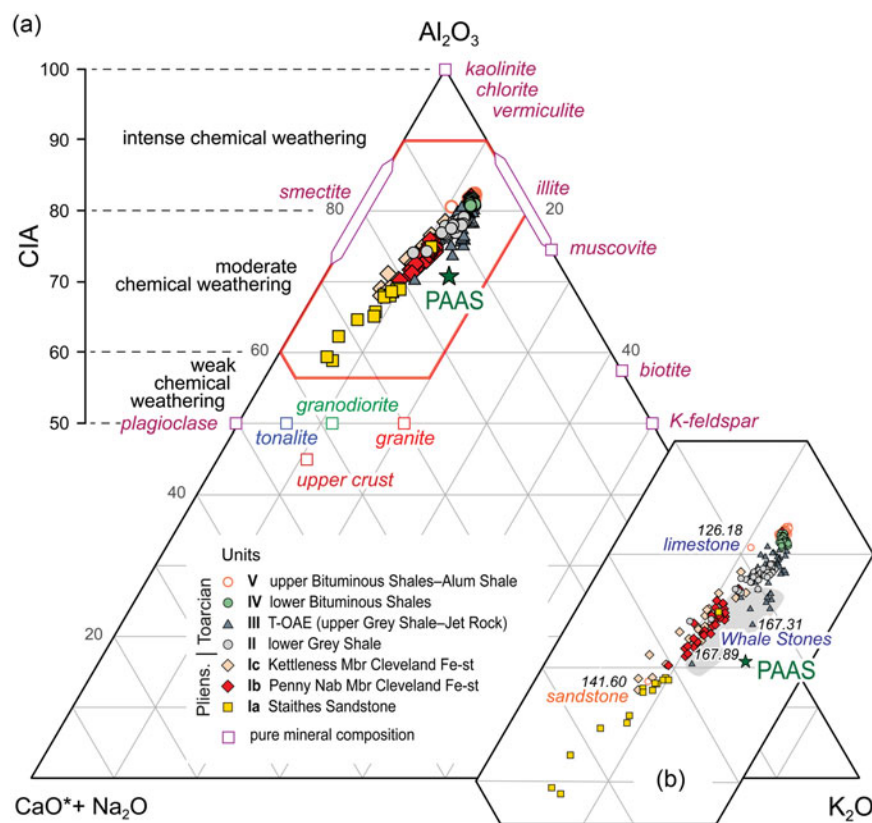


Figure 12. Ternary diagram of Al_2O_3 –(CaO^* + Na_2O)– K_2O in Dove's Nest rock samples. Values are molecular proportions. (a) CIA = Chemical Index of Alteration (Nesbitt & Young, 1982) with CaO^* moles assumed to be equivalent to Na_2O (McLennan, 1993; see text). Tonalite, granodiorite and granite compositions after Condie (1993). (b) Enlargement of plotted data in the top sector of the diagram (red outline in a) with selected sample details. Grey shading represents the field of the Subunit IIIb illite and weathering pulse with high K/Al and anomalous low CIA values.

11.d. Fe–Mn enrichment and carbonate cements

The Pearson correlation and PCA results for Dove's Nest show a close association between Fe, Mn and Mg, with r values of >0.6 (Table S3) and with Ca and P falling in the same sector of negative PC1 and positive PC2 scores (Fig. 9). The relationship between Fe–Mn enrichment and carbonate may be illustrated using a Fe+Mn–Ca–Mg ternary plot (Fig. 13). As with the detrital proxy elements (Fig. 11), the chemostratigraphic units display distinctive clusters and arrays on the Fe+Mn–Ca–Mg plot. The Pliensbachian formations of Unit I form a low-Ca cluster adjacent to muscovite and kaolinite mineral analyses from the Cleveland Ironstone (Aggett, 1990); Ca values lower than average shale (PASS) indicate negligible carbonate in most samples. Individual analyses falling outside the cluster incorporate calcite grains and/or cements, generating an array of scattered points towards the Ca vertex (Fig. 13) or are siderite-rich, exemplified by the Avicula Seam Ironstone (sample 200.39) the bulk chemistry of which displays high Fe+Mn and falls close to the siderite analyses of Aggett (1990). Generally low Si values of Fe-rich samples indicate that berthierine is not a significant mineral component in the sample suite analysed here.

Unit II, the lower Grey Shale, forms a tight cluster close to average shale (Fig. 13). The carbonaceous mudstones of Units III and IV form long scattered arrays between moderate Fe+Mn–Mg contents and the Ca vertex. The very high carbonate content of the Whale Stones sample (167.89), interpreted to represent a carbonate concretion, is demonstrated by its proximity to the calcite mineral analysis (Aggett, 1990). Samples from Units III and IV fall along a mixing line between calcite, ankerite and kaolinite. This may be fortuitous since the scatter towards the Fe+Mn vertex is likely

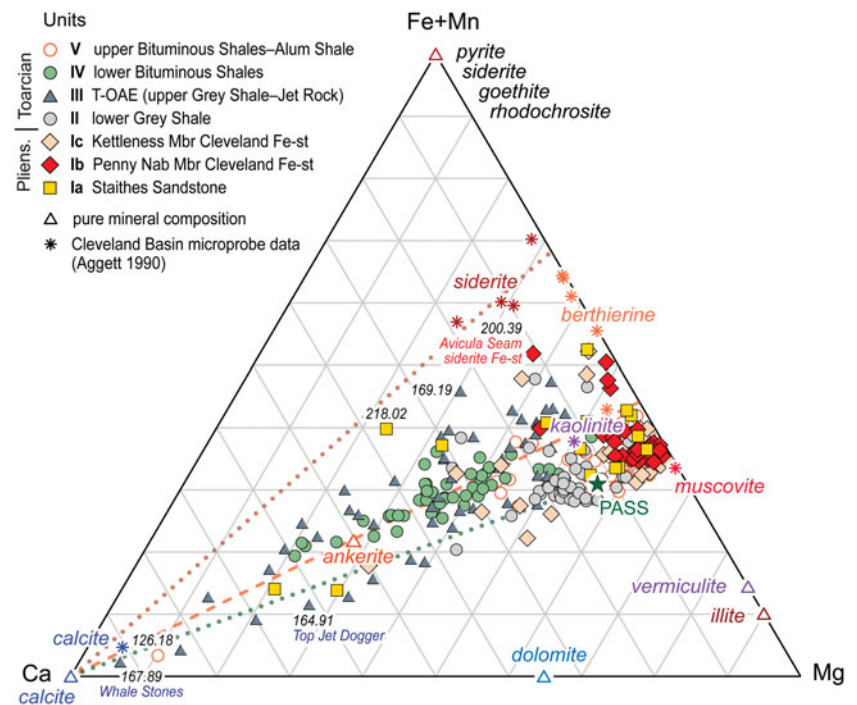
attributable in part to the presence of pyrite which is abundant in these units (e.g. Houben *et al.*, 2016b) but was not quantified in this study. Nonetheless, ankerite has been recorded as a minor mineral phase in these intervals (Houben *et al.*, 2016b). Offset of Unit III samples to higher Mg values is attributed to the presence of dolomite (cf. Pye, 1985).

Unit V samples cluster in the same low-Ca area of the Fe+Mn–Ca–Mg plot as those from the Cleveland Ironstone (Subunits Ib, Ic) indicating a return to less Fe–Mn enrichment and generally low carbonate contents (compare Fig. 9). Samples from the Hard Shales (Subunit Vb) are variably displaced to higher Ca values (Fig. 13), reflecting the presence of calcite cements.

12. Chemostratigraphic correlation and palaeoredox proxies

Chemostratigraphic correlation between Dove's Nest and the Yorkshire coast may be further illustrated by profiles for the redox-sensitive constituents TOC/P_T , Fe_{EF} , Mn_{EF} and P_{EF} (Fig. 14), which provide insights into facies and bottom-water evolution in the Cleveland Basin during the late Pliensbachian – middle Toarcian. High-resolution data are available for the lower Toarcian of both sections and excellent agreement exists between the fine structure and values of the profile pairs. Key marker bed horizons (e.g. Sulphur Bands 2, 3, Whale Stones, Top Jet Dogger, Millstones, Peak Stones, Ovatum Band; see also Fig. 7) provide a framework for bed-scale correlation between the sections. The Dove's Nest data additionally offer higher resolution and extended stratigraphic coverage of the upper Pliensbachian and basal middle Toarcian.

Figure 13. Ternary plot of iron and carbonate-associated elements Fe+Mn–Ca–Mg in Dove’s Nest rock samples compared to constituent mineral compositions. Stars are electron microprobe determinations of mineral fractions from the Cleveland Ironstone of Staithes (Aggett, 1990). Open triangles are calculated pure mineral values (webmineral.com). Average shale (PASS) composition after Taylor & McLennan (2001). Plot is scaled based on the maximum and minimum values of the three components (cf. de Lange *et al.*, 1987).



12.a. TOC/ P_T molar ratio

The TOC/ P_T ratio is a redox proxy based on the differing processes and rates of organic carbon and phosphorus remineralization under varying redox conditions (Ingall *et al.*, 1993; Van Cappellen & Ingall, 1994; Algeo & Ingall, 2007; Algeo & Li, 2020; Papadomanolaki *et al.*, 2022). Marine plankton biomass has a remarkably constant TOC/P molar ratio of 106:1, the Redfield ratio (Redfield *et al.*, 1963), and lacustrine particulates have a comparable composition (Hecky *et al.*, 1993). In modern oxic marine bottom waters and surficial sediments, organic carbon is mostly returned to the water column during bacterial respiration, but P is trapped by adsorption onto Fe-oxyhydroxides and the precipitation of carbonate-fluorapatite or its precursor in the sediment during iron reduction (Jarvis *et al.*, 1994, fig. 3; März *et al.*, 2018). These processes lead to a fall in the sediment TOC/ P_T molar ratio with values typically < 50 in oxic facies (Algeo & Ingall, 2007). Under anoxic conditions the preservation of organic matter is enhanced and, in the absence of Fe-oxyhydroxides, reactive P is released back to seawater leading to an increased TOC/ P_T molar ratio of > 106. Modern anoxic sediments generally display ratios of 100 – 200, with values exceeding 1000 in some ancient black shales (Algeo & Ingall, 2007; Papadomanolaki *et al.*, 2022).

TOC/ P_T molar ratios in the upper Pliensbachian Unit I at Dove’s Nest are indicative of oxic facies with a mean value of 52 ± 26 (Fig. 14). A small upward increase in the average ratio is seen from the Staithes Sandstone to the Kettleness Member of the Cleveland Ironstone, between three Subunits Ia – c. A mean TOC/ P_T molar ratio of 57 ± 24 in lower Grey Shale Unit II indicates predominantly oxic conditions with the notable exceptions of Sulphur Bands 2 and 3 that exceed 120 (SB1 was not sampled in the core but displays a TOC/ P_T ratio of >200 on the coast), evidencing short-lived episodes of anoxia – euxinia.

High TOC/ P_T molar ratios that consistently exceed the Redfield ratio characterize T-OAE Unit III of the top Grey Shale and Jet Rock (Fig. 14), with the highest values occurring in Subunit IIIb

(230 ± 69). These indicate that significant quantities of P must have been released back to anoxic bottom waters during the peak of the T-OAE. TOC/ P_T ratios fall sharply in Subunit IIIc but remain higher in Units IV and V than in the pre-T-OAE section (Units I and II) indicating continuing oxygen depletion in bottom waters during the later early Toarcian and early middle Toarcian, fluctuating within the dysoxic field with a molar ratio of 85 ± 18 (Fig. 14).

An identical pattern is displayed by Yorkshire coast data but with higher TOC/ P_T molar ratios recorded by the ultra-high-resolution data obtained for T-OAE Unit III (Thibault *et al.*, 2018) with values of 390 ± 104 for Subunit IIIb (Figs 14, 15).

12.b. Degree of pyritization DOP_T

The ‘degree of pyritization’ (DOP, Raiswell & Berner, 1985) is an established proxy for bottom-water redox conditions (Raiswell *et al.*, 1988, 2018). DOP values exceeding 0.5 have been suggested to provide evidence of euxinia (free H_2S in the water column) driving the addition of syngenetic pyrite precipitated in the water column to the sediment (Raiswell *et al.*, 2001; Algeo & Maynard, 2004), although more conservative threshold DOP values of <0.45 for oxic or dysoxic depositional environments and >0.75 for a euxinic environment were proposed by Raiswell *et al.* (2018).

Although originally defined as $DOP = \text{pyrite iron}/\text{total reactive iron}$ (Berner, 1970; Raiswell *et al.*, 1988), values may be closely approximated using whole-rock total iron and total sulfur data. Algeo & Li (2020) adopted the equation:

$$DOP_T = S_T \times (55.85/64.12)/Fe_T$$

where total sulfur (S_T) and total iron (Fe_T) and the coefficient 55.85/64.12 represent the weight ratio of Fe/S in stoichiometric pyrite. The use of S_T and Fe_T results in the inclusion of some non-pyrite sulfur (e.g. organic sulfur) and some non-reactive iron (e.g. silicate- or carbonate-bound Fe) in the calculation of the DOP_T

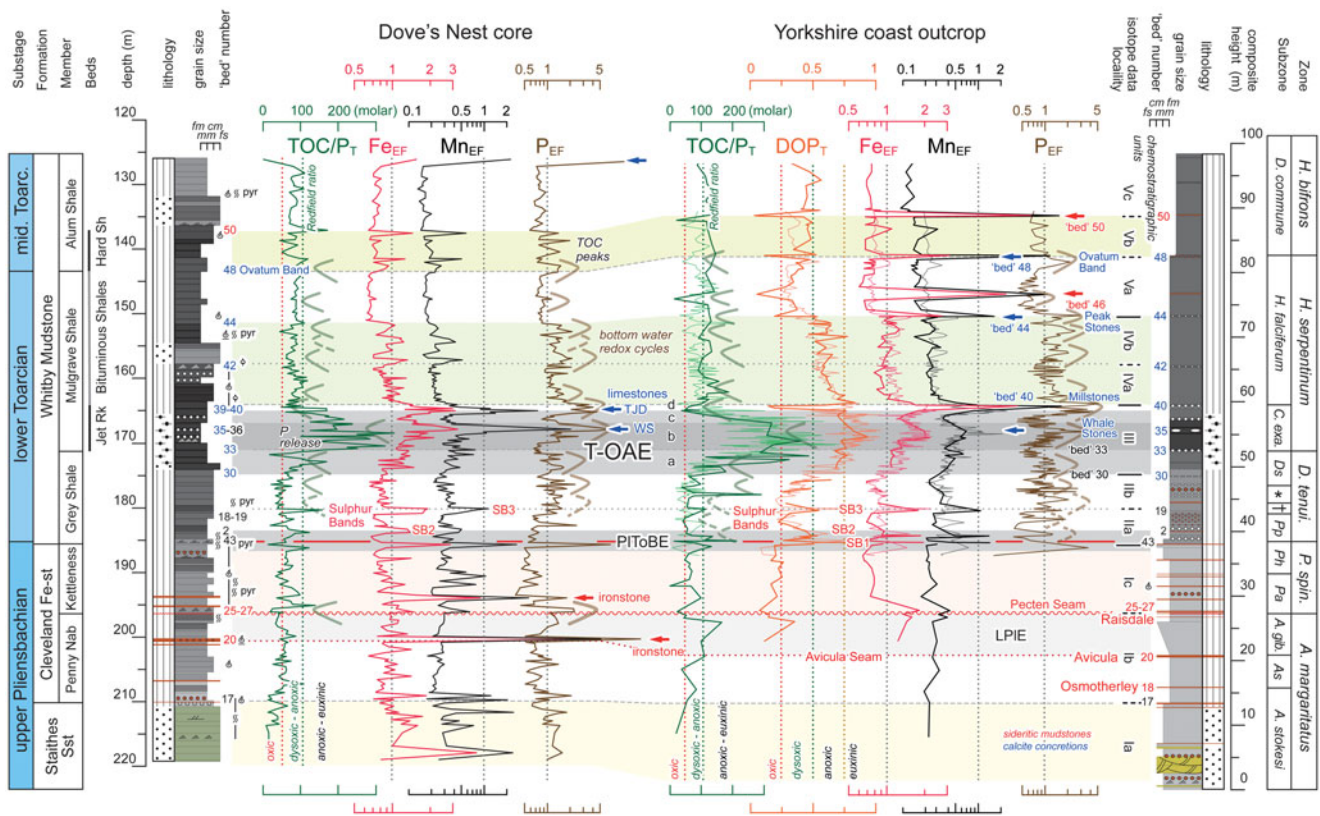


Figure 14. Correlation of TOC/P_T, DOP_T, Fe_{EF}, Mn_{EF} and P_{EF} between the Dove's Nest core and Yorkshire coastal outcrop sections. Coast geochemical profiles from McArthur *et al.* (2008), McArthur (2019) and Remíz & Algeo (2020) with additional high-resolution data (Thibault *et al.*, 2018); Yorkshire chemostratigraphic Units I – V modified from Remíz & Algeo (2020). Stratigraphy as in Figs 2, 4. WS = Whale Stones ('bed' 35); TJD = Top Jet Dogger ('bed' 39). Enrichment factors (EF) are calculated relative to PASS. Data of Thibault *et al.* (2018) are recalibrated relative to McArthur *et al.* (2008) and McArthur (2019): stratigraphic heights are increased by 1.1 m; Al values are increased by 20% to remove analytical bias. Vertical grey dotted lines are EF values of 1. Vertical green dotted lines indicate the Redfield ratio, a TOC/P ratio of ~106:1, typical of marine plankton biomass (Redfield *et al.*, 1963). Values of >106 indicate P-release from the sediment under reducing conditions. Vertical dotted lines on the TOC/P_T and DOP_T plots mark the positions of redox boundaries typically associated with values of 50 and 0.25 (red, oxic/suboxic), 106 and 0.5 (green, dysoxic/anoxic) respectively, following Algeo & Ingall (2007) and Algeo & Maynard (2004). More conservative threshold DOP values of <0.45 for oxic or dysoxic depositional environments and >0.75 for a euxinic environment (gold vertical dotted line) have been proposed by Raiswell *et al.* (2018).

ratio. These amounts are typically small but, nonetheless, they may result in different values of DOP and DOP_T for a given sample (e.g. Algeo *et al.*, 2008; Algeo & Liu, 2020). DOP vs DOP_T correlations are formation-specific, so DOP_T palaeoredox thresholds determined in the literature cannot be applied universally without validation.

Several studies have been undertaken on the Yorkshire coastal succession that include DOP data. DOP values of 0.84 ± 0.03 were reported for the Jet Rock (*C. exaratum* Subzone) by Raiswell & Berner (1985) and between 0.8 and 0.9 by Pearce *et al.* (2008). Recent studies on the Yorkshire coastal succession have used S_T and Fe_T data, where either DOP_T = 0.95 × S_T/Fe_T, the decrease in S content incorporated to allow for the presence of organic S (McArthur *et al.*, 2008) or simply DOP_T = S_T/Fe_T (Thibault *et al.*, 2018). DOP_T values calculated by McArthur *et al.* (2008) and Thibault *et al.* (2018) are comparable (0.84 ± 0.09 for Subunit IIIb) to published DOP results. Such high values significantly exceed the 0.75 threshold for euxinic environments (Figs 14, 15; Raiswell *et al.*, 2018) and offer very strong evidence for long-term euxinic bottom-water conditions in the Cleveland Basin during the T-OAE (Raiswell & Berner, 1985; Raiswell *et al.*, 1993; Wignall *et al.*, 2005; McArthur *et al.*, 2008; Pearce *et al.*, 2008; Thibault *et al.*, 2018). Nonetheless, petrographic evidence shows levels of fine-scale bioturbation even during this interval, despite an absence of visible trace fossils (Caswell & Herringshaw, 2023).

Sulfur contents and Fe speciation were not determined in the Dove's Nest samples. Additionally, it should be noted that the presence of significant siderite and berthierine in parts of the Yorkshire succession, particularly in the Cleveland Ironstone, will be particularly significant for raising Fe_T values (e.g. Thibault *et al.*, 2018, fig. 7A) and will generate lower than true DOP values in samples containing these minerals.

DOP_T profiles for the coastal succession from McArthur *et al.* (2008) and Thibault *et al.* (2018) are illustrated in Figures 14 and 15. The DOP_T curve morphology and redox interpretation are very similar to those provided by TOC/P_T. In both cases, largely oxic conditions with possible minor dysoxic intervals characterized the late Pliensbachian (Unit I). Oxic conditions prevailed during the earliest Toarcian but brief intervals of anoxia – euxinia first appeared at the start of the Toarcian (Sulphur Band 1) and reoccurred during the deposition of Sulphur Bands 2 and 3. A general drift towards persistent dysoxia preceded the onset of T-OAE which was marked by a rapid shift to anoxia – euxinia that prevailed in the area, with varying intensity, throughout the event.

T-OAE Unit III is the only interval where DOP_T values consistently fluctuate above the threshold of >0.75 for euxinic environments proposed by Raiswell *et al.* (2018), with the highest values present in Subunits IIIb and c. A decrease in pyrite framboid mean size to ≤5 μm accompanying rising TOC and TOC/P_T trends in Subunit IIIa is indicative of a fine fraction component

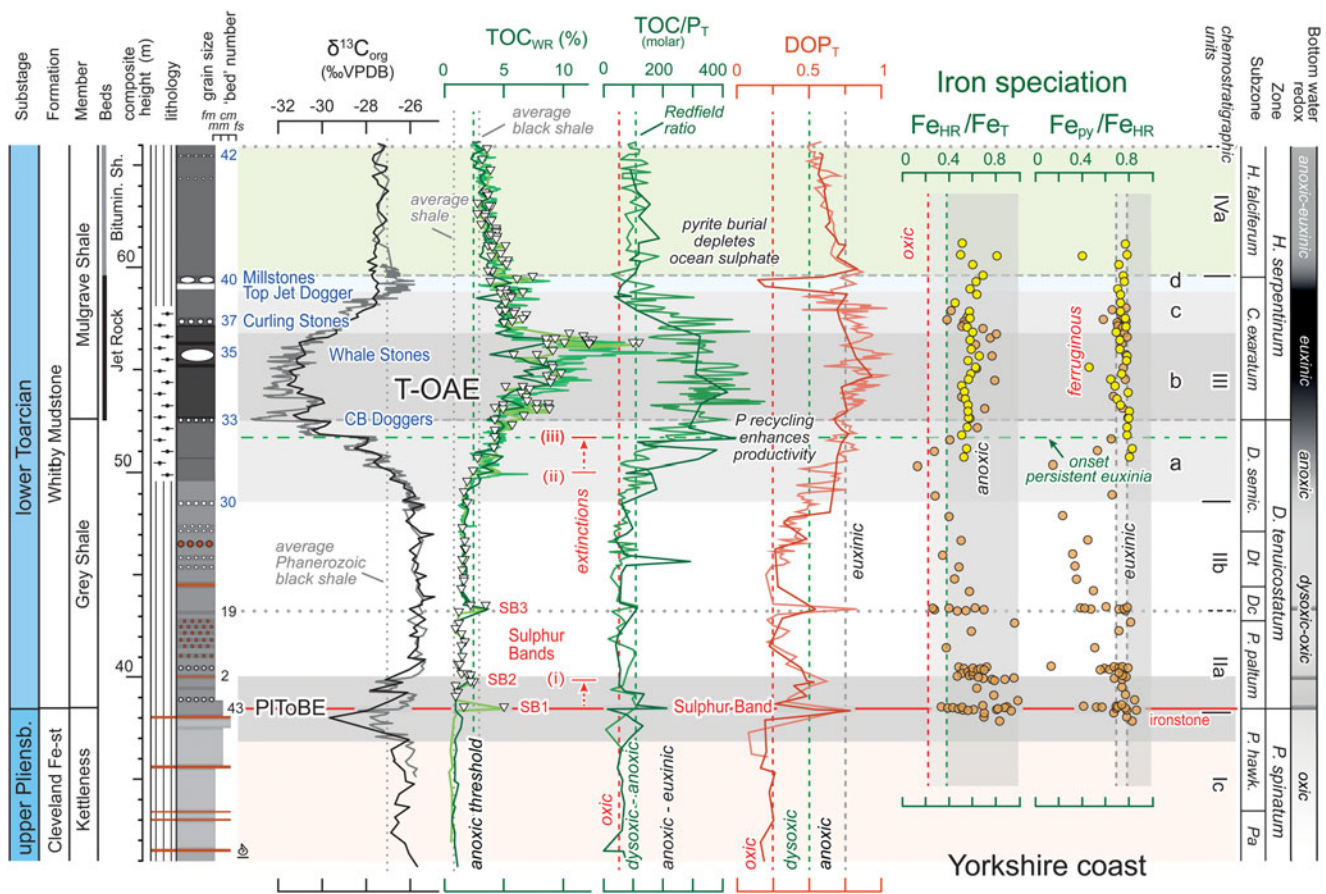


Figure 15. Bottom-water redox proxy interpretation for the upper Pliensbachian – lower Toarcian of the Cleveland Basin derived from TOC, TOC/P, DOP and Fe speciation. $\delta^{13}\text{C}_{\text{org}}$ profile for Dove's Nest (Trabucho-Alexandre *et al.*, 2022, black) rescaled to match coast composite data (see Fig. 2 for sources). Rescaled whole-rock TOC profile for Dove's Nest (Trabucho-Alexandre *et al.*, 2022, dark green) with coast composite data of Kemp *et al.* (2011; thin yellow-green high-resolution curve) and trend of the low-resolution coast datasets of Ruvalcaba Baroni *et al.* (2018, open triangles) and McArthur (2019) (thin pale green low-resolution curve; see Fig. 2). Average shale and black shale values as in Figure 2; 'anoxic threshold' of $\text{TOC}_{\text{WR}} = 2.5$ wt% follows Algeo & Maynard (2004). Low-resolution TOC/P_T (dark green) and DOP_T (dark orange) curves from McArthur *et al.* (2008) and Ramirez & Algeo (2020) with high-resolution data (thin pale curves) from Thibault *et al.* (2018); see Figure 14 for further information. Iron speciation data from Salem (2013, cream-filled circles) and Houben *et al.* (2021, yellow-filled circles) with redox field boundaries after Raiswell *et al.* (2018). Extinction levels (i)–(iii) after Caswell *et al.* (2009). Pliensb. = Pliensbachian; Bitumin. Sh. = Bituminous Shales; *D. semic.* = *Dactyloceras semicelatum*; *Dt* = *D. tenuicostatum*; *Dc* = *D. clevelandicum*; *P. hawk.* = *Pleuroceras hawskerense*; *Pa* = *P. apyrenum*.

precipitated from a euxinic water column (Wignall & Newton, 1998; Wignall *et al.*, 2005). Song *et al.* (2017) reported >95% of <7 μm syngenetic framboidal pyrite in T-OAE carbonaceous mudstones from Runswick Bay.

The TOC/P_T and DOP_T proxies show different trends following the OAE (Fig. 14): the former indicates a rapid return to fluctuating dysoxic conditions that prevailed through the remainder of the early Toarcian into the early middle Toarcian. The DOP_T proxy implies that anoxia persisted through most of the *H. falciferum* Subzone (Unit IV) prior to a shift to dysoxia in late *H. falciferum* Subzone time (Unit V). This interval of divergence coincides with a period of weaker basin restriction indicated by Mo vs TOC proxy (Section 13a) but also occurs with a step increase in $\delta^{34}\text{S}_{\text{CAS}}$ values (Section 16.a.2) interpreted to reflect the impact of global pyrite burial and indicate a significant fall in oceanic sulfate content.

12.c. Iron speciation $\text{Fe}_{\text{HR}}/\text{Fe}_{\text{T}}$ and $\text{Fe}_{\text{Py}}/\text{Fe}_{\text{HR}}$

Bottom-water redox interpretations for the Cleveland Basin derived from DOP_T values and pyrite framboid size may be further assessed using sedimentary rock Fe-speciation data

obtained from the Yorkshire coast succession by Salem (2013) and Houben *et al.* (2021). These proxies are based on the presence or absence of enrichments in key iron minerals (Raiswell & Canfield, 1998; Raiswell *et al.*, 2018) with data derived from chemical extracts of bulk rock samples. Highly reactive iron (Fe_{HR}) comprises ferric oxides, iron carbonates, magnetite and pyrite. A highly reactive iron to total iron ratio ($\text{Fe}_{\text{HR}}/\text{Fe}_{\text{T}}$) of below 0.38 is indicative of oxic – dysoxic bottom waters with values <0.22 unambiguously oxic. Values >0.38 provide strong evidence for anoxic depositional conditions (Fig. 15).

The extent of pyritization of the highly reactive Fe pool ($\text{Fe}_{\text{Py}}/\text{Fe}_{\text{HR}}$) indicates whether the bottom water was anoxic (i.e. oxygen depleted and ferruginous) or euxinic (Fe-free and sulfidic), provided that the $\text{Fe}_{\text{HR}}/\text{Fe}_{\text{T}}$ ratio is above 0.38. $\text{Fe}_{\text{Py}}/\text{Fe}_{\text{HR}}$ values of <0.7 reflect ferruginous water column conditions. The threshold between anoxic and euxinic bottom-water conditions is less well-defined but is generally placed between 0.7 and 0.8 (Fig. 15; Raiswell *et al.*, 2018). In cases where $\text{Fe}_{\text{Py}}/\text{Fe}_{\text{HR}}$ ratios of >0.7 indicate sulfidic conditions but $\text{Fe}_{\text{HR}}/\text{Fe}_{\text{T}}$ is <0.38 (i.e. oxic – dysoxic bottom water) H_2S production is thought to occur close to but below the sediment/water interface.

The use of Fe-speciation proxies needs to be assessed critically (Raiswell *et al.*, 2018). For example, carbonate-rich samples may include additional Fe²⁺ incorporated into diagenetic carbonates, which may lead to an overestimation of anoxia when Fe-speciation is applied to sediments with low Fe_T or low TOC contents (<0.5%). In this study, the Fe content of upper Pliensbachian – middle Toarcian rocks from Dove's Nest, for example, fluctuates around the average shale value of 5.1% (Fig. S1), with the lowest value of 1.7% Fe (with 3.9% TOC) obtained from the Whale Stones concretion sample, so palaeoredox interpretations should be robust.

Fe_{HR}/Fe_T and Fe_{py}/Fe_{HR} data from the Yorkshire coast (Fig. 15) support interpretations derived from the TOC/P_T and DOP_T profiles. Highly variable redox conditions during the earliest Toarcian are indicated by coincident high Fe_{HR}/Fe_T and Fe_{py}/Fe_{HR} values within the three Sulphur Bands (SB1 – 3), indicating three major episodes of bottom-water euxinia. Additionally, cm-scale sampling through the Sulphur Bands at Port Mulgrave and Hawsker Bottoms by Salem (2013) evidences shorter-term fluctuating palaeoredox conditions during their deposition, with cycling between euxinic and dysoxic conditions. The bioturbated mudstones below, between and above the Sulphur Bands show less enrichment of TOC, reactive iron and trace metals, with lower TOC/P_T and DOP_T values (Fig. 15), but nonetheless yield Fe_{HR}/Fe_T ratios that fluctuate around the Fe-proxy threshold characteristic of anoxia (0.38), equating to the dysoxic intervals of the TOC/P_T and DOP_T proxies. These observations demonstrate that short periods of anoxia – euxinia, beginning at the Pliensbachian – Toarcian boundary, preceded the T-OAE. This is consistent with thallium isotope data from western Canada that indicates that the onset of global deoxygenation of ocean water occurred at this time (Them *et al.*, 2018).

Samples through T-OAE Unit III into the base of the Bituminous Shales Subunit IVa yield Fe_{HR}/Fe_T values of >0.38 and generally ~0.6 (Salem, 2013; Houben *et al.*, 2021), which point to persisting anoxic bottom-water conditions (Fig. 15). However, short-lived oxic intervals on a seasonal or annual scale would not be resolved by the current sampling resolution. Brief oxygenation events are indicated by petrographic evidence of fine-scale bioturbation in the laminated mudstones. On the other hand, it is striking that there is a total absence of macroscopic trace fossils throughout the T-OAE in the Cleveland Basin. Elsewhere in the Toarcian of Europe, there are usually at least a few bioturbated intervals, reflecting geologically brief oxygenation events, but there is no ichnological evidence of this in the Yorkshire succession.

Fe_{py}/Fe_{HR} ratios of 0.7 to 0.8, lying at the threshold to euxinic conditions, indicate that H₂S was present in bottom waters, albeit not permanently.

12.d. Fe_{EF}, Mn_{EF} and P_{EF}

Profiles for Fe, Mn and P for Dove's Nest and the Yorkshire coast successions plotted as enrichment factors show excellent agreement between the sections (Fig. 14). Fe_{EF} and Mn_{EF} display highly coherent profiles that indicate common mineralogical and environmental controls on their distributions. The two elements are strongly associated by their co-occurrence in Fe–Mn oxyhydroxides, carbonates (calcite, dolomite and siderite) and berthierine (e.g. Aggett, 1990). Iron has an additional association with pyrite, and this is reflected by the relatively elevated values of the Fe_{EF} relative to the Mn_{EF} profile through Subunit IIIb, the interval of high DOP_T values indicative of high pyrite contents.

Highest Fe_{EF} and Mn_{EF} values occur in (1) ferruginous bands of the Staithes Sandstone where Fe–Mn oxyhydroxides (e.g. goethite) are likely the dominant minerals; (2) ironstones in the Cleveland Ironstone associated principally with high siderite and low phyllosilicate contents; (3) the Sulphur Bands of the Grey Shale (siderite); (4) concretionary carbonates (calcite, dolomite) in the Jet Rock – the Whale Stones and Top Jet Dogger; (5) concretionary calcitic (Peak Stones, Ovatum Band) or sideritic ('beds' 46, 50) levels in the Bituminous Shales and Hard Shales.

With the exception of the beds noted above, Fe_{EF} values generally fluctuate around average shale values through Units I, II and IV, are consistently enriched relative to PASS in Unit III (average 1.5), reflecting the addition of authigenic pyrite and show a plateau of low Fe_{EF} values (average 0.75) through Unit V (Fig. 14). By contrast, Mn is significantly depleted throughout the succession (Mn_{EF} ~0.2 – 0.3) and Mn_{EF} values of >1 occur only in ironstones and concretionary carbonates. The generally low Mn values are consistent with the presence of oxygen-depleted bottom waters that prevented the deposition, redox cycling and concentration of Mn in the sediments (Calvert & Pedersen, 1996) which retained Fe in carbonates, silicates and sulfides. The carbonaceous mudstones correspond to Thermodynamic Zone III (low Mn, high Fe, low V, sulfidic) facies of Quinby-Hunt & Wilde (1994), typically associated with anoxic bottom waters.

The P_{EF} profiles from Dove's Nest and the Yorkshire coast show excellent agreement (Fig. 14). A cyclic pattern is particularly apparent in the ultra-high-resolution P data of Thibault *et al.* (2018) from the coast, with regular P_{EF} peaks of >2 and intervening troughs with a typical minimum of <0.6. These cycles coincide with opposing shifts in the TOC/P_T profile that correspond to a transition to oxic bottom waters driving P enrichment and periods of anoxic bottom water leading to P depletion. A matching pattern is observed in the lower resolution data from Dove's Nest. This is consistent with the differing processes and rates of organic carbon and phosphorus remineralization under varying redox conditions (Section 12a) and evidences a cyclic pattern of bottom-water oxygenation in the Cleveland Basin during the early Toarcian.

Five P_{EF} cycles are recognized between the bases of the *D. clevelandicum* († symbol in Fig. 14) and *H. falciferum* subzones dated at 183.94 Ma and 182.06 Ma (Gradstein *et al.*, 2020), an interval of 1.88 Ma. This yields a periodicity approaching the Milankovitch ~405 ka long eccentricity cycle. Thibault *et al.* (2018) postulated a ~405 ka eccentricity cycle for detrital input in the *D. tenuicostatum* – *C. exaratum* subzones (see Fig. 4) in the Cleveland Basin based on spectral analysis of Zr/Al data from the coast (Hawsker Bottoms), but these do not show a consistent relationship to the P_{EF} cycles (compare Figs 4 and 14). By contrast, taking the base *D. tenuicostatum* and *H. bifrons* zone ages of 184.20 Ma and 181.17 Ma (3.03 Ma; Gradstein *et al.*, 2020) with 13 P_{EF} cycles (Fig. 14) yields a 250 ka periodicity. Applying other subzone ages generates a similar range of values. There is, therefore, no evidence for a consistent periodicity with potential orbital forcing of the P_{EF} cycles, but it is acknowledged that changes in sedimentation rate and/or hiatuses in the section (e.g. Suan *et al.*, 2008b; McArthur *et al.*, 2016) make spectral analysis challenging (Boulila *et al.*, 2014, 2019; Thibault *et al.*, 2018).

13. Chemostratigraphic correlation, TOC and redox-sensitive trace metals

TOC, Mo, U and V profiles for the Dove's Nest core are correlated to a compilation of data (Ruvalcaba Baroni *et al.*, 2018; Thibault

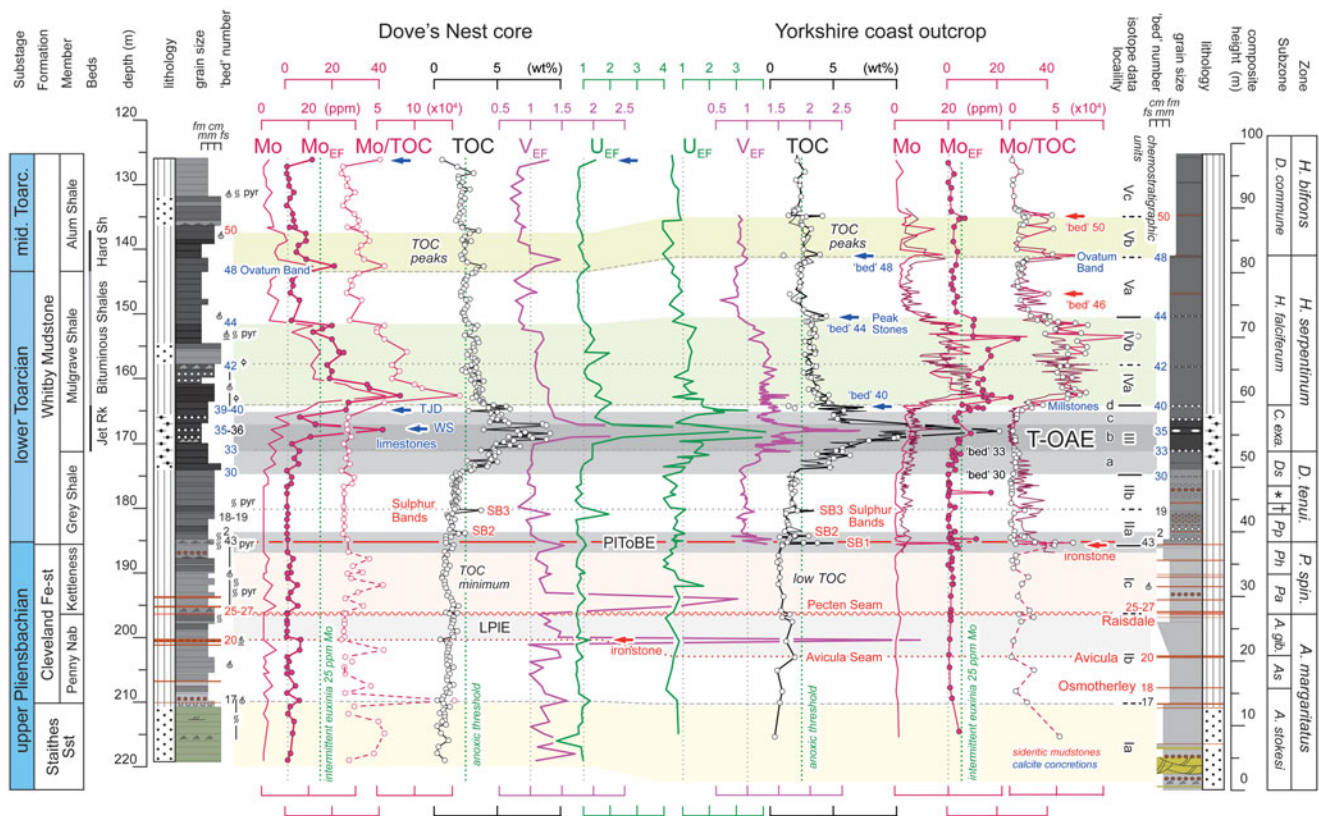


Figure 16. Correlation of Mo, TOC, V and U between the Dove's Nest core and Yorkshire coastal outcrop sections. Dove's Nest data this study. Yorkshire coast Mo and Mo/TOC and TOC plots from McArthur (2019) with additional high-resolution TOC (thin black line, see Fig. 2), Mo and Mo/TOC curves (thin dark red lines; Thibault *et al.*, 2018). Yorkshire V_{EF} data were calculated from Ruvalcaba Baroni *et al.* (2018) with Mo_{EF} , U and U_{EF} data after Remíz & Algeo (2020). Stratigraphy as in Figures 2, 4. WS = Whale Stones ('bed' 35'); TJD = Top Jet Dogger ('bed' 39). Enrichment factors (Section 6.d), e.g. Mo_{EF} , are calculated relative to PASS. Vertical grey dotted lines are EF values of 1. Vertical green dotted lines indicate the 'intermittent euxinia' boundary of 25 ppm Mo (Scott & Lyons, 2012) and the 'anoxic threshold' of TOC = 2.5 wt% (Algeo & Maynard, 2004). Consistent enrichment in authigenic uranium ($U_{EF} > 1$) characterizing Units III and IV is also well displayed in spectral gamma-ray logs of the coastal sections (Myers & Wignall, 1987; Parkinson, 1996).

et al., 2018; McArthur, 2019; Remíz & Algeo, 2020) for the equivalent Yorkshire coastal succession in Figure 16. Molybdenum content (Mo), enrichment factors (Mo_{EF}) and Mo/TOC ratios, together with uranium (U_{EF}) and vanadium (V_{EF}) enrichment factors, clearly differentiate intervals of substantial redox-driven transition metal enrichment that complement interpretations based on Fe speciation (Fig. 15, Section 12.c). The lower resolution of the Dove's Nest trace-metal profiles (Fig. 16) limits comparison to the ultra-high-resolution data available for the lower Toarcian of the coastal sections (Thibault *et al.*, 2018) but there is good correspondence between the Mo, U and V curves of the two successions.

The high-resolution structure and values of the Toarcian TOC curves are well correlated between the Dove's Nest core and the coastal succession (Figs 2, 15, 16). The 'anoxic threshold' (oxic – anoxic non-sulfidic bottom-water boundary) of 2.5% TOC (Algeo & Maynard, 2004) is initially exceeded briefly at the level of the three Sulphur Bands in the lower Grey Shale (Unit II). Peak TOC values then characterize T-OAE Unit III with an interval at the top of Subunit IIb documented in the higher resolution data from the coast that includes values of $>10\%$, indicative of euxinic conditions ('euxinic threshold').

The interval of the TOC maximum (summit of Subunit IIIb) displays the highest U_{EF} and V_{EF} values in the lower Toarcian (Fig. 16), peaking in the Whale Stones 'bed' 35 at 5.4 and 2.8,

respectively in the coast data and both reaching >7 at Dove's Nest. A return to anoxia is indicated at the top of Unit III and through Unit IV with lower TOC, U and V contents, then generally dysoxic bottom waters are interpreted for Unit V with TOC values around or below the anoxic threshold. Pulses of renewed anoxia at the bottom and top of Subunit Vb are documented in the Hard Shales at the base of the middle Toarcian.

Factors controlling the TOC content of sediments are complex (Tyson, 2005) and TOC alone cannot be regarded as a definitive indicator of bottom-water redox, since similar TOC contents may occur in sediments deposited under fully oxygenated to euxinic water columns (e.g. Canfield, 1994; Hartnett *et al.*, 1998; Kemp *et al.*, 2022b). Nonetheless, the application of a 2.5% TOC_{WR} cut-off to define the anoxic threshold coincides exactly with the disappearance of trace fossils in the Cleveland Basin succession (cf. Caswell & Herringshaw, 2023), which only reappear when bulk-rock contents fall consistently below that value (Section 19.a). Palaeontological evidence therefore fully supports the use of this value as an indicator of seafloor anoxia in the study sections.

Coincident TOC, Mo and U enrichments are generally considered to be strong indicators of deposition in oxygen-depleted bottom waters (e.g. Emerson & Husted, 1991; Calvert & Pedersen, 1993; Algeo & Tribouillard, 2009; Scott & Lyons, 2012; Tribouillard *et al.*, 2012; Algeo & Liu, 2020; Fernández-Martínez *et al.*, 2023; Paul *et al.*, 2023) with individual enrichment factors

providing information on bottom-water restriction and redox conditions, ranging from oxic through anoxic to euxinic. The current understanding of the geochemical behaviour of Mo and U in seawater and sediments has been reviewed by Paul *et al.* (2023).

Vanadium has also been advocated as a good redox proxy (e.g. Emerson & Huested, 1991; Quinby-Hunt & Wilde, 1994; Algeo & Maynard, 2004; Piper & Calvert, 2009; Scholz, 2018; Algeo & Liu, 2020; Bennett & Canfield, 2020). Unlike Mo and U, vanadium is present in high concentrations in the phyllosilicate fraction of sediments, as indicated by its high value in average marine shale (140 ppm vs 1 ppm Mo and 3 ppm U; Taylor & McLennan, 2001), so bulk-rock values are less sensitive to redox change.

Chemostratigraphic profiles for U and V show similar trends for the lower Toarcian that differ substantially from the Mo curves (Figs 5, 16). Despite their different stratigraphic trends, Mo and U are both positively correlated with TOC at Dove's Nest ($r \geq 0.4$, Table S3) and the three constituents show a close association on the PCA plot (Fig. 9) with negative PC1 and PC2 scores (Table S4) driven by samples from Units III and IV, the T-OAE and lower Bituminous Shales intervals. Some samples of the Hard Shales in Unit V fall in the same sector. Environmental factors responsible for the differing behaviour of Mo, U and V may be examined further using bivariate geochemical plots and knowledge of their distribution in sediments from modern ocean basins. TOC vs trace metal cross-plots of Yorkshire coast data have been used previously to interpret bottom-water redox conditions during the deposition of Cleveland Basin Toarcian mudstones (McArthur *et al.*, 2008; Pearce *et al.*, 2008; Thibault *et al.*, 2018; McArthur, 2019; Ramirez & Algeo, 2020).

13.a. Molybdenum

A plot of Mo vs Al of upper Pliensbachian – middle Toarcian samples from Dove's Nest and published data from the Yorkshire coastal succession (Fig. 17a) illustrates the significant enrichment in Mo (> 10 – 60 ppm) that characterizes the lower Bituminous Shales of Unit IV and to a lesser extent (> 3 ppm) the upper Grey Shale – Jet Rock interval of T-OAE Unit III, compared to other parts of the succession (≤ 2 ppm) and to average shale (1 ppm). Elevated Mo values also occur in the organic-rich intervals of the Sulphur Bands (SB1 – 3, 3 – 25 ppm) at the base of Subunit IIa, and at the bottom and top of the Hard Shales of Subunit Vb (up to 22 ppm). The Mo vs Al plot shows the lack of a clear correlation between the two elements, suggesting no significant association of Mo with the aluminosilicate fraction of the rocks. The Pearson correlation and PCA (Tables S3, S4) results both display a weak negative correlation ($r = -0.3$) between the two constituents.

The Mo vs TOC plot (Fig. 17b) illustrates that high Mo contents are associated with TOC enrichment, with Mo values increasing substantially in samples containing $\geq 2.5\%$ TOC, the 'anoxic threshold' of Algeo & Maynard (2004), but with substantial scatter. Relatively few samples exceed the 'intermittent euxinia' threshold of 25 ppm Mo proposed by Scott & Lyons (2012), all of which occur in Unit IV (Fig. 16). Positive correlations between Mo and TOC are observed for Unit III and IV sample suites but with very different slopes. In addition to the data plotted in Figure 17, samples with 10 – 20% TOC (exceeding the threshold for euxinic bottom waters) have been recorded from Unit III of the coastal outcrop (Fig. 2). These data fall outside the plot area of Figure 17a, d and f but lie on the trend of the Unit III lower regression line shown in Figure 17b.

The redox behaviour of Mo in marine environments has been reviewed by Tribouillard *et al.* (2006), Algeo & Tribouillard (2009),

Scott & Lyons (2012), Hardisty *et al.* (2018), Bennett & Canfield (2020), Them *et al.* (2022) and Paul *et al.* (2023), amongst others. Molybdenum is present in seawater principally in the form of molybdate (MoO_4^{2-}). Molybdenum is not concentrated by plankton and displays little affinity for the surfaces of clay minerals, CaCO_3 and, generally, Fe-oxyhydroxides (but see Scholz *et al.*, 2017) at marine pH values but may be captured by Mn-oxyhydroxides, typically at the sediment surface. Molybdenum accumulation in these deposits is very slow, but the overwhelming dominance of oxic environments in the modern oceans results in an estimated 35 – 50% of Mo being removed via adsorption onto Mn-oxyhydroxides.

Reduction of oxyhydroxides during diagenesis in organic-rich sediments liberates adsorbed Mo to pore waters. Molybdenum fixation is believed to take place principally by reduction to thiomolybdate complexes ($\text{MoO}_x\text{S}_{4-x}$, $x = 0 - 3$) in the presence of free H_2S and subsequent sequestration in organic matter and/or iron sulfides. Molybdenum fixation may also occur directly in a euxinic water column. Here, Mo is scavenged from seawater by settling the organic matter and sulfide particles, leading to substantial Mo enrichment (reaching 100 ppm) in the underlying organic-rich sediment. It is estimated that 50 – 65% of Mo is removed in the oceans via these processes today because even though only a very small proportion ($\ll 1\%$) of the modern seafloor is overlain by euxinic bottom waters, burial efficiency is very high.

McArthur *et al.* (2008) argued that the development of weak hydrographic restriction in the Cleveland Basin during the early *H. falciferum* Subzone (lower Bituminous Shales of Unit IV) was responsible for substantial Mo enrichment from sulfidic bottom waters. However, samples from Unit III (T-OAE) also display a significant positive correlation with TOC yet these show up to two orders of magnitude less enrichment. By analogy to modern anoxic basin environments (Algeo & Lyons, 2006; Algeo & Rowe, 2012), the low Mo values of the T-OAE black shales (Unit III) relative to their high TOC contents have been previously interpreted to reflect the presence of an extremely restricted water mass in the Cleveland Basin during the T-OAE (McArthur *et al.*, 2008; McArthur, 2019; Ramirez & Algeo, 2020), with local Mo drawdown limiting uptake of the element into the sediment.

The impact of water mass restriction on the Mo/TOC (ppm/%) ratio of sediments in modern basins may be illustrated by data from weakly restricted (e.g. Saanich Inlet, ~ 45) to very restricted (e.g. Black Sea, ~ 4.5) silled basins (Fig. 17). It should be noted, however, that a low Mo/TOC ratio of ~ 6 also characterizes sediments from strong upwelling systems, such as modern offshore Namibia (Algeo & Lyons, 2006). Here, very high productivity induced by coastal upwelling leads to a high rate of TOC deposition that overwhelms the supply of Mo from upwelling water.

TOC whole-rock concentrations determined in the Dove's Nest samples all fall below 10% (Fig. 17b) but values exceeding 15% have been recorded from the upper beds of Subunit IIIb on the Yorkshire coast (Figs 2, 7; Kemp *et al.*, 2011; Ruvalcaba Baroni *et al.*, 2018; McArthur, 2019; Houben *et al.*, 2021). The coast data form an array that continues the trend of the shallowest regression line plotted in Figure 17b, interpreted by McArthur *et al.* (2008) to represent the most extreme water mass restriction associated with the highest TOC deposits. However, Cleveland Basin T-OAE samples define trends that show considerably greater Mo depletion (Mo/TOC 0.4 – 2, Fig. 17) than the modern Black Sea.

Thibault *et al.* (2018) argued that comparable trends in Mo across the T-OAE interval in both Yorkshire and the Paris Basin (Hermoso *et al.*, 2013) suggest a similar oceanic drawdown of this

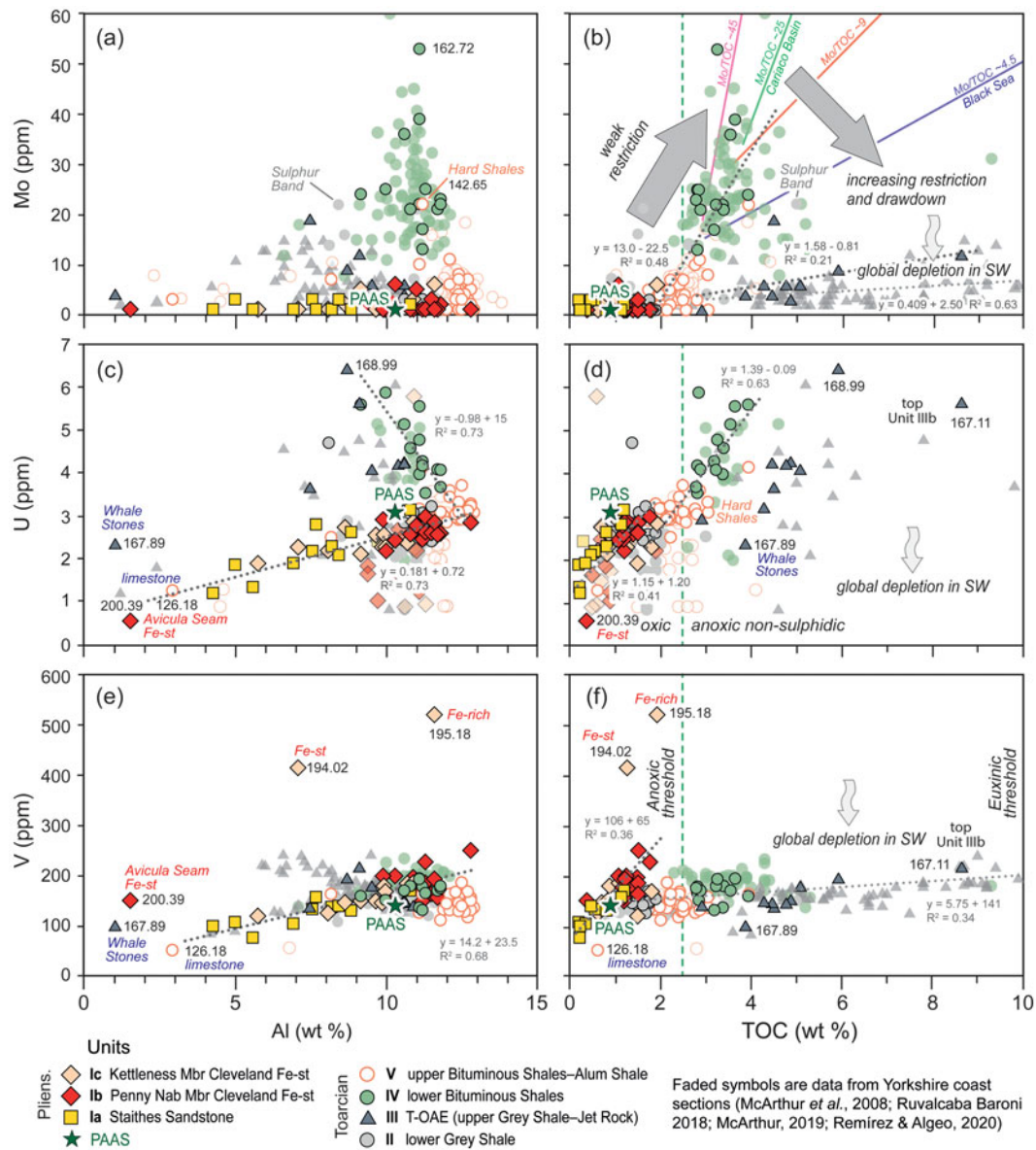


Figure 17. Cross-plots for key redox-sensitive trace metals. (a) Mo vs Al. Mo shows no clear relationship with Al. (b) Mo vs TOC. The steep upper regression line (small grey dots) for Units IV and V (left) derived from the Dove's Nest data, displaying a positive correlation between Mo and TOC, contrasts to the shallow lines (small grey dots) derived for T-OAE Unit III (right – upper line and statistics is for Dove's Nest samples, lower line is for Yorkshire coast samples of McArthur *et al.* 2008). Regression lines from selected modern anoxic silled basins representing increasing deep water renewal times of <10 – 650 ka (Algeo & Rowe, 2012) are Mo/TOC (ppm/%) ~45 Saanich Inlet (purple); ~25 Cariaco Basin (green); ~9 Framvaren Fjord (red); ~4.5 Black Sea (blue). Bottom water restriction trends after Algeo & Lyons (2006). (c) U vs Al. Lower regression line is for Pliensbachian Subunits Ia–c; upper line is for Toarcian Units IV and V (all samples ≥ 3 ppm U). (d) U vs TOC. Lower regression line (left) for Subunits Ia–c; upper regression line (right) for Units IV and V. (e) V vs Al. Regression line is for Pliensbachian Subunits Ia–c, excluding the three Fe-rich flyers. (f) V vs TOC. Regression lines are for Pliensbachian Subunits Ia–c (left, Dove's Nest) and Toarcian Units II–V (right, coast samples; Ruvalcaba Baroni *et al.*, 2018). TOC-based anoxic (2.5%, vertical dashed green line marking boundary between oxic and anoxic non-sulphidic conditions) and euxinic (10%, upper limit of x-axis) thresholds after Algeo & Maynard (2004). Solid symbols are from the Dove's Nest core (this study), faded symbols are for Yorkshire coastal outcrop samples (McArthur *et al.*, 2008; Ruvalcaba Baroni *et al.*, 2018; McArthur, 2019; Ramirez & Algeo, 2020). Dove's Nest TOC data are whole-rock values. Average shale (PASS) composition after Taylor & McLennan (2001). Note that samples with 10 – 20% TOC reported from Unit III of the coastal outcrops fall outside the plot area of (B), (D) and (F) but lie on the trends of the regression lines shown.

element accompanying widespread anoxia in both basins. Furthermore, clear evidence of a transgressive trend in the Cleveland Basin at the time of maximum Mo drawdown (Figs 10, 16) conflicts with the basin restriction model for the euxinic conditions that characterize the T-OAE interval. Data from a deep Panthalassic Ocean site in Japan (Inuyama area; Kemp *et al.*, 2022a) also evidences drawdown of Mo and U accompanying the T-OAE. Here also, a marked expansion of anoxic and possibly euxinic conditions to the seafloor occurred during both the PIToBE

and the T-OAE, accompanied by increased organic carbon burial, but Mo drawdown cannot be related to hydrographic restriction.

Them *et al.* (2022) documented comparable low Mo/TOC values (1 – 2) through the T-OAE intervals in a transect of 3 sites from the Western Canada Sedimentary Basin, an area that is interpreted to have maintained strong connections with Panthalassa open-ocean deep waters throughout the Early Jurassic. By contrast to the Cleveland Basin and Japan sites, this area experienced relatively stable anoxic and euxinic conditions

throughout late Pliensbachian – middle Toarcian (Them *et al.*, 2018), and there is no geological evidence to suggest that basin restriction played any role in the observed Mo/TOC trends. Sustained anoxic/euxinic conditions at a site are essential to successfully isolate global changes in the marine Mo reservoir from local factors.

The results of Them *et al.* (2022) confirm previous work (Pearce *et al.*, 2008; Thibault *et al.*, 2018; Kemp *et al.*, 2022a) indicating that global drawdown of oceanic Mo accompanied the T-OAE. In the upper Pliensbachian, the average Mo/TOC value from the three Western Canada sites is ~25 (range of ~22 – 30), which is similar to the modern euxinic Cariaco Basin (~25, Fig. 17; cf. Algeo & Lyons, 2006), suggesting a large global marine Mo inventory similar to today. The average Mo/TOC value of ~2 for anoxic/euxinic sediments deposited during the T-OAE in Western Canada is identical to that obtained for Dove's Nest, with an even lower value of 0.4 being derived from the larger Yorkshire coast dataset (Fig. 17b). These very low values suggest additional local Mo drawdown in the Cleveland Basin from already highly depleted ocean water. Post-T-OAE Mo/TOC values in the Canadian sites typically range from 4 to 10, like those seen in the lower Bituminous Shales, Unit IV of Yorkshire, indicative of a return to higher Mo contents in seawater (and contraction in the global area of euxinic bottom waters), but at lower concentrations than those that preceded the T-OAE.

Local basin restriction with the development of highly euxinic bottom waters, coincident with a global drawdown of Mo, has been interpreted for the T-OAE interval in the Dutch Central Graben, West Netherlands Basin, SW German Basin and Paris Basin (Fernández-Martínez *et al.*, 2023). Other areas in northern Europe including the Cardigan Bay Basin, together with Tethyan and Panthalassa Ocean sites, remained unrestricted but with evidence of the presence of euxinic pore waters at the sediment/water interface at some localities. The small global marine Mo reservoir during the T-OAE in combination with variable basin restriction explains the large regional differences in sediment Mo (and inferred water mass) concentrations and isotopes documented from European basins.

13.b. Uranium

The U vs Al plot (Fig. 17c) illustrates a strong positive correlation ($R^2 = 0.73$) between the two elements for the Pliensbachian samples of Subunits Ia – c and Toarcian Unit V that indicates an association between U and the aluminosilicate fraction (principally clay minerals and a heavy mineral suite) of the rocks, as generally seen in marine black shales (Swanson, 1961). Mudstones with the highest Al contents in the array, cluster around the average shale value of 3 ppm.

Low U concentrations of 2 – 4 ppm are generally found in mudstones (Swanson, 1961; Spirakis, 1996) and U contents of 1 – 3 ppm are typical throughout the Earth's crust (Hazen *et al.*, 2009). Scatter towards lower values on the U vs Al plot (Fig. 17c) is driven principally by increasing proportions of U-poor carbonates (calcite, siderite) and quartz diluting the bulk-rock content. Anomalously high U contents, up to 6.5 ppm, characterize Units III and IV and these show a strong negative correlation ($R^2 = 0.73$) with Al attributable to a positive correlation with TOC (Fig. 17d). The positive correlation between U vs Al and U vs TOC for Subunits Ia – c (Fig. 17c, d) contrasts to the absence of correlation displayed in the corresponding Mo plots. The low U and low TOC contents in the sideritic ironstone of the Avicula Seam are notable.

Uranium occurs in nature in two main redox states, U(IV) and U(VI). In oxygenated solutions, the hexavalent uranyl ($U^{VI}O_2^{2+}$) species forms highly soluble and non-reactive Ca and Mg complexes with $UO_2(CO_3)_3^{4-}$; the dominant aqueous U(VI) species in seawater is neutral $[Ca_2UO_2(CO_3)_3](aq)$ (Endrizzi & Rao, 2014). Under dysoxic – anoxic conditions, U is reduced and forms insoluble tetravalent U compounds and is ultimately fixed in sediments principally as uraninite (UO_2). This reduction, which is likely mediated by microorganisms, leads to preferential uptake of U by anoxic – euxinic sediments (Barnes & Cochran, 1990; Klinkhammer & Palmer, 1991; Khaustova *et al.*, 2021). Unlike Mo, uranium reduction has not been observed in the marine water column but occurs predominantly in association with near-surface iron reduction in organic-rich sediments with diffusion of U into the sediment from overlying bottom waters, favoured by lowered sedimentation rates (Algeo & Maynard, 2004).

Toarcian high-U samples plot consistently within the sulfidic field beyond the 'anoxic threshold' of Algeo & Maynard (2004) on the U vs TOC plot (Fig. 17d), evidencing the formation of authigenic U under anoxic conditions during sedimentation, as uranium was removed from solution. However, the mechanisms involved in this removal are complex (Cumberland *et al.*, 2016) and the phase partitioning in the sediment remains uncertain. Unit III samples of the T-OAE display substantial scatter due in part to variable dilution by carbonates in the concretion beds of the Jet Rock (Fig. 17d), while Unit IV samples from the lower Bituminous Shales define a tighter array with a steeper positive correlation between U and TOC than that defined by Subunits Ia – c.

The offset to lower U/TOC ratios for Unit III T-OAE samples compared to lower Bituminous Shales Unit IV is consistent with global drawdown of U accompanying the T-OAE, as discussed above for Mo (Section 13.a) and interpreted for other episodes of expanded anoxic seafloor area accompanying OAEs, based on uranium isotope studies (e.g. Montoya-Pino *et al.*, 2010; Clarkson *et al.*, 2018).

13.c. Vanadium

Pliensbachian Subunits Ia – c samples display a significant positive correlation between V and Al (Fig. 17e) with some Unit III and most Unit IV samples lying on the same trend. By contrast, Unit V samples form a distinct tight cluster that lies below the line. This offset reflects the lower V/Al ratio that differentiates Unit V from the older beds (Figs 5, 8). Samples of T-OAE Unit III from the Yorkshire coast form a linear array above the line with a negative trend between V and Al, attributable to the diluting effect of the high TOC content in V-rich samples.

Three Fe-rich samples display anomalous high V contents of up to 521 ppm (sample 195.18, Fig. 17e). Moderate enrichment of V in sideritic ironstones (average 114 ppm) from the Cleveland Ironstone was noted by Gad (1966), with distinctive higher values (average 560 ppm) recorded in berthierine (chamosite)-bearing samples. Vanadium enrichment in ironstones is well displayed in the V/Al stratigraphic profile for Dove's Nest (Fig. 5). The highest V samples also display anomalous high Th contents (Fig. S2) as observed elsewhere in berthierine (Yang *et al.*, 2021), consistent with the presence of the mineral in these ironstones. Thorium enrichment in these beds is responsible for their distinctive low U/Th ratio on the trace-element ratio profile (Fig. 5).

Positive correlations are observed between V and TOC with a steeper regression line generated by Subunit Ia – c samples compared to Units II – V (Fig. 17f). This steepening may be

attributed to the additional presence of Fe-mineral (berthierine/chamosite, siderite and goethite) associated V and the greater influence of quartz and feldspar dilution effects in the coarser grained, TOC-poor, oxic facies of the Pliensbachian, compared to predominantly phyllosilicate and TOC-associated V in the anoxic – euxinic Toarcian mudstones. The Toarcian sample V vs TOC regression line, derived from the V data from the Yorkshire coast of Ruvalcaba Baroni *et al.* (2018), has an intercept within error of average shale (PAAS = 140 ppm). Unit IV samples of the lower Bituminous Shales cluster above the Units II – V regression line indicate elevated V/TOC ratios compared to the full Toarcian sample suite, like, but less pronounced than, the offsets seen for Mo/TOC and U/TOC (Fig. 17b, d; also compare Figs 5 and S3).

Vanadium behaves as a conservative or near-conservative element in the modern oceans (Wu *et al.*, 2019). The early diagenetic behaviour of V in marine sedimentary environments is poorly studied. In oxic environments, it is considered that V is adsorbed on particulate organic matter and Fe–Mn oxyhydroxides, transferred from the water column to the sediment and released to pore waters during Mn and Fe reduction (e.g. Bennett & Canfield, 2020). Dissolved V is reduced to the strongly adsorbed $\text{VO}(\text{OH})_3^-$ under anoxic (= suboxic) conditions and is retained by the sediment during burial. Free sulfide in close proximity to the Mn and Fe reduction zone likely favours the reduction and capture of V from the pore water as authigenic V(III) hydroxide. Under anoxic bottom waters, a hydrogenous fraction may be added to the sediment directly through inorganic redox reactions. The element is therefore commonly enriched in carbonaceous mudstones where it is initially bound to organic compounds but may also partition into clay minerals (Breit & Wanty, 1991; Tribovillard *et al.*, 2006).

The largest V enrichments are observed in modern sediments being deposited within the core of perennial oxygen-minimum zones on continental margins. Hydrographically restricted euxinic basins typically do not show high levels of V enrichment due to low rates of sedimentation limiting the particulate V flux and low rates of deep-water renewal limiting hydrogenous V uptake (Scholz *et al.*, 2017; Bennett & Canfield, 2020). Importantly, V drawdown under reducing conditions does not require the presence of sulfide in the water column.

A study of Late Cretaceous (Cenomanian – Turonian) OAE2 indicates that drawdown of V accompanied the global expansion of oxygen-deficient but non-sulfidic waters, fingerprinting an expansion of anoxia prior to the development of euxinia evidence by subsequent drawdown of Mo (Owens *et al.*, 2016). The offset to lower V/TOC ratios that characterize Unit III compared to higher values in Unit IV (Fig. 17f) is consistent with a drawdown and reduced inventory of V during the period of maximum oxygen depletion accompanying the T-OAE, although the additional impact of basin restriction cannot be excluded.

13.d. Molybdenum – Uranium covariation

Algeo & Tribovillard (2009) and Tribovillard *et al.* (2012) advocated the use of Mo_{EF} vs U_{EF} covariation diagrams for marine sediments and rocks to interpret bottom-water redox conditions, the operation of metal-oxyhydroxide particulate shuttles in the water column, and the degree of water mass restriction driving the evolution of water chemistry.

Molybdenum and U exhibit conservative behaviour under oxic conditions but show progressive uptake by the sediment from

seawater where the bottom water mass and/or surface sediments are anoxic (Algeo & Tribovillard, 2009; Tribovillard *et al.*, 2012). Aqueous Mo and U are both removed from seawater across the sediment–water interface in reducing facies, but Mo requires a lower redox potential for sedimentary uptake than U: uptake of U begins at the Fe(II)–Fe(III) redox boundary and therefore exceeds that of Mo when redox conditions at the sediment/water interface are anoxic, while authigenic Mo enrichment requires the presence of H_2S and is favoured over U when benthic redox conditions are euxinic.

In unrestricted open-ocean environments such as continental margin upwelling systems, typified by those of the modern eastern tropical Pacific, it is argued that a general shift from oxic through anoxic to sulfidic benthic redox conditions enhances sediment uptake of both Mo and U (Fig. 17) by diffusion downwards across the sediment/seawater interface, but the change in redox state drives a progressive increase in Mo/U ratios from 0.1 – 0.3 to 1 – 3 times the seawater molar ratio (Algeo & Tribovillard, 2009).

In moderately restricted basins, such as the modern Cariaco Basin, with a deep or highly variable chemocline, the operation of a particulate Fe–Mn oxyhydroxide particulate shuttle may enhance the transfer of aqueous Mo to the sediment/water interface. Molybdenum is vigorously scavenged from seawater by Fe–Mn oxyhydroxide particles in the oxic water column. On reaching the sediment/water interface, these particles are reductively dissolved, releasing Mo to diffuse back into the bottom water or available to be scavenged by other phases within the sediment. Aqueous U is unaffected by this process, resulting in elevated Mo/U ratios that are typically 3 to 10 times those of seawater (Fig. 18).

In more restricted basins like the Black Sea, which are characterized by a shallow and stable chemocline, relative rates of authigenic Mo–U enrichment will depend on the degree of evolution of the water chemistry in the deep water mass. Initially, when the aqueous Mo/U molar ratio is close to that of seawater, sediment Mo/U ratios will be high (Fig. 18), but if aqueous Mo is depleted through sedimentation without compensatory resupply, the sediment Mo/U ratios will decline.

More recently, sequestration of Mo and U to particulate matter has been shown to occur at the seafloor in some open-ocean upwelling environments, exemplified by the Benguela upwelling system off Namibia, due to the intermittent presence of sulfide, either in bottom water or in pore water immediately at the sediment/water interface (He *et al.*, 2021). Mo and U are sequestered to the sediment during temporarily more reducing conditions. They subsequently undergo oxidative dissolution under less reducing conditions and diffuse away from local Mo and U pore-water concentration peaks. Mo and U are taken up again into reduced authigenic phases (sulfide-related) at depth, setting the final Mo and U content and isotope characteristics of the sediment. In this way, early diagenetic enrichment of Mo and U may be governed by temporal redox fluctuations.

He *et al.* (2021) have argued that early diagenetic processes in upwelling environments can produce patterns similar to those observed for coupled Mo–U covariation and isotope systematics in restricted and semi-restricted basins (see above) but via a different set of processes. Unambiguous identification of a restricted basin system therefore requires critical assessment of multiple proxies.

Samples from the upper Pliensbachian – lower Toarcian succession at Dove's Nest fall within 3 different areas on a Mo_{EF} vs U_{EF} cross-plot (Fig. 18). Samples from Units I (upper Pliensbachian), II (basal lower Toarcian) and V (upper lower to

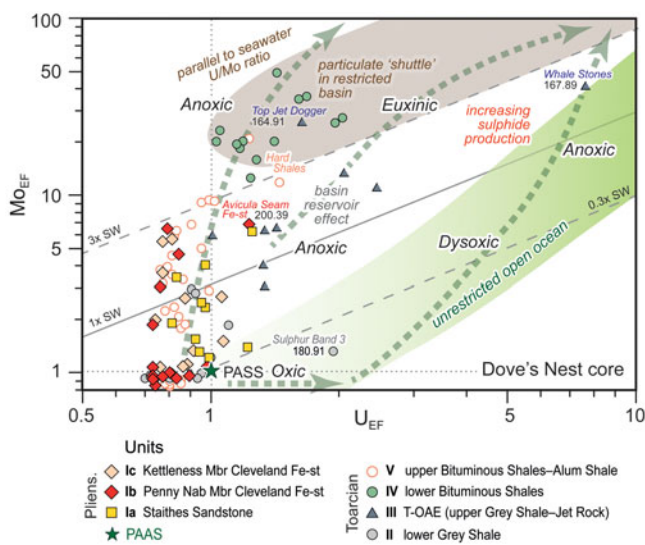


Figure 18. Mo_{EF} vs U_{EF} cross-plot for stratigraphic units comprising the upper Pliensbachian – middle Toarcian of Dove's Nest core. The three diagonal lines represent multiples (0.3, 1, 3) of the Mo:U ratio of present-day seawater (SW) converted to an average weight ratio of 3.1 for the purpose of comparison with sediment Mo:U weight ratios (Tribovillard *et al.*, 2012). General patterns of Mo_{EF} vs U_{EF} covariation in modern marine environments modified from Tribovillard *et al.* (2012) and Yano *et al.* (2020): unrestricted open ocean field based on the eastern tropical Pacific; particulate shuttle field based on the Cariaco Basin and Saanich Inlet. Trend lines show deoxygenation trends in modern marine environments (Tribovillard *et al.*, 2012) with positions based on data from restricted basins and coastal settings (Paul *et al.*, 2023). The anomalous high EF values of Whale Stones sample 167.89, interpreted as sampling a carbonate concretion, are likely an artifact of the high carbonate content (81%).

middle Toarcian) form a broad array with U_{EF} values close to or less than PAAS (i.e., no U enrichment) but Mo_{EF} values range from ~1 to ~10 (moderate Mo enrichment). The pattern of U–Mo covariation does not fall along the established unrestricted open ocean trend but rises upward towards the particulate shuttle field. Significant outliers include Avicula Seam sample 200.39 which exhibits greater Mo and U enrichment than other samples from the Cleveland Ironstone (Fig. 18), possibly an artefact of a very low Al_2O_3 content (2.9%) and Sulphur Band 3 sample 180.91, which displays U enrichment typical of anoxic unrestricted water masses. Samples from the Hard Shales at the base of Unit V are characterized by variable high Mo_{EF} and U_{EF} values.

Following the approach of Algeo & Tribovillard (2009) and Tribovillard *et al.* (2012), Yorkshire Pliensbachian samples lie within a poorly defined field of dominantly oxic – anoxic conditions (cf. Fig. 17) but with the levels of Mo enrichment potentially indicating periods of bottom water restriction and/or uptake under sulfidic conditions in the near-surface sediment. However, interpretation of Mo_{EF} values in these beds must be treated with caution since Mo concentrations in many samples were below the limit of quantification (2 ppm) for the Dove's Nest study (Table S2) and were allocated a nominal value of 1 ppm (=PAAS) for plotting purposes, equivalent to the average Mo value (1.2 ± 1.0 ppm) obtained for samples from this part of the succession on the coast by McArthur (2019).

It is observed that most Pliensbachian samples, together with those from Toarcian Units II and V, exhibit U_{EF} values of <1 (Fig. 18). The Lower Jurassic in the central Cleveland Basin has been buried into the oil window (~95° C) (Barnard & Cooper, 1983; Salem, 2013; French *et al.*, 2014; Song *et al.*, 2015; Song *et al.*, 2017), and low U_{EF} values have previously been attributed to U loss

accompanying hydrocarbon generation and migration (Wignall in Tribovillard *et al.*, 2012). However, a study of lower Toarcian black shales from the Alum Shale Formation of Sweden indicates that U remains immobile during catagenesis (Lecomte *et al.*, 2017), while U/TOC ratios increase with maturity in the lower Toarcian Posidonia Shale of the Lower Saxony Basin, northern Germany (Dickson *et al.*, 2022b), due to loss of organic matter with a low metal content during secondary migration. Low U_{EF} values in the Cleveland Basin are therefore judged to be a primary feature.

Samples from T-OAE Unit III, the top Grey Shale and Jet Rock, form an extended array of high U_{EF} (~1 – ~2) and high Mo_{EF} (~4 – ~13) values with a relatively constant U/Mo ratio that parallels the seawater trend (Fig. 18). A sample from the Top Jet Dogger (164.91 m) falls within the particulate shuttle field, another from the Whale Stones (167.89 m) displays very high Mo_{EF} and U_{EF} values of 42 and 7.6, respectively, associated with the high carbonate content (81%) in this concretion sample. Unit II samples generally fall on the lower segment of the Black Sea trend of Yano *et al.* (2020).

High Mo_{EF} values of ~10 – ~35 in lower Bituminous Shales Unit IV are accompanied by moderate U enrichment (U_{EF} ~1 – ~2) and Mo/U ratios that exceed 3× modern seawater. These values imply the operation of a particulate shuttle (Fig. 18), although one that was less active than that in the modern Saanich Inlet and Cariaco Basin (compare Yano *et al.*, 2020, fig. 6) where, in the latter, Mo_{EF} and U_{EF} reach 200 and >8, respectively. Lower Mo_{EF} values paired with Mo/U ratios of ~1 – 2× seawater in Unit III have been interpreted to reflect the drawdown of aqueous Mo as a consequence of transfer to the sediment in a highly restricted Cleveland Basin water mass during the T-OAE (McArthur *et al.*, 2008), the 'basin reservoir effect' (Algeo, 2004; Algeo & Lyons, 2006). Elevated U_{EF} values are consistent with the development of more reducing conditions in bottom waters.

Restriction of Cleveland Basin bottom waters has been linked to the development of a 'deep' pycnocline (a total water depth of 50 – 100 m was proposed for the Mulgrave Shale by Hallam, 1997) caused by increased freshwater runoff generating low-salinity surface waters that limited mixing between surface and bottom waters and exchange with the adjacent seas and open ocean (Küspert, 1982; Sælen *et al.*, 1996, 1998, 2000; Bailey *et al.*, 2003; van de Schootbrugge *et al.*, 2005; Wignall *et al.*, 2005; McArthur *et al.*, 2008; McArthur, 2019; Remírez & Algeo, 2020). However, the amplitude of any salinity decrease is hotly contested (Hesselbo *et al.*, 2020a) and palaeontological evidence and salinity proxies derived from the organic geochemical data (Section 15.b) indicate normal marine salinity throughout the T-OAE in the Cleveland Basin (Song *et al.*, 2017).

Reinterpretation of the Mo proxy (Section 13.a) weakens the geochemical argument for extreme basin restriction during the T-OAE. Like Mo, the oceans would have been subject to drawdown of U accompanying the global expansion of anoxic-euxinic bottom waters and seafloor area during the T-OAE. However, the differing redox sensitivities of the two elements would impose a trend of changing global Mo/U seawater ratios that compromise a simplistic interpretation of water mass restriction based on observations from modern basins.

14. Other trace-element redox proxies: Yorkshire coast studies

Several other trace elements documented in the Yorkshire coastal succession, not determined at Dove's Nest, have been considered as

redox proxies, including As, Cu, Cd and Co (Ruvalcaba Baroni *et al.*, 2018; Thibault *et al.*, 2018; McArthur, 2019).

14.a. Arsenic

Arsenic displays similarities to the distribution to Mo when plotted stratigraphically as As/TOC ratios but As contents of the Pliensbachian section (Unit I) overlap more strongly with those in the higher beds (Thibault *et al.*, 2018). The As_{EF} profile shows a very similar pattern to DOP_T (Fig. 14) that likely reflects deposition of As with Fe–Mn oxyhydroxides and subsequent incorporation by organic matter and diagenetic pyrite (Maher & Butler, 1988; Large *et al.*, 2011). Arsenic has been used as a redox proxy in some previous palaeoenvironmental studies (e.g. Bodin *et al.*, 2007; Atar *et al.*, 2019a, 2019b; Benamara *et al.*, 2020). However, critical analyses by Algeo & Liu (2020) and Tribovillard (2020, 2021) have concluded that arsenic is not a reliable proxy.

Arsenic shows marked enrichments in sediments from settings where dissolved reactive iron has been captured from seawater via shuttling by Fe–Mn oxyhydroxides and/or associated with cold seeps and is trapped in the sediment under reducing conditions (Tribovillard, 2020, 2021). Enrichment in arsenic indicates that reactive iron was present in sufficient abundance to keep free sulfide ions to low levels, thus preventing As solubilization, migration and loss from the sediment. However, when reactive iron availability is low, the development of high-sulfide and low-iron conditions prevent As capture and enrichment. In this case, protracted contact between free sulfide and organic matter induces sulfurization of the latter (Abubakar *et al.*, 2022), producing a high-TOC, high-Mo and low-As association (Tribovillard, 2020).

The good correlation between As vs Mo and U in the Yorkshire successions is consistent with a high reactive-Fe environment and supports the operation of a particulate shuttle during the deposition of the anoxic facies of the lower Bituminous Shales, Unit IV, evidenced by Mo vs U covariation (Fig. 18). However, it should be noted that Kemp *et al.* (2022a) proposed a coincident global drawdown of Mo, U and As from seawater accompanying the severe deep-ocean deoxygenation accompanying the T-OAE.

14.b. Copper

Copper is regarded as having a weak euxinic affinity (Algeo & Maynard, 2004) and correlates strongly with TOC in the Pliensbachian – Toarcian boundary succession of the Cleveland Basin. This association is demonstrated by the near-identical chemostratigraphic profiles for the two constituents illustrated by Ruvalcaba Baroni *et al.* (2018, fig. 2) and Thibault *et al.* (2018, fig. 2), with a high correlation coefficient ($R^2 = 0.7$) in both studies, but Cu shows no additional trends that may be considered to have palaeoenvironmental significance.

Cu_{EF} values are generally <1 throughout the succession, rise to >1 in samples with $>7\%$ TOC in T-OAE Subunit IIIb, reaching a maximum of 2.5 in the highest-TOC ($>12\%$) samples at the level of Whale Stones 'bed' 35. Low Cu_{EF} values (<3) similarly characterize oxic – euxinic settings in the modern Cariaco Basin. High Cu_{EF} values of 3 – 7 recorded in the euxinic sediments of the modern Black Sea and upwelling zones of the Peru margin (Little *et al.*, 2015) have not been documented in the Yorkshire succession.

14.c. Cadmium

McArthur (2019) presented Cd and Co data from the Yorkshire coastal succession and combined these with Mo and Mn results to apply the trace-metal palaeoenvironmental proxies proposed by Sweere *et al.* (2016), and assessed their concordance with the observations of Little *et al.* (2015).

Cadmium and Mo stand out as the two trace metals that typically show some of the highest enrichment factors in organic-rich sediments (Brumsack, 2006, fig. 2). Cadmium is enriched in plankton (35 ppm) but has a low concentration in terrigenous detritus, reflected by an average shale content of 0.3 ppm (Brumsack, 1989; Little *et al.*, 2015). Similar to C and P, Cd is rapidly regenerated in the ocean water column and shows a typical nutrient profile, but undergoes a dramatic solubility decrease at the O_2/H_2S boundary of anoxic basins. The Cd curve for the Pliensbachian – Toarcian boundary succession (McArthur, 2019, fig. 2) generally follows the S and DOP_T trends (Fig. 14), consistent with an association between Cd and sulfides (Cd vs S, $R^2 = 0.40$). However, low Cd contents (0.01 – 0.88 ppm) in the Yorkshire succession indicate an absence of significant CdS addition from euxinic bottom waters (cf. Sweere *et al.*, 2020) or a restricted Cd supply to the basin.

Unlike Cd, Mo does not bioaccumulate in phytoplankton (2 ppm), which have a Cd/Mo mass ratio of $\gg 1$. As a result, sediments in upwelling regions, which are subject to high export production of organic matter and Cd but not Mo, are characterized by high Cd/Mo ratios. In restricted environments, although anoxia/euxinia promote uptake of both Cd and Mo to the sediments, lower productivity limits plankton-derived export of Cd, leading to Cd/Mo ratios of $\ll 1$ that can approach the seawater value of 0.008. The hydrographically restricted and upwelling fields on the Cd/Mo discrimination diagrams of Sweere *et al.* (2016) are separated by a Cd/Mo value of 0.1.

The Cd/Mo profile from the Yorkshire succession (McArthur, 2019, fig. 3) generally follows the TOC and TOC/P trends (Figs 14, 16), consistent with a close association between Cd and TOC. However, despite a positive correlation ($R^2 = 0.50$) between Cd vs TOC (McArthur, 2019, fig. 4), low Cd/Mo ratios (generally <0.1) throughout the succession place the overwhelming majority of samples in the restricted water mass field of Sweere *et al.* (2016, fig. 4) and are indicative of a low productivity setting.

However, interpretation of the Cd/Mo proxy based on direct comparison to values from modern basins is again compromised by evidence of significant stratigraphic changes in the global Mo content of ocean water through the late Pliensbachian – middle Toarcian, with the global drawdown of Mo accompanying the T-OAE (Section 13.a). This would change the threshold values between the restricted vs open basin fields, potentially placing samples from the T-OAE interval into the unrestricted high-productivity field.

14.d. Cobalt

Downward-decreasing vertical profiles of Co and Mn in the ocean water column demonstrate that these elements are scavenged by settling particulates (terrigenous detritus and organic matter) and are taken up by bottom sediments, principally as oxyhydroxides (e.g. van Hulst *et al.*, 2017; Hawco *et al.*, 2018). In upwelling regions, the hydrogenous supply is limited by the depletion of both

elements in upwelled water. By contrast, restricted basins commonly have abundant Co and Mn supplied by rivers, providing a greater hydrogenous supply.

In oxic sediments, Co and Mn are buried as oxyhydroxides but may be remobilized by bacterial reduction driving anoxia with subsequent re-fixation, typically Co in pyrite and organic matter and Mn in rhodochrosite. However, where the oxic – anoxic boundary lies at or above the sediment/water interface, remobilized elements can escape from the sediment and be returned to bottom waters. In open-ocean (unrestricted) settings, such as coast upwelling systems, these elements can then be lost by lateral advection of bottom waters. Oxyhydroxide particulates settling from the surface waters into the underlying oxygen-minimum zone dissolve, releasing Mn and Co, which can be transported oceanward by a ‘Mn-conveyor belt’ (Brumsack, 2006), leading to low metal enrichments in the sediments.

In restricted settings, remobilized elements cannot escape and are returned to the sediment via redox cycling, causing significant enrichment over the original particulate supply. Sweere *et al.* (2016) determined that modern restricted environments have Co (ppm) \times Mn (%) values > 0.4 while unrestricted environment values are < 0.4 . McArthur (2019) proposed the same threshold value for a $Co_{EF} \times Mn_{EF}$ proxy and demonstrated the use of shale-normalized data offered no advantage over a concentration-based ratio.

Cobalt and Mn display similar profiles through the Yorkshire upper Pliensbachian – middle Toarcian succession (McArthur, 2019, fig. 2), excluding large Mn peaks associated with sideritic mudstone and calcite concretion horizons in Unit V (‘beds’ 44, 46, 48 and 50; Fig. 14) which are Co depleted. Other levels containing significant siderite and/or calcite contents similarly show relatively lower Co contents reflecting the presence of carbonate-bound Mn and, in the upper beds, Fe–Mn oxyhydroxides at omission surfaces in condensed intervals (McArthur, 2019).

The shape of the Co \times Mn profile (McArthur, 2019, fig. 3) is similar to those of Fe_{EF} and Mn_{EF} (Fig. 14), with high Co (ppm) \times Mn (%) values of > 0.4 in the Pliensbachian section (Unit I) interpreted by McArthur (2019) to indicate restricted circulation that pre-dated the onset of black shale deposition. Maximum Co \times Mn contents are recorded in the three Sulphur Bands and high values occur consistently through the T-OAE interval, Unit III, which features the highest average Mn content and Mn/Al ratio of the units in the succession (Fig. 8). A sharp decline in Mn and Mn_{EF} (Figs 8, 14), with Co (ppm) \times Mn (wt%) values falling to < 0.4 , occurs in the upper Bituminous Shales at the base of Unit V, consistent with a change to more open conditions. The subsequent decreasing stratigraphically upward trend implies increasing open circulation accompanied by sea-level rise from the late early Toarcian (cf. Fig. 10).

McArthur (2019) concluded that the Cd/Mo, Co \times Mn and Mo/TOC proxies together confirm that hydrographic restriction was a defining feature of black shale deposition in the early Toarcian of the Cleveland Basin. However, evidence of global depletion of Mo and other trace metals in the oceans during the T-OAE requires the application of Mo-based ratios to be re-evaluated.

14.e. Rhenium

The principal focus of work on Re and Os in the lower Toarcian has been the generation of $^{187}Os/^{188}Os$ and $^{187}Re/^{188}Os$ ratios for isochron construction and Re–Os dating of black shales, and the generation of $^{187}Os/^{188}Os$ _i seawater time series (Fig. 18, Section

16.b.4) to examine changes in the balance between continental weathering and hydrothermal input in the oceans (e.g. Cohen *et al.*, 1999, 2004; Percival *et al.*, 2016; Them *et al.*, 2017b; van Acken *et al.*, 2019; Kemp *et al.*, 2020). Rhenium abundances for the Yorkshire Toarcian have been presented by Pearce *et al.* (2008).

Rhenium has the largest enrichment factor of all redox-sensitive metals in anoxic sediments relative to the detrital background (Helz & Adelson, 2013). The average Re concentration of 66 ppb in modern anoxic sediments compares to an upper crust value of 0.2 – 0.4 ppb, an enrichment factor of > 200 (Sheen *et al.*, 2018). Rhenium occurs as the soluble $Re(VII)O_4^-$ oxyanion in oxic seawater and is a conservative element that occurs at low concentrations (average 7 parts per trillion in the modern ocean; Anbar *et al.*, 1992; Colodner *et al.*, 1993b; Morford *et al.*, 2012; Dickson *et al.*, 2020). The estimated residence time of Re in the ocean is 130 – 750 ka (Colodner *et al.*, 1993a; Miller *et al.*, 2011), likely marginally shorter than for Mo at 440 – 800 ka (Morford & Emerson, 1999; Miller *et al.*, 2011) and U at 400 ka (Ku *et al.*, 1977) but longer than V at 50 – 100 ka (Wu *et al.*, 2019).

Under anoxic conditions, Re(VII) is reduced to Re(IV), becomes insoluble and is removed to the sediment either through complexation with organic matter and/or incorporated into sulfides. Unlike Mo, Re can be efficiently removed from anoxic sediments at low dissolved H₂S levels when bottom waters are dysoxic or anoxic (Crusius *et al.*, 1996; Calvert & Pedersen, 2007). The ratio of Re/Mo in anoxic sediments is as much as 2.5 times greater than the seawater value, while the ratio is close to that of seawater in euxinic (sulfidic) sediments. Under oxic bottom waters the ratio may be less than that in seawater ($Re/Mo\ 0.74 \times 10^{-3}$; Bruland & Lohan, 2003) due to fixation of Mo by Mn-oxyhydroxides but no uptake of Re.

Sediment Re concentrations and Re/Mo ratios have been used as local redox proxies by Turgeon & Brumsack (2006), Pearce *et al.* (2008) and Kunert & Kendall (2023), amongst others. Rhenium offers a potential proxy for tracking general ocean oxygen depletion (i.e. combined euxinic and non-euxinic anoxia) because the magnitude of authigenic Re enrichment in anoxic marine sediments is significantly higher than the detrital background compared with U, for example, as reflected by higher Re enrichment factors in organic-rich sediments.

A geochemical study of a lower Toarcian succession in western Canada by Kunert & Kendall (2023) indicates that Re and Mo oceanic mass balance models can be used to infer the extent of seafloor total anoxia and euxinia, respectively, using concentrations of these metals in locally anoxic or euxinic carbonaceous mudstones deposited in an unrestricted marine setting. They calculated an expansion of up to ~7% of total global seafloor anoxia – euxinia, dominated by euxinia, during the early stages of the T-OAE, followed by a contraction before the end of the event.

A Re threshold of 5 ppb was used by Kunert & Kendall (2023) to identify samples where the sediment column was anoxic. Values rise consistently above this threshold from the base of the T-OAE interval Unit III in Yorkshire (Fig. 20), with a large step increase to ~40 ppb at the base of the laminated black shale facies in ‘bed’ 31 of Subunit IIIa interpreted to reflect bottom water anoxia and decreasing basin restriction.

Euxinic environments are predicted to be characterized by low Re/Mo ratios approaching those of seawater. Normal oxic environments show very variable but generally higher Re/Mo values. Re/Mo (ppb/ppm) thresholds of 10 – 15 for the oxic/dysoxic – anoxic boundary and 2 – 4 for the anoxic – euxinic boundary have been proposed by Turgeon & Brumsack (2006) and

Kunert & Kendall (2023). The latter authors reported Re/Mo ratios of 11 ± 5 , 6 ± 2 and 2 ± 1 for Toarcian carbonaceous mudstones assigned to dysoxic, anoxic and euxinic redox conditions based on independent criteria, respectively.

The Re/Mo profile spanning the T-OAE interval of the Yorkshire coast (Fig. 20) indicates: (1) a progressive transition from oxic – dysoxic conditions immediately preceding the onset of the T-OAE (top Subunit IIb and lower IIIa); (2) sharply falling ratios through ‘bed’ 32 at the top of Subunit IIIa, indicative of increasing local anoxia – euxinia; (3) consistently low values indicative of euxinic conditions throughout the $\delta^{13}\text{C}_{\text{org}}$ minimum of Subunit IIIb; and (4) variable higher values representing euxinic – anoxic conditions during the later stages and immediately following the T-OAE (Subunits IIIc – IVa). The Re/Mo ratio of modern euxinic sediments approaches that of seawater, so the values recorded in Yorkshire T-OAE Subunit IIIb likely reflect the composition of Toarcian seawater (Fig. 20). The higher Re/Mo ratio compared to modern seawater would reflect a higher proportion of euxinic : anoxic seafloor during the Toarcian compared to the modern ocean.

14.f. I/Ca ratios

Iodine/calcium ratios (I/Ca) in marine carbonate have been proposed as a geochemical proxy to constrain global seawater redox change (e.g. Lu *et al.*, 2010; Zhou *et al.*, 2015), and I/Ca ratios have been reported for belemnites collected from the Jet Rock (T-OAE Subunits IIIb – d) of the Yorkshire coast (Lu *et al.*, 2010). Iodine has a residence time of ~300 ka in the modern oceans resulting in a uniform total iodine concentration of 0.45 μM in most places, although the distribution of iodine species is complex (Wadley *et al.*, 2020; Luther, 2023). Low I/Ca ratios in the T-OAE and OAE2 intervals of Italy and England, respectively, have been interpreted to reflect the reduction of iodate (IO_3^-) to iodide (I^-) due to deoxygenation and global iodine drawdown by organic carbon burial (Lu *et al.*, 2010).

A fall to very low I/Ca ratios in bulk carbonate has been documented in a Toarcian shallow-water carbonate platform section in southern Italy (Monte Sorgenza; Lu *et al.*, 2010). The onset of falling I/Ca values begins at a peak of ~8 $\mu\text{M}/\text{M}$ at the Pliensbachian – Toarcian boundary interval at Monte Sorgenza based on its position in relation to the $\delta^{13}\text{C}_{\text{carb}}$ curve (cf. Woodfine *et al.*, 2008; Xu *et al.*, 2018). A sharp step fall from >2 $\mu\text{M}/\text{M}$ to a minimum ~0.5 $\mu\text{M}/\text{M}$ occurs at the base of, and continues throughout, the T-OAE interval. Interpretation of bulk carbonate I/Ca values in shallow-marine sediments requires caution due to the high sensitivity of I/Ca ratios to diagenesis (Lau & Hardisty, 2022), but it is significant that comparable low ratios were recorded from Yorkshire Jet Rock belemnites (Lu *et al.*, 2010, fig. 3).

I/Ca ratio values remain low until some distance above the T-OAE interval at Monte Sorgenza and only return to pre-excursion levels in the middle Toarcian. This is consistent with the persistence of global anoxia indicated by other geochemical (e.g. $\delta^{98}\text{Mo}$, Section 16.b.1; $e^{205}\text{Tl}$, Section 16.b.2) and fossil proxies (Section 19).

15. Organic geochemistry and biomarkers

The organic geochemistry of the Yorkshire lower Toarcian has been studied by Salem (2013), French *et al.* (2014) and Song *et al.* (2017).

15.a. Molecular carbon-isotope records

Compound-specific $\delta^{13}\text{C}$ analyses were performed by French *et al.* (2014) across the T-OAE interval at Hawsker Bottoms (‘beds’ 29 – 41) that provide information on changes in the isotopic composition of the marine vs atmospheric carbon reservoirs. All biomarkers record the negative CIE of the T-OAE through Unit III but have different amplitudes (Fig. 21), consistent with an earlier low-resolution study of Toarcian shales in SW Germany (Schouten *et al.*, 2000). The $n\text{-C}_{17}$, $n\text{-C}_{18}$ and $n\text{-C}_{19}$ alkanes display a negative excursion of ~2 – 3‰, with a marginally smaller excursion (~2‰) recorded by pristane and phytane; all of these compounds are considered to represent marine sources (French *et al.*, 2014). Long-chain n -alkanes ($n\text{-C}_{27}$, $n\text{-C}_{28}$, $n\text{-C}_{29}$), derived primarily from land plant wax lipids, provide a terrestrial record. These exhibit the largest compound-specific negative CIE of ~5‰, which is lower than that derived from bulk organic matter ($\delta^{13}\text{C}_{\text{org}} \sim 6 - 7\%$; Hesselbo *et al.*, 2000; DB Kemp *et al.*, 2005; Trabuco-Alexandre *et al.*, 2022).

The molecular C-isotope records show a more marked step down to lower values within the T-OAE than the bulk organic records, and within the CIE compound-specific $\delta^{13}\text{C}$ values are relatively stable compared to the $\delta^{13}\text{C}_{\text{org}}$ curve, which has a marked concave profile (Fig. 21). By comparison, matched $\delta^{13}\text{C}$ datasets from other Toarcian sections in Spain and China show good agreement in trends between n -alkane, bulk organic and carbonate carbon isotope records (e.g. Ruebsam *et al.*, 2020d, fig. 2). Offsets in the Yorkshire profiles may perhaps be, in part, an artefact of the low sampling resolution of the organic geochemical data (French *et al.*, 2014). Alternatively, short-distance migration of the bitumen fraction, which is mobile and can move in the pore space, may have modified the trend in the compound-specific $\delta^{13}\text{C}$ data. Changing organic matter composition between successive bulk samples may also play a role.

Organic matter source mixing will affect the trend and amplitude of the bulk organic $\delta^{13}\text{C}$ excursion. The Yorkshire Pliensbachian – middle Toarcian succession displays large variation in the proportions of marine to terrestrial organic matter (Bucefalo Palliani *et al.*, 2002; French *et al.*, 2014; Slater *et al.*, 2019). Calculated percentages of terrigenous organic matter based on linear regression of petrographic measurements of terrigenous organic matter and Rock-Eval Hydrogen Index (HI; French *et al.*, 2014) indicate a fall from ~80% at the top of Subunit IIb, immediately below T-OAE Unit III, to <20% in the TOC maximum in Whale Stones ‘bed’ 35 at the top of T-OAE Subunit IIIb, rising to ~40% at the base of Subunit IVa.

A similar trend is shown by the palynological count data of Slater *et al.* (2019) with corresponding terrestrial palynomorph values of 80 – 50% in Subunit IIb, falling to 8% in IIIb, then rising to 10 – 20% in Unit IV. It is notable that the ‘marine’ fraction in Units III and IV is overwhelmingly dominated by amorphous organic matter, peaking at 90% towards the top of Subunit IIIb. The amorphous organic matter is assumed here to be of predominantly marine origin based on its close association with prasinophyte algae and high HI values, but may include a terrestrial component (cf. Tyson, 1995).

The very large increase in the proportion of marine organic matter in the lower Toarcian and particularly within the T-OAE interval will increase the amplitude of the T-OAE CIE in the Yorkshire curve. Where matching data are available for samples (e.g. Suan *et al.*, 2015; Ruebsam *et al.*, 2018), the $\delta^{13}\text{C}_{\text{org}}$ curve may

be normalized using HI or carbon preference index (CPI; the odd over even predominance for long-chain *n*-alkanes, $n\text{-C}_{24}$ to $n\text{-C}_{34}$) values. Suan *et al.* (2015, fig. 5d) applied this method to the Yorkshire coast paired $\delta^{13}\text{C}_{\text{org}}$ and HI data of Sælen *et al.* (2000) and calculated an amplitude for the corrected negative excursion of 3 – 4‰ $\delta^{13}\text{C}_{\text{org}}$. This value is consistent with corrected $\delta^{13}\text{C}_{\text{org}}$, $\delta^{13}\text{C}_{\text{phytane}}$ and $\delta^{13}\text{C}_{\text{carb}}$ curves from two sections in SW Germany that are dominated by marine organic matter throughout the lower Toarcian (Suan *et al.*, 2015).

Insufficient data are available to fully assess the impact of changes in organic matter composition on the fine structure of the Yorkshire $\delta^{13}\text{C}_{\text{org}}$ profile. Palynological data do not show large sample-to-sample variation within the T-OAE (Slater *et al.*, 2019) interval, and steps within the Yorkshire $\delta^{13}\text{C}_{\text{org}}$ curve have been correlated to those in records from Bornholm (Denmark), Sancerre (Paris Basin), sections in the Polish Basin, and at Peniche (Lusitanian Basin) (Fig. 3; Hesselbo *et al.*, 2000; Hesselbo & Pieńkowski, 2011; Hermoso *et al.*, 2012; Thibault *et al.*, 2018, fig. 9; Fantasia *et al.*, 2019, fig. 12).

Most significantly, the presence of a large negative CIE in long-chain *n*-alkanes that parallels the terrestrial wood and bulk organic $\delta^{13}\text{C}$ trends in the T-OAE interval of the Cleveland Basin (Figs 3, 21) and $\delta^{13}\text{C}_{\text{carb}}$ trends at Peniche (Littler *et al.*, 2010, fig. 3) and elsewhere, confirms the synchronous ^{13}C -depletion of the entire exchangeable carbon reservoir, in both the oceans and the atmosphere.

15.b. Biomarkers as palaeoredox and salinity proxies

Specific organic molecules in the geological record provide biomarkers for green sulfur-reducing bacteria that are confined to environments with available sunlight and euxinic conditions (e.g. Koopmans *et al.*, 1996; Grice & Eiserbeck, 2014). Their presence provides a signature for photic zone euxinia (PZE). Isorenieratane is the only uniquely defining molecule of green sulfur-reducing bacteria Chlorobiaceae, but its derivatives and certain other molecular compounds such as chlorobactane can also be used as proxies for the presence of these bacteria in the water column.

There is organic geochemical evidence for PZE during the T-OAE from multiple locations throughout Europe, including the UK, France, Germany, Hungary and Italy (Schouten *et al.*, 2000; Pancost *et al.*, 2004; Schwark & Frimmel, 2004; Van Breugel *et al.*, 2006; Ruebsam *et al.*, 2018; Xu *et al.*, 2018; Ajuaba *et al.*, 2022; Burnaz *et al.*, 2024). Bowden *et al.* (2006) reported isorenieratane derivatives in four samples from the Whitby Mudstone Formation at Port Mulgrave ('beds' 35, 37, 38 and 41) with additional records from 'beds' 31, 32 and 34 provided by Salem (2013), indicating that the photic zone was intermittently euxinic. Isorenieratane is also present in the high TOC intervals in each of the three Sulphur Bands (Salem, 2013). Samples from Hawsker Bottoms confirm the presence of aromatic carotenoid biomarkers including isorenieratane from the Whitby Mudstone (Fig. 21), but samples also yield okenane, a biomarker derived from the red-coloured aromatic carotenoid okenone of purple sulfur bacteria (French *et al.*, 2014). The highest recorded isorenieratane/TOC values occur at the top of Unit III at Hawsker Bottoms (Fig. 21).

Iron-rich, anoxic and potentially non-sulfidic (ferruginous) bottom-water conditions have been interpreted for lower Toarcian shales from the Cleveland Basin (Runswick Bay; Song *et al.*, 2017), based on biomarkers [low dibenzothiophene/phenanthrene ratios (< 0.2) and gammacerane indices (< 0.1)] and elemental

composition (high total S and high S/TOC ratio). The abundance of small framboidal pyrite in these rocks (> 95% of < 7 μm diameter) suggests formation in the water column which depleted the free H_2S , leading to a low degree of sulfurization of organic matter. The reactive iron was supplied by a high terrigenous influx, which is also indicated by the biomarker data.

The aryl isoprenoid ratio (AIR) relates the proportions of low to high molecular weight aromatic compounds ($\text{C}_{13-17}/\text{C}_{18-22}$; Schwark & Frimmel, 2004). A high abundance of short-chain forms indicate intense aerobic degradation. AIR values of ≤ 0.5 are associated with persistent PZE (near year-round) and high values of 0.5 – 3 reflect short-term episodic PZE (possibly seasonal). Runswick Bay samples from the Jet Rock and Bituminous Shales have yielded AIR ratios of 2 – 3 indicative of episodic PZE (Song *et al.*, 2017), supporting the evidence provided by aromatic carotenoid biomarkers.

Caswell & Coe (2014) plotted the better-characterized Toarcian AIR record from Dotternhausen (Schwark & Frimmel, 2004) against the Yorkshire succession as a palaeoredox proxy, but it is unwise to assume that redox changes were synchronous and of the same amplitude in the two basins. For example, levels with significant bioturbation, indicating temporary oxygenation of bottom waters, characterize the beds immediately below and immediately above the Oberer Stein at Dotternhausen (Röhl *et al.*, 2001). The equivalent interval in the Yorkshire coastal and core successions (Top Jet Dogger – Millstone interval) shows no evidence of oxygenation and biomarkers suggest peak PZE (Fig. 21; French *et al.*, 2014).

Modern observations suggest that the presence of okenone would require an extremely shallow PZE and a highly restricted depositional environment. Based on the abundance of okenane and evidence of microbial wavy lamination in Yorkshire Toarcian shales (O'Brien, 1990), French *et al.* (2014) suggested that the okenane, and potentially chlorobactane and isorenieratane, may have formed in benthic microbial mats rather than a euxinic photic-zone water column. The biomarkers must, nonetheless, reflect the presence of photic zone anoxic – euxinic bottom waters.

Multiple salinity proxies derived from the organic geochemical data [e.g. gammacerane/(gammacerane + C_{30} -hopane) index] were interpreted as indicating normal marine salinity throughout the T-OAE in the Cleveland Basin by Song *et al.* (2017). These contradict the interpretation of strong brackish to freshwater conditions promoted by Ramirez & Algeo (2020) based on element-ratio data (Section 13.d). However, gammacerane is considered to originate from tetrahymanole produced by ciliates, whose habitat is in the anoxic part of the water column beneath the pycnocline, so gammacerane may be better regarded as a stratification parameter (cf. Sinninghe Damsté *et al.*, 1995) rather than a salinity indicator. Evidence of bacterial sources of tetrahymanole (Banta *et al.*, 2015) further complicate the use of the gammacerane proxy.

Other organic geochemical proxies (e.g. low ratio of steranes/hopanes, < 1.0; abundant long-chain *n*-alkanes) were interpreted by Song *et al.* (2017) to indicate a significantly higher input of terrigenous organic matter with more bacteria and/or cyanobacteria in Yorkshire compared to Toarcian black shale sections in the Netherlands, Germany and Luxemburg. These likely constitute components of the amorphous organic matter that dominates the palynofacies within the T-OAE interval (Section 19.b.2).

A comprehensive study of biomarkers in a core from southern Luxemburg (NE Paris Basin) by Ruebsam *et al.* (2022) indicates that the marine phytoplankton community structure during the

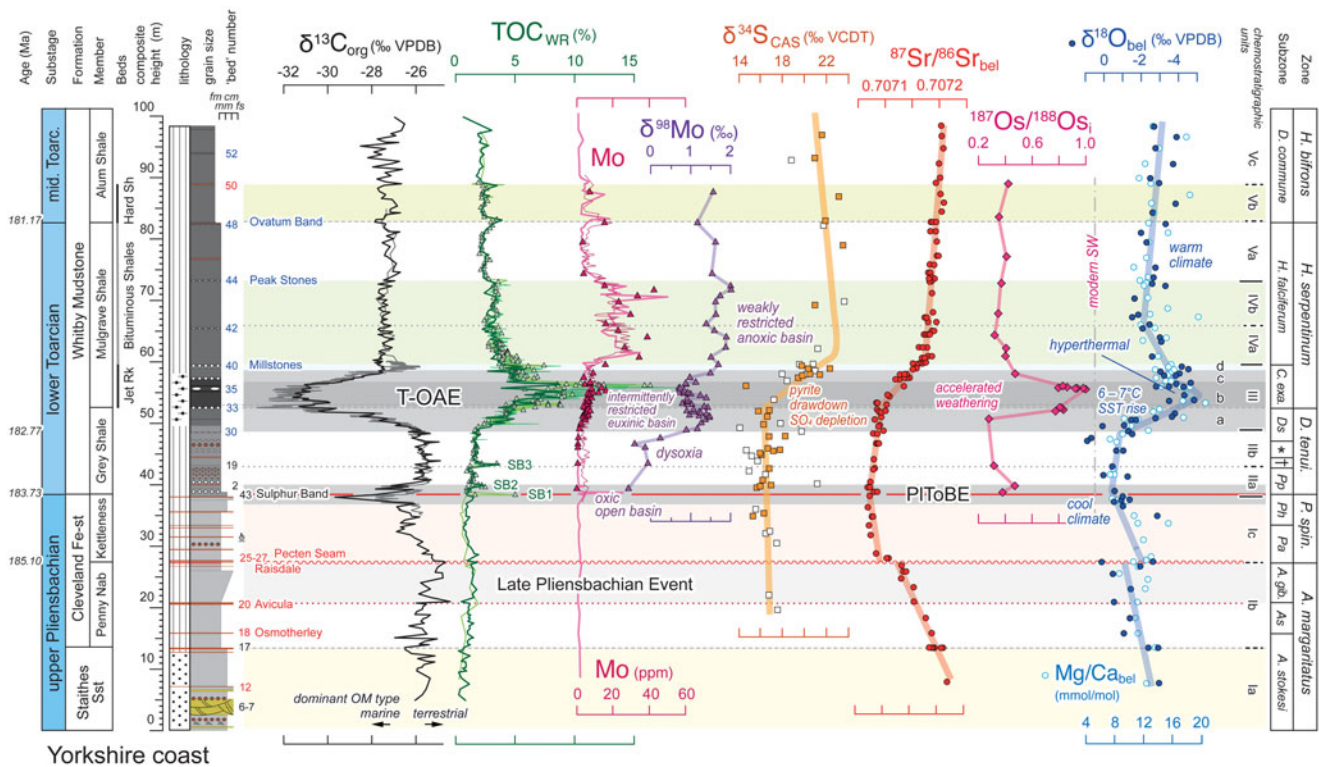


Figure 19. Stratigraphic variation in selected isotope geochemistry in the upper Pliensbachian – middle Toarcian of Yorkshire. $\delta^{13}\text{C}_{\text{org}}$ profile for Dove's Nest (Trabucho-Alexandre *et al.*, 2022, black) rescaled to coastal succession, with compiled high-resolution coast curve (grey, see Fig. 2; Cohen *et al.*, 2004; DB Kemp *et al.*, 2005; Littler *et al.*, 2010). Stratigraphic framework as in Figure 2. Rescaled whole-rock TOC profile for Dove's Nest (Trabucho-Alexandre *et al.*, 2022, dark green) with coast composite data of Kemp *et al.* (2011; thin yellow-green high-resolution curve), McArthur (2019; thin pale green low-resolution curve) and Ruvalcaba Baroni *et al.* (2018; green-filled triangles). Yorkshire coast Mo profile of McArthur (2019; thick pink line) with elemental results for Mo-isotope samples of Pearce *et al.* (2008; red filled triangles) and high-resolution data of Thibault *et al.* (2018; thin dark red line, see Fig. 16). $\delta^{98}\text{Mo}$ coast profile from Pearce *et al.* (2008). Details of the Mo concentration and isotope curves within Unit III (T-OAE) are presented in Figure 20. Belemnite carbonate-associated sulfur isotope profile ($\delta^{34}\text{S}_{\text{CAS}}$) from Gill *et al.* (2011; white filled squares) incorporating the data of Newton *et al.* (2011; orange squares). Belemnite $^{87}\text{Sr}/^{86}\text{Sr}$ coast curve after McArthur *et al.* (2000). $^{187}\text{Os}/^{188}\text{Os}_i$ profile of Cohen *et al.* (1999; 2004). Belemnite carbonate oxygen-isotope ($\delta^{18}\text{O}$, blue dots) and Mg/Ca ratios (blue circles) after McArthur *et al.* (2000).

T-OAE was dominated by eukaryotic algae, with a decrease in the proportion of prokaryotic bacterial biomass compared to the pre- and post-excursion intervals. A dominance of algae in the phytoplankton community during the T-OAE in the Cleveland Basin is similarly evidenced by palynological data (Section 19.b.2.).

Five distinct palaeoecological events within the interval of the $\delta^{13}\text{C}_{\text{org}}$ minimum of the Paris Basin core each show a proliferation of opportunistic green algae coincident with a decline in red algae groups and shallow- and deep-dwelling calcareous nannoplankton (Ruebsam *et al.*, 2022). These events correlate to biomarker evidence [increasing ratio of tri- /di-MTTCs (methylated 2-methyl-trimethyltridecylchromans)] for episodes of surface-water freshening. These were interpreted to have been caused by higher precipitation and surface run-off accompanying climate warming, paced by changes in the short eccentricity (100 kyr) orbital cycle (Ruebsam *et al.*, 2022). To our knowledge, comparable data are not currently available from the Yorkshire succession.

16. Isotope geochemistry: insights into global processes

Chemostratigraphic profiles of key isotope ratios ($\delta^{15}\text{N}$, $\delta^{34}\text{S}$, $\delta^{18}\text{O}$, $^{87}\text{Sr}/^{86}\text{Sr}$, $\delta^{98}\text{Mo}$, $^{187}\text{Os}/^{188}\text{Os}_i$, $\varepsilon^{205}\text{Tl}$) constructed using available data from the Yorkshire coast to complement the $\delta^{13}\text{C}$, TOC and elemental data from Dove's Nest presented herein, are plotted against a common composite succession (Fig. 2) based on

measured outcrop sections between Hawsker Bottoms and Port Mulgrave in Figures 19 – 21.

16.a. Nitrogen and sulfur isotopes

16.a.1. Nitrogen isotopes – increased algal productivity and partial denitrification

Reviews of the oceanic N-cycle have been provided by Ader *et al.* (2014) and Algeo *et al.* (2014). The $\delta^{15}\text{N}$ ($\delta^{15/14}\text{N}$ ‰_{air}) composition of seafloor sediments on modern continental margins and in anoxic basins generally records the isotopic composition of primary producers in the overlying surface waters. The $\delta^{15}\text{N}$ of the primary producers reflects the mass and isotope balance between the two main sources of nitrogen supporting new primary production: fixation of atmospheric N_2 by diazotrophs (NO_3^-) such as cyanobacteria and upwelled nitrate (NO_3^-) and/or ammonium (NH_4^+) reaching the photic zone, utilized by phytoplankton. Partial water-column denitrification (i.e. generation of ^{14}N -enriched gaseous species, N_2 and NO_2) and/or anammox (anaerobic ammonium oxidation) in dysoxic – anoxic environments results in an average $\delta^{15}\text{N}$ value of +5‰ for NO_3^- in the modern ocean. Assimilation of ^{15}N -enriched NO_3^- by phytoplankton leads to ocean sediments having typical $\delta^{15}\text{N}$ values of +5‰ – +6‰.

A $\delta^{15}\text{N}$ profile spanning the T-OAE interval at Hawsker Bottoms (Jenkyns *et al.*, 2001) comprises erratic low (< –2‰) but

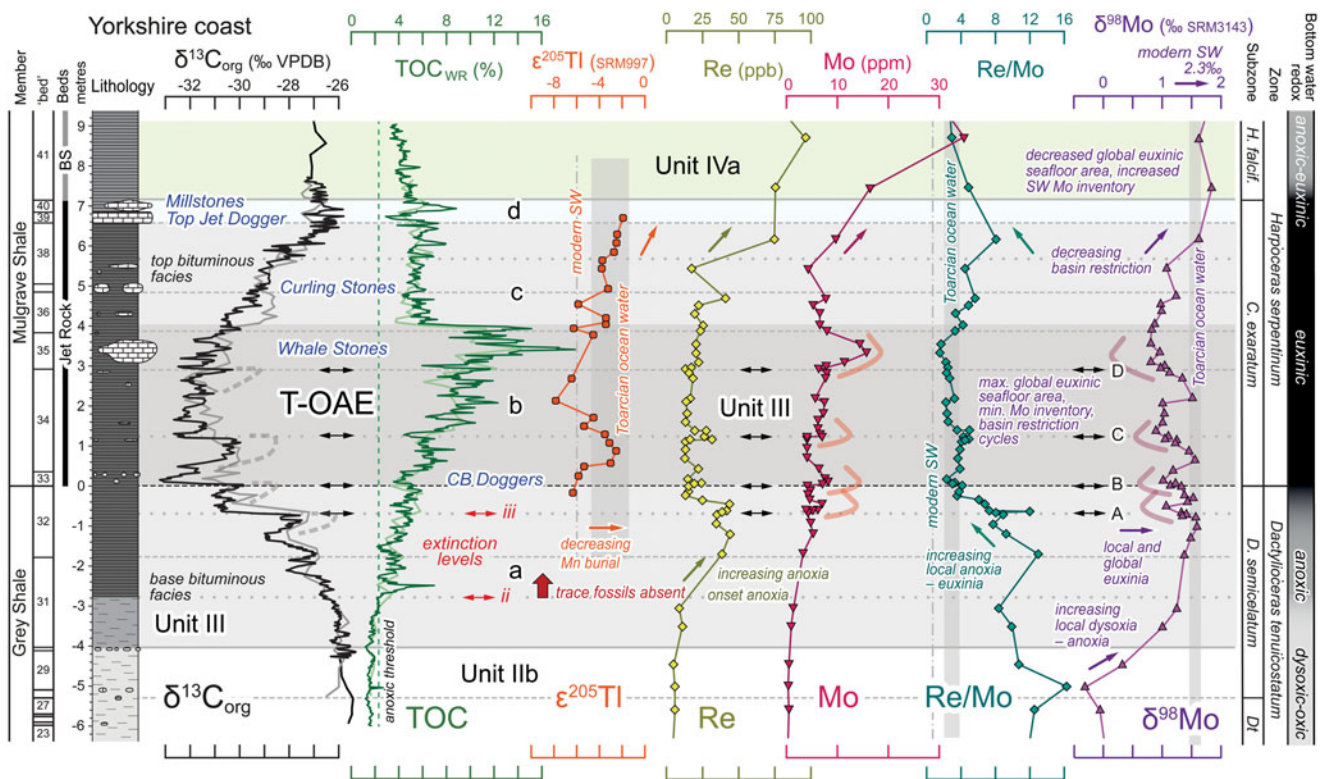


Figure 20. Stratigraphic profiles of $\delta^{13}\text{C}_{\text{org}}$, TOC and selected trace-metal isotopes within Unit III, the T-OAE interval of the Yorkshire coast. Stratigraphy as in Figures 6, 7. Bulk rock $\delta^{13}\text{C}_{\text{org}}$ and TOC profiles of the composite section from Hesselbo *et al.* (2000, pale coloured lines) and DB Kemp *et al.* (2005, dark lines), Kemp *et al.* (2011, dark lines) – see Figure 7. Shaded grey bands indicate Unit III Subunits a – c (see Section 8.c); shaded blue band is the interval of the carbonate maximum, Subunit III.d. A – D mark coincident sharp falls in $\delta^{13}\text{C}_{\text{org}}$ (after DB Kemp *et al.*, 2005; Cohen *et al.*, 2007) and $\delta^{98}\text{Mo}$, with increased Mo, as noted by Kemp *et al.* (2011). Biotic extinction levels *ii* and *iii* after Caswell *et al.* (2009); base of trace fossil absent interval follows Caswell & Herringshaw (2023). Thallium isotopes ($\epsilon^{205}\text{Tl}$) from Nielsen *et al.* (2011). Rhenium, Mo, Re/Mo and $\delta^{98}\text{Mo}$ profiles from Pearce *et al.* (2008). Note that Nielsen *et al.*'s (2011, fig. 5) comparison figure of $\epsilon^{205}\text{Tl}$ vs $\delta^{98}\text{Mo}$ at Port Mulgrave incorrectly plotted the position of the Mo dataset relative to the stratigraphy, as presented by Pearce *et al.* (2008, fig. 2). The replotted data in our figure do not support an anti-correlation between these two isotope systems, as proposed by Nielsen *et al.* (2011) and modelled by Owens *et al.* (2017).

rising values from the base that reach a maximum of $\sim +2\text{‰}$ around the TOC maximum in Whale Stones ‘bed’ 35 (Fig. 21). Values fall sharply to between -1‰ and -2‰ at the base of ‘bed’ 36 (base Subunit IIIc), coincident with a marked fall in TOC and the onset of rising $\delta^{13}\text{C}_{\text{org}}$. $\delta^{15}\text{N}$ displays a minimum value of $\sim -4\text{‰}$ at the base of ‘bed’ 41, immediately above the T-OAE interval. Very similar stratigraphic profiles and values were shown by lower resolution data from other UK successions in the Winterborne Kingston and Mochras boreholes from the Wessex and Cardigan Bay basins (Jenkyns *et al.*, 2001).

The interval of enhanced carbonate deposition exemplified by Whale Stones ‘bed’ 35 in Yorkshire, which can be traced across Germany (Unterer Stein), France and Switzerland (e.g. Riegraf, 1982), contains the TOC and $\delta^{15}\text{N}$ maxima (Fig. 21). Current evidence does not support the suggestion of van de Schootbrugge *et al.* (2005) that this represents a regional pulse in calcareous nannofossil productivity. In Germany, the Unterer Stein contains only rare nannofossils and exhibits a unique granular laminated fabric of submicrometric – micrometric anhedral calcite grains (microcarbs) and $\delta^{13}\text{C}_{\text{carb}}$ values of $\sim -12\text{‰}$ (Röhl *et al.*, 2001; Bour *et al.*, 2007; Wang *et al.*, 2020). These indicate bacterially induced carbonate precipitation associated with organic matter remineralization enhanced by microbial sulfate reduction. However, the supraregional extent of this diagenetic limestone indicates a period of significant palaeoenvironmental change immediately preceding the onset of rising global $\delta^{13}\text{C}$ values.

A massive influx of prasinophyte algae (*Halosphaeropsis liassica* Mädlér) and acritarchs occurs at this level in Yorkshire (Houben *et al.*, 2021), together with a dense clustered AOM-dominated palynofacies, that may be indicative of photo-autotrophic prokaryotes (e.g. cyanobacteria, green- and purple sulfur bacteria) during peak euxinic conditions, supported by the presence of isorenieratane (French *et al.*, 2014; Fig. 21). Prasinophyte algae possess a strong preference for ammonium over nitrate (Cochlan & Harrison, 1991) and can use NH_4^+ released by nitrogen fixers as their own nitrogen source. Stratification and photic-zone anoxia driving denitrification/anammox would favour organisms with low requirements for nitrate.

A $\delta^{15}\text{N}$ curve spanning the T-OAE interval at Dotternhausen (Wang *et al.*, 2021, fig. 4), shows a similar profile shape, but higher and less variable values, predominantly between $+0.3\text{‰}$ and $+2.5\text{‰}$. There, a peak, and step down in bulk rock $\delta^{15}\text{N}$, is associated with the Unterer Stein limestone in the mid-exaratum Zone and occurs at an identical stratigraphic position to the Whale Stones in Yorkshire with respect to the $\delta^{13}\text{C}_{\text{org}}$ curve. Elevated $\delta^{15}\text{N}$ values positively correlated with intervals of high TOC are apparent in other T-OAE sections in Europe (Jenkyns *et al.*, 2001; Ruebsam *et al.*, 2018; Wang *et al.*, 2021). Enhanced export of organic matter and its subsequent preservation under reducing conditions was associated with elevated denitrification rates. Thus, increased primary productivity combined with the intensification of water mass denitrification are proposed as the main processes controlling the changes in $\delta^{15}\text{N}$ values.

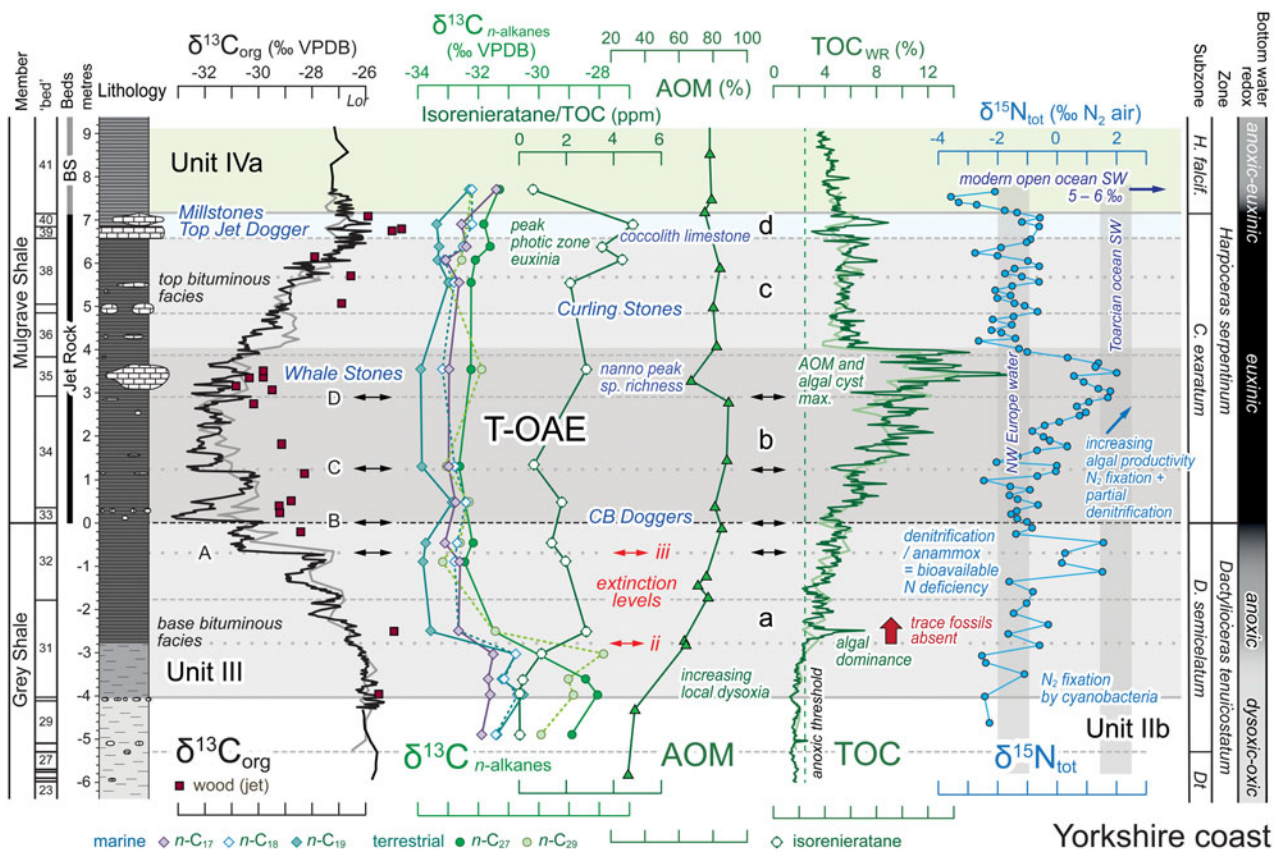


Figure 21. Stratigraphic profiles of $\delta^{13}\text{C}_{\text{org}}$, $\delta^{13}\text{C}_{n\text{-alkanes}}$, isorenieratane, AOM, TOC and $\delta^{15}\text{N}_{\text{tot}}$ within Unit III, the T-OAE interval of the Yorkshire coast. Bulk rock $\delta^{13}\text{C}_{\text{org}}$ and TOC profiles of the composite section from Hesselbo *et al.* (2000, pale coloured lines) and DB Kemp *et al.* (2005, dark lines), Kemp *et al.* (2011, dark lines) – see Figure 7; ‘anoxic threshold’ of $\text{TOC}_{\text{WR}} = 2.5 \text{ wt}\%$ follows Algeo & Maynard (2004). $\delta^{13}\text{C}$ data for terrestrial wood (Hesselbo *et al.*, 2000, brown squares) are offset but track the bulk sediment $\delta^{13}\text{C}_{\text{org}}$ curve. Carbon isotope values from Hawsker Bottoms of representative long-chain n -alkane biomarkers ($\delta^{13}\text{C}_{n\text{-alkane}}$) derived from terrestrial plants ($n\text{-C}_{27}$, $n\text{-C}_{29}$) also display the negative excursion of the T-OAE (French *et al.*, 2014). Short-chain n -alkanes ($n\text{-C}_{17}$ – $n\text{-C}_{19}$) attributed to marine plants follow an identical $\delta^{13}\text{C}$ trend (French *et al.*, 2014, fig. 7). The isorenieratane profile, a biomarker for anaerobic phototrophic green sulfur bacteria, provides evidence of reducing conditions developing during the initial phase of the T-OAE, peaking at the time of deposition of ‘bed’ 40 (Millstones); chlorobactane and okenane (not shown) display identical patterns (French *et al.*, 2014, fig. 5). Amorphous organic matter (AOM) and algal cysts dominate (50–>90%) the palynological assemblages (after Slater *et al.*, 2019) of the high-TOC anoxic–euxinic facies. Peak species richness of calcareous nannofossils, preserved as carbonate and external moulds in organic matter throughout the section (Slater *et al.*, 2022), occurs in Whale Stones ‘bed’ 35, together with a pulse of prasinophyte algae and dense granular organic matter (Houben *et al.*, 2021). Nitrogen isotopes ($\delta^{15}\text{N}_{\text{tot}}$) display low values attributable to enhanced N_2 fixation by cyanobacteria in a strongly redox-stratified marine environment (Wang *et al.*, 2021). Toarcian open ocean seawater field derived from Tethyan sections (Section 16.a.1). The $\delta^{15}\text{N}_{\text{tot}}$ profile (Jenkyns *et al.*, 2001) broadly follows TOC. A–D mark coincident sharp falls in $\delta^{13}\text{C}_{\text{org}}$ (after DB Kemp *et al.*, 2005; Cohen *et al.*, 2007) and $\delta^{98}\text{Mo}$, as noted by Kemp *et al.* (2011) – see Figure 20. Biotic extinction levels *ii* and *iii* after Caswell *et al.* (2009); base of trace fossil absent interval follows Caswell & Herringshaw (2023).

Positive near-0‰ $\delta^{15}\text{N}$ values recorded from Dotternhausen and other north European basins within the T-OAE interval were attributed by Wang *et al.* (2021) to an episode of enhanced N_2 fixation by cyanobacteria using Mo-based nitrogenase to compensate for severe bioavailable N loss. This was explained by the near-complete consumption of NO_3^- in strongly restricted redox-stratified water masses following extensive denitrification and/or anammox accompanying the T-OAE (Wang *et al.*, 2021). However, it is seen that the 3 UK sections studied by Jenkyns *et al.* (2001), located in 3 different basins, yielded $\delta^{15}\text{N}$ values $\sim -1\text{‰}$ to -2‰ in organic-lean (<1% TOC) upper Pliensbachian and post-OAE Toarcian sediments that lack evidence of basin restriction. These negative values imply long-term ^{15}N depletion in a regional NW European water mass rather than being driven by increasing basin restriction and environmental change accompanying the T-OAE.

The low $\delta^{15}\text{N}$ values from levels outside the T-OAE interval are surprising. Nitrogen isotopic compositions that are significantly less than 0‰ in marine settings are typically restricted to organic matter-rich sediments and mudstones from Mediterranean

sapropels and Mesozoic black shales (Junium *et al.*, 2018). Such low values could potentially reflect highly oligotrophic conditions that lacked significant denitrification and had low levels of nitrate utilization, similar to the modern eastern Mediterranean which has seawater $\delta^{15}\text{N}$ values $\sim -1\text{‰}$ (Jenkyns *et al.*, 2001).

Low ^{15}N values (-4‰ to -1‰) have been documented in Cenomanian–Turonian boundary OAE2 successions (Algeo *et al.*, 2014, fig. 6; Zhai *et al.*, 2023, fig. 3) and other Phanerozoic OAE sediments (Ader *et al.*, 2014) but significant spatial variant exists. Higgins *et al.* (2012) attributed these low values to new production being driven by direct NH_4^- assimilation from upwelled anoxic deep water, supplemented by diazotrophy, with chemocline denitrification and anammox quantitatively consuming NO_3^- . A marine nitrogen reservoir dominated by NH_4^- , in combination with kinetic isotope effects, would have led to eukaryotic biomass depleted in ^{15}N (Higgins *et al.*, 2012). Although this is a feasible explanation for the low $\delta^{15}\text{N}$ values accompanying OAE2 it is difficult to apply to the long-term ^{15}N depletion that characterizes Lower Jurassic records reported by Jenkyns *et al.* (2001) outside the T-OAE interval. Furthermore, by contrast to OAE2, trends within the T-OAE

evidence increasing rather than decreasing $\delta^{15}\text{N}$ values accompanied by intensified euxinia (Fig. 21).

It is evident that $\delta^{15}\text{N}$ values reported at all sites in the Jenkyns *et al.* (2001) study consistently include a high proportion of values of $\ll 0\%$. This contrasts with the N-isotope data reported in all later Toarcian studies, including those from Switzerland (Riethem; Montero-Serrano *et al.*, 2015), Germany (Dotternhausen; Wang *et al.*, 2021), Hungary (Réka Valley; Ruebsam *et al.*, 2018) and Algeria (Ratnek El Kahla, Ruebsam *et al.*, 2020b; Mellala, Baghli *et al.*, 2022), where $\delta^{15}\text{N}$ values are consistently positive and generally lie between $+1 - +3\%$. These values are typical of greenhouse climate ocean sediments throughout the Phanerozoic (Algeo *et al.*, 2014) and likely reflect the $\delta^{15}\text{N}$ composition of early Toarcian open-ocean seawater (Fig. 21).

It should be noted that the incorrect use of HCl for decarbonation can generate $\delta^{15}\text{N}$ values as low as -12% from samples with positive values. Provisional results from the Dove's Nest core have yielded $\delta^{15}\text{N}$ values of $+2 - +3\%$ for selected samples throughout the succession. We recommend that additional nitrogen isotope studies of the Yorkshire and other T-OAE successions should be carried out to test the reliability of the Jenkyns *et al.* (2001) data. In the meantime, the $\delta^{15}\text{N}$ values reported in that work should be treated with caution.

16.a.2. Sulfur isotopes – ^{32}S drawdown and oceanic sulfate depletion

The sulfur isotope composition of ocean water is controlled principally by a balance between the input of relatively ^{34}S -enriched sulfate from weathering of the continents and the output of ^{34}S -depleted sulfur fixed and buried as pyrite and organic sulfur in sediments (Claypool *et al.*, 1980). Modern rivers have variable $\delta^{34}\text{S}$ ($\delta^{34/32}\text{S} \text{‰}_{\text{VCDT}}$) sulfate values of 0% to $+10\%$; sulfides in modern marine sediments are typically around -40% $\delta^{34}\text{S}$, although a large range is observed (Paytan *et al.*, 2020). Sulfate is the second most abundant anion in the oceans and has a residence time of 10 – 20 Ma, which far exceeds the mixing time of the ocean $\sim 1 - 2 \text{ ka}$ (Paytan *et al.*, 2004) and seawater sulfate today has a constant $\delta^{34}\text{S}$ value of $+21.0 \pm 0.2\%$ (Rees *et al.*, 1978).

The sulfur isotope composition of carbonate-associated sulfate ($\delta^{34}\text{S}_{\text{CAS}}$; i.e. sulfate substituted in the crystal lattice of carbonate minerals) provides a means of establishing past seawater values (Kampschulte & Strauss, 2004). Data obtained from belemnite guards through the Pliensbachian – Toarcian of the Yorkshire coast (Kampschulte & Strauss, 2004; Gill *et al.*, 2011; Newton *et al.*, 2011) display a marked 6% $\delta^{34}\text{S}_{\text{CAS}}$ increase from $\sim +16\%$ to $+22\%$ through the *C. exaratum* Subzone (T-OAE Subunits IIIb – d; Fig. 19). By comparison, Raiswell *et al.* (1993) analysed 11 pyrite samples from the same interval (i.e. Jet Rock) with an average $\delta^{34}\text{S}_{\text{pyrite}}$ value of $-24 \pm 2\%$.

Samples from Dotternhausen (belemnites) and Monte Sengenza, Italy (whole-rock carbonate) display similar $\delta^{34}\text{S}$ values and increases across the T-OAE interval to those in Yorkshire (Gill *et al.*, 2011) indicating a consistent pattern of sulfur isotope variation throughout northern European basins and western Tethys. A compilation of global widely spaced $\delta^{34}\text{S}_{\text{CAS}}$ and $\delta^{34}\text{S}$ evaporite data spanning the Jurassic suggests a return to pre-T-OAE seawater $\delta^{34}\text{S}$ values of $\sim +17\%$ through the later Toarcian into the Aalenian (Gill *et al.*, 2011, fig. 6), representing an $\sim 8 \text{ Ma}$ recovery period. This indicates a relatively long residence time for sulfate in the Jurassic ocean; estimates from modelling by Gill *et al.* (2011) put Toarcian marine sulfate concentrations at 4 to 8 mM compared to 28 mM today.

By contrast to the European data, sections in southern Tibet, representative of the southeastern open Tethys, display a much larger positive sulfur-isotope excursion, rising from $\sim +20\%$ around the Pl–To boundary to $\sim +40\%$ at the top of the T-OAE interval (Newton *et al.*, 2011; Han *et al.*, 2022, 2023). The rate of isotopic change with time based on the Tibetan sections indicates that early Jurassic seawater sulfate concentrations may have been as low as 1 – 5 mM.

The $\delta^{34}\text{S}$ increase accompanying the T-OAE demonstrates a globally significant perturbation in the sulfur cycle driven by the drawdown of isotopically light ^{32}S by pyrite and organic sulfur burial in euxinic environments. Modelling by Gill *et al.* (2011) indicated that pyrite deposition in the northern European epicontinental seaway was insufficient to cause the observed isotope excursion, accounting for at most 4% of the pyrite burial required. Substantial additional pyrite burial would be needed to drive the documented excursion, requiring a much wider extent of euxinic conditions in the world ocean during the T-OAE, although the impacts of an increase in ^{32}S -enriched organic sulfur burial and a possible near cessation Ca-sulfate evaporite deposition during the T-OAE also need to be considered (Han *et al.*, 2023).

The large differences in $\delta^{34}\text{S}_{\text{CAS}}$ values and the amplitude of the excursions accompanying the T-OAE in Europe and Tibet imply substantial regional differences in local sulfur cycling (Gill *et al.*, 2011; Han *et al.*, 2022, 2023). The contrasting records might be attributed to varying modifications of open-ocean sulfate isotopic compositions by water-mass isolation and the effects of changing regional weathering and pyrite burial fluxes. Significant spatial heterogeneity of $\delta^{34}\text{S}_{\text{CAS}}$ values and trends have also been observed over OAE2 (Zhai *et al.*, 2023) indicating that sulfate in the Cretaceous ocean was also not as well mixed as today and that $\delta^{34}\text{S}_{\text{CAS}}$ was influenced by regional oceanic redox conditions.

Modelling by Han *et al.* (2022) indicates that the initial formation of an isotopically heterogeneous ocean for seawater sulfate began in the Pliensbachian as concentrations began to fall. At the time of maximum early Toarcian euxinia, during the T-OAE, this may have culminated in a large difference in the scale of response between the European epicontinental sea and western Tethyan continental margin, where coeval isotopic values are comparable, and the easterly Tibetan shelf of southern Tethys. The greater amplitude of the sulfur isotope excursion in Tibet has been ascribed to the upwelling of ^{34}S -enriched equatorial deep water, while the lower magnitude of the Toarcian sulfur excursion in Europe reflects a smaller, local reduced-sulfur sink (Han *et al.*, 2023).

A two-phase pattern of ocean deoxygenation during the early Toarcian is indicated by the Tibetan $\delta^{34}\text{S}_{\text{CAS}}$ data: the first began around the Pl–To boundary and continued up to the onset of the T-OAE; the second coincided with the onset of rising $\delta^{13}\text{C}$ values and terminated around the end of the T-OAE. The termination of deoxygenation also marks the point where the sulfur cycle reaches a new steady state with a negligible Ca-sulfate burial flux. Higher positive $\delta^{34}\text{S}$ values were maintained after the T-OAE by a long-term global reduction in Ca-sulfate (gypsum and anhydrite) burial, driven by falling and then continuous low seawater-sulfate concentrations during and after the T-OAE.

The depletion of marine sulfate during the T-OAE has implications for other geochemical processes. Adams *et al.* (2010) have argued that sulfate levels regulate the recycling of phosphorus during remineralization of organic matter by microbial sulfate reduction. Efficient phosphorus recycling is considered to be essential to maintaining high levels of primary productivity

and anoxic conditions during OAEs (Van Cappellen & Ingall, 1994). Thus, sulfate depletion accompanying and following the T-OAE, driven by pyrite burial, provides a significant negative feedback mechanism that would favour the termination of widespread anoxia and the T-OAE.

16.b. Trace-metal isotopes – Mo, Tl, U, Os

The relatively long modern ocean residence times of Mo (440 – 800 ka), U (~450 ka), Tl (~20 ka) and Os (~10 – 40 ka) compared to the ocean mixing time of ~1 – 2 ka, combined with distinctive stable-isotope fractionation association with different marine sinks, means that the isotopic composition of these metals has potential to serve as global oceanic tracers (Kendall *et al.*, 2021). Uranium and Mo isotope systems offer established tracers of global oceanic redox conditions, particularly for the extent of anoxic and euxinic seafloor, and Tl isotopes provide a proxy for the extent of well-oxygenated seafloor characterized by Mn oxyhydroxide burial (Kendall *et al.*, 2021). Marine carbonaceous mudstones provide the principal archive for reconstructing palaeoredox histories from these isotope records. Osmium isotopes enable the identification of changes in weathering versus hydrothermal fluxes (Peucker-Ehrenbrink & Ravizza, 2020) that might impact global productivity.

Variations in trace-metal isotope records from the Toarcian of Yorkshire have previously been attributed principally to local changes in water chemistry in the Cleveland Basin (Cohen *et al.*, 2004; McArthur *et al.*, 2008; Pearce *et al.*, 2008; Nielsen *et al.*, 2011; Dickson *et al.*, 2017), but there is now increasing evidence that they incorporate a significant component of global ocean change (e.g. Them *et al.*, 2022).

16.b.1. Molybdenum isotopes – a proxy for global euxinic seafloor area

Molybdenum isotopes, reported as $\delta^{98}\text{Mo}$ ($\delta^{98/95}\text{Mo}$ ‰_{SRM3143}), have become established as a valuable proxy to assess temporal variation in the global extent of seafloor euxinia and organic burial in the oceans. The redox sensitivity of Mo isotopes has been reviewed by Kendall *et al.* (2021). Chemically inert molybdate (MoO_4^{2-}) is the principal species in oxygenated rivers and seawater, but this is converted to particle-reactive thiomolybdates ($\text{MoO}_4-x\text{S}_x^{2-}$) and polysulfides in sulfidic bottom waters and pore waters.

Modern seawater has a $\delta^{98}\text{Mo}$ value of $2.3 \pm 0.1\text{‰}$. The dominant Mo input (95%) to the oceans, from rivers and groundwater, has an isotopic composition similar to the average upper crust value of $\sim 0.6\text{‰}$ $\delta^{98}\text{Mo}$. The influence of hydrothermal fluids ($\sim 1.5\text{‰}$ $\delta^{98}\text{Mo}$) is negligible (5%). Molybdenum isotope fractionation in marine environments results in preferential removal of light Mo isotopes to sediments. The largest fractionation (-3‰) occurs in well-oxygenated settings, where Mo is adsorbed to Mn oxyhydroxides with average values of around -0.7‰ $\delta^{98}\text{Mo}$, leading to ^{98}Mo enrichment of seawater.

Under dysoxic to anoxic bottom waters, where dissolved sulfide occurs in sediment pore waters, Mo isotope fractionation is variable. Here, it depends on the type of oxyhydroxides delivering Mo to sediments and pore-water H_2S concentration, with Mo burial efficiency increasing with the level of dissolved sulfide. The average fractionation is -0.8‰ and an output value of $\sim 1.5\text{‰}$ $\delta^{98}\text{Mo}$. Larger fractionations reflect weakly to intermittently euxinic conditions and/or a strong Fe–Mn oxyhydroxide particulate flux that delivers isotopically light Mo to sediments.

The $\delta^{98}\text{Mo}$ of euxinic sediments approaches that of seawater when Mo removal from bottom waters is near quantitative, particularly in significantly restricted, but not isolated, basins with water stratification and highly sulfidic bottom waters like the modern Black Sea (Kendall *et al.*, 2021). The $\delta^{98}\text{Mo}$ of seawater sequestered into euxinic mudstones is therefore hypothesized to reflect the $\delta^{98}\text{Mo}$ of seawater, and variations in $\delta^{98}\text{Mo}$ with stratigraphic level through a black shale section have been interpreted to reflect a changing balance of sequestration globally into oxic and euxinic sediments (McArthur *et al.*, 2008; Pearce *et al.*, 2008). The oceanic Mo mass balance is highly sensitive to the extent of sulfidic (especially euxinic) environments. Hence, seawater Mo concentrations and residence times will be lower in ancient oceans with a greater extent of euxinic seafloor than today (Reinhard *et al.*, 2013).

A Mo isotope profile for the Yorkshire coast spanning the lower Toarcian, sampled at Port Mulgrave, Saltwick Bay and Hawsker Bottoms, was published by Pearce *et al.* (2008). Their Mo and $\delta^{98}\text{Mo}$ data are plotted in Figures 19 and 20 and compared to companion curves for $\epsilon^{205}\text{Tl}$, Re and Re/Mo spanning the T-OAE interval in Figure 20. Light $\delta^{98}\text{Mo}$ values of $\sim 0\text{‰}$ and low Mo concentrations of ~ 0.5 ppm below the T-OAE interval in basal Toarcian Unit II (Figs 18, 20) are consistent with adsorption of Mo to Mn oxyhydroxides in sediments underlying an oxic water column.

Molybdenum isotope values increase markedly to $>1\text{‰}$ $\delta^{98}\text{Mo}$ and Mo concentrations rise to ≥ 4 ppm at the base of T-OAE Unit III indicating the establishment of dysoxic and then anoxic bottom waters (Fig. 20; Pearce *et al.*, 2008). $\delta^{98}\text{Mo}$ oscillates with an amplitude of $\sim 0.7\text{‰}$ through the T-OAE interval. Mo contents show small sharp increases (reflecting a higher availability of Mo in the basin seawater) at stratigraphic levels where $\delta^{98}\text{Mo}$ becomes lighter and $\delta^{13}\text{C}_{\text{org}}$ falls (events A – D of Pearce *et al.*, 2008), highlighted by the pale-coloured curves in Figure 20. Associated Re/Mo ratios remain low, consistent with persistent euxinia and show no consistent pattern. The four $\delta^{98}\text{Mo}$ maxima are $\sim 1.5\text{‰}$. Evidence of significant environmental change at these levels is provided by the biota: the abundance and average size of *Pseudomytiloides dubius* (Sowerby) shells vary within the same stratigraphic levels as the $\delta^{98}\text{Mo}$ record (Caswell *et al.*, 2009; Caswell & Coe, 2013). Periods of higher primary productivity and greater oxygenation accompanying more open basin conditions, indicated by increased $\delta^{98}\text{Mo}$ values, supported larger bivalves.

Molybdenum isotope values increase from the top of the T-OAE interval into the Bituminous Shales (*H. falciferum* Subzone, Fig. 19) with $\delta^{98}\text{Mo}$ values of $1.8 \pm 0.2\text{‰}$ in Unit IV. The increase begins immediately above the top of the laminated black shale facies of the Jet Rock at the level of the Upper Pseudovertebrae concretions (cf. Howarth, 1962) in ‘bed’ 38 and coincides with the onset of increasing Re and Mo contents, falling Re/Mo ratio and increasing $\epsilon^{205}\text{Tl}$ (Fig. 20). Subunits IVa and b each display a broad peak in $\delta^{98}\text{Mo}$ with a maximum of up to 2.1‰ , associated with high Mo and Re values, with the two subunits being separated by a trough in all three constituents. $\delta^{98}\text{Mo}$ values fall back to $\sim 1.5\text{‰}$ in uppermost lower and basal middle Toarcian Unit V, based on 4 data points (Fig. 19).

Global expansion of oceanic euxinia, evidenced by low Mo and Mo/TOC values in T-OAE black shales from open marine basins imply a significant drawdown of the marine Mo inventory during the early Toarcian (Them *et al.*, 2022; Section 13.a); this would be expected to cause a decrease in seawater $\delta^{98}\text{Mo}$. The observed opposing shift to higher $\delta^{98}\text{Mo}$ accompanying the onset of the

T-OAE in the Cleveland Basin, therefore, is interpreted to reflect the local change to more intensely reducing conditions at the onset of the T-OAE, as evidenced by Fe-speciation and other redox proxy data (Fig. 14). Changes in local bottom-water redox exerted a greater control on stratigraphic changes in $\delta^{98}\text{Mo}$ than the global expansion of oceanic euxinia (Fig. 20).

Drawdown of Mo during the T-OAE (Section 13.a) potentially decreased the oceanic residence time of Mo sufficiently to cause seawater $\delta^{98}\text{Mo}$ values to fluctuate rapidly in response to redox variations or even become spatially heterogeneous between different ocean basins. Sections of carbonaceous mudstones in Germany (Dotternhausen) and the Netherlands (Rijswijk core) do not show high-amplitude oscillations in $\delta^{98}\text{Mo}$ within the T-OAE interval like those observed in Yorkshire (Dickson *et al.*, 2017), so the Yorkshire cycles are unlikely to reflect global changes in the Mo continental weathering flux or euxinic seafloor area as proposed by Pearce *et al.* (2008).

A small global marine-Mo reservoir in conjunction with basin restriction potentially resulted in the large regional variability of water mass (and therefore sedimentary) Mo concentrations and $\delta^{98}\text{Mo}$ observed in different European basins during the early Toarcian. However, it is significant that Mo/TOC ratios, which may also reflect the inventory of dissolved Mo in euxinic marine basins (Algeo & Lyons, 2006) display similar minimum values of ~ 1 within the T-OAE intervals in Yorkshire (Fig. 16), Germany and the Netherlands (Dickson *et al.*, 2017, fig. 6).

Dickson *et al.* (2017) and Kendall *et al.* (2021) suggested that the highest $\delta^{98}\text{Mo}$ values of $\sim 1.45\text{‰}$ in the T-OAE interval in Yorkshire may represent a close estimate of global seawater $\delta^{98}\text{Mo}$ during the early Toarcian. Episodes of decreased restriction of the Cleveland Basin, however, might allow an increased inflow of Mo from open ocean seawater at a rate faster than the removal of Mo to sediments (Dickson *et al.*, 2017). This would lead to a euxinic basin with incomplete Mo drawdown (i.e. non-quantitative Mo removal) and sediments fractionated by $\sim -0.7\text{‰}$ from open ocean seawater, as seen in the modern Cariaco Basin (Arnold *et al.*, 2004). T-OAE sections in SW Germany (Dotternhausen) and the Netherlands (Rijswijk core) also have lower $\delta^{98}\text{Mo}$ than the inferred seawater $\delta^{98}\text{Mo}$ value of $\sim 1.45\text{‰}$ within the T-OAE interval (Dickson *et al.*, 2017), consistent with less restricted and/or less reducing conditions at those localities.

High $\delta^{98}\text{Mo}$ values of up to 2.1‰ characterize Unit IV (Fig. 19). Authigenic phases in modern marine sediments do not record $\delta^{98}\text{Mo}$ values higher than coeval seawater, so this higher value implies rising seawater $\delta^{98}\text{Mo}$ accompanying a global decrease in euxinic seafloor area during the later early Toarcian.

16.b.2. Thallium isotopes – assessing the extent of oxic seafloor area

Thallium isotopes offer further potential to constrain the geological evolution of seawater oxygenation on a basin to a global scale (Nielsen *et al.*, 2017; Ostrander *et al.*, 2017; Owens *et al.*, 2017; Owens, 2019). Thallium isotopes are reported relative to Tl metal standard SRM997 using the epsilon notation where:

$$\epsilon^{205}\text{Tl} = \left[\left(\frac{^{205}\text{Tl}}{^{203}\text{Tl}} \right)_{\text{sample}} / \left(\frac{^{205}\text{Tl}}{^{203}\text{Tl}} \right)_{\text{SRM997}} - 1 \right] \times 10^4$$

Thallium is supplied to the oceans by rivers, mineral aerosols (dust), volcanic gases and particles and high-temperature hydrothermal fluids, all of which have similar $\epsilon^{205}\text{Tl}$ values of around -2 and pore-water fluxes from continental-margin sediments $\epsilon^{205}\text{Tl}$

with a value of around 0. The only two important marine Tl sinks are adsorption by authigenic phases, principally Mn oxyhydroxides in pelagic clays, with $\epsilon^{205}\text{Tl}$ values of $\sim +8$ to $+12$ and uptake of Tl during low-temperature alteration of oceanic crust with an $\epsilon^{205}\text{Tl}$ value of -7.2 . For short-term ≤ 1 Ma redox events it is considered that changes in the Tl isotopic composition of seawater are driven principally by changing rates of Mn-oxyhydroxide burial (Owens *et al.*, 2017), since changes in the rate of oceanic crust alteration will operate on longer time scales.

The relatively short modern ocean residence time for Tl of ~ 20 ka, which is nonetheless one order of magnitude longer than the ocean mixing time, ensures a uniform $\epsilon^{205}\text{Tl}$ value of -6.0 ± 0.6 in modern open-ocean seawater (Nielsen *et al.*, 2017; Owens *et al.*, 2017; Owens, 2019). Mn-oxyhydroxides that are ubiquitous in sediments deposited from oxygenated bottom waters, combined with the detrital mineral fraction, generate $\epsilon^{205}\text{Tl}$ signatures in bulk sediments and partial extracts that are generally isotopically heavier than ambient seawater (e.g. Wang *et al.*, 2022, but see discussion therein). Oxyhydroxides are absent under anoxic or euxinic conditions because the reduction of insoluble Mn (IV) to more soluble Mn (II) and Mn (III) occurs when oxygen is removed from the water in contact with the sediment. In this case, the $\epsilon^{205}\text{Tl}$ composition from the oxic part of the water column has been shown to transfer quantitatively to the authigenic fraction (principally Fe sulfides) in sediments underlying euxinic (Owens *et al.*, 2017) or highly reducing anoxic bottom waters (Fan *et al.*, 2020), which may then provide a record of the isotopic evolution of the surface ocean. In partially and predominantly restricted basins $\epsilon^{205}\text{Tl}$ values vary between open-ocean (-6) and continental material (-2), scaling with the degree of restriction, as exemplified by the Cariaco Basin (-5.4 – weak restriction) and the Black Sea (-2.3 – strong restriction) (Owens *et al.*, 2017).

Thallium isotope data in early diagenetic pyrite from the upper beds of the T-OAE (top ‘bed’ 32 – 39) at Port Mulgrave were published by Nielsen *et al.* (2011). $\epsilon^{205}\text{Tl}$ values show a large range from -8 to -2 (Fig. 20). Thallium isotope data for authigenic Tl, based on bulk rock extracts from the upper Pliensbachian – middle Toarcian of 3 sections from the Western Canada Sedimentary Basin, Alberta, Canada and SW German Basin (Dotternhausen) were presented by Them *et al.* (2018). The Canada profiles, obtained from sections that were subject to consistent anoxic – euxinic conditions throughout the study interval (based on $\text{Fe}_{\text{HR}}/\text{Fe}_{\text{T}}$ and $\text{Fe}_{\text{Py}}/\text{Fe}_{\text{HR}}$ Fe-speciation proxies) yielded $\epsilon^{205}\text{Tl}$ values close to modern seawater of -6 through the upper Pliensbachian. They then rise upward from around the bottom of the base Toarcian *D. tenuicostatum* Zone equivalent, to -2 at the onset of the T-OAE. $\epsilon^{205}\text{Tl}$ falls back to a broad trough of -4 mid-T-OAE, with a second peak of -2 at the top of the T-OAE and then falls upward towards -4 in the *H. bifrons* equivalent Zone. A similar trend and values were observed in the SW German Basin Toarcian profile (Them *et al.*, 2018, fig. 3).

The increase in $\epsilon^{205}\text{Tl}$ at the Pliensbachian – Toarcian boundary in the Western Canada Sedimentary Basin was interpreted by Them *et al.* (2018) to mark the onset of increasing global bottom-water anoxia that preceded the T-OAE by 600 ka and was sustained into the middle Toarcian *H. bifrons* Zone, representing an interval of ~ 2 Ma. Rising values were attributed to a global reduction in Fe–Mn oxyhydroxide precipitation accompanying oxygen depletion, with an accompanying decrease in ^{205}Tl output flux leading to rising $\epsilon^{205}\text{Tl}$ seawater values. Authigenic Tl concentrations show no systematic variation throughout the section (Them *et al.*, 2018),

which suggests the marine inventory was not depleted due to increased anoxic conditions.

Thallium isotopes from the T-OAE interval in Yorkshire show a wider range and extend to lower values ($\epsilon^{205}\text{Tl}$ –8 to –2; Nielsen *et al.*, 2011) compared to Toarcian seawater values interpreted from the successions in western Canada and Germany ($\epsilon^{205}\text{Tl}$ –4 to –2; Them *et al.*, 2018). Shifts to values below those of open ocean water (Fig. 20) might be attributed to short-term basin-scale Mn-oxyhydroxide burial events in oxic areas of the Cleveland Basin margin driving local episodes of ^{205}Tl drawdown from the local water mass.

Interestingly, the increase of $\epsilon^{205}\text{Tl}$ in the lower Toarcian profile in Canada and to some extent in Yorkshire (Fig. 20), is matched by an increasing $\delta^{34}\text{S}_{\text{CAS}}$ trend in the Cleveland Basin (Fig. 19) but also in Italy (Monte Sorghena) and southern Tibet (Han *et al.*, 2022, 2023). Broadly parallel trends for thallium and sulfur isotopes are a characteristic feature of the long-term Cenozoic record (Nielsen *et al.*, 2017).

Finally, it should be noted that the comparison figure of $\epsilon^{205}\text{Tl}$ vs $\delta^{98}\text{Mo}$ at Port Mulgrave by Nielsen *et al.* (2011, fig. 5) incorrectly plots the position of the Mo dataset relative to the stratigraphy, as presented by Pearce *et al.* (2008, fig. 2). The correctly aligned stratigraphic profiles are shown in Figure 20. These do not support an anti-correlation between these two isotope systems, as proposed by Nielsen *et al.* (2011) and modelled by Owens *et al.* (2017).

16.b.3 Uranium isotopes – potential insights into global anoxia

Uranium is insoluble in its reduced form and, in contrast to Mo, does not require dissolved sulfide for its incorporation and burial in sediments (Sections 13.b, d). U-isotope data ($\delta^{238/235}\text{U}$ ‰_{SRM145}) from organic-rich mudstones and carbonates are increasingly employed as a tool for tracing global oceanic redox changes during Phanerozoic anoxic events (e.g. Clarkson *et al.*, 2018; Lau *et al.*, 2019; Cheng *et al.*, 2020; McDonald *et al.*, 2022; Kulenguski *et al.*, 2023). However, isotope fractionation factors and U removal mechanisms in anoxic marine environments need to be better constrained (Kendall *et al.*, 2021), and the basis for global oceanic redox interpretations has been questioned (Cole *et al.*, 2020; Zhang *et al.*, 2020; Gangl *et al.*, 2023). Surprisingly, to our knowledge, no U-isotope study has been published for the T-OAE.

16.b.4 Osmium isotopes – radiometric age and constraining continental weathering

The rhenium–osmium (Re–Os) isotope system can be used to obtain absolute ages for the deposition of marine mudstone successions, although the precision of Re–Os dates generally remains poorer than that currently achievable using U–Pb and $^{40}\text{Ar}/^{39}\text{Ar}$ geochronometers (Schmitz *et al.*, 2020). By contrast, the $^{187}\text{Os}/^{188}\text{Os}$ composition of ancient marine sediments, when age corrected for the contribution of ^{187}Re decay ($^{187}\text{Os}/^{188}\text{Os}_i$), records temporal variation in seawater that provides valuable evidence of palaeoenvironmental change (e.g. Cohen, 2004; Katchinoff *et al.*, 2021).

Samples from the *C. exaratum* and *H. falciferum* subzones of the Yorkshire coast have yielded imprecise Re–Os isochron ages of 181 ± 13 Ma (Cohen *et al.*, 1999) and 178 ± 5 Ma (Cohen *et al.*, 2004), respectively. Subsequently, an older, more precise, Re–Os age of 183.0 ± 2.0 Ma has been obtained for the equivalent Toarcian *H. falciferum* Subzone Posidonia Shale of SW Germany (van Acken *et al.*, 2019), consistent with the base Toarcian age of the 184.20 Ma assigned by GTS2020 (Hesselbo *et al.*, 2020b) and

183.73 ± 0.35 – 0.50 Ma calculated using U–Pb zircon ages from Argentina (Al-Suwaidi *et al.*, 2022).

Modern deep ocean water has a globally uniform $^{187}\text{Os}/^{188}\text{Os}$ value of 1.06 ± 0.1 . The $^{187}\text{Os}/^{188}\text{Os}$ composition is predominantly controlled by the mass balance of two end-member Os isotope components: weathered continental crust (~ 1.4) and mantle inputs (0.13) derived from submarine volcanism and basalt weathering (Peucker-Ehrenbrink & Ravizza, 2002, 2020). This, coupled with the short residence time of Os in seawater of ~ 10 – 40 ka (Levasseur *et al.*, 1999; Oxburgh, 2001) makes the $^{187}\text{Os}/^{188}\text{Os}_i$ composition of marine sediments an excellent monitor of palaeoenvironmental change in the geological record (Cohen, 2004; Peucker-Ehrenbrink & Ravizza, 2020).

The first $^{187}\text{Os}/^{188}\text{Os}$ data spanning the lower Toarcian and the T-OAE interval, published by Cohen *et al.* (2004), were derived from the Yorkshire coastal succession. $^{187}\text{Os}/^{188}\text{Os}_i$ values of ~ 0.3 in the lowest Toarcian rise sharply to a maximum of ~ 1.0 within the CIE interval and fall back to ~ 0.4 immediately above (Fig. 19). Comparable data have been generated subsequently for Mochras, Wales (Percival *et al.*, 2016); East Tributary, Alberta, Canada (Them *et al.*, 2017b); Dormettingen, SW Germany (van Acken *et al.*, 2019); and Sakuraguchi-dani, Japan (Kemp *et al.*, 2020) with similar trends observed in all sections. This peak in $^{187}\text{Os}/^{188}\text{Os}_i$ values suggests that the flux of radiogenic ^{187}Os derived from continental crust weathering increased significantly during the T-OAE but declined rapidly after the event.

It has been suggested that weathering of juvenile basalt from LIPs (Jenkyns *et al.*, 2017), including the Karoo–Ferrar (Cohen & Coe, 2007), would have significantly increased the input of non-radiogenic Os into seawater during and after their emplacement. As a result, the increase in continental weathering of ancient crust must have been of much greater magnitude than prior to LIP emplacement to cause the excursion to more radiogenic Os values developed during the T-OAE. Evidence from the Karoo, however, indicates the lavas were emplaced very rapidly as a succession of single eruptive events each lasting less than a century, and with the total duration of the main eruptive phase perhaps as short as 250 kyr (Moulin *et al.*, 2017). Individual flows generally lack macroscopically distinct weathering products, one of the lines of evidence supporting their rapid outpouring, which precludes basalt weathering from being a major source of non-radiogenic Os to seawater during the T-OAE.

Previously, McArthur *et al.* (2008) have argued that the increase in $^{187}\text{Os}/^{188}\text{Os}_i$ in the Yorkshire succession was a local artefact caused by marine Os drawdown in a restricted local water mass sensitising the system to small changes in riverine input that drove large excursions in $^{187}\text{Os}/^{188}\text{Os}_i$. These, it was suggested, also compromised the Re–Os dating, generating the large errors associated with the Yorkshire ages (Cohen *et al.*, 1999, 2004). However, synchronous positive $^{187}\text{Os}/^{188}\text{Os}_i$ excursions on a global scale, including sites in western North America and Japan that show no evidence for water-mass restriction (Them *et al.*, 2017b; Kemp *et al.*, 2020) refute this argument.

The pattern and magnitude of $^{187}\text{Os}/^{188}\text{Os}_i$ changes in Japan and North America at the onset of the $\delta^{13}\text{C}_{\text{org}}$ negative excursion (chemostratigraphic Subunit IIIa of the Yorkshire stratigraphy) match closely, rising from 0.2 to 0.6 in both sections, before falling back to a plateau of ~ 0.4 in the post-T-OAE section. Matching patterns in sections on two sides of the Panthalassa Ocean (Fig. 1) strongly suggest that these variations reflect changes in the composition of global seawater Os at the onset of the T-OAE. However, the drawdown of redox-sensitive trace metals

accompanying the T-OAE, combined with a pulse of radiogenic Os driven by enhanced weathering, might adversely impact age modelling, particularly for the *C. exaratum* Zone.

The inverse relationship between $\delta^{13}\text{C}_{\text{org}}$ and $^{187}\text{Os}/^{188}\text{Os}_i$ at the onset of the T-OAE demonstrates that the flux of radiogenic osmium to the oceans increased synchronously with the decrease in carbon-isotope values, evidence of coupling between a massive release of isotopically light carbon and enhanced global continental crust weathering (Kemp *et al.*, 2020). However, the greater amplitude of the $^{187}\text{Os}/^{188}\text{Os}_i$ peak in Yorkshire compared to Canada and Japan may reflect the influence of regional weathering and basin restriction enhancing the global seawater signal. Deviations from open ocean $^{187}\text{Os}/^{188}\text{Os}_i$ values have been observed in marginal seas (Marquez *et al.*, 2017) and restricted ocean basins (Dickson *et al.*, 2022a) of various ages.

The $^{187}\text{Os}/^{188}\text{Os}_i$ excursion in Yorkshire was interpreted by Cohen *et al.* (2004) as resulting from a 400 – 800% increase in continental chemical weathering rates due to an accelerated hydrological cycle. Using data from western North America and numerical modelling Them *et al.* (2017b) calculated that weathering may have increased by 215% and potentially up to 530% during the T-OAE compared to the pre-event baseline. Kemp *et al.* (2020) compared $^{187}\text{Os}/^{188}\text{Os}_i$ and $\delta^{13}\text{C}_{\text{org}}$ data from Japan with the European and North American profiles and concluded that abrupt negative shifts in carbon isotopes in the Japan profile were coeval with rapid increases in weathering by >40% across each of these intervals. Overall, they concluded that global weathering rates may have increased up to 600% through the entire T-OAE.

Values derived from osmium isotope data are consistent with an independent estimate of a ~500% increase in global weathering rate during the T-OAE based on Ca isotopes ($\delta^{44}/^{40}\text{Ca}$) in brachiopods and bulk carbonate from Peniche (Brazier *et al.*, 2015). However, $\delta^{44}/^{40}\text{Ca}$ belemnite values from Peniche and Yorkshire (Q Li *et al.*, 2021), when corrected for temperature and normalized to a constant Mg/Ca ratio, indicate that no significant change in the Ca isotope composition of seawater accompanied the T-OAE, so the comparable weathering estimates may be fortuitous. Better constraints on the rates and magnitudes of change in the radiogenic (continental weathering) vs non-radiogenic (hydrothermal) Os fluxes are required to further reduce uncertainty.

16.c. Strontium isotopes

The strontium (Sr) isotope composition of seawater essentially represents a mixture of unradiogenic Sr from the hydrothermal alteration of mid-ocean ridge basalt ($^{87}\text{Sr}/^{86}\text{Sr} \cong 0.703$) and radiogenic Sr in rivers ($\cong 0.711$) from the weathering of ancient continental crust (McArthur *et al.*, 2020). Modern seawater has an $^{87}\text{Sr}/^{86}\text{Sr}$ value of 0.709174 ± 0.000002 . A record of ancient seawater $^{87}\text{Sr}/^{86}\text{Sr}$ ratios may be obtained from the analysis of biogenic calcite in marine fossils including belemnites, brachiopods and foraminifera.

$^{87}\text{Sr}/^{86}\text{Sr}$ ratio data obtained from Yorkshire coast belemnites (Jones *et al.*, 1994; McArthur *et al.*, 2000) underpin the construction of the upper Pliensbachian – lower Toarcian global Sr-isotope reference curve of McArthur *et al.* (2020). The stratigraphic profile (Fig. 19) shows falling values through the *A. margaritatus* Zone (Staites Sandstone and Cleveland Ironstone Penny Nab Member; Subunits Ia – b), the continuation of a long-term trend beginning in the early Sinemurian (~200 Ma). A step fall in $^{87}\text{Sr}/^{86}\text{Sr}$ ratios at the base of the *P. spinatum* Zone (Kettleness Member; Subunit Ic), together with possible steps in

$\delta^{18}\text{O}_{\text{bel}}$ and Mg/Ca_{bel} ratio (Fig. 19), support the presence of a large stratigraphic gap at the disconformity. The Sr-isotope trend through the *P. spinatum* Zone is less well defined but shows generally falling-upward values, with a reversal to gently rising values at the base of the PIToBE, towards the top of the zone. This pattern represents one of the most rapid reversals in $^{87}\text{Sr}/^{86}\text{Sr}$ of the Phanerozoic record (McArthur *et al.*, 2020, fig. 7.2).

A marked change to steeply rising $^{87}\text{Sr}/^{86}\text{Sr}$ ratios is observed through the *C. exaratum* Subzone (Jet Rock; Subunits IIIb – d) of the T-OAE interval (Fig. 19), prior to a return to more gently increasing values through the remainder of the Toarcian. The change at the base of the *C. exaratum* Subzone has been ascribed to an increase in the flux of radiogenic Sr from the chemical weathering of continental crust because it coincides with a marked excursion in the seawater osmium (Cohen & Coe, 2007; Section 16.b.4) and other weathering proxies. The increase in chemical weathering has been linked to an increase in average temperatures across the T-OAE (Fig. 19, Section 21.d.7) and an accelerated hydrological cycle (Cohen *et al.*, 2004; Them *et al.*, 2017b; Izumi *et al.*, 2018).

McArthur *et al.* (2000, 2016) have suggested that the increase in the Yorkshire profile (Fig. 19) is attributable to a decrease in the sedimentation rate driven by condensation and hiatuses in the *C. exaratum* Subzone (Subunits IIIb – d). Condensation at this level based on changes in the $^{87}\text{Sr}/^{86}\text{Sr}$ profile was also indicated by Jenkyns *et al.* (2002, fig. 13). Indeed, the sharp break in slope of the $^{87}\text{Sr}/^{86}\text{Sr}$ at the base of the *P. spinatum* Zone (Fig. 19) coincides with the disconformity at the base Pecten Seam in coastal sections (Section 8.a.2). However, as noted by Cohen *et al.* (2004), an *a priori* assumption that $^{87}\text{Sr}/^{86}\text{Sr}$ ratios ratio must always change linearly with time is hard to justify in view of the reversal of the seawater Sr-isotope curve in the latest Pliensbachian ~1 Ma earlier.

Nonetheless, the presence of prominent carbonate concretion horizons throughout the laminated black carbonaceous mudstones of the *C. exaratum* Subzone supports the presence of significant hiatuses (cf. Raiswell, 1987, 1988; Marshall & Pirrie, 2013) and an overall reduction in bulk sedimentation rates. The interval showing an increased slope in the Sr-isotope profile is bounded by the Cannon Ball Doggers at the bottom and the Millstones at the top of the subzone (Fig. 19).

17. Geochronology and cyclostratigraphy – age and duration of the T-OAE

The current international chronostratigraphic chart of the ICS (<https://stratigraphy.org/ICSchart/ChronostratChart2023-09.pdf>) retains the GTS2020 age of 184.2 ± 0.3 Ma for the base of the Toarcian Stage (Gradstein *et al.*, 2020). New radiometric dates (U–Pb zircon ages) from the T-OAE interval of the Neuquén Basin, Argentina (Al-Suwaidi *et al.*, 2022) have provided an age of $183.73 + 0.35/-0.50$ Ma for the Pliensbachian – Toarcian boundary, which is consistent with an astronomical age of 183.70 ± 0.50 Ma derived from the Mochras succession (Storm *et al.*, 2020).

An age of $182.77 + 0.11/-0.15$ Ma was calculated for the Tethyan *D. tenuicostatum* – *H. serpentinum* zonal boundary by Al-Suwaidi *et al.* (2022), but this was judged to be coincident with onset of the $\delta^{13}\text{C}$ fall at the base of the T-OAE. The onset of the $\delta^{13}\text{C}$ fall lies in the upper *D. tenuicostatum* Zone in Yorkshire (mid-*D. semicelatum* Subzone) and not at the base of the *H. serpentinum* Zone (Fig. 2). By comparison, a base *H. serpentinum* Zone age of 182.8 Ma was calculated by

Ruebsam *et al.* (2019) and 183.16 Ma was assigned by GTS2020 (Hesselbo *et al.*, 2020b). The correlation between South America and Europe requires additional constraints. Other U–Pb ages from Peru, USA and Canada lack sufficient stratigraphic control with respect to European ammonite zones for high-resolution correlation to Yorkshire or the Toarcian GSSP at Peniche (Al-Suwaidi *et al.*, 2022). Available radiometric dates are insufficient to rigorously assess changes in sedimentation rate within the Pliensbachian – Toarcian succession.

Cohen *et al.* (2007), following DB Kemp *et al.* (2005), offered an estimate of ~350 ka for the duration of the T-OAE as defined here in Yorkshire. Cyclostratigraphically inferred durations of the T-OAE, mainly derived from the Paris and Lusitanian basins, remain controversial, with two notably different estimates of 300 – 500 ka (e.g. Boulila *et al.*, 2014) and ~900 ka (Suan *et al.*, 2008b; Huang & Hesselbo, 2014). Differences relate principally to the allocation of obliquity (35 or 37.5 ka) vs short eccentricity (100 ka) as periodicities to the dominant cyclicity.

Spectral analysis of Yorkshire coast carbonate and $\delta^{13}\text{C}_{\text{org}}$ data by Kemp *et al.* (2011) clearly identified cyclicity within the upper *D. tenuicostatum* – lower *H. exaratum* subzones, and lower *H. falciferum* Subzone, but cycles were absent in the upper *C. exaratum* Subzone. Spectral analysis of high-resolution elemental time series from Yorkshire by Thibault *et al.* (2018) provided a continuous cycle record spanning the T-OAE (Fig. 7), including the complete *C. exaratum* Subzone, that enabled a cycle-to-cycle correlation between Yorkshire, Peniche and Sancerre. A suggested duration of either 560 ka (obliquity-based) or 1500 ka (short-eccentricity based) was assigned to the T-OAE.

Orbital tuning of uppermost Pliensbachian – lower Toarcian $\delta^{13}\text{C}$ and CaCO_3 time series, based on the short and long, stable 405 ka (g2–g5) eccentricity cycles, from the Talghemt section in Morocco provided a duration of ~400 – 500 ka for the T-OAE (Boulila *et al.*, 2019). This time interval is very close to that inferred by Boulila *et al.* (2014) from the Sancerre core in the Paris Basin (300 – 500 ka) and to a revised estimate from the Peniche section of ~472 ka (Boulila & Hinnov, 2017). By contrast, a cyclostratigraphic study of high-resolution CaCO_3 and TOC data from the Posidonia Shale of Dotternhausen (SW German Basin) tuned to the 100 ka and 405 ka eccentricity cycles, yielded ~1.2 Ma for the event (Ruebsam *et al.*, 2023) based on the recognition of 3 long-eccentricity cycles spanning the interval of the negative CIE.

A duration of ~1.2 Ma is consistent with the assignment of a 405 ka periodicity to the Zr/Rb and other geochemical detrital-proxy cycles observed through the T-OAE in Yorkshire (Figs 4, 7; Thibault *et al.*, 2018), as illustrated by Ruebsam *et al.* (2023, fig. 7). Incorporating our lower placement of the base of the T-OAE (Fig. 7, 174.5 – 164.1 m in the Dove's Nest core) compared to Ruebsam *et al.* (2023) yields ~1.4 Ma for Unit III and the full extent of the CIE in Yorkshire. Fendley *et al.* (2024), incorporating recent U–Pb dates, derived a duration of ~1 Ma for the negative CIE interval in their Mochras study. By comparison, McArthur *et al.* (2016) derived an estimated duration for the *C. exaratum* Subzone alone (i.e. the upper part of the T-OAE) of 1.1 – 2.4 Ma based on global rates of change in Sr isotopes.

Kemp *et al.* (2011) found no evidence for changing sedimentation rate before, during or after the T-OAE in Yorkshire, although a small hiatus at the large negative $\delta^{13}\text{C}_{\text{org}}$ step within 'bed' 34 has been proposed (Kemp *et al.*, 2011; Boulila & Hinnov, 2017; Boulila *et al.*, 2019; Ruebsam *et al.*, 2019). Nonetheless, the presence of prominent concretion horizons indicates that multiple levels of significant condensation and likely

hiatuses are present in the succession (cf. Raiswell, 1987, 1988; Marshall & Pirrie, 2013).

Significant differences exist between authors in the placement of boundaries for the T-OAE, the recognition and duration of cycles, the equivalence of biostratigraphic marker taxa and correlation of the lower Toarcian between Yorkshire, Mochras, Sancerre, Peniche and other sections (e.g. compare Boulila & Hinnov, 2017; Thibault *et al.*, 2018; Boulila *et al.*, 2019; Ruebsam *et al.*, 2023). The carbon isotope correlation (Fig. 3) reveals very large differences in absolute and relative thicknesses of biozones between sites in different basins. Further work is required to obtain higher resolution, stratigraphically longer, radiometrically dated time series for rigorous cyclostratigraphic analysis.

18. The Toarcian hyperthermal – temperature and salinity records

Carbonate oxygen-isotope ($\delta^{18}\text{O}_{\text{bel}}$) and Mg/Ca ratios obtained from belemnites ($\text{Mg}/\text{Ca}_{\text{bel}}$) collected from multiple Pliensbachian – Toarcian sections along the Yorkshire coast have been reported by Sælen *et al.* (1996), McArthur *et al.* (2000), Bailey *et al.* (2003) and Ullmann *et al.* (2014, 2015). Based on the Mg/Ca temperature dependency observed in modern biogenic calcites, an increase in $\text{Mg}/\text{Ca}_{\text{bel}}$ values from ~8 to 16 mmol/mol (Fig. 19), coincident with decreasing $\delta^{13}\text{C}_{\text{org}}$ values in the lower T-OAE interval (Subunits IIIa – b), was interpreted by Bailey *et al.* (2003) to indicate a warming of 6 – 7° C.

However, Ullmann *et al.*'s (2015) study of the chemical and isotopic architecture of a belemnite rostrum from the Grey Shale Member ('bed' 21, *D. tenuicostatum* Subzone) at Hawsker Bottoms, showed no correlation between $\delta^{18}\text{O}$ and Mg/Ca ratios in the rostrum, arguing against a significant temperature dependence in Mg/Ca ratios. Instead, the data were interpreted to indicate a strong dependency of Mg/Ca ratios on metabolic effects on element ratios within the (internal) mineralizing fluids, alongside growth rates and crystal orientation effects. Nonetheless, the strong coherence between stratigraphic trends of the $\text{Mg}/\text{Ca}_{\text{bel}}$ and $\delta^{18}\text{O}_{\text{bel}}$ palaeotemperature proxies (Fig. 19) remains compelling.

A concomitant $\delta^{18}\text{O}_{\text{carb}}$ negative shift of 3‰ at the onset of the T-OAE [from –0.5‰ to –3.5‰; Fig. 19], if caused by temperature alone, would imply an increase of 13° C, but was interpreted to be the product of 6 – 7° C warming accompanied by a small salinity decrease of ~2.5 psu by Bailey *et al.* (2003). Additionally, Ullmann *et al.* (2014) proposed that a change in belemnite life habits from cool bottom-water to warm surface-water dwelling taxa accompanied the development of anoxic bottom waters, leading to an overestimation of the true increase in average water temperature. More generally, $\delta^{18}\text{O}_{\text{bel}}$ (and arguably $\text{Mg}/\text{Ca}_{\text{bel}}$) values from the upper Pliensbachian indicate the presence of cooler and relatively more saline waters, with a cooling trend prior to early Toarcian warming and hyperthermal conditions accompanying the T-OAE (Fig. 19).

A salinity decrease of ~5 psu for surface waters in the Cleveland Basin during the T-OAE was calculated by Sælen *et al.* (1996) based on salinity modelling of their Yorkshire $\delta^{13}\text{C}_{\text{bel}}$ and $\delta^{18}\text{O}_{\text{bel}}$ data. Dera & Donnadiou (2012) used a fully coupled ocean–atmosphere model (FOAM) to study the palaeoclimatic and palaeoceanographic consequences of increases in atmospheric $p\text{CO}_2$ levels at a multiscale resolution. They interpreted a regional reduction in salinity (~1 – 5 psu) across NW European basins during early Toarcian warming due to an input of brackish water from the

Arctic Ocean through the Viking Corridor. Modelling by Ruvalcaba Baroni *et al.* (2018) indicated a near mean-ocean salinity of ~35 psu in southern European epicontinental basins, falling to ~33 psu in more northerly areas like the Cleveland Basin.

Extreme brackish (10–25 psu) waters during the T-OAE in the Cleveland Basin, with freshwater conditions during late *C. exaratum* Subzone time (top Subunit IIIb and IIIc), were proposed by Remírez & Algeo (2020) based principally on the use of a Ba/Ga proxy. However, as noted by Hesselbo *et al.* (2020a), the presence of belemnites throughout the study interval (Doyle, 1990; Caswell & Coe, 2014, fig. 2; Ullmann *et al.*, 2014, fig. 2), particularly during the supposed ‘freshwater’ interval and their incorporated geochemical data (Fig. 19), together with abundant ammonites (Howarth, 1962) and pseudoplanktonic crinoids, contradict such low salinity conditions. They are also arguably inconsistent with organic biomarker data (Section 15.b).

Belemnite O-isotope and Mg/Ca records from the Pliensbachian–Toarcian of Mochras (Fig. 1a) follow the same trends but show lower isotopic variability than in the Cleveland Basin (Ullmann *et al.*, 2022), but data are lacking for the T-OAE interval. $\delta^{18}\text{O}_{\text{bel}}$ and Mg/Ca_{bel} values from the Junction Bed in Dorset indicate significant warming during the Toarcian hyperthermal (Jenkyns & Macfarlane, 2021). $\delta^{18}\text{O}$ data from marine calcite fossils from a range of other European basins show a consistent shift to very light values accompanying the T-OAE (e.g. Jenkyns *et al.*, 2002; Dera *et al.*, 2011; Korte *et al.*, 2015, fig. 2). Significantly, $\delta^{18}\text{O}_{\text{bel}}$ and Mg/Ca_{bel} data from open basin settings in central and northern Spain with no evidence of salinity changes, indicate a 5–8°C temperature rise in the western Tethys during the T-OAE (Rosales *et al.*, 2004; Gómez *et al.*, 2008; Comas-Rengifo *et al.*, 2010).

Oxygen isotope data from calcite shells of benthic fauna (rhychonellid brachiopods and *Gryphaea* bivalves) from Spain and Portugal suggest that bottom-water temperatures were elevated by ~3.5°C through the entire T-OAE (Ullmann *et al.*, 2020) compared to the underlying Toarcian. Based on results from Peniche (Fig. 1a), temperatures increased by ~7°C between the latest Pliensbachian to the T-OAE maximum with a brief episode of temporary cooling of 4–5°C accompanying the PIToBE (Suan *et al.*, 2008a).

Marine fossil-based $\delta^{18}\text{O}$ water temperature estimates from Europe are consistent with global carbon-isotope mass-balance modelling that indicates a 3–5°C increase in global land surface temperature during the T-OAE (Beerling *et al.*, 2002). Cooling followed by rapid global warming of ~6.5°C during the T-OAE has also been inferred from stomatal index analysis of fossil leaves from Bornholm, Denmark (McElwain *et al.*, 2005). The early Toarcian hyperthermal event appears synchronous throughout Europe within the limitations of sampling, when calibrated against $\delta^{13}\text{C}$ profiles.

The TEX₈₆ proxy, derived from fossilized archaeal lipids, was employed by Ruebsam *et al.* (2020c) to reconstruct absolute sea surface temperatures (SSTs) for the NW Tethys Shelf during the late Pliensbachian to early Toarcian based on the concatenation of data from Spain (southern Iberian margin) and Italy (Umbria-Marche Basin). The overall trend of the molecular palaeothermometry data covaries with $\delta^{18}\text{O}$ signatures derived from brachiopods and belemnites, evidencing coupled warming of surface and bottom waters. Reconstructed late Pliensbachian to early Toarcian SSTs of 22°–32°C in NW Tethys are comparable to current tropical SSTs (Locarnini *et al.*, 2019). A long-term rise of ~10°C was documented through the earliest Toarcian, with

maximum SSTs attained during the T-OAE, but with the time series incorporating transient temperature excursions of >5°C magnitude with lapse rates of ~0.1°C/kyr. These transient events were interpreted as evidencing the existence of a labile cryosphere driving rapid climate fluctuations and providing a reservoir that facilitated pronounced $\delta^{13}\text{C}$ excursions (Ruebsam *et al.*, 2019, 2020c).

19. The fossil record – biotic response to the T-OAE

The Pliensbachian–Toarcian boundary succession in the Cleveland Basin records a major extinction event that is observable throughout Western Europe at species and genus levels affecting benthic foraminifera, ostracods, bivalves, rhychonellid brachiopods and corals, and marks a turnover in ammonites and belemnites (Hesselbo *et al.*, 2020b; Vasseur *et al.*, 2021). The multi-phase extinctions in the earliest Toarcian are a global event that extended across the Boreal, Tethyan and Panthalassa oceans (Caruthers *et al.*, 2013); this is an expression of the second-order ‘Pliensbachian’ global extinction event recognized by Raup & Sepkoski (1984; Bambach, 2006).

The base of the Toarcian in Yorkshire is marked by the extinction of Boreal amaltheid family ammonites and a surge of dactylioceratids and hildoceratids of Tethyan derivation (e.g. Dera *et al.*, 2010). The base-Toarcian extinction was followed by a second pronounced extinction among benthic invertebrates, particularly bivalves and brachiopods, that coincides with the onset of the T-OAE and black shale deposition in northern Europe but is not restricted to anoxic facies (Wignall & Bond, 2008). Among the bivalves, 84% of species became extinct in Europe with the onset of black shale deposition, which represents by far the most important extinction event of the whole Jurassic (Hallam, 1986). Comparable extinctions of bivalves occurred during the early Toarcian in the Andean basins of South America (Aberhan & Baumiller, 2003).

19.a. Macrofauna and trace fossils

The Yorkshire coastal succession provides one of the most detailed published palaeontological records of the upper Pliensbachian–middle Toarcian. Howarth (1955, 1962, 1973, 1992) published comprehensive ammonite and associated faunal records based on bed-by-bed collecting of the coastal sections. Further macrofossil records and a species-level range chart for the Cleveland Basin were produced by Little (1995) and presented by Little (1996), Little & Benton (1995), Harries & Little (1999) and, in part, by Wignall *et al.* (2005). Additional records and a revised range chart were published by Caswell *et al.* (2009), with further collection reported by Danise *et al.* (2013) and Atkinson *et al.* (2023). The trace-fossil record has been described by Morris (1979), Martin (2004), Caswell & Frid (2017), Caswell & Dawn (2019) and Caswell & Herringshaw (2023). The last of these studies included data from the Dove’s Nest core.

The upper Pliensbachian of the Cleveland Basin (Unit I–Staithe Sandstone and Cleveland Ironstone formations) yields rich trace-fossil and high-diversity benthic body-fossil assemblages, with most species being evenly represented and including a wide range of ecological groups that occupy all levels of benthic tiering (Little, 1995; Caswell *et al.*, 2009; Danise *et al.*, 2013; Caswell & Frid, 2017; Atkinson *et al.*, 2023; Caswell & Herringshaw, 2023), indicative of well-oxygenated conditions.

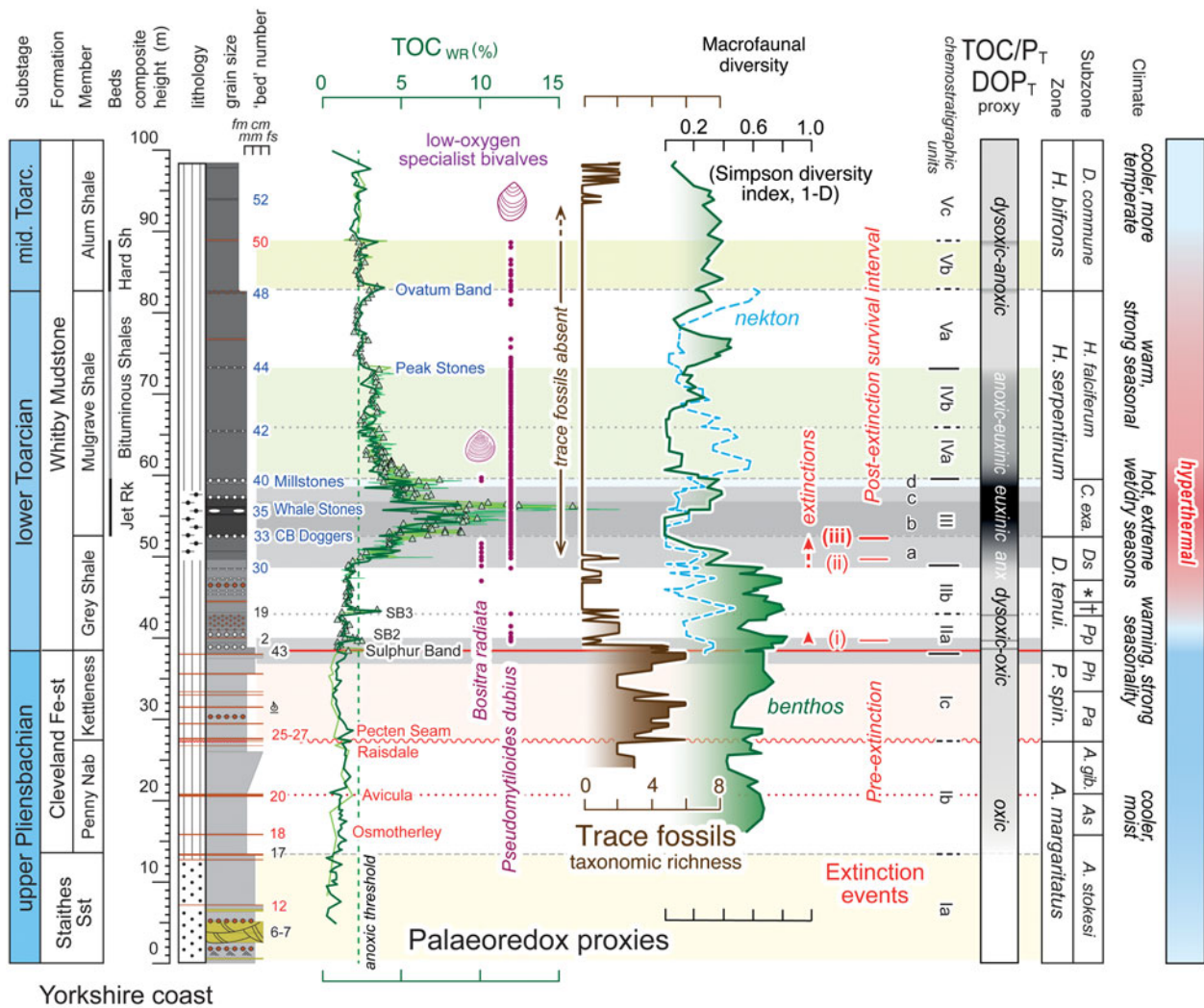


Figure 22. TOC, biotic trends, extinction levels and palaeoredox change through the upper Pliensbachian – middle Toarcian of the Cleveland Basin, Yorkshire coast stratigraphy as in Figure 2. Rescaled whole-rock TOC profile for Dove’s Nest (Trabucho-Alexandre et al., 2022, dark green) with coast composite data of Kemp et al. (2011; thin yellow-green high-resolution curve) and trend of the low-resolution coast datasets of Ruvalcaba Baroni et al. (2018) and McArthur (2019) (thin pale green low-resolution curve; see Fig. 2). Ranges of low-oxygen specialist bivalve taxa compiled from Little (1995) and Caswell et al. (2009). Trace-fossil taxonomic richness from Caswell & Frid (2017), Caswell & Dawn (2019) and Caswell & Herringshaw (2023). Macrofaunal diversity after Danise et al. (2013, 2015). Profiles rescaled to reference stratigraphy (Fig. 2) using subzone and marker bed datum levels. Extinction levels (i) – (iii) from Caswell et al. (2009). The boundary between pre-extinction and post-extinction survival intervals of Atkinson et al. (2023) lies at the base of the *C. exaratum* Subzone (level iii). The top of the ‘survival interval’, the base of recovery phase 1, occurs in the lower *H. bifrons* Zone above the top of our study interval. Geochemical palaeoredox interpretations from this study (see text). Climate interpretation incorporates palynological interpretation of Slater et al. (2019) with oxygen isotope and Mg/Ca trends from belemnites (Fig. 21).

The extinction of Amaltheidae family ammonites marking the base of the Toarcian occurs at Sulphur Band 1 (Little et al., 2010), a short distance above the base of the Whitby Mudstone Formation (Sections 7.b, 8.b). This is followed by a sharp drop in the taxonomic richness of trace fossils (Fig. 22; Caswell & Frid, 2017; Caswell & Herringshaw, 2023) but with no clear decline in benthic macrofossil diversity (Danise et al., 2013; Caswell & Frid, 2017; Atkinson et al., 2023). A first extinction horizon (level i, Fig. 22; extinction level (i) – (iii) from Harries & Little, 1999; ii of Caswell & Herringshaw, 2023), which is followed by an influx of the low-oxygen specialist bivalve *Pseudomytiloides dubius* (Sowerby), was placed at the base of Sulphur Band 2 (Hawsker Bottoms ‘bed’ 2) by Caswell et al. (2009).

The lower Toarcian Grey Shale (Subunit IIa) initially yields a sparse normal marine benthic and nektonic fauna reflecting continuing sedimentation in a relatively well-oxygenated

environment but with increasingly dysoxic, intermittently anoxic (Sulphur Bands 1 – 3) seafloor conditions indicated by reduced species richness and the changing characteristics of trace-fossil assemblages. An interval of greater oxygen depletion is evidenced in the lower part of Subunit IIb, following step increases in TOC and P_{EF} , by an interval barren of trace fossils and characterized by low body-fossil diversity (Fig. 22; see also Caswell & Herringshaw, 2023). Geochemical redox proxies (e.g. Figs 15, 16) generally fail to capture evidence of this event. Trace-fossil and benthic diversity temporarily recover towards the top of Subunit IIb. Disappearances of typical upper Pliensbachian benthic macrofossil taxa then occur progressively, beginning towards the top of the Grey Shale within T-OAE Subunit IIIa through ‘beds’ 31 – 32 (Caswell et al., 2009, fig. 2).

The onset of a major phase of extinction is placed at the base of the consistently laminated black carbonaceous mudstones (black

shale facies) in mid-‘bed’ 31 (level ii of Caswell *et al.*, 2009), with the main extinction horizon (level iii) occurring around 2 m higher, coincident with the first large step-fall in the $\delta^{13}\text{C}_{\text{org}}$ profile (upper ‘bed’ 32, A in Fig. 18; DB Kemp *et al.*, 2005). Trace fossils disappear at level ii and, with the sole exception of a record of pyritized *Trichichnus* in ‘bed’ 48 at Saltwick Bay, remain unrecorded from all Yorkshire sections until the reappearance of an impoverished assemblage in the middle Toarcian Main Alum Shale Beds (Subunit Vc), towards the base of ‘bed’ 51 (Caswell & Herringshaw, 2023). This stratigraphically extended absence of macroscopic trace fossils indicates a longer period of continuous deoxygenation than elsewhere in NW Tethys and the adjacent European shelf basins.

A steady decline in macrofaunal diversity is observed between datum levels ii and iii (Fig. 22; Danise *et al.*, 2013). The bivalve *Bositra radiata* (Goldfuss) dominates the benthic fauna of the extinction interval, with shell size doubling as $\delta^{13}\text{C}_{\text{org}}$ decreases within Subunit IIIa. *Pseudomytiloides dubius* is also common at some levels. *Pseudomytiloides dubius* and *B. radiata* occur as parautochthonous – autochthonous assemblages, respectively, forming 1 – 2-shell-thick monospecific shell pavements (Little, 1995; Caswell *et al.*, 2009; Caswell & Coe, 2013). The two low-oxygen specialist taxa rarely co-occur.

Pseudomytiloides dubius is the only abundant and consistently occurring benthic macrofossil in the laminated black shales of Subunits IIIb – Va inclusive (*C. exaratum* – *H. falciferum* subzones), evidencing the development of strongly oxygen-depleted bottom waters and anoxic – euxinic sediments within the lower part of the ‘survival interval’, following the extinctions (Fig. 22). Sporadic occurrences of the scallop *Meleagrinnella substriata* (Munster) is the only other taxon to occur consistently through the Jet Rock (Caswell *et al.*, 2009).

Bositra radiata temporarily reappears in T-OAE Subunit IIId immediately following the reappearance of *Oxytoma inequivalve* (J. Sowerby) along with the lowest occurrences and temporary appearances of new bivalve species and inarticulate brachiopods towards the top of Subunit IIIc (Caswell *et al.*, 2009). These define a short interval of increased benthic diversity (Fig. 22) in the upper *C. exaratum* Subzone at the termination of the T-OAE. The temporary influx of a more diverse faunal assemblage coincides with a shift to intermittent dysoxic bottom waters based on the TOC/P_T and DOP_T proxies (Fig. 15) and decreasing basin restriction based on Re and Mo isotopes (Fig. 20).

Remarkably, records of *P. dubius* almost perfectly track the TOC curve, only occurring where values exceed the 2.5% anoxic threshold (Fig. 22). The species is largely absent from the upper Bituminous Shales Subunit Va but reappears in association with the higher-TOC beds that characterize the Hard Shales Subunit Vb, before disappearing again above. Benthic diversity increases significantly in the lower part of Subunit Va and generally remains high in Subunits Vb – c, above. Increases in benthic diversity and the re-establishment of a Toarcian infauna after the T-OAE were gradual. Diversity does not return to the level observed in the pre-T-OAE section until the upper Toarcian *Phlyseogrammoceras dispansum* Zone (Atkinson *et al.*, 2023). The absence and then low abundance and taxonomic richness of trace fossils in the *D. commune* Subzone suggest that dissolved oxygen remained below 0.5 mL L^{-1} into the middle Toarcian (Caswell & Dawn, 2019; Caswell & Herringshaw, 2023), consistent with evidence of persisting dysoxia provided by the TOC/P_T and DOP_T redox proxies (Fig. 14).

Ammonites and belemnites occur throughout the upper Pliensbachian – middle Toarcian succession in Yorkshire, including the T-OAE interval. A ‘belemnite gap’ was proposed in T-OAE Subunits IIIa – IIIb from mid-‘bed’ 32 to lower ‘bed’ 34 in Yorkshire coastal sections by Xu *et al.* (2018) based on literature data. However, McArthur *et al.* (2000) recorded belemnites from every ‘bed’ in T-OAE Unit III except ‘beds’ 33 (Cannon Ball Doggers) and 40 (Millstones). The ‘belemnite gap’ in the Cleveland Basin coincides with a turnover in belemnite taxa characterized by the disappearance of *Passaloteuthis* and the appearance of *Acrocoelites* in the Cleveland Basin (Ullmann *et al.*, 2014), attributed as a response to the progressive expansion and shoaling of euxinic bottom waters during the initiation of the T-OAE. Remarkably, *Acrocoelites* are relatively common in the upper beds of the T-OAE interval (mid- to upper *C. exaratum* Subzone, e.g. Ullman *et al.*, 2014, fig. 2) despite evidence of increasing episodes of PZE (Section 15b). It has been inferred that this turnover represents belemnites adapting to environmental change by shifting their habitat from cold bottom waters to warm surface waters in response to expanded seafloor anoxia.

Stratigraphically more extended ‘belemnite gaps’ but continuous ammonite records have been documented in the lower Toarcian at Mochras and Peniche, which were attributed to unfavourable redox conditions in the deeper water column (Hesselbo *et al.*, 2007; Xu *et al.*, 2018, fig. 4), reflecting the nektobenthic lifestyle of the former taxon (Hoffmann & Stevens, 2020). However, neither of these sections show palaeontological or geochemical evidence of extended anoxic – euxinic bottom-water conditions during the T-OAE. Bioturbation and low-diversity benthonic macrofauna are present throughout the sections, sediment TOC contents generally remain significantly below the 2.5% anoxic threshold and redox-sensitive trace metals show no enrichment (e.g. Fantasia *et al.*, 2019). Rare thin laminated beds with biomarkers that suggest transient PZE and episodic anoxia at the seafloor occurred (Xu *et al.*, 2018), like those associated with the lower Toarcian Sulphur Bands of Yorkshire, but the evidence supports predominantly oxic – dysoxic bottom-water conditions throughout the T-OAE. It is unlikely, therefore, that water column oxygenation provided the main control on belemnite occurrences at Mochras and Peniche, given that belemnites remain present in association with bottom-water euxinia in the Cleveland Basin.

Water temperature and salinity may have played a role. Belemnites are considered to favour temperatures of $10 - 30^\circ \text{C}$ and salinities of $27 - 37 \text{ psu}$ (Hoffmann & Stevens, 2020), and have been postulated to have migrated into warm surface waters during the T-OAE in response to deep water anoxia (Ullmann *et al.*, 2014). Ruebsam *et al.* (2020) reported tropical SSTs of 32°C on the NW Tethyan shelf during peak hyperthermal conditions at the height of the T-OAE, with southern areas dominated by a warm equatorial Tethyan current. More northerly areas were influenced by cool lower salinity Boreal arctic surface waters (Section 18).

If water temperatures, and perhaps salinity, in southern areas, exceeded the tolerance of belemnites, they would have been temporarily excluded until temperatures declined following the climate optimum. It is notable that brachiopods are also temporarily absent from the T-OAE interval of many Tethyan sites, despite evidence for the continual presence of oxygenated bottom waters (García Joral *et al.*, 2011; Danise *et al.*, 2019; Ullmann *et al.*, 2020). The northerly location of the Cleveland Basin would have seen a greater influence of cool currents flowing through the Viking Corridor (Fig. 1), enabling belemnites to

maintain their presence in the area's surface waters throughout the early Toarcian hyperthermal, while being excluded from the anoxic – euxinic bottom waters that developed during the T-OAE.

It is significant that a marked increase in nekton diversity occurs immediately above the T-OAE interval in Yorkshire (Fig. 22, Unit IVa) with an influx of ammonites indicative of a better oxygenated upper water column and/or improved connection with open ocean water masses.

19.b. Plankton records

19.b.1. Calcareous nannofossils

In stark contrast to the macrofauna, the late Pliensbachian – early Toarcian, including the T-OAE, was not marked by a major extinction event in phytoplankton but was, nonetheless, a significant time for calcareous nannofossil evolution. Major speciation took place and some of the most common Jurassic and Cretaceous genera (*Biscutum*, *Lotharingius*, *Discorhabdus*, *Watznaueria*) appeared and rapidly evolved (Bown *et al.*, 2004).

Increased biological productivity with increased calcareous nannofossil speciation, preceding the T-OAE, have been documented in north Tethyan and north European successions in the upper Pliensbachian – basal Toarcian (e.g. Erba, 2004; Erba *et al.*, 2019; Menini *et al.*, 2021). A decrease in the abundance of *Schizosphaerella* and *Mitrolithus jansae* (Wiegand) together with a fall in the size of *Schizosphaerella* occurs around the Pliensbachian – Toarcian boundary in Portugal, Spain, France and Italy (Suan *et al.*, 2008a, 2010; Reolid *et al.*, 2014; Clémence *et al.*, 2015; Peti & Thibault, 2017; Erba *et al.*, 2019; Fraguas *et al.*, 2021; Visentin & Erba, 2021; Faucher *et al.*, 2022). A more pronounced decline in *Schizosphaerella* size accompanies the onset of the T-OAE, the 'Schizosphaerella crisis' (Visentin & Erba, 2021; Faucher *et al.*, 2022), with a small size persisting up towards the top of the T-OAE interval and highest occurrence of *M. jansae*. These changes have variously been attributed to global warming, ocean fertilization and possibly acidification leading to a dominance of opportunistic taxa.

A decline in calcareous nannofossil abundance and a sharp size decrease of *Schizosphaerella* spp. have been observed at the onset of the T-OAE CIE in the Mochras borehole of the Cardigan Bay Basin (Menini *et al.*, 2021), with a size peak in the recovery phase of the CIE. Samples of T-OAE interval mudstones from the Brown Moor borehole in the southern Cleveland Basin studied by Bucefalo Palliani *et al.* (2002) were recorded as being barren of calcareous nannofossils from the high-TOC interval of the upper *D. semicelatum* – lower *C. exaratum* subzones. Calcareous nannofossils reappeared and increased in absolute abundance and species richness with falling TOC values through the top *C. exaratum* and *H. falciferum* subzones. Rare occurrences of *Schizosphaerella* were recorded in these upper beds.

Abundant coccoliths were reported in the laminated limestone of the Top Jet Dogger 'bed' 39 from the Yorkshire coast by Sælen *et al.* (1996), who noted low abundances in the adjacent beds. The presence of coccolith-rich pellets in the Jet Rock was illustrated by Macquaker *et al.* (2010). However, more generally, samples taken through the upper Pliensbachian – middle Toarcian of the coastal succession have been reported to be barren or yield very rare to rare coccolith body fossils (e.g. Slater *et al.*, 2022).

New work has demonstrated that although Toarcian black shale facies generally yield few calcareous nannofossils, or are barren, this is a preservation artefact. 'Ghost' nannofossils, including *Schizosphaerella*, preserved as external moulds in amorphous organic matter are abundant throughout the lower Toarcian of the

Yorkshire coast and Japan (Slater *et al.*, 2022). Near monospecific assemblages of nannofossil moulds or prasinophytes (principally sphaeromorphs, cf. Slater *et al.*, 2019) during the T-OAE in Yorkshire likely represent persistent algal blooms. The absence of carbonate is a product of early diagenetic dissolution by acidic pore waters or, for coastal exposures, weathering (cf. Littke *et al.*, 1991; Brantley *et al.*, 2013). Future study of calcareous nannofossils in the Dove's Nest core would enable the impact of weathering to be assessed.

At a community level, the 'ghost' records show that contrary to the conclusions of a previous study in the Cleveland Basin (Bucefalo Palliani *et al.*, 2002), calcareous nannoplankton flourished throughout the T-OAE with increased speciation rates and no evidence of increased extinctions. This challenges the view that ocean acidification (e.g. Hönisch *et al.*, 2012; Erba *et al.*, 2019) played a dominant role in driving the biotic changes associated with the T-OAE. Boron-isotope ($\delta^{11}\text{B}$) results from Peniche reported as showing declining ocean pH in the early Toarcian (Müller *et al.*, 2020) is not supported by Ca and Sr isotope data (Q Li *et al.*, 2021).

19.b.2. Organic-walled phytoplankton

The palynology of the upper Pliensbachian – middle Toarcian of the Yorkshire coast was described by Slater *et al.* (2019). Abundances of organic-walled dinoflagellate cysts (dinocysts) and spiny acritarchs decrease significantly at the base of the Toarcian, then decline markedly at the base of the T-OAE interval. Here, they are replaced by a substantial increase in sphaeromorphs, interpreted as the prasinophyte algae *Halosphaeropsis liassica*, a marker taxon for the T-OAE. These co-occur with abundant amorphous organic matter considered to represent euxinic marine conditions. The prasinophyte *Tasmanites* also increases in abundance at the base of the T-OAE section. Similar trends were documented in the Brown Moor borehole by Bucefalo Palliani *et al.* (2002). Short-term increases in sphaeromorphs with large spikes and amorphous organic matter content occur also in the Sulphur Bands (Slater *et al.*, 2019).

The algal dominance and associated low abundance of dinocysts continue upwards through the lower Bituminous Shales (Unit IV), decline at the top of the Bituminous Shales (Subunit Va) and increase again in the Hard Shales (Subunit Vb) before declining above. Dinocysts only return to pre-event abundances in the main Alum Shale beds (Subunit Vc) demonstrating the persistence of algal-dominated marine plankton in the Cleveland Basin from the onset of the T-OAE in the *D. semicelatum* Subzone to the *D. commune* Subzone of early middle Toarcian.

A marine phytoplankton community structure dominated by eukaryotic algae within the interval of the $\delta^{13}\text{C}_{\text{org}}$ minimum (our Subunit IIIb) in the Paris Basin is evidenced by biomarker data (Section 15.b.; Ruebsam *et al.*, 2022). Here, a proliferous of green algae and a decline in red algae groups accompanied five surface-water freshening events during the T-OAE. These were interpreted to represent recurrent warming phases, paced by changes in the short eccentricity (100 kyr) orbital cycle, that initiated higher precipitation and increased surface run-off (Ruebsam *et al.*, 2022).

19.b.3. Geochemical and biotic interaction

Redox-sensitive trace metals, including Mo, V and Cu, are important micronutrients that are necessary for several metabolic processes, including photosynthesis. Metals modulate the growth of organisms and their cycling of major nutrients, including C and

N (Morel & Price, 2003). Trace metal availability can significantly influence ecosystem structure: a healthy and fully functioning phytoplankton-driven ecosystem is directly controlled by nutrient availability in the oxygenated upper ocean.

The drawdown of trace metals, especially Mo, during the T-OAE would potentially impact the basal ecology of the oceans (Owens *et al.*, 2016; Dickson *et al.*, 2017; Them *et al.*, 2022). A larger impact on eukaryotes would be expected due to their higher trace metal metabolic requirements (Liu *et al.*, 2021). It is notable that organic geochemical studies of the T-OAE intervals on the NE western Tethyan shelf (Hungary; Ruebsam *et al.*, 2018) and in eastern Tethys (Tibet; Liu *et al.*, 2021) indicate a transition to bacterial-dominated microbial ecosystems coincident with the change to low-diversity macrofaunal assemblages.

The interval of rising $\epsilon^{205}\text{Tl}$ in western Canada and the SW German Basin during the early Toarcian with peak values at the onset of the T-OAE (Them *et al.*, 2018), considered to represent a minimum in global oxic seafloor area, corresponds to the interval of trace-fossil decline and macrofossil stepped extinctions recorded in the Cleveland Basin and elsewhere (Fig. 22). The extinctions may potentially, therefore, be related to the global spread of anoxic bottom waters and more general oxygen depletion of the oceans. The slow biotic recovery that followed in the middle Toarcian, which did not accelerate until the late Toarcian (Atkinson *et al.*, 2023), might have been a product of persisting poor ocean oxygenation, as indicated by continuing high $\epsilon^{205}\text{Tl}$ values.

20. T-OAE – a Jurassic global anoxic event?

The concept of an oceanic anoxic event was introduced by Schlanger & Jenkyns (1976) to describe the global development of Cretaceous organic-rich pelagic sediments formed in a variety of palaeobathymetric settings, including oceanic plateaus and basins sampled by ocean drilling, continental margins and shelf seas. This was attributed to a coincidence of high sea level and warm climate that favoured the formation of an expanded oxygen-minimum layer and where this intersected the sediment-water interface, the deposition of organic carbon-rich deposits. It was recognized that although an OAE was global in nature, organic-rich sediments would show a widespread but irregular distribution.

Despite organic carbon being a key sedimentary signature of an OAE, even the most intense Cretaceous event, OAE2 at the Cenomanian – Turonian boundary, the best documented and perhaps the most widespread marine organic carbon burial event in Earth history (e.g. Reershemius & Planavsky, 2021), is not represented by organic enrichment in all sedimentary settings (Jenkyns, 1980; Trabucho-Alexandre *et al.*, 2010; Owens *et al.*, 2018, fig. 2; Zhai *et al.*, 2023). The associated positive carbon-isotope excursion (cf. Scholle & Arthur, 1980; Schlanger *et al.*, 1987), however, provides a reliable stratigraphic marker observable in all carbon phases (e.g. Jenkyns, 2010).

In contrast to Cretaceous OAEs, the general absence of Lower Jurassic oceanic crust and pelagic sediments prevents a physical assessment of the global extent of anoxic waters and black shale deposition associated with the T-OAE in the deep sea. Marine records are mostly limited to shallow epicontinental seas, shelves and marginal basins. Extensive black shale deposits are a defining feature of most north European Boreal lower Toarcian sections but the majority of southern European Tethyan sites are organic lean (e.g. Ramirez & Algeo, 2020a, fig. 3; Kemp *et al.*, 2022b, fig. 2). Based on the lack of evidence for globally extensive anoxia in the early Toarcian and evidence of hydrographic control on anoxia in

northern Europe, McArthur (2019) proposed abandoning the term ‘OAE’ for the Toarcian event.

Most sites globally show an increase in TOC with the T-OAE, defined by the interval of the negative CIE, relative to pre-event lower Toarcian values (Kemp *et al.*, 2022b), even on shallow-water carbonate platforms (e.g. Ettinger *et al.*, 2021). TOC enrichment is best displayed in sections dominated by marine rather than terrestrial organic matter. Furthermore, although stratigraphic control is commonly poor, there is evidence for lower Toarcian organic-rich facies in many areas outside Europe – North Africa, including western and Arctic Canada, Arctic Siberia, Madagascar and Australia (Jenkyns, 1988; Nikitenko & Mickey, 2004; Them *et al.*, 2017a, 2018, 2022).

Deep-water black shales and cherts attributed to the T-OAE are recorded from Panthalassa Ocean sites including Japan and Kamchatka Russia (Gröcke *et al.*, 2011; Ikeda & Hori, 2014; Ikeda *et al.*, 2018; Filatova *et al.*, 2022; Kemp *et al.*, 2022a) although, again, not all Panthalassa sites display anoxia (e.g. Kemp & Izumi, 2014; Fantasia *et al.*, 2018a). Furthermore, deep-water black shales deposited during Cretaceous OAEs have been shown to be redeposited shallow-water deposits (Dean *et al.*, 1984; Trabucho-Alexandre *et al.*, 2011). Nonetheless, there is strong evidence that the T-OAE was globally distributed and widely associated with enhanced organic matter deposition.

Geochemical proxies offer unique insights into global-scale processes and their impact during the T-OAE. In oxic environments, organic-lean sediments (TOC <1%) show a positive correlation between TOC and burial rate (e.g. Kemp *et al.*, 2022b and references therein). This relationship is lost in dysoxic – anoxic settings where oxygen depletion promotes enhanced preservation of organic matter on the seafloor and during early burial, producing higher sediment TOC contents (1 – 2.5%). However, the very high TOC contents (>5%) observed for sediments deposited in the basins of NW Europe and elsewhere during the early Toarcian can be attributed principally to low sedimentation rates (Kemp *et al.*, 2022b) caused by reduced siliciclastic and biogenic (carbonate and silica) sediment fluxes rather than solely bottom-water anoxia – euxinia.

Based on a review of global TOC data for the lower Toarcian, Kemp *et al.* (2022b) offered a conservative estimate that the amount of extra marine organic carbon buried in shallow seas during the T-OAE relative to the preceding early Toarcian was ~9000 Gt. Surprisingly, calculated rates of organic carbon burial during the T-OAE are low relative to shallow-water settings at the present day. Kemp *et al.* (2022b) used a duration of 900 ka for the T-OAE interval compared with ~450 ka estimated by others (Section 17) but the shorter duration does not affect the conclusions. The modern global median continental shelf organic carbon burial rate of 19.6 g C m⁻² a⁻¹ (Wilkinson *et al.*, 2018) is more than an order of magnitude higher than the calculated mean T-OAE rates (0.6 – 1.6 g C m⁻² a⁻¹) and the average of 0.89 g C m⁻² a⁻¹ derived for northern Europe (Kemp *et al.*, 2022b).

Documented TOC increases are generally highest where deoxygenation was most severe: carbon burial rates in anoxic – euxinic basins may have increased ~500% on average during the T-OAE, potentially sequestering an extra ~800 Gt relative to the same time interval immediately preceding the event (Kemp *et al.*, 2022b). Nonetheless, less than 10% of the excess organic carbon in shallow-marine settings was buried in the anoxic – euxinic basins of northern Europe.

Deep open-ocean carbon burial fluxes are very poorly constrained, and it can be speculated that the deep ocean may

have accounted for a significant fraction of the total amount of carbon buried during the T-OAE. Similar issues arise when considering the carbon burial budget during OAE2 where a small but significant increase in deep ocean OC burial offers one potential explanation for the ‘missing’ carbon (Owens *et al.*, 2018). It is worth noting that Ikeda *et al.* (2018) reported TOC contents of $\geq 30\%$ in lower Toarcian black bedded cherts from Inuyama, Japan, considered to represent a deep-sea central Panthalassa Ocean setting during the T-OAE.

Molybdenum and TOC data from a deep-water Panthalassa chert succession in Japan evidence a globally significant drawdown of seawater Mo accompanying the T-OAE (Section 13.a; Kemp *et al.*, 2022a), consistent with and Mo- and Tl-isotope data that demonstrate a substantially increased global extent of anoxia (Sections 16.b.1, 16.b.2; Dickson, 2017; Dickson *et al.*, 2017; Them *et al.*, 2018). A global increase in pyrite burial under oxygen-depleted conditions is also indicated by sulfur isotopes (Section 16.a.2; Gill *et al.*, 2011; Newton *et al.*, 2011).

Them *et al.* (2022) used open-ocean Mo records from the Western Canada Sedimentary Basin, with comparisons to a global compilation of Pliensbachian – Toarcian Mo data, to estimate the amount of Mo buried globally, incorporating values for local sedimentation rates and global weathering rates during the T-OAE (Them *et al.*, 2017b, 2018). These data indicate that ~ 41 Gt of Mo was buried during the T-OAE which, using Mo/TOC values derived from modern basins, derived a value of $\sim 244,000$ Gt organic carbon buried globally at that time. This is more than one order of magnitude larger than that estimated to be buried in shallow-marine sediments by Kemp *et al.* (2022b).

The global value of $\sim 244,000$ Gt C burial derived by Them *et al.* (2022) would require a minimum of 3% of the ocean floor to be covered by euxinic waters compared to $< 0.3\%$ today (Algeo, 2004; Helly & Levin, 2004; Ruvalcaba Baroni *et al.*, 2020). This implies that, despite their prominent black shale sections, European basins, with an estimated < 2000 Gt C buried during the T-OAE (Kemp *et al.*, 2022b), made a very small contribution to driving the observed changes in the carbon cycle. Sulfur isotope data and modelling similarly indicate that European basins played only a minor role in sulfide and therefore organic carbon, sequestration during the T-OAE interval (Gill *et al.*, 2011). For comparison, increased lacustrine organic productivity during the T-OAE attributed to elevated fluvial nutrient supply, resulted in the burial of ~ 460 Gt of organic carbon in the Sichuan Basin alone (Xu *et al.*, 2017, 2021), one of three major Early Jurassic lake systems in China.

Based on a negative CIE of about -3% , the total amount of carbon released during the T-OAE was estimated to be $\sim 10,000$ Gt by Ruebsam *et al.* (2019) assuming a biogenic methane source of carbon ($\delta^{13}\text{C} = -60\%$ to -80%), but $> 50,000$ Gt would be required for a purely volcanic CO_2 source ($\delta^{13}\text{C} = -7\%$ to -10%). The release of $10,000$ Gt C over a period of about 800 ka (see Section 17 for a discussion of the duration of the T-OAE, ~ 1400 ka is an alternative estimate) was calculated to increase global temperatures by about 5°C and cause a two- to three-fold increase in $p\text{CO}_2$ (Ruebsam *et al.*, 2019). For comparison, an increase in atmospheric $p\text{CO}_2$ from ~ 500 ppmv to ~ 1000 ppmv during the T-OAE has been derived from reconstructions using the stomatal index and the difference in the magnitude of the CIE in marine and terrestrial environments (McElwain *et al.*, 2005; Ruebsam *et al.*, 2020d). A seawater temperature rise of $6 - 7^\circ\text{C}$ is indicated for the Cleveland Basin (Section 18).

Ruebsam *et al.* (2019) argued that a volcanic-driven modest rise in temperature in the early Toarcian triggered a melt-down of Earth’s cryosphere that had expanded during the icehouse episode of the late Pliensbachian, and the rapid release of greenhouse gases, mainly as ^{13}C -depleted CH_4 , driving the negative $\delta^{13}\text{C}$ excursion. However, the contribution of volcanic CO_2 and the mass of carbon released during the T-OAE may have been significantly underestimated since a globally rapid silicate weathering response, surface ocean uptake and increased organic carbon burial would have consumed atmospheric CO_2 , preventing an atmospheric build-up and its climate impact.

21. Regional to global warming and anoxia

The Cleveland Basin provides a global reference for the T-OAE. An unprecedented range of existing high-quality, high-resolution sedimentological, palaeontological and geochemical data, including multiple elemental and isotopic proxies, available from the upper Pliensbachian – middle Toarcian of the Yorkshire coast, supplemented by results from the Dove’s Nest core, provide a unique framework for interpreting regional palaeoenvironmental change and the global impact of the T-OAE.

21.a. Late Pliensbachian – a well-oxygenated shallow-marine basin

The Staithes Sandstone and Cleveland Ironstone formations (*A. margaritatus* – *P. spinatum* zones) display the greatest lithological and geochemical variation in the study interval with short-term mineralogical and grain-size changes reflecting a shallow-water and high-energy epeiric setting. Deposition of the Staithes Sandstone (Subunit Ia) occurred above the storm wave-base, deepening to largely sub-storm wave-base conditions for the Cleveland Ironstone (Subunits Ib – c). The high silt – fine sand fraction of the Staithes Sandstone is reflected in high and variable Si/Al, Na/Al, Ti/Al and Zr/Al ratios (quartz, feldspar and heavy mineral proxies) with an overall decreasing upward (fining) trend. Low CIA values point to a dominance of physical weathering processes supplying sediment to the basin and cool climate conditions.

The Cleveland Ironstone Formation presents more stable geochemical profiles interspersed with large Fe, Mn and Mg peaks associated with sideritic ironstone horizons. Five stacked CU cycles are evidenced within the Cleveland Ironstone Penny Nab and Kettleless members (cf. Rawson *et al.*, 1983; Powell, 2010) from detrital proxy element ratios and CIA values. Cycle 2 terminates with the Avicula Seam, a prominent siderite ironstone. Subunit Ib in coarsening-upward cycle 3, spanning the *Amaltheus gibbosus* Subzone, incorporates high $\delta^{13}\text{C}_{\text{org}}$ values corresponding to the late Pliensbachian CIE and terminates at a regional disconformity below the Pecten Seam, a series of beds with 3 ironstones in the core. This cryptic disconformity, at the base of the Kettleless Member (*P. spinatum* Zone), is represented by an unremarkable bedding plane in the core but is a prominent feature of its chemostratigraphic profiles. The coarsening-upward cycles are interpreted as shallowing-upwards parasequences (‘sequences’ of Macquaker & Taylor, 1996); medium-term cycle stacking patterns correspond well to the sequences and inferred relative sea-level curve for the Cleveland Basin proposed by Hesselbo (2008). The base *P. spinatum* Zone disconformity is interpreted to represent a sequence boundary and superimposed transgressive surface.

Persistent oxic bottom-water conditions during the late Pliensbachian throughout the deposition of Unit I are evidenced by low TOC, TOC/P_T and DOP_T values and low redox-sensitive trace metal (e.g. U, Mo) contents. This is supported by a high trace-fossil taxonomic richness and a high benthic macrofossil diversity that includes bivalves, gastropods, brachiopods and benthic crinoids indicating a well-oxygenated open-marine environment. A proximal basin setting is indicated by palynofacies comprising 70–90% terrestrial palynomorphs. Assemblages are dominated by fern spores and bisaccate pollen indicative of a cool moist climate, with subordinate dinocysts (Slater *et al.*, 2019), and low-abundance, low-diversity nannofossil assemblages representing marine plankton (Slater *et al.*, 2022).

General cooling through the latest Pliensbachian is evidenced by belemnite calcite geochemistry: rising $\delta^{18}\text{O}_{\text{bel}}$ and falling Mg/Ca_{bel} ratios. The presence of glendonites in the *P. spinatum* Zone of southern Germany (Ruebsam *et al.*, 2019; Merkel & Munnecke, 2023) points to the episodic presence of cold bottom water masses in Europe. These have been associated with the establishment of a late Pliensbachian icehouse climate (Ruebsam *et al.*, 2019; Ruebsam & Schwark, 2021; Nordt *et al.*, 2022), including a persistent northern-hemisphere cryosphere with the likely presence of a NE Siberia icecap and extensive permafrost. Evidence provided in support of this includes regionally distributed glaciogenic sediments (pebbly argillites, tillites and matrix-supported conglomerates), potential periglacial sediments, dropstones and glendonites in Arctic Russia (Ruebsam & Schwark, 2021, fig. 8).

21.b. Pliensbachian – Toarcian boundary event – precursor to the T-OAE

The interval of the Pliensbachian – Toarcian Boundary CIE (PIToBE) marks a major shift in the chemostratigraphic profiles, reflecting the transition from the Cleveland Ironstone Formation to finer-grained mudstones of the Grey Shale Member (*D. tenuicostatum* Zone) at the base of the Whitby Mudstone Formation. This represents a significant long-term change in depositional conditions in the Cleveland Basin accompanying sea-level rise and coincides with the onset of a cascade of global environmental changes during the early Toarcian.

Hallam (1997) estimated a relative sea-level rise of ~35–85 m during the early Toarcian based on the facies change from the Staithes Sandstone to the Mulgrave Shale. A second-order eustatic sea-level rise of up to 100 m beginning in the earliest Toarcian *D. tenuicostatum* Zone and reaching a maximum in the middle Toarcian upper *H. bifrons* Zone has been proposed (Hardenbol *et al.*, 1998; Haq, 2018) that flooded large parts of the European shelf and other epicontinental areas globally. A transition from shallow-water limestones and/or sandstones to deeper-water mudstones is observed in many regions including the Paris (Hermoso *et al.*, 2013) and SE France basins (Bodin *et al.*, 2023), Middle and High Atlas Morocco (Ait-Itto *et al.*, 2017), NE Siberia Russia (Zakharov *et al.*, 2006) and Neuquén Basin Argentina (Al-Suwaidi *et al.*, 2022). Combined with the rising eustatic sea level, the collapse of the neritic carbonate factory in the earliest Toarcian halted carbonate mud export and caused sediment starvation in many basins previously dominated by carbonate-rich facies, as seen in the Central High Atlas Basin and elsewhere (Krencker *et al.*, 2020, 2022; Bodin *et al.*, 2023).

Step falls in detrital silicate and heavy mineral proxy element ratios at the facies change in the Cleveland Basin are matched by

step increases in phyllosilicate proxies (K₂O, K/Al, Cs/Al and Rb/Al) and CIA values indicative of decreased sand and silt fractions and the change to fine mudstones with an illite-rich clay-mineral assemblage. A coincident step rise in TOC may in-part reflect enhanced organic matter preservation via adsorption to the increased number of clay mineral surfaces (cf. Kennedy *et al.*, 2002).

21.b.1. Sulphur Band events and onset of anoxia

The PIToBE comprises an interval with a pair of negative $\delta^{13}\text{C}_{\text{org}}$ excursions of ~2.5‰, the minima of which coincide with thin laminated mudstones containing up to 6% TOC (Littler *et al.*, 2010). These represent the first episodes of seawater anoxia and carbonaceous mudstone deposition in the Cleveland Basin, precursors to the thick black shales of the Jet Rock and Bituminous Shales, above. The Sulphur Band (SB1; Kettleless 'bed' 26, Hawsker Bottoms mid-'bed' 43, Howarth, 1955) located a few decimetres above the base of the mudstones marks the base Toarcian. The laminated beds display geochemical evidence (DOP_T, iron speciation, Mo_{EF} and isorenieratane proxies) for the intermittent development of an anoxic – euxinic water column.

High-resolution (cm-scale) geochemical records from the 15-cm thick Sulphur Band (SB1) (Salem, 2013) demonstrate 2–3 short-term anoxia/euxinia to oxic cycles within the laminated interval over a period of < 10 ka (cf. McArthur *et al.*, 2008). Trace fossils immediately above the Sulphur Band likely represent a single, very brief oxygenation event. A return to more well-oxygenated bottom waters during the PIToBE is demonstrated by the presence of a diverse benthic fauna in the 1 m of sediment overlying SB1. However, geochemical proxies indicate predominantly dysoxic – anoxic conditions prior to the deposition of a second 50-cm interval of laminated mudstone, Sulphur Band 2 (SB2), at the top of the PIToBE interval. Palynofacies of the two 'sulphur' bands include high proportions (≥60%) of amorphous organic matter with small increases in marine algal cysts but spores and pollen continue to dominate (≥80%) the palynomorph assemblages (Slater *et al.*, 2019).

21.b.2. Relationship to Karoo–Ferrar LIPs magmatism

Sediments within and immediately below SB1 display significant enrichment in mercury; values of up to 0.5 ppm Hg at Hawsker Bottoms are one order of magnitude higher than in the immediately underlying and overlying strata (Percival *et al.*, 2015). Mercury enrichment is not confined to the black shale horizon. The highest Hg/TOC (ppm/%) ratios of up to 0.4 occur at the stage boundary immediately below the main black shale of SB1. Other levels within the PIToBE, including SB2, show no Hg/TOC enrichment. Mercury and Hg/TOC peaks at the level of the stage boundary, which also occur at Mochras, Peniche and in the Neuquén Basin of Argentina but are not seen in all Toarcian boundary sections (Them *et al.*, 2019), have been attributed to released volatiles from the onset of Karoo–Ferrar LIPs volcanism.

Robust ⁴⁰Ar/³⁹Ar and U–Pb geochronology indicates that peak Karoo–LIP basaltic magmatism postdated the PIToBE at 183.73 Ma (Greber *et al.*, 2020; Jiang *et al.*, 2023). Nonetheless, the PIToBE has been equated to the onset of Karoo magmatism (Al-Suwaidi *et al.*, 2022), based on records of older volcanic ages spanning the stage boundary (e.g. Ruebsam *et al.*, 2019, fig. S4; Luttinen *et al.*, 2022) and the presence of Hg/TOC anomalies in many sections. Furthermore, new high-precision plagioclase ⁴⁰Ar/³⁹Ar dates from Ferrar intrusions suggest earlier peak volcanism coincident with the PIToBE (Ware *et al.*, 2023), followed by waning and cessation

~182 Ma at the termination of the T-OAE. An increase in $^{187}\text{Os}/^{188}\text{Os}_i$ ratio from ~0.4 to ~0.5 within and above the PIToBE in Yorkshire and at Mochras evidence enhanced weathering accompanied the event (Percival *et al.*, 2016) which was potentially triggered by increasing atmospheric CO_2 levels sourced from volcanic emissions.

Ruebsam *et al.* (2019) argued that rising CO_2 initiated a period of global warming that accelerated in *D. semicelatum* Subzone times and drove a transition from late Pliensbachian icehouse to early Toarcian greenhouse climate that caused ice sheet melting, thermal expansion of the oceans and glacioeustatic sea-level rise.

21.b.3. A Toarcian global reference section

Bodin *et al.* (2023) proposed that the top Pliensbachian uppermost *P. spinatum* Zone is missing at Hawsker Bottoms and more generally in NW European sections and that a significant hiatus occurs at the base of the Sulphur Band (Bodin *et al.*, 2023, fig. 10). However, their interpretation does not incorporate the onset of the PIToBE negative CIE preceding the stage boundary (Fig. 2). The double negative $\delta^{13}\text{C}$ excursion spanning the stage boundary can be correlated between Yorkshire, Peniche, Mochras and the Lorraine Sub-Basin (Fig. 3; Ruebsam *et al.*, 2019, fig. 5), and there is a close association between a well-defined negative $\delta^{13}\text{C}_{\text{org}}$ excursion and the faunal turnover of ammonite taxa associated with the stage boundary in the Neuquén Basin, Argentina (Al-Suwaidi *et al.*, 2022).

There is no clear biostratigraphic or sedimentological evidence of a hiatus at the stage boundary at Hawsker Bottoms (cf. Kemp & Sadler, 2022) although some condensation at the level of the uppermost *P. spinatum* Zone ironstone ('bed' 42, top of the Cleveland Ironstone Formation), below, is likely. Nonetheless, we consider that the Yorkshire expression of the PIToBE remains a viable reference for global correlation.

21.b.4. Biotic change and Toarcian extinctions

The PIToBE marks a period of major biotic change with the disappearance of many bivalve taxa and a major decline in trace-fossil taxonomic richness indicating increasingly dysoxic bottom conditions. Marine palynomorphs display a decline in dinocysts and increase in spiny acritarchs and algal cysts. Caswell *et al.* (2009) considered that macrofossil extinctions in the *P. paltum* Subzone at the top of the PIToBE level (their extinction horizon i), described in detail from Yorkshire, were of global significance. Major changes in pollen assemblages across the stage boundary in the Cleveland Basin, including a decline in bisaccates and substantial increases in *Classopollis* spp. and *Chasmatosporites* spp., are indicative of a transition to a strongly seasonal warmer climate (Slater *et al.*, 2019).

21.c. Earliest Toarcian – sea-level rise, oxygen depletion and climate warming

Following the PIToBE, the Grey Shale of the *P. paltum* to lower *D. semicelatum* subzones (Unit II) shows more uniform mineralogy and geochemistry compared to the underlying Pliensbachian reflecting a deeper water environment, likely close to the limit of storm wave-base (typically 15 – 40 m depth), established following sea-level rise. Detrital proxies (Ti/Al ratio, quartz and silt content) display variation but no long-term trend following their marked fall within the interval of the PIToBE. A third thin interval of laminated black shales in the lower *D. clevelandicum* Subzone, Sulphur Band 3 (SB3), evidences a

further short-lived episode of temporary bottom-water anoxia. This occurs above a minor CU cycle with rising K/Al ratios pointing to an increase in the proportion of illitic clays. SB3 marks a further significant environment shift, reflected by the Subunit IIA – b boundary, with a step change to higher TOC and amorphous organic matter contents, geochemical evidence of increasingly dysoxic bottom waters (e.g. rising DOP_T values), and the temporary disappearance of trace fossils.

A climate shift to a warming trend through the earliest Toarcian is indicated by falling $\delta^{18}\text{O}_{\text{bel}}$ and rising Mg/Ca_{bel} ratios from the Yorkshire coast (Section 18), consistent with brachiopod oxygen-isotope data from Portugal (Suan *et al.*, 2008a; Müller *et al.*, 2020) and TEX₈₆ results from Spain and Italy (Ruebsam *et al.*, 2020c). Palynological trends include a rising upward proportion of *Chasmatosporites* spp. cycad pollen, a warm/dry climate indicator, and amorphous organic matter, but the proportion of terrestrial palynomorphs remains generally $\geq 80\%$ (Slater *et al.*, 2019). The impact of early Toarcian climate warming on terrestrial vegetation was not limited to the Cleveland Basin, with palynological evidence of significant warming recorded from many regions, including continental settings in Central Asia (Schnyder *et al.*, 2017).

21.d. T-OAE (Unit III) – expansion of anoxia and a hyperthermal event

The interval of the negative $\delta^{13}\text{C}$ excursion defining the T-OAE (Unit III), spanning the upper *D. semicelatum* and *C. exaratum* subzones, represents the period of most extensive palaeoenvironmental change in the Cleveland Basin and globally. The base of T-OAE Unit III is defined by the onset of falling $\delta^{13}\text{C}$ values recorded in bulk sediment organic matter, terrestrial wood, individual marine and terrestrial biomarkers, and rising TOC content, followed, a short distance above, by the onset of laminated black shale deposition and the disappearance of trace fossils and most benthic fauna. This reflects the establishment of more persistent anoxia and then, from the base of the Jet Rock (*C. exaratum* Subzone), euxinic bottom waters that dominated through the interval of the $\delta^{13}\text{C}_{\text{org}}$ minimum that characterizes Subunit IIIb. Anoxia persisted after the T-OAE, throughout Unit IV, into the later early Toarcian, upper *H. falciferum* Subzone.

21.d.1. Global mass extinction, ocean anoxia and a Toarcian hyperthermal

Biotic turnover with numerous highest occurrences in the upper *D. semicelatum* Subzone (Subunit IIIa) is well documented in the Cleveland Basin and has been widely observed in other Boreal and Tethyan sections, with the recognition of two extinction levels (ii, iii) by Caswell *et al.* (2009). The highest of these, at the base of the *C. exaratum* Subzone and the fall to a $\delta^{13}\text{C}_{\text{org}}$ minimum (Subunit IIIb), marks the level of a second-order global mass extinction which, based on geochemical proxies (e.g. Re/Mo, $\delta^{98}\text{Mo}$, $\delta^{18}\text{O}_{\text{bel}}$), coincided with the maximum spread of anoxic and euxinic seafloor area in the oceans and peak hyperthermal conditions. Terrestrial palynomorphs evidence an increasingly hot climate with extreme wet/dry seasons in the Cleveland Basin at that time.

21.d.2. A euxinic basin

Iron speciation ($\text{Fe}_{\text{HR}}/\text{Fe}_{\text{T}}$, $\text{Fe}_{\text{py}}/\text{Fe}_{\text{HR}}$), TOC/ P_T and DOP_T together with trace-metal enrichment (Mo, U) indicate that euxinic bottom waters became established progressively in the Cleveland Basin during the onset of the T-OAE (Subunit IIIa) and remained present throughout the subsequent phases of the event

(Subunits IIIb – d). Isorenieratane/TOC ratios and other biomarkers suggest that PZE, which occurred initially for short periods during the deposition of the black shales of the Sulphur Bands, was commonplace during the T-OAE. However, horizons of low-oxygen specialist bivalves, principally *Pseudomytiloides dubius*, throughout the black shale succession point to common brief episodes of improved oxygenation that fail to be resolved by the sediment geochemical proxies.

Oxidation events may have been caused by large storms mixing the stratified water column and mobilizing surface sediments but having little impact on the deeper sediment geochemical record. A dramatic increase of tropical cyclone intensity during the T-OAE global warming that affected large areas of NW Tethys, including the European epicontinental seas, has been proposed based on sedimentological evidence obtained in a number of west European and Moroccan sections (Krencker *et al.*, 2015) and modelling that indicates two potential storm genesis centres located around NW and SE Tethys (Marsaglia & Klein, 1983; Yan *et al.*, 2023).

21.d.3. The Whale Stones Event

Black shale deposition accompanied the T-OAE in the Cleveland Basin. The stratigraphic pattern of TOC enrichment shows a large right-skewed peak centred in the mid-C. *exaratum* Subzone at Whale Stones 'bed' 35. Here, maximum TOC contents of >12% (maximum 19%) immediately precede the reversal to rising $\delta^{13}\text{C}$ values in the mid-C. *exaratum* Subzone ('bed' 36) and coincide with a maximum in the relative abundance of amorphous organic matter (~90%) and algal cysts and peak nannofossil species richness.

Whale Stones 'bed' 35 shows peak values for detrital grain-size proxies and a CIA minimum with maximum $^{187}\text{Os}/^{188}\text{Os}$ values and an increase in the slope of the Sr-isotope profile. An increase in physical weathering and/or relative sea-level fall promoted an increased input of illitic clay and coarser detritus into the basin. However, the large carbonate concretions that characterize this 'bed' imply a reduction in bulk sedimentation rate and/or hiatus (Raiswell, 1987, 1988; Marshall & Pirrie, 2013). Sharp falls in TOC and detrital proxy elements occur at the base of 'bed' 36 (Figs 4, 7) together with a marked increase in the slope of the $^{87}\text{Sr}/^{86}\text{Sr}_{\text{bel}}$ profile (Fig. 19). These point to a possible hiatus at this level, followed by a period of slower deposition. Concretion formation likely occurred at this time.

Peak DOP_T and $\text{Fe}_{\text{HR}}/\text{Fe}_T$ values, high Mo_{EF} , V_{EF} , U_{EF} and a Re/Mo minimum indicate peak euxinia accompanying maximum TOC in the Basin. Despite a near absence of benthic fauna and a lack of visible bioturbation, Whale Stones 'bed' 35 yields diverse ammonite and nannofossil assemblages and belemnites demonstrating a continuing connection, at least intermittently, with oxygenated open-marine surface waters and a stratified water column. A maximum Cd/Mo ratio (McArthur, 2019) at this level supports minimum basin restriction but will have been influenced by the global drawdown of redox-sensitive trace metals at this time. A Mo/TOC minimum and low $\delta^{98}\text{Mo}$ point to a coincident maximum in the global seafloor area indicating that basin water chemistry generally follows a global trend, albeit modified by episodes of basin restriction.

Primary productivity did not collapse in response to the PZE in the Cleveland Basin. Rather, an ecosystem dominated by anoxygenic photosynthesizers provided an increased organic matter flux to the sediment, which was better preserved under the prevailing euxinic bottom-water conditions, generating

maximum TOC enrichment. High TOC/ P_T molar ratios of >200 point to extensive P release from euxinic sediments maintain water column productivity, while $\delta^{15}\text{N}_{\text{tot}}$ values of $\sim +2$ indicate that increased algal productivity drove partial denitrification.

A major change in both palaeoenvironmental conditions in the basin and globally occurred following the deposition of Whale Stones 'bed' 35, this *Whale Stones Event* marked the onset of global cooling, associated with decreasing volcanic emissions, falling $p\text{CO}_2$, decreased continental weathering and better oxygenation of the global ocean with rising $\delta^{13}\text{C}$ marking the final stages of the T-OAE. A sharp increase in *Cerebropollenites* pollen above Whale Stones 'bed' 35 that persists to the top of the T-OAE interval is a prominent feature on the Yorkshire coast (Slater *et al.*, 2019) and is likely a response of the terrestrial vegetation to the hyperthermal maximum. The coincident changes in multiple marine and terrestrial proxies at this level represent a major event that offers potential as a global marker.

21.d.4. TOC and carbon burial rates

TOC enrichment accompanying the T-OAE is widespread, with a majority of sites globally (albeit heavily biased towards European sections) showing an increase in TOC relative to pre-event values, but each basin displays a unique stratigraphic pattern (Remirez & Algeo, 2020; Kemp *et al.*, 2022b). The highest mean values are recorded in NW and SW German euxinic basins. TOC increases are generally highest where deoxygenation is most severe but multiple local factors including productivity and sedimentation rate fundamentally affect the final stratigraphic record and the distribution of black shales through a succession. Kemp *et al.* (2022b) observed that in anoxic – euxinic environments of the T-OAE, TOC content displays a non-linear inverse correlation with sedimentation rate indicating that clastic dilution plays a major role in limiting organic richness.

Surprisingly, the T-OAE was characterized by relatively low organic carbon burial rates, even in places where TOC concentrations are high (e.g. Suan *et al.*, 2016; Fantasia *et al.*, 2018b). An organic carbon burial rate of $1.63 \text{ g C m}^{-2} \text{ a}^{-1}$ has been calculated for the T-OAE interval in Yorkshire, assuming a T-OAE duration of 900 ka (Kemp *et al.*, 2022b). Globally, C burial rates during the CIE interval are $<3 \text{ g C m}^{-2} \text{ a}^{-1}$ with a mean rate of $0.57 \text{ g C m}^{-2} \text{ a}^{-1}$ based on the same time scale. These contrast to a modern global median continental-shelf organic carbon burial rate of $19.6 \text{ g C m}^{-2} \text{ a}^{-1}$ (Wilkinson *et al.*, 2018) and rates are up to $\sim 100 \text{ g C m}^{-2} \text{ a}^{-1}$ in high-productivity upwelling zones such as the Peru margin (Föllmi *et al.*, 2005).

Post-depositional oxidation and diagenetic loss of organic carbon complicate comparison with modern environments but, nonetheless, the relatively low rates of burial in anoxic – euxinic settings like the Cleveland Basin, areas of potentially high burial efficiency, indicate that rates of surface ocean productivity and export production were low during the T-OAE relative to modern shelves. Nonetheless, it has been estimated that organic carbon burial rates may have increased $\sim 500\%$ on average during the T-OAE compared to the earlier Toarcian in the anoxic–euxinic marine basins of Europe (Kemp *et al.*, 2022b).

21.d.5. Basin restriction versus global anoxia

Geochemical proxies in the black shales of the Jet Rock and Bituminous Shales predominantly record global-scale changes in ocean chemistry that occurred during and immediately following the T-OAE. Euxinia in the Cleveland Basin was a local manifestation of the global expansion of anoxic and euxinic

seafloor area, which led to a fall in seawater sulfate, evidenced by rising $\delta^{34}\text{S}_{\text{CAS}}$ in sediments and depletion of redox-sensitive trace metals (Mo, Re, U, V) in the oceans, reflected in anomalous low trace-metal/TOC and Re/Mo ratios and a depleted isotopic composition ($\delta^{98}\text{Mo}$).

Estimates of local basin restriction using geochemical data derived from modern basins are misleading if they fail to incorporate the large changes in global ocean chemistry that occurred during the early Toarcian. However, extreme depletion of Mo (and to a lesser extent U and V) in the Cleveland Basin within the T-OAE Unit III interval during peak euxinia is consistent with a restriction at that time, prior to the development of a more open connection accompanying sea-level rise during the later early Toarcian *H. falciferum* Subzone (Unit IV). Cyclic decreases in $\delta^{98}\text{Mo}$ to $\sim 1\%$ coincident with rising Mo concentrations in the T-OAE interval are indicative of basin restriction cycles.

21.d.6. Salinity change

A widespread reduction in salinity across the NW European Shelf during the T-OAE has been widely postulated, including a shift to nearly freshwater conditions in the Cleveland Basin based on geochemical proxies (principally B/Ga ratio; Ramirez & Algeo, 2020; Ramirez & Algeo, 2020). Although minor regional freshening of surface waters likely occurred, as indicated by regional ocean circulation models (Bjerrum *et al.*, 2001; Dera & Donnadieu, 2012; Ruvalcaba Baroni *et al.*, 2018) and interpretation of $\delta^{18}\text{O}$ data, with salinity falling to a minimum of 30 – 32 psu, there is no geologically consistent evidence of extreme brackish or freshwater conditions in the basin during the T-OAE. The presence of abundant ammonites, belemnites and pseudoplanktonic crinoids demonstrates open-marine (likely stenohaline) conditions, in association with peak levels of amorphous organic matter and marine algal cysts and greatest nannofossil species richness.

21.d.7. A hyperthermal event with enhanced weathering

The T-OAE is recognized as one of the six most significant hyperthermals in the last 300 Ma (Foster *et al.*, 2018). An increase in seawater temperatures of 6 – 7° C in the Cleveland Basin, estimated from $\delta^{18}\text{O}$ values in belemnite calcite, led to hyperthermal conditions at the peak of the T-OAE (Subunit IIIb). Globally, the magnitude of seawater warming is estimated to have ranged between +3° C and +7° C, depending on latitude (Bailey *et al.*, 2003; Suan *et al.*, 2008a; Gómez & Goy, 2011; Dera & Donnadieu, 2012; Danise *et al.*, 2019).

A coincident large $^{187}\text{Os}/^{188}\text{Os}_i$ peak of >1.0 , a pulse of illite and rising $^{87}\text{Sr}/^{86}\text{Sr}$ in belemnites, point to an episode of accelerated weathering accompanying warming. An associated small increase in the proportion (maximum 3.5%) of freshwater algae, which are present sporadically ($<1\%$) throughout the Yorkshire succession, is consistent with an input of additional terrestrial material that might incorporate freshwater-derived palynomorphs. Comparable temperature rises and weathering pulses have been widely documented coincident with the T-OAE in Wales, Germany, Canada and Japan (e.g. Percival *et al.*, 2016; Them *et al.*, 2017b; Kemp *et al.*, 2020).

An increase in the proportion of *Classopollis* spp. pollen with decreasing taxonomic terrestrial palynomorph richness and diversity occur at the onset of the T-OAE in the Cleveland Basin (Subunit IIIa) (Slater *et al.*, 2019). This is followed by a large pulse of *Cerebropollenites* accompanying the Whale Stones Event in the upper *C. exaratum* Zone. These changes in terrestrial

vegetation point to the temporary establishment of a hot climate with extreme wet/dry seasons, followed by a return to a warm climate and strong seasonality immediately following the T-OAE. The disappearance of glendonites in polar sections (North Siberia) coincident with an influx of abundant *Classopollis* spp. pollen at the onset of the T-OAE has similarly been attributed to high-latitude warming that persisted into the middle Toarcian (Suan *et al.*, 2011).

A phase of overall aridity linked to dominance of dry season conditions during the later stages of the T-OAE (Units IIIc, d) is evidenced by coincident peaks in the relative proportion of *Cerebropollenites* in Yorkshire and maximum charcoal abundance (incidence of wildfires) in equivalent levels at Mochras and Peniche (Baker *et al.*, 2017). There is increasing evidence of arid phases during the T-OAE throughout the warm temperate belt of the Northern Hemisphere (Baranyi *et al.*, 2024). Increased wildfire activity during the later stages of the T-OAE has been linked to increasing $p\text{O}_2$ driven by organic carbon and pyrite burial (Baker *et al.*, 2017).

21.d.8. The Karoo–Ferrar LIPs, $p\text{CO}_2$ and the T-OAE

The peak of the main magmatic phase of the Karoo LIP between 183.5 and 182.5 Ma (Jiang *et al.*, 2023) and the reinterpreted Ferrar LIP peak between 184 and 182.5 Ma (Ware *et al.*, 2023) coincide with the acceleration of early Toarcian global warming and immediately pre-date the beginning of the T-OAE negative $\delta^{13}\text{C}$ excursion at $182.77 \pm 0.11 / -0.15$ Ma (Al-Suwaidi *et al.*, 2022). In contrast to the Karoo–Ferrar LIPs, Chon Aike, which has also been implicated in the T-OAE (e.g. Krencker *et al.*, 2020), is a silicic magmatic province that may not be plume-related (Bastias *et al.*, 2021). It was emplaced over a long period ~ 153 – 188 Ma with one of three pulses between 178 – 188 Ma (Pankhurst *et al.*, 2000) and likely did not result in rapid hydrothermal venting of greenhouse gases.

Variations in the concentration of mercury (Hg) in sedimentary archives, generally expressed as Hg/TOC ratios, are increasingly being used as a proxy for past global volcanic activity (e.g. Percival *et al.*, 2015, 2021) but the interpretation of sedimentary Hg anomalies is not straightforward (Grasby *et al.*, 2019). Unlike the PliToBE and despite significant mercury increases, no Hg/TOC anomaly has been documented in the T-OAE interval of the Cleveland Basin, in contrast to Mochras and many sections in Portugal, Spain, Canada, Chile and Argentina (e.g. Them *et al.*, 2019; Ruhl *et al.*, 2022).

Kovács *et al.* (2024) reassessed Hg distributions in the Pliensbachian – Toarcian of the Cleveland Basin and at Mochras and La Cerradura (Subbetic Basin, southern Spain). The study showed that the use of Hg/TOC ratio alone as a volcanic emission proxy may be misleading since it does not always fully correct for host-phase biases, nor does it quantify the additional environmental Hg present over background levels during periods of sedimentary Hg enhancement (Fendley *et al.*, 2024). For example, sulfides rather than organic matter provide the main Hg host in some Lower Jurassic successions (Zhu *et al.*, 2024).

A strong affinity of Hg with organic carbon – sulfide phases was observed by Kovács *et al.* (2024) solely in the anoxic – euxinic intervals of the Cleveland Basin. Under oxic – dysoxic conditions, both in Yorkshire and elsewhere, Hg principally co-varied with redox-sensitive trace metals, suggesting an association with Fe–Mn oxyhydroxides and/or detrital (clay) minerals. Nonetheless, substantial Hg enrichment characterized the T-OAE interval in

all redox environments, consistent with an increase in Hg loading contemporaneous with LIP volcanism.

Hg/TOC enrichments associated with the T-OAE have been recorded mainly in shallow-marine settings and show evidence of cycling and redistribution of Hg in intermediate terrestrial reservoirs prior to being incorporated in the marine record. Mercury enrichment in fossil leaves from a T-OAE section in south China has been reported (Näslund, 2021), while Hg concentration and Hg-isotope data from a lacustrine T-OAE section in the Ordos Basin of north China point to Hg enrichment solely from a terrestrial source and exclude direct increased atmospheric Hg deposition (Jin *et al.*, 2022). Thus, although volcanogenic outgassing remains the potential primary source of Hg associated with the T-OAE, an increase in terrestrially derived Hg in the global ocean may have been enhanced by continental weathering (evidenced by Os and Sr isotope data) in response to rapid climate warming.

The primary environmental impact of LIP emplacement was the release of volcanic volatiles, principally CO₂, into the atmosphere that drove global warming (cf. Jenkyns, 1999). Fendley *et al.* (2024) used excess Hg loading data from Mochras to calculate LIP-associated carbon emissions during the late Sinemurian – late Toarcian. They estimated that a total of ~12,000 Gt C was released during the entire T-OAE interval, with an estimated duration of ~1 Ma, in contrast to faster and larger carbon inputs of up to 81,000 Gt C over 150 ka that have been derived from carbon-cycle modelling (Ullman *et al.*, 2020; Heimdal *et al.*, 2021).

A pCO₂ increase from 400 – 1200 ppmv in the early Toarcian to 1100 – 1800 ppmv during the T-OAE is indicated by leaf stomata data from Denmark (McElwain *et al.*, 2005). A doubling of pCO₂ from ~500 ppmv to ~1000 ppmv during the T-OAE is supported by the changing offset between terrestrial δ¹³C_{n-alkane} and marine δ¹³C_{carb} data (Ruebsam *et al.*, 2020d).

21.d.9. pCO₂, ocean circulation and anoxia

Modelling by Dera & Donnadiou (2012) suggests that a 2 – 6 × increase in atmospheric pCO₂ during the early Toarcian would have led to an average global warming of +4.5° C associated with stronger high-latitude precipitation rates, enhanced continental runoff and the demise of polar sea ice, causing a regional freshening of Arctic surface seawater. The model shows a progressive slowdown of global oceanic circulation that would promote widespread ocean stratification and bottom anoxia in deep oceanic settings and epicontinental basins.

The mass balance model for the coupled marine P and C cycles of Slomp & Van Cappellen (2007) predicts that deep-ocean anoxia would occur if the present ocean's circulation rate was reduced by 50% while the supply of reactive phosphorus from the continents was simultaneously boosted by 20%. They suggested that such an increase could be caused by coastal erosion linked to sea-level rise. The transition between oxic to anoxic deep-ocean state is likely very rapid (Donohue *et al.*, 2023).

Slomp & Van Cappellen's (2007) model indicates that a slowdown of global ocean circulation decreases primary production in the open ocean, but increases that in marginal seas. Slower ocean circulation increases global organic carbon burial, because of enhanced preservation of organic matter under anoxia – euxinia in deep-sea environments and higher primary productivity along continental margins. Carbon burial is enhanced further when reduced oceanic circulation also causes the spreading of bottom-water anoxia in the coastal ocean.

Unlike Cretaceous oceanic anoxic events (Montoya-Pino *et al.*, 2010; Owens *et al.*, 2013; Ostrander *et al.*, 2017; Clarkson *et al.*,

2018), little is known about the intensity and global extent of oceanic anoxia in the Toarcian. It seems likely, however, that the area of anoxic seafloor during the T-OAE would have been similar to that during the latest Cenomanian OAE2 (Dickson *et al.*, 2017), when that area expanded by ~40% to occupy perhaps ~20% of the global seafloor (Ostrander *et al.*, 2017). Constraints on the area of seafloor overlain by euxinic seawater in that case indicate that ~5% of the seafloor was euxinic (Owens *et al.*, 2013; Dickson *et al.*, 2017). These numbers may seem low (cf. Monteiro *et al.*, 2012), but even in warm oceans, it is difficult to establish and maintain an anoxic water column away from productive margins (Lyons & Reinhard, 2012).

It is important to note that the results of Dera & Donnadiou (2012) contrast with the results of other modelling studies of ocean circulation during OAEs which show no collapse of ocean circulation but rather similar to slightly higher intensities of overturning (Poulsen *et al.*, 2001; Otto-Bliesner *et al.*, 2002; Trabucho-Alexandre *et al.*, 2010). The meridional gradient of density at the ocean surface increases with increasing CO₂ concentration for warmer climates because the coefficient of expansion of seawater is greatly increased at higher temperatures (Manabe & Bryan Jr, 1985). For this reason, ocean circulation in warmer climates does not slow down.

A recent modelling study suggests that the Tethys Ocean and the SW European epicontinental sea were mostly well-oxygenated (Ruvalcaba Baroni *et al.*, 2018). More northern parts of Europe were too shallow for currents of oxygenated Tethyan water to penetrate deep into the epeiric sea with its abundant sills and islands (Fig. 1), which was highly prone to stratification (Ruvalcaba Baroni *et al.*, 2018). Salinity stratification, either due to runoff from the surrounding land, to rainfall, or both, would have promoted anoxia and burial of organic carbon in the basins, although suggestions of freshwater episodes in the Cleveland Basin (McArthur *et al.*, 2008; Remírez & Algeo, 2020) are not supported by the geological evidence.

Relatively low organic carbon burial rates during the T-OAE in the Cleveland Basin and globally (Kemp *et al.*, 2022b) point to high burial efficiency in anoxic – euxinic environments, rather than increased rates of surface ocean productivity and export production being the primary cause of TOC enrichment in epeiric seas. Nonetheless, high ratios of TOC/P indicate strong recycling of phosphorus relative to organic carbon which likely helped sustain productivity and anoxia. However, an expansion of anoxic – euxinic seafloor area and increased organic carbon preservation in the Tethyan and Panthalassic oceans is required to explain the elemental and isotopic changes recorded in Toarcian black shales.

21.d.10. Magnitude of the T-OAE global negative δ¹³C excursion

The magnitude of the negative δ¹³C_{org} excursion of ~6‰ that characterizes the T-OAE in the Cleveland Basin and many other northern European sections is such that an input of mantle-derived carbon alone would require unrealistic volumes of CO₂ emission. However, large variation exists in the amplitudes of negative δ¹³C_{carb} and δ¹³C_{org} excursions observed globally (Fig. 3; Remírez & Algeo, 2020, figs 4, 5), reflecting a combination of global and local controls.

Organic matter type and bottom-water redox, in particular, significantly impact bulk δ¹³C_{org} values (Remírez & Algeo, 2020): terrestrial-derived organic matter preserved in relatively well-oxygenated conditions exhibits a mean value that is 3.8‰ higher than marine-derived organic matter preserved during the T-OAE in relatively more reducing bottom waters (–28.8‰ versus –32.6‰),

with mixed-source organic matter exhibiting an intermediate value (-30.1‰). These compare to the average Phanerozoic black shale value of -27‰ (Meyers, 2014). Changes in the relative abundance of the isotopic endmembers will significantly influence the carbon isotope curve (Suan *et al.*, 2015). This is particularly problematic for the Yorkshire succession where the terrestrial component values from $>90\%$ in some upper Pliensbachian samples to $<5\%$ during the latter part of the T-OAE (Slater *et al.*, 2019).

The HI obtained by Rock-Eval pyrolysis can be used to track organic matter sources because fresh and weakly degraded algal and marine-derived organic matter (kerogen Types I and II) are hydrogen-rich, whereas terrestrial-derived and highly-degraded marine-derived organic matter (kerogen Type III) has a lower hydrogen content (Espitalié *et al.*, 1985; Tyson, 1995). Suan *et al.* (2015, fig. 5d) used the Yorkshire coast paired $\delta^{13}\text{C}_{\text{org}}$ and HI data of Sælen *et al.* (2000) to compensate for the changing proportion of terrestrial vs marine organic matter through the succession. They calculated an amplitude for the corrected negative excursion of $3\text{‰} - 4\text{‰}$ $\delta^{13}\text{C}_{\text{org}}$, consistent with corrected $\delta^{13}\text{C}_{\text{org}}$, $\delta^{13}\text{C}_{\text{phytane}}$ and $\delta^{13}\text{C}_{\text{carb}}$ curves from two sections in SW Germany (Denkingen, Dotternhausen) that are dominated by marine organic matter throughout the lower Toarcian.

Remirez & Algeo (2020) concluded that the T-OAE CIE is perhaps best interpreted as a combination of a relatively small negative shift of -2‰ to -3‰ in the isotopic composition of the global carbon cycle, overprinted by larger local or regional shifts of up to $\pm 5\text{‰}$ (e.g. Fig. 3) caused by, for example, differences in organic matter type, changes in marine productivity, water mass restriction, assimilatory uptake of variable amounts of recycled CO_2 from bacterial respiration and burial history. Additionally, the shape of the isotope curve will be affected by local physical sedimentary processes, which means that both the shape and the magnitude of the curves are a combination of global and local factors.

The large amplitude of the T-OAE negative $\delta^{13}\text{C}$ excursion has been interpreted to require a large release of isotopically light methane to the atmosphere caused by the dissociation of methane clathrates on continental margins (Hesselbo *et al.*, 2000; Beerling *et al.*, 2002; DB Kemp *et al.*, 2005) or associated with permafrost melting (Ruebsam *et al.*, 2019) or thermogenically released by igneous intrusions into coals and carbonaceous mudstones (McElwain *et al.*, 2005; Svensen *et al.*, 2007; Deegan *et al.*, 2022). Based on a negative CIE of about -3‰ , the total amount of carbon released during the T-OAE was estimated to be $\sim 10,000$ Gt by Ruebsam *et al.* (2019) assuming a biogenic methane source of carbon ($\delta^{13}\text{C} = -60\text{‰}$ to -80‰), but $>50,000$ Gt would be required for a purely volcanic CO_2 source ($\delta^{13}\text{C} = -7\text{‰}$ to -10‰). Furthermore, massive carbon burial during the T-OAE would potentially move the carbon-isotope value of the ocean-atmosphere system to more positive values, against which the input of isotopically negative carbon would be balanced. This has implications for calculating the amount of carbon involved in the generation of the T-OAE negative excursion and/or its isotopic composition. Additional modelling is required to address this further.

The release of $10,000$ Gt carbon over a period of about 800 ka (see Section 17 for a discussion of the duration of the T-OAE) has been calculated to increase global temperatures by about 5°C and cause a two- to three-fold increase in $p\text{CO}_2$ (Ruebsam *et al.*, 2019). For comparison, an increase in atmospheric $p\text{CO}_2$ from ~ 500 to ~ 1000 ppmv during the T-OAE is derived from reconstructions using the stomatal index and the difference in the magnitude of the CIE in marine and terrestrial environments (McElwain *et al.*, 2005;

Ruebsam *et al.*, 2020d). A seawater temperature rise of $6 - 7^\circ\text{C}$ is indicated for the Cleveland Basin (Section 18).

Kemp *et al.* (2022b) estimated that globally an extra ~ 9000 Gt of carbon may have been buried in shallow seas during the T-OAE relative to before the event, including ~ 800 Gt in European anoxic – euxinic basins.

21.e. Early Toarcian – post-T-OAE anoxia and global cooling

Anoxic – euxinic conditions persisted through the lower *H. falciferum* Subzone (lower Bituminous Shales) in the Cleveland Basin following the T-OAE with continuing deposition of carbonaceous ($>2.5\%$ TOC) mudstones (lower Bituminous Shales) that display the greatest Mo, U, V and other redox-sensitive trace metal enrichment in the succession (Unit IV). Consistently high DOP_T and $\text{Fe}_{\text{HR}}/\text{Fe}_T$ values point to continuing anoxic conditions with cyclic redox variation indicated by P_{EF} and trace-metal profiles. $\delta^{98}\text{Mo}$ data indicate a weakly restricted anoxic basin with sufficient exchange to display open ocean isotopic values. The high levels of redox-sensitive metals relative to TOC reflect their increase in ocean water in response to a decline in the areal extent of global anoxic and euxinic seafloor with the termination of the T-OAE. The step fall in trace metals in the upper *H. falciferum* Subzone (base Unit V) reflects a shift to dysoxic bottom waters in the basin with sediments no longer capturing a global trace-metal signature except during brief euxinic episodes like those in the Hard Shales.

The T-OAE hyperthermal marks a step change in the long-term $\delta^{18}\text{O}_{\text{bel}}$ and $\text{Mg}/\text{Ca}_{\text{bel}}$ records (Fig. 19) indicating a shift from relatively cool-water conditions in the Cleveland Basin before the event and the persistence of warm waters following the termination of the hyperthermal. It has been suggested that this reflects a major change in the Earth's climate system (Ruebsam *et al.*, 2019, 2020b; Ruebsam & Schwark, 2021). It is argued that volcanic CO_2 emissions from the Karoo–Ferrar LIPs initiated global warming that destabilized the ice caps and cryosphere-stored carbon reservoirs. Massive carbon release from the cryosphere, including highly ^{13}C -depleted CH_4 , combined with orbitally forced climate cycles accelerated global warming. This caused a runaway effect that drove Earth's climate system from an icehouse in the late Pliensbachian into a prolonged greenhouse mode in the Toarcian. Deglaciation and ocean warming were responsible for eustatic sea-level rise.

21.f. Middle Toarcian – continuing oxygen depletion

Relative sea-level rise in the Cleveland Basin that began at the Pliensbachian – Toarcian boundary reached a maximum for the Early Jurassic around the *H. serpentinum* – *H. bifrons* zone boundary (Hesselbo, 2008), coincident with maximum flooding linked to the Pliensbachian – Toarcian 2nd order Boreal standard sequence of de Graciansky *et al.* (1998). This reflects the eustatic sea-level trend. An onset of regression during the early *H. falciferum* Subzone in the Cleveland Basin is indicated by the beginning of gradually rising Ti/Al ratios and quartz mean grain-size indicative of upward coarsening of grain sizes in the Mulgrave and Alum shales. Maximum flooding associated with third-order sequences in the NW and SW German basins has also been recorded in the late *H. serpentinum* Zone (e.g. Arp *et al.*, 2021, 2023). An interval of coarser planar laminated mudstones was observed immediately above the Hard Shales in the Dove's Nest core (Trabucho-Alexandre *et al.*, 2022) but these are not associated with a significant shift in the geochemical profiles. These may

reflect a period of increased current action but, nonetheless, water depths in the study area likely remained generally below storm wave-base (i.e., > 30 m).

Two episodes of renewed anoxia and intermittent euxinia characterize the earliest middle Toarcian *D. commune* Subzone in the Cleveland Basin (Hard Shales, Subunit Vb) evidenced by levels of increased TOC content and trace metal enrichment. TOC/P_T and DOP_T proxies demonstrate dysoxia persisting into the middle Toarcian. A gradual return to better oxygenation conditions in the middle of the subzone is indicated by an increase in body fossils and macrofossil diversity, the disappearance of low-oxygen specialist bivalves and the reappearance of trace fossils at the top of the study interval. Nonetheless, the benthos had still not recovered to late Pliensbachian pre-OAE state by the *P. fibulatum* Subzone (mid-*H. bifrons* Zone) (Caswell & Herringshaw, 2023) indicating that dysoxic anoxic bottom waters persisted, at least intermittently.

Extended intervals displaying an absence of macroscopic bioturbation, indicative of bottom water anoxia – euxinia during the T-OAE and later early Toarcian, have been observed from sections in NW Tethys, the North African (North Gondwana Palaeomargin) and northern Iberian margins, Panthalassa Ocean sites in Alberta, Canada and the Arctic Basin, northern Siberia (Caswell & Herringshaw, 2023). In the western Canadian and Arctic basins, as in the Cleveland Basin, macroscopic trace fossils were absent for much longer (*D. tenuicostatum* – lower *H. bifrons* zones). A cessation of bottom sediment irrigation would have significantly impacted biogeochemical dynamics across the benthic boundary layer, favouring the preservation of organic matter and the release of phosphate and ammonia to bottom waters.

Increased oxygenation in the Cleveland Basin during the early middle Toarcian *H. bifrons* Zone may be related to an increased influx of cool low-salinity Arctic water through the Viking Corridor, evidenced by the southward spread of high-latitude phytoplankton (*Parvocysta* – *Phallocysta* dinocyst suite) following the T-OAE (van de Schootbrugge *et al.*, 2020). Palynological evidence indicates the transition to a cooler more temperate terrestrial vegetation (Slater *et al.*, 2019) although belemnite oxygen isotope and Mg/Ca ratios point to continuing warm waters in the basin.

22. Conclusions

Well-exposed upper Pliensbachian – middle Toarcian sections in the Cleveland Basin along the North Yorkshire coast and core from the Dove's Nest borehole display a thick succession of carbonaceous mudstones incorporating a large negative $\delta^{13}\text{C}$ excursion (the T-OAE). They represent a typical expression of the T-OAE in the Boreal epicontinental seas of Europe bordering the NW Tethys Ocean although, in contrast to successions like the Posidonia Shale of the SW German Basin (e.g. at Dotternhausen), periodic intervals showing macroscopic bioturbation are absent. A uniquely comprehensive suite of palaeontological and geochemical data (elemental, isotopic and organic) available from the Yorkshire succession offers a global standard for constraining palaeoenvironmental change preceding, during and following the T-OAE.

Oxic conditions prevailed in the Cleveland Basin during the late Pliensbachian, with fossil evidence and geochemical sediment redox proxies indicating an increasing influence of dysoxic and anoxic bottom waters during the earliest Toarcian, culminating in extended euxinia at the height of the T-OAE during the late

D. semicelatum and *C. exaratum* subzones. Three short intervals of euxinia preceded the T-OAE, the oldest two occurring during the Pliensbachian – Toarcian Boundary Event, a prominent earlier negative $\delta^{13}\text{C}$ excursion. Biomarkers point to periods of PZE during these events and the T-OAE. Generally, dysoxic – anoxic, temporarily euxinic, bottom-water conditions persisted into the early middle Toarcian *D. commune* Subzone.

Redox changes in the Cleveland Basin are representative of a global pattern. An $\epsilon^{205}\text{Tl}$ increase of –6 to –4 in Pliensbachian – Toarcian sediments of the Western Canada Sedimentary Basin is attributed to a global reduction in Fe–Mn oxyhydroxide precipitation accompanying oxygen depletion. The Tl-isotope data indicate that increasing global bottom-water anoxia began at the Pliensbachian – Toarcian boundary and was sustained into the middle Toarcian *H. bifrons* Zone, representing an interval of ~2 Ma.

Redox-sensitive trace-metal and isotopic trends recorded in the Yorkshire mudstones principally reflect changes in global ocean chemistry with a secondary influence of local factors, including episodes of enhanced local basin restriction during the T-OAE. Previous suggestions of severe basin restriction and the establishment of freshwater conditions during the T-OAE are untenable. Elevated Mo, U, V and other trace-metal enrichment factors but low trace-metal/TOC ratios in T-OAE black shales reflect the global drawdown of trace metals from ocean water driven by an expansion of anoxic and euxinic seafloor area in both epicontinental seas and the deep ocean.

Globally, carbon burial rates in anoxic – euxinic basins may have increased ~500% on average during the T-OAE. Nonetheless, despite the prominence of black shale facies including the Jet Rock, Posidonia Shale and Schistes carton that characterize the T-OAE through much of NW Europe, mass balance calculations using organic matter and pyrite contents and sulfur isotope data indicate that the area provided only a minor contribution (< 10%) to the geochemical changes effecting the global ocean.

Consensus on the duration of the T-OAE negative excursion remains elusive with estimates of ~400 – 500 ka, ~800 – 900 ka, ~1 Ma or ~1.2 Ma commonly quoted. A value of 1.4 Ma is proposed here. Nonetheless, calculated rates of organic carbon burial during the T-OAE are generally low relative to modern shallow-water settings indicating that preservation rather than productivity provided the dominant control on black shale accumulation during the early Toarcian.

Modelling of the $\delta^{34}\text{S}$ increase accompanying the T-OAE incorporating drawdown of isotopically light ^{32}S by pyrite and organic sulfur burial in euxinic environments indicates that pyrite deposition in northern Europe accounted for at most 4% of the pyrite burial. Substantial additional pyrite burial is needed to drive the documented S-isotope excursion, requiring a much greater extent of euxinic conditions in the world ocean during the T-OAE, although documented heterogeneity in Toarcian seawater sulfate- $\delta^{34}\text{S}$ poses challenges for estimating global reduced-sulfur burial fluxes and the extent of oceanic anoxia.

Rhenium and Mo oceanic mass balance models incorporating data from anoxic or euxinic carbonaceous mudstones deposited in unrestricted marine settings in western Canada indicate an expansion of up to ~7% total global seafloor anoxia – euxinia, dominated by euxinia, during the early stages of the T-OAE. Similarly, estimates of organic carbon burial derived from open ocean records of Mo drawdown into reducing sediments during the T-OAE require that $\geq 3\%$ of the ocean floor was covered by euxinic bottom waters compared to < 0.3% today.

Water temperatures rose sharply by 6 – 7° C in the Cleveland Basin during the onset of the T-OAE, reflecting a global hyperthermal event. Increased temperature was likely accompanied by a reduction in salinity of ~2 psu due to regional changes in ocean circulation and a wetter climate. Water temperatures peaked in the early *C. exaratum* Subzone coincident with the $\delta^{13}\text{C}_{\text{org}}$ minimum (–32‰) and maximum TOC values (10%) that accompanied peak bottom-water euxinia evidenced by TOC/P_T, DOP_T, iron speciation, Re/Mo and other trace-metal data, an absence of bioturbation and a benthic fauna limited to intermittent influxes of low-oxygen specialist bivalves. Temperatures declined in the *H. falciferum* Subzone immediately following the T-OAE but remained several degrees higher through the early – mid-Toarcian compared to before the event. A regional change from a cool moist climate during the late Pliensbachian to a hot climate with extreme wet/dry seasons of the hyperthermal back to a warm strongly seasonal climate following the T-OAE is indicated by palynological data.

The biotic changes documented in detail from the Cleveland Basin reflect the global impact of the T-OAE. A stepped second-order mass extinction principally affecting benthic taxa resulted from the global expansion of anoxic – euxinic bottom waters in epicontinental seas, on shelves and in the deep ocean, with additional stress imposed by substantial global warming and climate change.

Increased volcanic emissions, principally CO₂, provided the primary climate driver. The peak of the main magmatic phase of the Karoo LIP coincided with the acceleration of early Toarcian global warming and immediately pre-dates the beginning of the T-OAE, with volcanic activity continuing during and immediately following the event. Like the Karoo, Ferrar-LIP activity displayed multiple magmatic pulses, contributing CO₂ that likely impacted both the Pliensbachian – Toarcian Boundary Event and the T-OAE. A significant CO₂ contribution from the Chon Aike magmatic province is considered to be unlikely.

An accelerated hydrological cycle accompanied the T-OAE hyperthermal. A large positive $^{187}\text{Os}/^{188}\text{Os}_i$ excursion in the T-OAE interval in the Cleveland Basin is consistent with a 400 – 800% increase in continental weathering rates. A coarsening-upward cycle (increasing Ti/Al ratio) and a peak in K/Al ratio reflecting a pulse of illitic clay coincident with the Os-isotope excursion further evidence the event in the Yorkshire succession. Steeply rising $^{87}\text{Sr}/^{86}\text{Sr}$ ratios through the *C. exaratum* Subzone demonstrate a high flux of radiogenic Sr from the chemical weathering of continental crust, although the stratigraphic trend is influenced by reduced sedimentation rates.

$^{187}\text{Os}/^{188}\text{Os}_i$ and $\delta^{13}\text{C}_{\text{org}}$ data from Japan, Europe and North America display patterns consistent with the Yorkshire profiles and indicate an increased global weathering rate of up to 600% through the entire T-OAE, although variation in the amplitude of the osmium isotope excursions points to inhomogeneity in the Os-isotopic composition of the Toarcian seawater. Silicate weathering and carbon burial sequestering CO₂ provided negative feedback that combined with decreasing volcanism to terminate the T-OAE hyperthermal.

Large variations in the amplitude of the negative $\delta^{13}\text{C}$ excursions recorded across the T-OAE in different archives and at different sites can be attributed to multiple factors including large stratigraphic and geographic changes in the type, proportions and composition of terrestrial and marine organic matter, regional and depth variation in water column DIC $\delta^{13}\text{C}$, mineralogical and sedimentological differences in carbonate composition and

diagenesis. A value of 3 – 4‰ $\delta^{13}\text{C}$ provides the best estimate for the primary decrease in global surface carbon reservoirs accompanying the T-OAE.

In addition to volcanic CO₂ the contribution of a highly ^{13}C -depleted source, likely biogenic CH₄, is required to explain the rapid fall and large amplitude of the negative $\delta^{13}\text{C}$ excursion characterizing the T-OAE. An initial modest rise in temperature caused by volcanic CO₂ released in the early Toarcian caused the dissociation of terrestrial and seafloor methane clathrates, CH₄ release and further warming. A melt-down of Earth's cryosphere that had expanded during the icehouse episode of the late Pliensbachian, and the rapid release of greenhouse gases, mainly as ^{13}C -depleted CH₄, drove the negative $\delta^{13}\text{C}$ excursion. However, the volume of greenhouse gas emissions may have been underestimated.

Supplementary material. To view supplementary material for this article, please visit <https://doi.org/10.1017/S0016756824000244>

Data availability. All data generated during this study are included in the Supplementary Material files for this article.

Acknowledgements. Thanks are due to Hugh Jenkyns (Oxford University), Guillaume Suan (Université de Lyon), two anonymous referees and editor Emese Bordy (University of Cape Town) for their thoughtful comments and suggestions that greatly improved the quality of this manuscript. We thank Anglo American Woodsmith Project (formerly Sirius Minerals) for allowing us to study and sample the Dove's Nest core; Howard Armstrong for help describing and sampling the core; Simon DeMars, Kate Olde and Julian Swinden provided invaluable assistance during analytical work by EA in the Kingston laboratories. Analytical costs were supported by the UK Natural Environment Research Council (I.J. grant number NE/H020756/1), (D.G. grant number NE/H021868/1).

Author contributions. **IJ:** conceptualization (equal), data curation (equal), formal analysis (equal), funding acquisition (equal), methodology (lead), validation (equal), visualization (lead), writing — original draft (lead), review & editing (lead); **EA:** conceptualization (equal), data curation (equal), formal analysis (equal), investigation (lead), methodology (supporting), validation (equal) and writing — review & editing (supporting); **DRG:** formal analysis (supporting), funding acquisition (equal) and methodology (supporting); **LGH:** conceptualization (supporting), formal analysis (supporting) and writing — review & editing (supporting); **JPTA:** conceptualization (equal), formal analysis (supporting), methodology (supporting) and writing — review & editing (supporting).

Competing interests. The authors have no potential conflicts of interest.

References

- Aberhan M and Baumiller TZ** (2003) Selective extinction among Early Jurassic bivalves: a consequence of anoxia. *Geology* **31**, 1077–1080.
- Abubakar Y, Taylor KG, Coker V, Wogelius RA and van Dongen BE** (2022) Fundamental controls on organic matter preservation in organic- and sulfur-rich hydrocarbon source rocks. *Marine and Petroleum Geology* **141**, 105684.
- Adams DD, Hurtgen MT and Sageman BB** (2010) Volcanic triggering of a biogeochemical cascade during Oceanic Anoxic Event 2. *Nature Geoscience* **3**, 201–204.
- Ader M, Sansjofre P, Halverson GP, Busigny V, Trindade RIF, Kunzmann M and Nogueira ACR** (2014) Ocean redox structure across the Late Neoproterozoic Oxygenation Event: a nitrogen isotope perspective. *Earth and Planetary Science Letters* **396**, 1–13.
- Agbi I, Ozibo B and Newton R** (2015) Pyrite framboid size distribution of the Grey Shales (Yorkshire UK) as an indication of redox conditions. *IOSR Journal of Applied Geology and Geophysics* **3**, 36–42.
- Aggett JR** (1990) The sedimentology, mineralogy and geochemistry of the Frodingham ironstone formation: implications for the genesis of ooidal

- ironstones. PhD thesis, University of Manchester, Manchester, 549 pp. Published thesis https://uomlibrary.access.preservica.com/uncategorized/IO_82f89037-72ca-469d-b569-a65e18cedea1.
- Ait-Itto F-Z, Martinez M, Price GD and Addi AA** (2018) Synchronization of the astronomical time scales in the Early Toarcian: a link between anoxia, carbon-cycle perturbation, mass extinction and volcanism. *Earth and Planetary Science Letters* **493**, 1–11.
- Ait-Itto F-Z, Price GD, Ait Addi A, Chafiki D and Mannani I** (2017) Bulk-carbonate and belemnite carbon-isotope records across the Pliensbachian–Toarcian boundary on the northern margin of Gondwana (Issouka, Middle Atlas, Morocco). *Palaeogeography, Palaeoclimatology, Palaeoecology* **466**, 128–136.
- Aitchison J** (1986) *The statistical analysis of compositional data*. New York: Chapman & Hall, 416 pp.
- Ajuaba S, Sachsenhofer RF, Bechtel A, Galasso F, Gross D, Misch D and Schneebeil-Hermann E** (2022) Biomarker and compound-specific isotope records across the Toarcian CIE at the Dormettingen section in SW Germany. *International Journal of Earth Sciences* **111**, 1631–1661.
- Al-Suwaidi AH, Ruhl M, Jenkyns HC, Damborenea SE, Manceñido MO, Condon DJ, Angelozzi GN, Kamo SL, Storm M, Riccardi AC and Hesselbo SP** (2022) New age constraints on the Lower Jurassic Pliensbachian–Toarcian Boundary at Chacay Melehue (Neuquén Basin, Argentina). *Scientific Reports* **12**, 4975.
- Algeo TJ** (2004) Can marine anoxic events draw down the trace element inventory of seawater? *Geology* **32**, 1057–1060.
- Algeo TJ and Ingall E** (2007) Sedimentary C_{org} : P ratios, paleocean ventilation, and Phanerozoic atmospheric pO_2 . *Palaeogeography, Palaeoclimatology, Palaeoecology* **256**, 130–155.
- Algeo TJ and Li C** (2020) Redox classification and calibration of redox thresholds in sedimentary systems. *Geochimica et Cosmochimica Acta* **287**, 8–26.
- Algeo TJ and Liu J** (2020) A re-assessment of elemental proxies for paleoredox analysis. *Chemical Geology* **540**, 1–12.
- Algeo TJ and Lyons TW** (2006) Mo–total organic carbon covariation in modern anoxic marine environments: implications for analysis of paleoredox and paleohydrographic conditions. *Paleoceanography* **21**, 1–23.
- Algeo TJ and Maynard JB** (2004) Trace-element behavior and redox facies in core shales of Upper Pennsylvanian Kansas-type cyclothems. *Chemical Geology* **206**, 289–318.
- Algeo TJ, Meyers PA, Robinson RS, Rowe H and Jiang GQ** (2014) Icehouse–greenhouse variations in marine denitrification. *Biogeosciences* **11**, 1273–1295.
- Algeo TJ and Rowe H** (2012) Paleoceanographic applications of trace-metal concentration data. *Chemical Geology* **324–325**, 6–18.
- Algeo TJ, Rowe H, Hower JC, Schwark L, Merrmann A and Heckel P** (2008) Changes in ocean denitrification during Late Carboniferous glacial–interglacial cycles. *Nature Geoscience* **1**, 709–714.
- Algeo TJ and Tribouillard N** (2009) Environmental analysis of paleoceanographic systems based on molybdenum–uranium covariation. *Chemical Geology* **268**, 211–225.
- Alnazghah M, Koeshidayatullah A, Al-Hussaini A, Amao A, Song H and Al-Ramadan K** (2022) Evidence for the early Toarcian Carbon Isotope Excursion (T-CIE) from the shallow marine siliciclastic red beds of Arabia. *Scientific Reports* **12**, 18124.
- Anbar AD, Creaser RA, Papanastassiou DA and Wasserburg GJ** (1992) Rhenium in seawater: confirmation of generally conservative behavior. *Geochimica et Cosmochimica Acta* **56**, 4099–4103.
- Arnold GL, Anbar AD, Barling J and Lyons TW** (2004) Molybdenum isotope evidence for widespread anoxia in mid-Proterozoic oceans. *Science* **304**, 87–90.
- Arp G, Balmuk Y, Seppelt S and Reimer A** (2023) Biostratigraphy and sedimentary sequences of the Toarcian Hainberg section (northwestern Harz foreland, northern Germany). *Zitteliana* **97**, 1–27.
- Arp G, Gropengießer S, Schulbert C, Jung D and Reimer A** (2021) Biostratigraphy and sequence stratigraphy of the Toarcian Ludwigskanal section (Franconian Alb, Southern Germany). *Zitteliana* **95**, 57–94.
- Atar E** (2015) Inorganic geochemistry and palaeoenvironments of the Early Jurassic Cleveland Basin. MSc thesis, Durham University, Durham, 93 pp. Published thesis <http://etheses.dur.ac.uk/10948/>.
- Atar E, Marz C, Aplin AC, Dellwig O, Herringshaw LG, Lamoureux-Var V, Leng MJ, Schnetger B and Wagner T** (2019a) Dynamic climate-driven controls on the deposition of the Kimmeridge Clay Formation in the Cleveland Basin, Yorkshire, UK. *Climate of the Past* **15**, 1581–1601.
- Atar E, Marz C, Schnetger B, Wagner T and Aplin A** (2019b) Local to global controls on the deposition of organic-rich muds across the Late Jurassic Laurasian Seaway. *Journal of the Geological Society* **176**, 1143–1153.
- Atkinson JW, Little CTS and Dunhill AM** (2023) Long duration of benthic ecological recovery from the early Toarcian (Lower Jurassic) mass extinction event in the Cleveland Basin, UK. *Journal of the Geological Society* **180**, jgs2022–2126.
- Baghli H, Mattioli E, Spangenberg JE, Ruebsam W, Schwark L, Bensalah M, Sebane A, Pittet B, Pellenard P and Suan G** (2022) Stratification and productivity in the Western Tethys (NW Algeria) during early Toarcian. *Palaeogeography, Palaeoclimatology, Palaeoecology* **591**, 110864.
- Bailey TR, Rosenthal Y, McArthur JM, van de Schootbrugge B and Thirlwall MF** (2003) Paleoceanographic changes of the Late Pliensbachian–Early Toarcian interval: a possible link to the genesis of an Oceanic Anoxic Event. *Earth and Planetary Science Letters* **212**, 307–320.
- Baker SJ, Hesselbo SP, Lenton TM, Duarte LV and Belcher CM** (2017) Charcoal evidence that rising atmospheric oxygen terminated Early Jurassic ocean anoxia. *Nature Communications* **8**, 15018.
- Bambach RK** (2006) Phanerozoic biodiversity mass extinctions. *Annual Review of the Earth and Planetary Sciences* **34**, 127–155.
- Banta AB, Wei JH and Welander PV** (2015) A distinct pathway for tetrahymanol synthesis in bacteria. *PNAS* **112**, 13478–13483.
- Baranyi V, Jin X, Dal Corso J, Li B and Kemp DB** (2024) Vegetation response to climate change during an Early Jurassic hyperthermal event (Jenkyns Event) from Northern China (Ordos Basin). *Palaeogeography, Palaeoclimatology, Palaeoecology* **643**, 112180.
- Baranyi V, Jin X, Dal Corso J, Shi Z, Grasby SE and Kemp DB** (2023) Collapse of terrestrial ecosystems linked to heavy metal poisoning during the Toarcian oceanic anoxic event. *Geology* **51**, 652–656.
- Barnard PC and Cooper BS** (1983) A review of geochemical data related to the northwest European gas province. In *Petroleum Geochemistry and Exploration of Europe* (ed J Brooks), pp. 19–33. Geological Society London, Special Publications 12.
- Barnes CE and Cochran JK** (1990) Uranium removal in oceanic sediments and the oceanic U balance. *Earth and Planetary Science Letters* **97**, 94–101.
- Bastias J, Spikings R, Riley T, Ulianov A, Grunow A, Chiaradia M and Hervé F** (2021) A revised interpretation of the Chon Aike magmatic province: active margin origin and implications for the opening of the Weddell Sea. *Lithos* **386–387**, 106013.
- Beerling DJ, Lomas MR and Gröcke DR** (2002) On the nature of methane gas-hydrate dissociation during the Toarcian and Aptian Oceanic Anoxic Events. *American Journal of Science* **302**, 28–49.
- Benamara A, Charbonnier G, Adatte T, Spangenberg JE and Föllmi KB** (2020) Precession-driven monsoonal activity controlled the development of the early Albian Paquier oceanic anoxic event (OAE1b): evidence from the Vocontian Basin, SE France. *Palaeogeography, Palaeoclimatology, Palaeoecology* **537**, 109406.
- Bennett WW and Canfield DE** (2020) Redox-sensitive trace metals as paleoredox proxies: a review and analysis of data from modern sediments. *Earth-Science Reviews* **204**, 103175.
- Bergman SC, Eldrett JS and Minisini D** (2021) Phanerozoic Large Igneous Province, petroleum system, and source rock links. In *Large Igneous Provinces: A Driver of Global Environmental and Biotic Changes* (eds RE Ernst, AJ Dickson and A Bekker). Geophysical Monograph Series, pp. 191–228. Hoboken NJ: American Geophysical Union and John Wiley and Sons, Inc.
- Berner RA** (1970) Sedimentary pyrite formation. *American Journal of Science* **268**, 1–23.
- Bjerrum CJ, Surlyk F, Callomon JH and Slingerland RL** (2001) Numerical paleoceanographic study of the Early Jurassic Transcontinental Laurasian Seaway. *Paleoceanography* **16**, 390–404.
- Blakey R** (2012) Paleogeography of Europe series, Cretaceous ca. 75 Ma. *Colorado Plateau Geosystems (now DeepTimeMaps™)*, Flagstaff AZ. <https://deeptimemaps.com>.

- Blakey R** (2016) Mesozoic: 180 Ma Moll_Jur, Global Paleogeography and Tectonics in Deep Time. *Colorado Plateau Geosystems (now DeepTimeMaps™)*, Flagstaff AZ. <https://deeptimemaps.com>.
- Bodin S, Fantasia A, Krencker F-N, Nebstjerg B, Christiansen L and Andrieu S** (2023) More gaps than record! A new look at the Pliensbachian/Toarcian boundary event guided by coupled chemo-sequence stratigraphy. *Palaeogeography, Palaeoclimatology, Palaeoecology* **610**, 111344.
- Bodin S, Godet A, Matera V, Steinmann P, Vermeulen J, Gardin S, Adatte T, Coccioni R and Föllmi KB** (2007) Enrichment of redox-sensitive trace metals (U, V, Mo, As) associated with the late Hauterivian Faraoni oceanic anoxic event. *International Journal of Earth Sciences (Geologisches Rundschau)* **96**, 327–341.
- Bomou B, Suan G, Schlögl J, Grosjean A-S, Suchéras-Marx B, Adatte T, Spangenberg J, Fouché S, Zacaï A, Gibert C, Brazier J-M, Perrier V, Vincent P, Janneau K and Martin JE** (2021) The palaeoenvironmental context of Toarcian vertebrate yielding shales of southern France (Hérault). In *Carbon Cycle and Ecosystem Response to the Jenkyns Event in the Early Toarcian (Jurassic)* (eds M Reolid, LV Duarte, E Mattioli and W Ruebsam), pp. 121–152. Geological Society London, Special Publications 514.
- Bond DPG, Wignall PB, Wang W, Izon G, Jiang HS, Lai XL, Sun YD, Newton RJ, Shao LY, Vedrine S and Cope H** (2010) The mid-Capitanian (Middle Permian) mass extinction and carbon isotope record of South China. *Palaeogeography, Palaeoclimatology, Palaeoecology* **292**, 282–294.
- Bougeault C, Pellenard P, Deconinck JF, Hesselbo SP, Dommergues JL, Bruneau I, Cocquerez T, Laffont R, Huret E and Thibault N** (2017) Climatic and palaeoceanographic changes during the Pliensbachian (Early Jurassic) inferred from clay mineralogy and stable isotope (C–O) geochemistry (NW Europe). *Global and Planetary Change* **149**, 139–152.
- Boulila S, Galbrun B, Huret E, Hinnov LA, Rouget I, Gardin S and Bartolini A** (2014) Astronomical calibration of the Toarcian Stage: implications for sequence stratigraphy and duration of the early Toarcian OAE. *Earth and Planetary Science Letters* **386**, 98–111.
- Boulila S, Galbrun B, Sadki D, Gardin S and Bartolini A** (2019) Constraints on the duration of the early Toarcian T-OAE and evidence for carbon-reservoir change from the High Atlas (Morocco). *Global and Planetary Change* **175**, 113–128.
- Boulila S and Hinnov LA** (2017) A review of tempo and scale of the early Jurassic Toarcian OAE: implications for carbon cycle and sea level variations. *Newsletters on Stratigraphy* **50**, 363–389.
- Bour I, Mattioli E and Pittet B** (2007) Nannofacies analysis as a tool to reconstruct palaeoenvironmental changes during the Early Toarcian anoxic event. *Palaeogeography, Palaeoclimatology, Palaeoecology* **249**, 58–79.
- Bowden SA, Farrimond P, Snape CE and Love GD** (2006) Compositional differences in biomarker constituents of the hydrocarbon, resin, asphaltene and kerogen fractions: an example from the Jet Rock (Yorkshire, UK). *Organic Geochemistry* **37**, 369–383.
- Bown PR, Lees JA and Young JR** (2004) Calcareous nannoplankton evolution and diversity through time. In *Coccolithophores: from Molecular Processes to Global Impact* (eds HR Thierstein and JR Young), pp. 481–508. Berlin Heidelberg: Springer-Verlag.
- Bradshaw MJ, Cope JCW, Cripps DW, Donovan DT, Howarth MK, Rawson PF, West IM and Wimbledon WA** (1992) Jurassic. In *Atlas of Palaeogeography and Lithofacies* (eds JCW Cope, JK Ingham and PF Rawson). Geological Society London, *Memoir* **13**, 107–129.
- Brański P** (2012) The mineralogical record of the Early Toarcian stepwise climate changes and other environmental variations (Ciechocinek Formation, Polish Basin). *Volumina Jurassica* **10**, 1–24.
- Brantley SL, Holleran ME, Jin L and Bazilevskaya E** (2013) Probing deep weathering in the Shale Hills Critical Zone Observatory, Pennsylvania (USA): the hypothesis of nested chemical reaction fronts in the subsurface. *Earth Surface Processes and Landforms* **38**, 1280–1298.
- Brazier JM, Suan G, Tacail T, Simon L, Martin JE, Mattioli E and Balter V** (2015) Calcium isotope evidence for dramatic increase of continental weathering during the Toarcian oceanic anoxic event (Early Jurassic). *Earth and Planetary Science Letters* **411**, 164–176.
- Breit GN and Wanty RB** (1991) Vanadium accumulation in carbonaceous rocks: a review of geochemical controls during deposition and diagenesis. *Chemical Geology* **91**, 83–97.
- Bruland KW and Lohan MC** (2003) Controls of trace metals in seawater. In *The Oceans and Marine Geochemistry* (ed H Elderfield), *Treatise on Geochemistry* **6**, pp. 23–47. Amsterdam: Elsevier.
- Brumsack H-J** (1989) Seawater chemistry - update on trace-metal data. *Naturwissenschaften* **76**, 99–106.
- Brumsack H-J** (2006) The trace metal content of recent organic carbon-rich sediments: implications for Cretaceous black shale formation. *Palaeogeography, Palaeoclimatology, Palaeoecology* **232**, 344–361.
- Bucefalo Palliani R, Mattioli E and Riding JB** (2002) The response of marine phytoplankton and sedimentary organic matter to the early Toarcian (Lower Jurassic) oceanic anoxic event in northern England. *Marine Micropaleontology* **46**, 223–245.
- Buckman SS** (1915) A palaeontological classification of the Jurassic rocks of the Whitby district, with a zonal table of Liassic ammonites. In *The Geology of the Country between Whitby and Scarborough* (eds C Fox-Strangways and G Barrow) *Memoirs of the Geological Survey, England and Wales*, pp. 59–102. London: HMSO.
- Burnaz L, Littke R, Grohmann S, Erbacher J, Strauss H and Amann F** (2024). Lower Jurassic (Pliensbachian–Toarcian) marine palaeoenvironment in Western Europe: sedimentology, geochemistry and organic petrology of the wells Mainzholzen and Wickensen, Hils Syncline, Lower Saxony Basin. *International Journal of Earth Sciences (Geologische Rundschau)* <https://doi.org/10.1007/s00531-023-02381-8>.
- Caldwell Steele S** (2020) Is Whitby Jet Monkey Puzzle wood? Ebor Jetworks Blog. Available at <https://whatiswhitbyjet.com/2020/08/14/is-whitby-jet-monkey-puzzle/> 14/08/2020 (accessed 14/11/2023).
- Calvert SE and Pedersen TF** (1993) Geochemistry of Recent oxic and anoxic marine sediments: implications for the geological record. *Marine Geology* **13**, 67–88.
- Calvert SE and Pedersen TF** (1996) Sedimentary geochemistry of manganese: implications for the environment of formation of manganese black shales. *Economic Geology* **91**, 36–47.
- Calvert SE and Pedersen TF** (2007) Elemental proxies for palaeoclimatic and palaeoceanographic variability in marine sediments: Interpretation and application. In *Proxies in Late Cenozoic Paleooceanography* (eds C Hillaire-Marcel and A de Vernal), pp. 568–644. Developments in Marine Geology 1, Amsterdam: Elsevier.
- Campbell CV** (1967) Lamina, laminaset, bed and bedset. *Sedimentology* **8**, 7–26.
- Canfield DE** (1994) Factors influencing organic carbon preservation in marine sediments. *Chemical Geology* **114**, 315–329.
- Caruthers AH, Smith PL and Gröcke DR** (2013) The Pliensbachian–Toarcian (Early Jurassic) extinction, a global multi-phased event. *Palaeogeography, Palaeoclimatology, Palaeoecology* **386**, 104–118.
- Caruthers AH, Smith PL and Gröcke DR** (2014) The Pliensbachian–Toarcian (Early Jurassic) extinction: a North American perspective. *Geological Society of America, Special Paper* **505**, 225–243.
- Caswell BA and Coe AL** (2013) Primary productivity controls on opportunistic bivalves during Early Jurassic oceanic deoxygenation. *Geology* **41**, 1163–1166.
- Caswell BA and Coe AL** (2014) The impact of anoxia on pelagic macrofauna during the Toarcian Oceanic Anoxic Event (Early Jurassic). *Proceedings of the Geologists' Association* **125**, 383–391.
- Caswell BA, Coe AL and Cohen AS** (2009) New range data for marine invertebrate species across the early Toarcian (Early Jurassic) mass extinction. *Journal of the Geological Society* **166**, 859–872.
- Caswell BA and Dawn SJ** (2019) Recovery of benthic communities following the Toarcian oceanic anoxic event in the Cleveland Basin, UK. *Palaeogeography, Palaeoclimatology, Palaeoecology* **521**, 114–126.
- Caswell BA and Frid CLJ** (2017) Marine ecosystem resilience during extreme deoxygenation: the Early Jurassic oceanic anoxic event. *Oecologia* **183**, 275–290.
- Caswell BA and Herringshaw L** (2023) Marine bioturbation collapse during Early Jurassic deoxygenation: implications for post-extinction marine

- ecosystem functioning. In *Conservation Palaeobiology of Marine Ecosystems* (eds R Nawrot, S Dominici, A Tomašových and M Zuschin), pp. 311–344. Geological Society of London, Special Publications 529.
- Catt JA, Gad MA, Le Riche HH and Lord AR** (1971) Geochemistry, micropalaeontology and origin of the Middle Lias ironstones in northeast Yorkshire (Great Britain). *Chemical Geology* **8**, 61–76.
- Chamley H** (1989) *Clay Sedimentology*. Berlin, Heidelberg: Springer-Verlag, 623 pp.
- Chen W, Kemp DB, He T, Newton RJ, Xiong Y, Jenkyns HC, Izumi K, Cho T, Huang C and Poulton SW** (2023) Shallow-and deep-ocean Fe cycling and redox evolution across the Pliensbachian–Toarcian boundary and Toarcian Oceanic Anoxic Event in Panthalassa. *Earth and Planetary Science Letters* **602**, 1–12.
- Chen WH, Kemp DB, He TC, Huang CJ, Jin SM, Xiong YJ and Newton RJ** (2021) First record of the early Toarcian Oceanic Anoxic Event in the Hebrides Basin (UK) and implications for redox and weathering changes. *Global and Planetary Change* **207**, 103685.
- Cheng K, Elrick M and Romaniello SJ** (2020) Early Mississippian ocean anoxia triggered organic carbon burial and late Paleozoic cooling: evidence from uranium isotopes recorded in marine limestone. *Geology* **48**, 363–367.
- Chowins TM** (1966) Depositional environment of the Cleveland Ironstone Series. *Nature* **211**, 1286–1287.
- Chowins TM** (1968) Environmental and diagenetic studies of the Cleveland Ironstone Formation of north east Yorkshire. PhD thesis, Newcastle University, Newcastle upon Tyne, 432 pp. Published thesis <http://theses.ncl.ac.uk/jspui/handle/10443/268>.
- Clarkson MO, Stirling CH, Jenkyns HC, Dickson AJ, Porcelli D, Moy CM, Pogge von Strandman PAE, Cooke IR and Lenton TM** (2018) Uranium isotope evidence for two episodes of deoxygenation during Oceanic Anoxic Event 2. *Proceedings of the National Academy of Sciences* **115**, 2918–2923.
- Claypool GE, Holzer WT, Kaplan IR, Sakai H and Zak I** (1980) The age curve of sulphur and oxygen isotopes in marine sulphates and their mutual interpretation. *Chemical Geology* **28**, 199–260.
- Clémence ME, Gardin S and Bartolini A** (2015) New insights in the pattern and timing of the Early Jurassic calcareous nannofossil crisis. *Palaeogeography, Palaeoclimatology, Palaeoecology* **427**, 100–108.
- Cochlan WP and Harrison PJ** (1991) Kinetics of nitrogen (nitrate, ammonium and urea) uptake by the picoflagellate *Micromonas pusilla* (Prasinophyceae). *Journal of Experimental Marine Biology and Ecology* **153**, 129–141.
- Cohen AS** (2004) The rhenium–osmium isotope system: applications to geochronological and palaeoenvironmental problems. *Journal of the Geological Society* **161**, 729–734.
- Cohen AS and Coe AL** (2007) The impact of the Central Atlantic Magmatic Province on climate and on the Sr- and Os-isotope evolution of seawater. *Palaeogeography, Palaeoclimatology, Palaeoecology* **244**, 374–390.
- Cohen AS, Coe AL, Bartlett JM and Hawkesworth CJ** (1999) Precise Re–Os ages of organic-rich mudrocks and the Os isotope composition of Jurassic seawater. *Earth and Planetary Science Letters* **167**, 159–173.
- Cohen AS, Coe AL, Harding SM and Schwark L** (2004) Osmium isotope evidence for the regulation of atmospheric CO₂ by continental weathering. *Geology* **32**, 157–160.
- Cohen AS, Coe AL and Kemp DB** (2007) The Late Palaeocene–Early Eocene and Toarcian (Early Jurassic) carbon isotope excursions: a comparison of their time scales, associated environmental changes, causes and consequences. *Journal of the Geological Society* **164**, 1093–1108.
- Cole DB, Planavsky NJ, Longley M, Böning P, Wilkes D, Wang X, Swanner ED, Wittkop C, Loydell DK, Busigny V, Knudsen AC and Sperling EA** (2020) Uranium isotope fractionation in non-sulfidic anoxic settings and the global uranium isotope mass balance. *Global Biogeochemical Cycles* **34**, e2020GB006649.
- Coleman ML and Raiswell R** (1981) Carbon, oxygen and sulphur isotope variations in concretions from the Upper Lias of N.E. England. *Geochimica et Cosmochimica Acta* **45**, 329–340.
- Colodner DC, Boyle EA and Edmond JM** (1993a) Determination of rhenium and platinum in natural waters and sediments, and iridium in sediments by flow injection isotope dilution inductively coupled plasma mass spectrometry. *Analytical Chemistry* **65**, 1419–1425.
- Colodner DC, Sachs J, Ravizza G, Turekian K, Edmond J and Boyle E** (1993b) The geochemical cycle of rhenium: a reconnaissance. *Earth and Planetary Science Letters* **117**, 205–221.
- Comas-Rengifo MJ, Arias C, Gómez JJ, Goy A, Herrero C, Osete ML and Palencia A** (2010) A complementary section for the proposed Toarcian (Lower Jurassic) global stratotype: the Almonacid de la Cuba section (Spain). *Stratigraphy and Geological Correlation* **18**, 133–152.
- Condie KC** (1993) Chemical composition and evolution of the upper continental crust: contrasting results from surface samples and shales. *Chemical Geology* **104**, 1–37.
- Cope JCW, Getty TA, Howarth MK, Morton N and Torrens HS** (1980) A Correlation of Jurassic Rock in the British Isles Part One: Introduction and Lower Jurassic. Geological Society London, Special Report 14, Oxford: Blackwell, 73 pp.
- Cox BM, Sumblar MG and Ivimey-Cook HC** (1999) A formational framework for the Lower Jurassic of England and Wales (onshore area). British Geological Survey Research Report RR/99/01, Keyworth, 28 pp.
- Cramer BS and Jarvis I** (2020) Carbon isotope stratigraphy. In *The Geologic Time Scale 2020* (eds F Gradstein, JG Ogg and G Ogg), **1**, pp. 309–343. Amsterdam: Elsevier.
- Crusius J, Calvert SE, Pedersen TF and Sage D** (1996) Rhenium and molybdenum enrichments in sediments as indicators of oxic, suboxic and sulfidic conditions of deposition. *Earth and Planetary Science Letters* **145**, 65–78.
- Cumberland SA, Douglas G, Grice K and Moreau JW** (2016) Uranium mobility in organic matter-rich sediments: a review of geological and geochemical processes. *Earth-Science Reviews* **159**, 160–185.
- da Rocha RB, Mattioli E, Duarte LV, Pittet B, Elmi S, Mouterde R, Cabral MC, Comas-Rengifo MJ, Gomez JJ, Goy A, Hesselbo SP, Jenkyns HC, Littler K, Mailliot S, de Oliveira LCV, Osete ML, Perilli N, Pinto S, Ruget C and Suan G** (2016) Base of the Toarcian Stage of the Lower Jurassic defined by the Global Boundary Stratotype Section and Point (GSSP) at the Peniche section (Portugal). *Episodes* **39**, 460–481.
- Danise S, Clemence ME, Price GD, Murphy DP, Gomez JJ and Twitchett RJ** (2019) Stratigraphic and environmental control on marine benthic community change through the early Toarcian extinction event (Iberian Range, Spain). *Palaeogeography, Palaeoclimatology, Palaeoecology* **524**, 183–200.
- Danise S, Slater SM, Vajda V and Twitchett RJ** (2022) Land-sea ecological connectivity during a Jurassic warming event. *Earth and Planetary Science Letters* **578**, 117290.
- Danise S, Twitchett RJ and Little CTS** (2015) Environmental controls on Jurassic marine ecosystems during global warming. *Geology* **43**, 263–266.
- Danise S, Twitchett RJ, Little CTS and Clémence M-E** (2013) The impact of global warming and anoxia on marine benthic community dynamics: an example from the Toarcian (Early Jurassic). *Plos One* **8**, 1–14.
- De Baets K, Nätscher PS, Rita P, Fara E, Neige P, Bardin J, Dera G, Duarte LV, Hughes Z, Laschinger P, Garcia-Ramos JC, Piñuela L, Übelacker C and Weis R** (2021) The impact of the Pliensbachian–Toarcian crisis on belemnite assemblages and size distribution. *Swiss Journal of Palaeontology* **140**, 1–14.
- de Graciansky P-C, Dardeau G, Dommergues JL, Durllet C, Marchand D, Dumont T, Hesselbo SP, Jacquin T, Goggin V, Meister C, Mouterde R, Rey J and Vail PR** (1998) Ammonite biostratigraphic correlation and Early Jurassic sequence stratigraphy in France: Comparisons with some U.K. sections. In *Mesozoic and Cenozoic Sequence Stratigraphy of European Basins* (eds P-C de Graciansky, J Hardenbol, T Jacquin and PR Vail). SEPM, Special Publication 60, 583–622.
- de Lange GJ, Jarvis I and Kuijpers A** (1987) Geochemical characteristics and provenance of late Quaternary sediments from the Madeira Abyssal Plain, N. Atlantic. In *Geology and Geochemistry of Abyssal Plains* (eds PPE Weaver and J Thomson). Geological Society London, Special Publications **31**, 147–165.
- De Lena LF, Taylor D, Guex J, Bartolini A, Adatte T, van Acken D, Spangenberg JE, Samankassou E, Vennemann T and Schaltegger U** (2019) The driving mechanisms of the carbon cycle perturbations in the late Pliensbachian (Early Jurassic). *Scientific Reports* **9**, 18430.

- de Vos R (2017) Textural and mineralogical characterization of the late Pliensbachian–early Toarcian sediments of the Cleveland Basin, Yorkshire, U.K. MSc thesis, Utrecht University, Utrecht, 86 pp. Published thesis <https://studenttheses.uu.nl/handle/20.500.12932/28170>.
- Dean WE, Arthur MA and Stow DAV (1984) Origin and geochemistry of Cretaceous deep-sea black shales and multicolored claystones, with emphasis on Deep–Sea Drilling Project Site 530, southern Angola Basin. *Initial Reports of the Deep Sea Drilling Project* 75, 819–844.
- Deconinck JF, Hesselbo SP and Pellenard P (2019) Climatic and sea-level control of Jurassic (Pliensbachian) clay mineral sedimentation in the Cardigan Bay Basin, Llanbedr (Mochras Farm) borehole, Wales. *Sedimentology* 66, 2769–2783.
- Deegan FM, Bédard JH, Grasby SE, Dewing K, Geiger H, Misiti V, Capriola M, Callegaro S, Svensen HH, Yakymchuk C, Aradi LE, Fedá C and Troll VR (2022) Magma–shale interaction in large igneous provinces: implications for climate warming and sulfide genesis. *Journal of Petrology* 63, 1–10.
- Dera G, Brigaud B, Monna F, Laffont R, Pucaat E, Deconinck JF, Pellenard P, Joachimski MM and Durllet C (2011) Climatic ups and downs in a disturbed Jurassic world. *Geology* 39, 215–218.
- Dera G and Donnadieu Y (2012) Modeling evidences for global warming, Arctic seawater freshening, and sluggish oceanic circulation during the Early Toarcian anoxic event. *Paleoceanography* 27, PA2211.
- Dera G, Neige P, Dommergues J-L, Fara E, Laffont R and Pellenard P (2010) High-resolution dynamics of Early Jurassic marine extinctions: the case of Pliensbachian–Toarcian ammonites (Cephalopoda). *Journal of the Geological Society* 167, 21–33.
- Dera G, Pellenard P, Neige P, Deconinck J-F, Pucéat E and Dommergues J-L (2009) Distribution of clay minerals in Early Jurassic Peritethyan seas: palaeoclimatic significance inferred from multiproxy comparisons. *Palaeogeography, Palaeoclimatology, Palaeoecology* 271, 39–51.
- Dickens GR, Oneil JR, Rea DK and Owen RM (1995) Dissociation of oceanic methane hydrate as a cause of the carbon-isotope excursion at the end of the Paleocene. *Paleoceanography* 10, 965–971.
- Dickson AJ (2017) A molybdenum-isotope perspective on Phanerozoic deoxygenation events. *Nature Geoscience* 10, 721–726.
- Dickson AJ, Davies M, Bagard M-L and Cohen AS (2022a) Quantifying seawater exchange rates in the Eocene Arctic Basin using osmium isotopes. *Geochemical Perspective Letters* 24, 7–11.
- Dickson AJ, Gill BC, Ruhl M, Jenkyns HC, Porcelli D, Idiz E, Lyons TW and van den Boorn SHJM (2017) Molybdenum-isotope chemostratigraphy and paleoceanography of the Toarcian Oceanic Anoxic Event (Early Jurassic). *Paleoceanography* 32, 813–829.
- Dickson AJ, Hsieh Y-T and Bryan A (2020) The rhenium isotope composition of Atlantic Ocean seawater. *Geochimica et Cosmochimica Acta* 287, 221–228.
- Dickson AJ, Idiz E, Porcelli D, Murphy MJ, Celestino R, Jenkyns HC, Poulton SW, Hesselbo SP, Hooker JN, Ruhl M and van der Boorn SHJM (2022b) No effect of thermal maturity on the Mo, U, Cd, and Zn isotope compositions of Lower Jurassic organic-rich sediments. *Geology* 50, 598–602.
- Dinis P, Garzanti E, Vermeesch P and Huvi J (2017) Climatic zonation and weathering control on sediment composition (Angola). *Chemical Geology* 467, 110–121.
- Donohue JG, Florio BJ and Fowler AC (2023) The development of deep-ocean anoxia in a comprehensive ocean phosphorus model. *GEM - International Journal on Geomathematics* 14, 12.
- Doyle P (1990) The British Toarcian (Lower Jurassic) belemnites. *Monographs of the Paleontological Society* 144, 1–49.
- Dunham KC (1961) Black shale, oil and sulphide ore. *Advancement of Science* 18, 284–299.
- Emerson SR and Husted SS (1991) Ocean anoxia and the concentration of molybdenum and vanadium in seawater. *Marine Chemistry* 34, 177–196.
- Endrizzi F and Rao L (2014) Chemical speciation of uranium(VI) in marine environments: complexation of calcium and magnesium ions with $[(\text{UO}_2)(\text{CO}_3)_3]^{4-}$ and the effect on the extraction of uranium from seawater. *Chemistry A European Journal* 20, 14499–14506.
- Erba E (2004) Calcareous nannofossils and Mesozoic oceanic anoxic events. *Marine Micropaleontology* 52, 85–106.
- Erba E, Bottini C, Faucher G, Gambacorta G and Visentin S (2019) The response of calcareous nannoplankton to Oceanic Anoxic Events: the Italian pelagic record. *Bollettino della Società Paleontologica Italiana* 58, 51–71.
- Erba E, Cavalheiro L, Dickson AJ, Faucher G, Gambacorta G, Jenkyns HC and Wagner T (2022) Carbon- and oxygen-isotope signature of the Toarcian Oceanic Anoxic Event: insights from two Tethyan pelagic sequences (Gajum and Sogno Cores – Lombardy Basin, northern Italy). *Newsletters on Stratigraphy* 55, 451–477.
- Ernst TW (1970) *Geochemical Facies Analysis*. Amsterdam: Elsevier, 152 pp.
- Espitalié J, Deroo G and Marquis F (1985) La pyrolyse Rock-Eval et ses applications. Deuxième partie. *Revue de l'Institut français du Pétrole* 40, 755–784.
- Ettinger NP, Larson TE, Kerans C, Thibodeau AM, Hattori KE, Kacur SM and Martindale RC (2021) Ocean acidification and photic-zone anoxia at the Toarcian Oceanic Anoxic Event: insights from the Adriatic Carbonate Platform. *Sedimentology* 68, 63–107.
- Fagel N (2007) Clay minerals, deep circulation and climate. In *Proxies in Late Cenozoic Paleoclimatology* (eds C Hillaire-Marcel and A De Vernal), pp. 139–184. Developments in Marine Geology 1, Amsterdam: Elsevier.
- Fan H, Nielsen SG, Owens JD, Auro M, Shu SA, Hardisty DS, Horner TJ, Bowman CN, Young SA and Wen H (2020) Constraining oceanic oxygenation during the Shuram excursion in South China using thallium isotopes. *Geobiology* 18, 348–365.
- Fantasia A, Adatte T, Spangenberg JE, Font E, Duarte LV and Föllmi KB (2019) Global versus local processes during the Pliensbachian–Toarcian transition at the Peniche GSSP, Portugal: a multi-proxy record. *Earth-Science Reviews* 198, 1–16.
- Fantasia A, Föllmi KB, Adatte T, Bernárdez E, Spangenberg JE and Mattioli E (2018a) The Toarcian Oceanic Anoxic Event in southwestern Gondwana: an example from the Andean Basin, northern Chile. *Journal of the Geological Society* 175, 883–902.
- Fantasia A, Föllmi KB, Adatte T, Spangenberg JE and Montero-Serrano J-C (2018b) The Early Toarcian oceanic anoxic event: paleoenvironmental and paleoclimatic change across the Alpine Tethys (Switzerland). *Global and Planetary Change* 162, 53–68.
- Faucher G, Visentin S, Gambacorta G and Erba E (2022) *Schizosphaerella* size and abundance variations across the Toarcian Oceanic Anoxic Event in the Sogno Core (Lombardy Basin, Southern Alps). *Palaeogeography, Palaeoclimatology, Palaeoecology* 595, 1–15.
- Fendley IM, Frieling J, Mather TA, Ruhl M, Hesselbo SP and Jenkyns HC (2024) Early Jurassic large igneous province carbon emissions constrained by sedimentary mercury. *Nature Geoscience*, <https://doi.org/10.1038/s41561-024-01378-5>.
- Fernández-Martínez J, Martínez Ruiz F, Rodríguez-Tovar FJ, Piñuela L, García-Ramos JC and Algeo TJ (2023) Euxinia and hydrographic restriction in the Tethys Ocean: reassessing global oceanic anoxia during the early Toarcian. *Global and Planetary Change* 221, 1–13.
- Ferrari M, Little CTS and Atkinson JW (2021) Upper Toarcian (Lower Jurassic) marine gastropods from the Cleveland Basin, England: systematics, palaeobiogeography and contribution to biotic recovery from the early Toarcian extinction event. *Papers in Palaeontology* 7, 885–912.
- Filatova NI, Konstantinovskaya E and Vishnevskaya V (2022) Jurassic-Lower Cretaceous siliceous rocks and black shales from allochthonous complexes of the Koryak–Western Kamchatka orogenic belt, East Asia. *International Geology Review* 64, 311–330.
- Fleischmann S, Picotti V, Caves Rugenstein JK, Cobianchi M and Bernasconi SM (2022) Effects of the Pliensbachian–Toarcian Boundary Event on carbonate productivity of a Tethyan platform and slope. *Paleoceanography and Paleoclimatology* 37, e2021PA004392.
- Föllmi KB, Badertscher C, de Kaenel E, Stille P, John CM, Adatte T and Steinmann P (2005) Phosphogenesis and organic-carbon preservation in the Miocene Monterey Formation at Naples beach, California – The Monterey Hypothesis revisited. *Geological Society of America Bulletin* 117, 589–619.
- Foster GL, Hull P, Lunt D and Zachos J (2018) Placing our current ‘hyperthermal’ in the context of rapid climate change in our geological past. *Philosophical Transactions of the Royal Society A* 375, 20170086.

- Fox-Strangways C** (1892) *The Jurassic Rocks of Britain. Vol. 1. Yorkshire.* Memoirs of the Geological Survey of the United Kingdom. London: HMSO, 551 pp.
- Fraguas A, Gómez JJ, Goy A and Comas-Rengifo MJ** (2021) The response of calcareous nannoplankton to the latest Pliensbachian–early Toarcian environmental changes in the Camino Section (Basque Cantabrian Basin, northern Spain). In *Carbon Cycle and Ecosystem Response to the Jenkyns Event in the Early Toarcian (Jurassic)* (eds M Reolid, LV Duarte, E Mattioli and W Ruebsam), pp. 31–58. Geological Society London, Special Publications 514.
- French KL, Sepulveda J, Trabucho-Alexandre J, Gröcke DR and Summons RE** (2014) Organic geochemistry of the early Toarcian oceanic anoxic event in Hawsker Bottoms, Yorkshire, England. *Earth and Planetary Science Letters* **390**, 116–127.
- Fu X, Wang J, Wen H, Song C, Wang Z, Zeng S, Feng X and Wei H** (2021) A Toarcian Ocean Anoxic Event record from an open-ocean setting in the eastern Tethys: implications for global climatic change and regional environmental perturbation. *Science China Earth Sciences* **64**, 1860–1872.
- Fu X, Wang J, Zeng S, Feng X, Wang D and Song C** (2017) Continental weathering and palaeoclimatic changes through the onset of the Early Toarcian oceanic anoxic event in the Qiangtang Basin, eastern Tethys. *Palaeogeography, Palaeoclimatology, Palaeoecology* **487**, 241–250.
- Gad MA** (1966) A geochemical study of the Liassic rocks of the Yorkshire coast. PhD thesis, University of London, London, 269 pp. Published thesis <https://ethos.bl.uk/OrderDetails.do?uin=uk.bl.ethos.761665>.
- Gad MA, Catt JA and Le Riche HH** (1969) Geochemistry of the Whitbian (Upper Lias) sediments of the Yorkshire coast. *Proceedings of the Yorkshire Geological Society* **37**, 105–136.
- Galasso F, Feist-Burkhardt S and Schneebeli-Hermann E** (2022) The palynology of the Toarcian Oceanic Anoxic Event at Dormettingen, southwest Germany, with emphasis on changes in vegetational dynamics. *Review of Palaeobotany and Palynology* **304**, 1–33.
- Gambacorta G, Brumsack H-J, Jenkyns HC and Erba E** (2024) The early Toarcian Oceanic Anoxic Event (Jenkyns Event) in the Alpine-Mediterranean Tethys, north African margin, and north European epicontinental seaway. *Earth-Science Reviews* **248**, 104636.
- Gambacorta G, Cavalheiro L, Brumsack H-J, Dickson AJ, Jenkyns HC, Schnetger B, Wagner T and Erba E** (2023) Suboxic conditions prevailed during the Toarcian Oceanic Anoxic Event in the Alpine-Mediterranean Tethys: the Sogno Core pelagic record (Lombardy Basin, northern Italy). *Global and Planetary Change* **223**, 104089.
- Gangl SK, Stirling CH, Jenkyns HC, Preston WJ, Clarkson MO, Moy CM, Dickson AJ and Porcelli D** (2023) Regional conditions cause contrasting behaviour in U-isotope fractionation in black shales: constraints for global ocean palaeo-redox reconstructions. *Chemical Geology* **623**, 121411.
- García Joral F, Gómez JJ and Goy A** (2011) Mass extinction and recovery of the Early Toarcian (Early Jurassic) brachiopods linked to climate change in Northern and Central Spain. *Palaeogeography, Palaeoclimatology, Palaeoecology* **302**, 367–380.
- Garzanti E, Padoan M, Setti M, López-Galindo A and Villa IM** (2014) Provenance versus weathering control on the composition of tropical river mud (southern Africa). *Chemical Geology* **366**, 61–74.
- Gaynor SP, Svensen HH, Polteau S and Schaltegger U** (2022) Local melt contamination and global climate impact: dating the emplacement of Karoo LIP sills into organic-rich shale. *Earth and Planetary Science Letters* **579**, 1–10.
- Ghadeer S** (2011) An investigation of the sediment dispersal operating to control lithofacies variability and organic carbon preservation in an ancient mud-dominated succession: a case study of the Lower Jurassic mudstone dominated succession exposed in the Cleveland Basin (North Yorkshire). PhD thesis, University of Manchester, Manchester, 196 pp. Published thesis https://pure.manchester.ac.uk/ws/portalfiles/portal/54510396/full_text.pdf.
- Ghadeer SG and Macquaker JHS** (2011) Sediment transport processes in an ancient mud-dominated succession: a comparison of processes operating in marine offshore settings and anoxic basinal environments. *Journal of the Geological Society* **168**, 1121–1132.
- Gibbs RJ** (1977) Clay mineral segregation in the marine environment. *Journal of Sedimentary Petrology* **47**, 237–242.
- Gill BC, Lyons TW and Jenkyns HC** (2011) A global perturbation to the sulfur cycle during the Toarcian Oceanic Anoxic Event. *Earth and Planetary Science Letters* **312**, 484–496.
- Godet A, Bodin S, Adatte T and Föllmi KB** (2008) Platform-induced clay-mineral fractionation along a northern Tethyan basin-platform transect: implications for the interpretation of Early Cretaceous climate change (Late Hauterivian–Early Aptian). *Cretaceous Research* **29**, 830–847.
- Gómez JJ, Comas-Rengifo MJ and Goy A** (2016) Palaeoclimatic oscillations in the Pliensbachian (Early Jurassic) of the Asturian Basin (Northern Spain). *Climate of the Past* **12**, 1199–1214.
- Gómez JJ and Goy A** (2011) Warming-driven mass extinction in the Early Toarcian (Early Jurassic) of northern and central Spain. Correlation with other time-equivalent European sections. *Palaeogeography, Palaeoclimatology, Palaeoecology* **306**, 176–195.
- Gómez JJ, Goy A and Canales ML** (2008) Seawater temperature and carbon isotope variations in belemnites linked to mass extinction during the Toarcian (Early Jurassic) in central and northern Spain. Comparison with other European sections. *Palaeogeography, Palaeoclimatology, Palaeoecology* **258**, 28–58.
- González López JM, Bauluz B, Yuste A, Mayayo MJ and Fernández-Nieto C** (2005) Mineralogical and trace element composition of clay-sized fractions from Albian siliciclastic rocks (Oliete Basin, NE Spain). *Clay Minerals* **40**, 565–580.
- Gradstein FM, Ogg JG, Schmitz MD and Ogg GM, eds.** (2020) *Geologic Time Scale 2020*, 1357 pp. Amsterdam: Elsevier.
- Grasby SE, Them TR II, Chen ZH, Yin RS and Ardakani OH** (2019) Mercury as a proxy for volcanic emissions in the geologic record. *Earth-Science Reviews* **196**, 102880.
- Greber ND, Davies JHFL, Gaynor SP, Jourdan F, Bertrand H and Schaltegger U** (2020) New high precision U–Pb ages and Hf isotope data from the Karoo large igneous province; implications for pulsed magmatism and early Toarcian environmental perturbations. *Results in Geochemistry* **1**, 100005.
- Greensmith JT, Rawson PF and Shalaby SE** (1980) An association of minor fining-upward cycles and aligned gutter marks in the Middle Lias (Lower Jurassic) of the Yorkshire coast. *Proceedings of the Yorkshire Geological Society* **42**, 525–538.
- Grice K and Eiserbeck C** (2014) The analysis and application of biomarkers. In *Treatise on Geochemistry* (2nd Edn) (eds HD Holland and KK Turekian), **12**, pp. 47–78. Amsterdam: Elsevier.
- Gröcke DR, Hori RS, Trabucho-Alexandre J, Kemp DB and Schwark L** (2011) An open ocean record of the Toarcian oceanic anoxic event. *Solid Earth* **2**, 245–257.
- Gröcke DR, Rimmer SM, Yoksoulian LE, Cairncross B, Tsikos H and van Hunen J** (2009) No evidence for thermogenic methane release in coal from the Karoo–Ferrar large igneous province. *Earth and Planetary Science Letters* **277**, 204–212.
- Guex J, Pilet S, Müntener O, Bartolini A, Spangenberg J, Schoene B, Sell B and Schaltegger U** (2016) Thermal erosion of cratonic lithosphere as a potential trigger for mass-extinction. *Scientific Reports* **6**, 23168.
- Hall A and Bishop P** (2002) Scotland's denudational history: An integrated view of erosion and sedimentation at an uplifted passive margin. In *Exhumation of the North Atlantic Margin: Timing, Mechanisms and Implications for Petroleum Exploration* (eds AG Doré, JA Cartwright, MS Stoker, JP Turner and N White), pp. 271–290. Geological Society London, Special Publications 196.
- Hallam A** (1962) A band of extraordinary calcareous concretions in the Upper Lias of Yorkshire, England. *Journal of Sedimentary Petrology* **32**, 840–847.
- Hallam A** (1986) The Pliensbachian and Tithonian extinction events. *Nature* **319**, 765–768.
- Hallam A** (1997) Estimates of the amount and rate of sea-level change across the Rhaetian–Hettangian and Pliensbachian–Toarcian boundaries (latest Triassic to early Jurassic). *Journal of the Geological Society* **154**, 773–779.

- Hallam A (2001) A review of the broad pattern of Jurassic sea-level changes and their possible causes in the light of current knowledge. *Palaeogeography, Palaeoclimatology, Palaeoecology* **167**, 23–37.
- Hallimond AF, Ennos FR and Sutcliffe R (1925) Iron Ores: Bedded Ores of England and Wales. Petrography and Chemistry. Memoirs of the Geological Survey Special Reports on the Mineral Resources of Great Britain 29, London: HMSO, 139 pp.
- Hammer Ø, Harper DAT and Ryan PD (2001) PAST: Paleontological Statistics Software Package for Education and Data Analysis. *Palaeontologia Electronica* **4**, 1–9.
- Han Z, Hu X, He T, Newton RJ, Jenkyns HC, Jamieson RA and Franceschi M (2022) Early Jurassic long-term oceanic sulfur-cycle perturbations in the Tibetan Himalaya. *Earth and Planetary Science Letter* **578**, 1–13.
- Han Z, Hu X, Newton RJ, He T, Mills BJW, Jenkyns HC, Ruhl M and Jamieson RA (2023) Spatially heterogeneous seawater $\delta^{34}\text{S}$ and global cessation of Ca-sulfate burial during the Toarcian oceanic anoxic event. *Earth and Planetary Science Letters* **622**, 118404.
- Haq BU (2018) Jurassic sea-level variations: a reappraisal. *GSA Today* **28**, 4–10.
- Hardenbol J, Thierry J, Farley MB, Jacquin T, Graciansky P-Cd and Vail PR (1998) Mesozoic and Cenozoic sequence chronostratigraphic framework in European basins. In *Mesozoic and Cenozoic Sequence Stratigraphy of European Basins* (eds P-Cd Graciansky, J Hardenbol, T Jacquin and PR Vail), pp. 3–13. SEPM, Special Publication 60.
- Hardisty DS, Lyons TW, Riedinger N, Isson TT, Owens JD, Aller RC, Rye DM, Planavsky NJ, Reinhard CT, Gill BC, Masterson AL, Asael D and Johnston DT (2018) An evaluation of sedimentary molybdenum and iron as proxies for pore fluid paleoredox conditions. *American Journal of Science* **318**, 527–556.
- Harries PJ and Little CTS (1999) The early Toarcian (Early Jurassic) and the Cenomanian–Turonian (Late Cretaceous) mass extinctions: similarities and contrasts. *Palaeogeography, Palaeoclimatology, Palaeoecology* **154**, 39–66.
- Hartnett HE, Keil RG, Hedges JI and Devol AH (1998) Influence of oxygen exposure time on organic carbon preservation in continental margin sediments. *Nature* **391**, 572–574.
- Hawco NJ, Lam PJ, Lee J-M, Ohnemus DC, Noble AE, Wyatt NJ, Lohan MC and Saito MA (2018) Cobalt scavenging in the mesopelagic ocean and its influence on global mass balance: synthesizing water column and sedimentary fluxes. *Marine Chemistry* **201**, 151–166.
- Hazen RM, Ewing RC and Sverjensky DA (2009) Evolution of uranium and thorium minerals. *American Mineralogist* **94**, 1293–1311.
- He ZW, Clarkson MO, Andersen M, Archer C, Sweere TC, Kraal P, Guthausen A, Huang F and Vance D (2021) Temporally and spatially dynamic redox conditions on an upwelling margin: the impact on coupled sedimentary Mo and U isotope systematics, and implications for the Mo–U paleoredox proxy. *Geochimica et Cosmochimica Acta* **309**, 251–271.
- Head MJH, Aubry M-P, Piller WE and Walker M (2023) Standard Auxiliary Boundary Stratotype (SABS) approved to support the Global boundary Stratotype Section and Point (GSSP). *Episodes* **46**, 99–100.
- Hecky RE, Campbell M and Hendzel LL (1993) The stoichiometry of carbon, nitrogen, and phosphorus in particulate matter of lakes and oceans. *Limnology and Oceanography* **38**, 709–724.
- Heimdal TH, Godd eris Y, Jones MT and Svensen HH (2021) Assessing the importance of thermogenic degassing from the Karoo Large Igneous Province (LIP) in driving Toarcian carbon cycle perturbations. *Nature Communications* **12**, 1–7.
- Helly JJ and Levin LA (2004) Global distribution of naturally occurring marine hypoxia on continental margins. *Deep-Sea Research I* **51**, 1159–1168.
- Helz GR and Adelson JM (2013) Trace element profiles in sediments as proxies of dead zone history; rhenium compared to molybdenum. *Environmental Science and Technology* **47**, 1257–1264.
- Hemingway JE (1933) *Whitby jet and its relation to Upper Lias sedimentation in the Yorkshire basin*. PhD thesis, University of Leeds, Leeds, 119 pp. Published thesis https://etheses.whiterose.ac.uk/2312/1/uk_bl_ethos_539893.pdf.
- Hemingway JE (1974) Jurassic. In *The Geology and Mineral Resources of Yorkshire* (eds DH Rayner and JE Hemingway), pp. 161–223. Leeds: Maney and Son.
- Hermoso M, Le Callonnec L, Minoletti F, Renard M and Hesselbo SP (2009a) Expression of the Early Toarcian negative carbon-isotope excursion in separated carbonate microfractions (Jurassic, Paris Basin). *Earth and Planetary Science Letters* **277**, 194–203.
- Hermoso M, Minoletti F, Le Callonnec L, Jenkyns HC, Hesselbo SP, Rickaby REM, Renard M, de Rafelis M and Emmanuel L (2009b) Global and local forcing of Early Toarcian seawater chemistry: a comparative study of different paleoceanographic settings (Paris and Lusitanian basins). *Paleoceanography* **24**, PA4208.
- Hermoso M, Minoletti F and Pellenard P (2013) Black shale deposition during Toarcian super-greenhouse driven by sea level. *Climate of the Past* **9**, 2703–2712.
- Hermoso M, Minoletti F, Rickaby REM, Hesselbo SP, Baudin F and Jenkyns HC (2012) Dynamics of a stepped carbon-isotope excursion: ultra high-resolution study of Early Toarcian environmental change. *Earth and Planetary Science Letters* **319**, 45–54.
- Hermoso M and Pellenard P (2014) Continental weathering and climatic changes inferred from clay mineralogy and paired carbon isotopes across the early to middle Toarcian in the Paris Basin. *Palaeogeography, Palaeoclimatology, Palaeoecology* **399**, 385–393.
- Hesselbo SP (2008) Sequence stratigraphy and inferred relative sea-level change from the onshore British Jurassic. *Proceedings of the Geologists' Association* **119**, 19–34.
- Hesselbo SP, Gr ocke DR, Jenkyns HC, Bjerrum CJ, Farrimond P, Bell HSM and Green OR (2000) Massive dissociation of gas hydrate during a Jurassic oceanic anoxic event. *Nature* **406**, 392–395.
- Hesselbo SP, Jenkyns HC, Duarte LV and Oliveira LCV (2007) Carbon-isotope record of the Early Jurassic (Toarcian) Oceanic Anoxic Event from fossil wood and marine carbonate (Lusitanian Basin, Portugal). *Earth and Planetary Science Letters* **253**, 455–470.
- Hesselbo SP and Jenkyns HC (1995) A comparison of the Hettangian to Bajocian successions of Dorset and Yorkshire. In *Field Geology of the British Jurassic* (ed PD Taylor), pp. 105–150. London: The Geological Society.
- Hesselbo SP and King C (2019) Stratigraphic framework for the Yorkshire Lias. In *Fossils from the Lias of the Yorkshire Coast* (ed AR Lord), Field Guide to Fossils, pp. 30–40. Palaeontological Association.
- Hesselbo SP, Little CTS, Ruhl M, Thibault N and Ullmann CV (2020a) Comments on “Paleosalinity determination in ancient epicontinental seas: a case study of the T-OAE in the Cleveland Basin (UK)” by Ramirez, M.N. and Algeo, T.J. *Earth-Science Reviews* **208**, 103290.
- Hesselbo SP, Ogg JG, Ruhl M, Hinnov LA and Huang CJ (2020b) The Jurassic Period. In *Geologic Time Scale 2020* (eds FM Gradstein, JG Ogg, MD Schmitz and GM Ogg), **2**, pp. 955–1021. Amsterdam: Elsevier.
- Hesselbo SP and Pieńkowski G (2011) Stepwise atmospheric carbon-isotope excursion during the Toarcian Oceanic Anoxic Event (Early Jurassic, Polish Basin). *Earth and Planetary Science Letters* **301**, 365–372.
- Higgins MB, Robinson RS, Husson JM, Carter SJ and Pearson A (2012) Dominant eukaryotic export production during ocean anoxic events reflects the importance of recycled NH_4^+ . *Proceedings of the National Academy of Sciences* **109**, 2269–2274.
- Hoffmann R and Stevens K (2020) The palaeobiology of belemnites – foundation for the interpretation of rostrum geochemistry. *Biological Reviews* **95**, 94–123.
- Hollaar TP, Hesselbo SP, Deconinck J-F, Damaschke M, Ullmann CV, Jiang M and Belcher CM (2023) Environmental changes during the onset of the Late Pliensbachian Event (Early Jurassic) in the Cardigan Bay Basin, Wales. *Climate of the Past* **19**, 979–997.
- H onisch B, Ridgwell A, Schmidt DN, Thomas E, Gibbs SJ, Sluijs A, Zeebe R, Kump L, Martindale RC, Greene SE, Kiessling W, Ries J, Zachos JC, Royer DL, Barker S, Marchitto TM, Moyer R, Pelejero C, Ziveri P, Foster GL and Williams B (2012) The geological record of ocean acidification. *Science* **335**, 1058–1063.
- Houben AJP, Goldberg T and Slomp CP (2021) Biogeochemical evolution and organic carbon deposition on the Northwestern European Shelf during the Toarcian Ocean Anoxic Event. *Palaeogeography, Palaeoclimatology, Palaeoecology* **565**, 1–13.
- Houben ME, Barnhoorn A, Lie-A-Fat J, Ravestein T, Peach CJ and Drury MR (2016a) Microstructural characteristics of the Whitby Mudstone Formation (UK). *Marine and Petroleum Geology* **70**, 185–200.

- Houben ME, Barnhoorn A, Wasch L, Trabucho-Alexandre J, Peach CJ and Drury MR** (2016b) Microstructures of Early Jurassic (Toarcian) shales of Northern Europe. *International Journal of Coal Geology* **165**, 76–89.
- Howard AS** (1985) Lithostratigraphy of the Staithes Sandstone and Cleveland Ironstone formations (Lower Jurassic) of north-east Yorkshire. *Proceedings of the Yorkshire Geological Society* **45**, 261–275.
- Howarth MK** (1955) Domerian of the Yorkshire coast. *Proceedings of the Yorkshire Geological Society* **30**, 147–175.
- Howarth MK** (1962) The Jet Rock Series and the Alum Shale Series of the Yorkshire coast. *Proceedings of the Yorkshire Geological Society* **33**, 381–422.
- Howarth MK** (1973) The stratigraphy and ammonite fauna of the Upper Liassic Grey Shales of the Yorkshire coast. *Bulletin of the British Museum (Natural History) Geology* **24**, 235–277.
- Howarth MK** (1992) The ammonite family Hildoceratidae in the Lower Jurassic of Britain. *Monograph of the Palaeontographical Society* **145–146**, 1–200.
- Huang CJ and Hesselbo SP** (2014) Pacing of the Toarcian Oceanic Anoxic Event (Early Jurassic) from astronomical correlation of marine sections. *Gondwana Research* **25**, 1348–1356.
- Huang Y, Jin X, Pancost RD, Kemp DB and Naafs BDA** (2024) An intensified lacustrine methane cycle during the Toarcian OAE (Jenkyns Event) in the Ordos Basin, northern China. *Earth and Planetary Science Letters* **639**, 118766.
- Hurst A** (1985) The implications of clay mineralogy to palaeoclimate and provenance during the Jurassic in NE Scotland. *Scottish Journal of Geology* **21**, 143–160.
- Ikeda M and Hori RS** (2014) Effects of Karoo–Ferrar volcanism and astronomical cycles on the Toarcian Oceanic Anoxic Events (Early Jurassic). *Palaeogeography, Palaeoclimatology, Palaeoecology* **410**, 134–142.
- Ikeda M, Hori RS, Ikehara M, Miyashita R, Chino M and Yamada K** (2018) Carbon cycle dynamics linked with Karoo–Ferrar volcanism and astronomical cycles during Pliensbachian–Toarcian (Early Jurassic). *Global and Planetary Change* **170**, 163–171.
- Imber J, Armstrong H, Clancy S, Daniels S, Herringshaw L, McCaffrey K, Rodriguez J, Trabucho-Alexandre J and Warren C** (2014) Natural fractures in a United Kingdom shale reservoir analog, Cleveland Basin, northeast England. *AAPG Bulletin* **98**, 2411–2437.
- Immenhauser A** (2009) Estimating palaeo-water depth from the physical rock record. *Earth-Science Reviews* **96**, 107–139.
- Ingall ED, Bustin RM and Van Cappellen P** (1993) Influence of water column anoxia on the burial and preservation of carbon and phosphorus in marine shales. *Geochimica et Cosmochimica Acta* **57**, 303–316.
- Izumi K, Kemp DB, Itamiya S and Inui M** (2018) Sedimentary evidence for enhanced hydrological cycling in response to rapid carbon release during the early Toarcian oceanic anoxic event. *Earth and Planetary Science Letters* **481**, 162–170.
- Jarvis I, Burnett WC, Nathan Y, Almbaydin FSM, Attia AKM, Castro LN, Flicoteaux R, Hilmy ME, Husain V, Qutawnah AA, Serjani A and Zanin YN** (1994) Phosphorite geochemistry: state-of-the-art and environmental concerns. *Eclogae Geologicae Helvetiae* **87**, 643–700.
- Jarvis I** (2003) Sample preparation in ICP-MS. In *Handbook of Inductively Coupled Plasma Mass Spectrometry* (eds KE Jarvis, AL Gray and RS Houk). pp. 172–224. Woking: Viridian.
- Jeans CV** (2006) Clay mineralogy of the Jurassic strata of the British Isles. *Clay Minerals* **41**, 187–307.
- Jenkyns HC** (1980) Cretaceous anoxic events: from continents to oceans. *Journal of the Geological Society* **137**, 171–188.
- Jenkyns HC** (1985) The early Toarcian and Cenomanian–Turonian anoxic events in Europe - comparisons and contrasts. *Geologische Rundschau* **74**, 505–518.
- Jenkyns HC** (1988) The early Toarcian (Jurassic) anoxic event - stratigraphic, sedimentary, and geochemical evidence. *American Journal of Science* **288**, 101–151.
- Jenkyns HC** (1999) Mesozoic anoxic events and palaeoclimate. *Zentralblatt für Geologie und Paläontologie. Teil I, Allgemeine, Angewandte, Regionale und Historische Geologie* **7–9**, 943–949.
- Jenkyns HC** (2010) Geochemistry of oceanic anoxic events. *Geochemistry Geophysics Geosystems* **11**, Q03004.
- Jenkyns HC and Clayton CJ** (1997) Lower Jurassic epicontinental carbonates and mudstones from England and Wales: chemostratigraphic signals and the early Toarcian anoxic event. *Sedimentology* **44**, 687–706.
- Jenkyns HC, Dickson AJ, Ruhl M and Van den Boorn SHJM** (2017) Basalt–seawater interaction, the Plenus Cold Event, enhanced weathering and geochemical change: deconstructing Oceanic Anoxic Event 2 (Cenomanian–Turonian, Late Cretaceous). *Sedimentology* **64**, 16–43.
- Jenkyns HC, Gröcke DR and Hesselbo SP** (2001) Nitrogen isotope evidence for water mass denitrification during the early Toarcian (Jurassic) oceanic anoxic event. *Paleoceanography* **16**, 593–603.
- Jenkyns HC, Jones CE, Gröcke DR, Hesselbo SP and Parkinson DN** (2002) Chemostratigraphy of the Jurassic System: applications, limitations and implications for palaeoceanography. *Journal of the Geological Society* **159**, 351–378.
- Jenkyns HC and Macfarlane S** (2021) The chemostratigraphy and environmental significance of the Marlstone and Junction Bed (Beacon Limestone, Toarcian, Lower Jurassic, Dorset, UK). *Geological Magazine* **159**, 357–371.
- Jiang Q, Jourdan F, Olierook HKH and Merle RE** (2023) An appraisal of the ages of Phanerozoic large igneous provinces. *Earth-Science Reviews* **237**, 104314.
- Jiang SY, Song HJ, Kemp DB, Dai X and Liu XK** (2020) Two pulses of extinction of larger benthic foraminifera during the Pliensbachian–Toarcian and early Toarcian environmental crises. *Palaeogeography, Palaeoclimatology, Palaeoecology* **560**, 109998.
- Jin X, Shi Z, Baranyi V, Kemp DB, Han Z, Luo G, Hu J, He F, Chen L and Preto N** (2020) The Jenkyns Event (early Toarcian OAE) in the Ordos Basin, North China. *Global and Planetary Change* **193**, 1–15.
- Jin X, Zhang F, Baranyi V, Kemp DB, Feng X, Grasby SE, Sun G, Shi Z, Chen W and Dal Corso J** (2022) Early Jurassic massive release of terrestrial mercury linked to floral crisis. *Earth and Planetary Science Letters* **598**, 1–12.
- Jones B and Manning DAC** (1994) Comparison of geochemical indexes used for the interpretation of paleoredox conditions in ancient mudstones. *Chemical Geology* **111**, 111–129.
- Jones CE, Jenkyns HC and Hesselbo SP** (1994) Strontium isotopes in Early Jurassic seawater. *Geochimica et Cosmochimica Acta* **58**, 1285–1301.
- Junium CK, Dickson AJ and Uveges BT** (2018) Perturbation to the nitrogen cycle during rapid Early Eocene global warming. *Nature Communications* **9**, 3186.
- Kampshulte A and Strauss H** (2004) The sulfur isotopic evolution of Phanerozoic seawater based on the analysis of structurally substituted sulfate in carbonates. *Chemical Geology* **204**, 255–286.
- Katchinoff JAR, Syverson DD, Planavsky NJ, Evans ESJ and Rooney AD** (2021) Seawater chemistry and hydrothermal controls on the Cenozoic osmium cycle. *Geophysical Research Letters* **48**, e2021GL095558.
- Kearsley AT** (1989) Iron-rich ooids, their mineralogy and microfabric: clues to their origin and evolution. In *Phanerozoic Ironstones* (eds TP Young and WEG Taylor), pp. 141–164. Geological Society London, Special Publications 46.
- Kemp DB, Chen W, Cho T, Algeo TJ, Shen J and Ikeda M** (2022a) Deep-ocean anoxia across the Pliensbachian–Toarcian boundary and the Toarcian Oceanic Anoxic Event in the Panthalassic Ocean. *Global and Planetary Change* **212**, 1–14.
- Kemp DB, Coe AL, Cohen AS and Schwark L** (2005) Astronomical pacing of methane release in the Early Jurassic period. *Nature* **437**, 396–399.
- Kemp DB, Coe AL, Cohen AS and Weedon GP** (2011) Astronomical forcing and chronology of the early Toarcian (Early Jurassic) oceanic anoxic event in Yorkshire, UK. *Paleoceanography* **26**, PA4210.
- Kemp DB, Fraser WT and Izumi K** (2018) Stratigraphic completeness and resolution in an ancient mudrock succession. *Sedimentology* **65**, 1875–1890.
- Kemp DB and Izumi K** (2014) Multiproxy geochemical analysis of a Panthalassic margin record of the early Toarcian oceanic anoxic event (Toyora area, Japan). *Palaeogeography, Palaeoclimatology, Palaeoecology* **414**, 332–341.
- Kemp DB and Sadler PM** (2022) Incompleteness: Dealing with an imperfect stratigraphical record. In *Deciphering Earth's History: the Practice of Stratigraphy* (ed AL Coe), pp. 213–226. GSL Geoscience in Practice.

- Kemp DB, Selby D and Izumi K** (2020) Direct coupling between carbon release and weathering during the Toarcian oceanic anoxic event. *Geology* **48**, 976–980.
- Kemp DB, Suan G, Fantasia A, Jin SM and Chen WH** (2022b) Global organic carbon burial during the Toarcian oceanic anoxic event: patterns and controls. *Earth-Science Reviews* **231**, 104086.
- Kemp SJ and McKervey JA** (2001) The mineralogy of mudrocks from the Lias Group of England. British Geological Survey Internal Report IR/01/124, Keyworth: British Geological Survey, 38 pp.
- Kemp SJ, Merriman RJ and Bouch JE** (2005) Clay mineral reaction progress – the maturity and burial history of the Lias Group of England and Wales. *Clay Minerals* **40**, 43–61.
- Kendall B, Andersen MB and Owens JD** (2021) Assessing the effect of Large Igneous Provinces on global oceanic redox conditions using non-traditional metal isotopes (molybdenum, uranium, thallium). In *Large Igneous Provinces: A Driver of Global Environmental and Biotic Changes* (eds RE Ernst, AJ Dickson and A Bekker), pp. 305–323. Geophysical Monograph 255, American Geophysical Union and John Wiley and Sons, Inc.
- Kennedy MJ, Pevear DR and Hill RJ** (2002) Mineral surface control of organic carbon in black shale. *Science* **295**, 657–660.
- Kent PE** (1980) Subsidence and uplift in east Yorkshire and Lincolnshire: a double inversion. *Proceedings of the Yorkshire Geological Society* **42**, 505–524.
- Khaustova N, Tikhomirova Y, Korost S, Poludetkina E, Voropaev A, Mironenko M and Spasennykh M** (2021) The study of uranium accumulation in marine bottom sediments: effect of redox conditions at the time of sedimentation. *Geosciences* **11**, 332.
- Klinkhammer GP and Palmer MR** (1991) Uranium in the oceans: where it goes and why. *Geochimica et Cosmochimica Acta* **55**, 1791–1806.
- Koopmans MP, Koster J, vanKaamPeters HME, Kenig F, Schouten S, Hartgers WA, deLeeuw JW and Sissingh Damsté JS** (1996) Diagenetic and catagenetic products of isorenieratene: molecular indicators for photic zone anoxia. *Geochimica et Cosmochimica Acta* **60**, 4467–4496.
- Korte C and Hesselbo SP** (2011) Shallow marine carbon and oxygen isotope and elemental records indicate icehouse–greenhouse cycles during the Early Jurassic. *Paleoceanography* **26**, PA4219.
- Korte C, Hesselbo SP, Ullmann CV, Diel G, Ruhl M, Schweigert G and Thibault N** (2015) Jurassic climate mode governed by ocean gateway. *Nature Communications* **6**, 10015.
- Kovács EB, Ruhl M, Silva RL, McElwain JC, Reolid M, Korte C, Ruebsam W and Hesselbo SP** (2024) Mercury sequestration pathways under varying depositional conditions during Early Jurassic (Pliensbachian and Toarcian) Karoo–Ferrar volcanism. *Palaeogeography, Palaeoclimatology, Palaeoecology* **637**, 111977.
- Krencker F-N, Bodin S, Suan G, Heimhofer U, Kabiri L and Immenhauser A** (2015) Toarcian extreme warmth led to tropical cyclone intensification. *Earth and Planetary Science Letters* **425**, 120–130.
- Krencker F-N, Fantasia A, Danisch J, Martindale R, Kabiri L, El Ouali M and Bodin S** (2020) Two-phased collapse of the shallow-water carbonate factory during the late Pliensbachian–Toarcian driven by changing climate and enhanced continental weathering in the Northwestern Gondwana Margin. *Earth-Science Reviews* **208**, 103254.
- Krencker F-N, Fantasia A, El Ouali M, Kabiri L and Bodin S** (2022) The effects of strong sediment-supply variability on the sequence stratigraphic architecture: insights from early Toarcian carbonate factory collapses. *Marine and Petroleum Geology* **136**, 105469.
- Krencker F-N, Lindström S and Bodin S** (2019) A major sea-level drop briefly precedes the Toarcian oceanic anoxic event: implication for Early Jurassic climate and carbon cycle. *Scientific Reports* **9**, 12518.
- Ku T-L, Knauss KG and Mathieu GG** (1977) Uranium in open ocean: concentration and isotopic composition. *Deep-Sea Research* **24**, 1005–1017.
- Kuenen PH** (1966) Experimental turbidite lamination in a circular flume. *Journal of Geology* **74**, 523–545.
- Kuloguski JT, Gilleaudeau GJ, Kaufman AJ, Kipp MA, Tissot FLH, Goeppfert TJ, Pitts AD, Pierantoni P, Evans MN and Elrick M** (2023) Carbonate uranium isotopes across Cretaceous OAE 2 in southern Mexico: new constraints on the global spread of marine anoxia and organic carbon burial. *Palaeogeography, Palaeoclimatology, Palaeoecology* **628**, 111756.
- Kunert A and Kendall B** (2023) Global ocean redox changes before and during the Toarcian Oceanic Anoxic Event. *Nature Communications* **14**, 1–10.
- Küspert W** (1982) Environmental changes during oil shale deposition as deduced from stable isotope ratios. In *Cyclic and Event Stratification* (eds G Einsele and A Seilacher), pp. 482–501. Berlin: Springer-Verlag.
- LaGrange MT, Konhauser KO, Catuneanu O, Harris BS, Playter TL and Gingras MK** (2020) Sequence stratigraphy in organic-rich marine mudstone successions using chemostratigraphic datasets. *Earth-Science Reviews* **203**, 103137.
- Large RR, Bull SW and Maslennikov VV** (2011) A carbonaceous sedimentary source-rock model for Carlin-type and orogenic gold deposits. *Economic Geology* **106**, 331–358.
- Lau KV and Hardisty DS** (2022) Modeling the impacts of diagenesis on carbonate paleoredox proxies. *Geochimica et Cosmochimica Acta* **337**, 123–139.
- Lau KV, Romaniello SJ and Zhang F** (2019) *The Uranium Isotope Paleoredox Proxy*. Elements in Geochemical Tracers in Earth System Science, Cambridge: Cambridge University Press, 28 pp.
- Law CA** (1999) Evaluating source rocks. In *Exploring for Oil and Gas Traps* (eds EA Beaumont and NH Foster). AAPG Treatise Handbook pp. 6–1–6–41. Tulsa: American Association of Petroleum Geologists.
- Lazar OR, Bohacs KM, Macquaker JHS, Schieber J and Demko TM** (2015) Capturing key attributes of fine-grained sedimentary rocks in outcrops, cores, and thin sections: nomenclature and description guidelines. *Journal of Sedimentary Research* **85**, 230–246.
- Lecomte A, Cathelineau M, Michels R, Peiffert C and Brouand M** (2017) Uranium mineralization in the Alum Shale Formation (Sweden): evolution of a U-rich marine black shale from sedimentation to metamorphism. *Ore Geology Reviews* **88**, 71–98.
- Levasseur S, Birck J-L and Allègre CJ** (1999) The osmium riverine flux and the oceanic mass balance of osmium. *Earth and Planetary Science Letters* **174**, 7–23.
- Li Q, McArthur JM, Thirlwall MF, Turchyn AV, Page K, Bradbury HJ, Weis R and Lowry D** (2021) Testing for ocean acidification during the Early Toarcian using $\delta^{44}/^{40}\text{Ca}$ and $\delta^{88}/^{86}\text{Sr}$. *Chemical Geology* **574**, 120228.
- Li Z, Schieber J and Pedersen PK** (2021) On the origin and significance of composite particles in mudstones: examples from the Cenomanian Dunvegan Formation. *Sedimentology* **68**, 737–754.
- Littke R, Klussmann U, Krooss B and Leythaeuser D** (1991) Quantification of loss of calcite, pyrite, and organic matter due to weathering of Toarcian black shales and effects on kerogen and bitumen characteristics. *Geochimica et Cosmochimica Acta* **55**, 3369–3378.
- Little CTS** (1995) The Pliensbachian–Toarcian (Lower Jurassic) extinction event. PhD thesis, University of Bristol, Bristol, 144 pp. Published thesis <http://ethos.bl.uk/OrderDetails.do?uin=uk.bl.ethos.294903>.
- Little CTS and Benton MJ** (1995) Early Jurassic mass extinction: a global long-term event. *Geology* **23**, 495–498.
- Little CTS** (1996) The Pliensbachian–Toarcian (Lower Jurassic) extinction event. In *The Cretaceous–Tertiary Event and other Catastrophes in Earth History* (eds G Ryder, D Fastovsky and S Gartner), pp. 505–512. Geological Society of America Special Papers 307.
- Little SH, Vance D, Lyons TW and McManus J** (2015) Controls on trace metal authigenic enrichment in reducing sediments: insights from modern oxygen-deficient settings. *American Journal of Science* **315**, 77–119.
- Littler K, Hesselbo SP and Jenkyns HC** (2010) A carbon-isotope perturbation at the Pliensbachian–Toarcian boundary: evidence from the Lias Group, NE England. *Geological Magazine* **147**, 181–192.
- Liu J, Cao J, He T, Liang F, Pu J and Wang Y** (2022) Lacustrine redox variations in the Toarcian Sichuan Basin across the Jenkyns Event. *Global and Planetary Change* **215**, 103860.
- Liu M, Ji CJ, Hu HW, Xia GQ, Yi HS, Them TR II, Sun P and Chen DZ** (2021) Variations in microbial ecology during the Toarcian Oceanic Anoxic Event (Early Jurassic) in the Qiangtang Basin, Tibet: evidence from biomarker and carbon isotopes. *Palaeogeography, Palaeoclimatology, Palaeoecology* **580**, 110626.
- Locarnini RA, Mishonov AV, Baranova OK, Boyer TP, Zweng MM, Garcia HE, Reagan JR, Seidov D, Weathers KW, Paver CR and Smolyar IV** (2019) *World Ocean Atlas 2018, Volume 1: Temperature*. NOAA Atlas

- NESDIS 81, Silver Springs MD: National Oceanic and Atmospheric Administration, 52 pp.
- Lord AR** (2019) *Fossils from the Lias of the Yorkshire Coast*. Palaeontological Association Field Guide. London: Palaeontological Association, 403 pp.
- Lu Z, Jenkyns HC and Rickaby REM** (2010) Iodine to calcium ratios in marine carbonate as a paleo-redox proxy during oceanic anoxic events. *Geology* **38**, 1107–1110.
- Luther GWI** (2023) Review on the physical chemistry of iodine transformations in the oceans. *Frontiers in Marine Science* **10**, 1085618.
- Luttinen A, Kurhila M, Puttonen R, Whitehouse M and Andersen T** (2022) Periodicity of Karoo rift zone magmatism inferred from zircon ages of silicic rocks: implications for the origin and environmental impact of the large igneous province. *Gondwana Research* **107**, 107–122.
- Lyons TW and Reinhard CT** (2012) Deoxygenation in warming oceans—looking back to the future. *Geology* **40**, 671–672.
- Macquaker JHS, Keller MA and Davies SJ** (2010) Algal blooms and “marine snow”: mechanisms that enhance preservation of organic carbon in ancient fine-grained sediments. *Journal of Sedimentary Research* **80**, 934–942.
- Macquaker JHS and Taylor KG** (1996) A sequence-stratigraphic interpretation of a mudstone-dominated succession: the Lower Jurassic Cleveland Ironstone Formation, UK. *Journal of the Geological Society* **153**, 759–770.
- Maher W and Butler E** (1988) Arsenic in the marine environment. *Applied Organometallic Chemistry* **3**, 191–214.
- Manabe S and Bryan Jr K** (1985) CO₂-induced change in a coupled ocean-atmosphere model and its paleoclimatic implications. *Journal of Geophysical Research: Oceans* **90**, 11689–11707.
- Marley J** (1857) Cleveland Ironstone. Outline of the main or thick stratified bed, its discovery, application and results, in connection with the iron works in the north of England. *Transactions North of England Institute of Mining Engineers* **5**, 165–219.
- Marquez RTC, Tejada MLG, Suzuki K, Peleo-Alampay AM, Goto KT, Hyun S and Senda R** (2017) The seawater osmium isotope record of South China Sea: implications on its history and evolution. *Marine Geology* **394**, 98–115.
- Marsaglia KM and Klein GD** (1983) The paleogeography of Paleozoic and Mesozoic storm depositional systems. *Journal of Geology* **91**, 117–142.
- Marshall JD and Pirrie D** (2013) Carbonate concretions — explained. *Geology Today* **29**, 53–62.
- Martin KD** (2004) A re-evaluation of the relationship between trace fossils and dysoxia. In *The Application of Ichnology to Palaeoenvironmental and Stratigraphic Analysis* (ed D McIlroy), pp. 141–156. Geological Society London, Special Publications 228.
- Martinez M, Krencker F-N, Mattioli E and Bodin S** (2017) Orbital chronology of the Pliensbachian – Toarcian transition from the Central High Atlas Basin (Morocco). *Newsletters on Stratigraphy* **50**, 47–69.
- März C, Riedinger N, Sena C and Kasten S** (2018) Phosphorus dynamics around the sulphate–methane transition in continental margin sediments: authigenic apatite and Fe(II) phosphates. *Marine Geology* **404**, 84–96.
- Maynard JB** (1986) Geochemistry of oolitic iron ores, an electron microprobe study. *Economic Geology* **81**, 1473–1483.
- McArthur JM** (2019) Early Toarcian black shales: a response to an oceanic anoxic event or anoxia in marginal basins? *Chemical Geology* **522**, 71–83.
- McArthur JM, Algeo TJ, van de Schootbrugge B, Li Q and Howarth RJ** (2008) Basinal restriction, black shales, Re–Os dating, and the Early Toarcian (Jurassic) oceanic anoxic event. *Paleoceanography* **23**, PA4217.
- McArthur JM, Donovan DT, Thirlwall MF, Fouke BW and Mathey D** (2000) Strontium isotope profile of the early Toarcian (Jurassic) oceanic anoxic event, the duration of ammonite biozones, and belemnite palaeotemperatures. *Earth and Planetary Science Letters* **179**, 269–285.
- McArthur JM, Howarth RJ, Shields GA and Zhou Y** (2020) Strontium isotope stratigraphy. In *Geologic Time Scale 2020* (eds FM Gradstein, JG Ogg, MD Schmitz and GM Ogg), pp. 211–238. Amsterdam: Elsevier.
- McArthur JM, Steuber T, Page KN and Landman NH** (2016) Sr-isotope stratigraphy: assigning time in the Campanian, Pliensbachian, Toarcian, and Valanginian. *Journal of Geology* **124**, 569–586.
- McDonald BS, Partin CA, Sageman B and Holmden C** (2022) Uranium isotope reconstruction of ocean deoxygenation during OAE 2 hampered by uncertainties in fractionation factors and local U-cycling. *Geochimica et Cosmochimica Acta* **331**, 143–164.
- McElwain JC, Wade-Murphy J and Hesselbo SP** (2005) Changes in carbon dioxide during an oceanic anoxic event linked to intrusion into Gondwana coals. *Nature* **435**, 479–482.
- McKee ED and Weir GW** (1953) Terminology for stratification and cross-stratification in sedimentary rocks. *GSA Bulletin* **64**, 381–390.
- McLennan SM** (1993) Weathering and global denudation. *Journal of Geology* **101**, 295–303.
- Meister C, Aberhan M, Blau J, Dommergues JL, Feist-Burkhardt S, Hailwood EA, Hart M, Hesselbo SP, Hounslow MW, Hylton M, Morton N, Page K and Price GD** (2006) The Global Boundary Stratotype Section and Point (GSSP) for the base of the Pliensbachian Stage (Lower Jurassic), Wine Haven, Yorkshire, UK. *Episodes* **29**, 93–106.
- Menini A, Mattioli E, Hesselbo SP, Ruhl M and Sun G** (2021) Primary v. carbonate production in the Toarcian, a case study from the Llanbedr (Mochras Farm) borehole, Wales. In *Carbon Cycle and Ecosystem Response to the Jenkyns Event in the Early Toarcian (Jurassic)*. (eds M Reolid, LV Duarte, E Mattioli and W Ruebsam), pp. 59–81. Geological Society London, Special Publications 514.
- Merkel A and Munncke A** (2023) Glendonite-bearing concretions from the upper Pliensbachian (Lower Jurassic) of South Germany: indicators for a massive cooling in the European epicontinental sea. *Facies* **69**, 10.
- Meyers PA** (2014) Why are the $\delta^{13}\text{C}_{\text{org}}$ values in Phanerozoic black shales more negative than in modern marine organic matter? *Geochemistry Geophysics Geosystems* **15**, 3085–3106.
- Miller CA, Peucker-Ehrenbrink B, Walker BD and Marcantonio F** (2011) Re-assessing the surface cycling of molybdenum and rhenium. *Geochimica et Cosmochimica Acta* **75**, 7146–7179.
- Min H, Zhang T, Li Y, Zhao S, Li J, Lin D and Wang J** (2019) The albitization of K-feldspar in organic- and silt-rich fine-grained rocks of the Lower Cambrian Qiongzhusi Formation in the southwestern Upper Yangtze Region, China. *Minerals* **9**, 1–22.
- Monteiro FM, Pancost RD, Ridgwell A and Donnadieu Y** (2012) Nutrients as the dominant control on the spread of anoxia and euxinia across the Cenomanian–Turonian oceanic anoxic event (OAE2): model–data comparison. *Paleoceanography* **27**, PA4209.
- Montero-Serrano JC, Föllmi KB, Adatte T, Spangenberg JE, Tribouillard N, Fantasia A and Sun G** (2015) Continental weathering and redox conditions during the early Toarcian Oceanic Anoxic Event in the northwestern Tethys: insight from the Posidonia Shale section in the Swiss Jura Mountains. *Paleogeography, Palaeoclimatology, Palaeoecology* **429**, 83–99.
- Montoya-Pino C, Weyer S, Anbar AD, Pross J, Oschmann W, van de Schootbrugge B and Arz HW** (2010) Global enhancement of ocean anoxia during Oceanic Anoxic Event 2: a quantitative approach using U isotopes. *Geology* **38**, 315–318.
- Moor C, Lymberopoulou T and Dietrich VJ** (2001) Determination of heavy metals in soils, sediments and geological materials by ICP-AES and ICP-MS. *Mikrochimica Acta* **136**, 123–128.
- Morel FMM and Price NM** (2003) The biogeochemical cycles of trace metals in the oceans. *Science* **300**, 944–947.
- Morford JL and Emerson S** (1999) The geochemistry of redox sensitive trace metals in sediments. *Geochimica et Cosmochimica Acta* **63**, 1735–1750.
- Morford JL, Martin WR and Carney CM** (2012) Rhenium geochemical cycling: insights from continental margins. *Chemical Geology* **324–325**, 73–86.
- Morris KA** (1979) A classification of Jurassic marine shale sequences: an example from the Toarcian (Lower Jurassic) of Great Britain. *Paleogeography, Palaeoclimatology, Palaeoecology* **26**, 117–126.
- Morris KA** (1980) Comparison of major sequences of organic-rich mud deposition in the British Jurassic. *Journal of the Geological Society* **137**, 157–170.
- Moulin M, Fluteau F, Courtillot V, Marsh J, Delpéch G, Quidelleur X and Gérard M** (2017) Eruptive history of the Karoo lava flows and their impact on early Jurassic environmental change. *Journal of Geophysical Research: Solid Earth* **122**, 738–772.

- Mücke A and Farshad F (2005) Whole-rock and mineralogical composition of Phanerozoic ooidal ironstones: comparison and differentiation of types and subtypes. *Ore Geology Reviews* **26**, 227–262.
- Müller T, Jurikova H, Gutjahr M, Tomasovych A, Schlogl J, Liebetrau V, Duarte LV, Milovsky R, Suan G, Mattioli E, Pittet B and Eisenhauer A (2020) Ocean acidification during the early Toarcian extinction event: evidence from boron isotopes in brachiopods. *Geology* **48**, 1184–1188.
- Müller T, Price GD, Bajnai D, Nyerges A, Kesjár D, Raucsik B, Varga A, Judik K, Fekete J, May Z and Pálffy J (2017) New multiproxy record of the Jenkyns Event (also known as the Toarcian Oceanic Anoxic Event) from the Mecsek Mountains (Hungary): differences, duration and drivers. *Sedimentology* **64**, 66–86.
- Myers KJ and Wignall PB (1987) Understanding Jurassic organic rich mudrocks – new concepts using gamma-ray spectrometry and palaeoecology: Examples from the Kimmeridge Clay of Dorset and the Jet Rock of Yorkshire. In *Marine Clastic Sedimentology* (eds JK Leggett and GG Zuffa), pp. 172–189. London: Graham and Trotman.
- Myers KJ (1989) The origin of the Lower Jurassic Cleveland Ironstone Formation of North-East England: evidence from portable gamma-ray spectrometry. In *Phanerozoic Ironstones* (eds TP Young and WE Gordon Taylor), pp. 221–228. Geological Society London, Special Publications 46.
- Näslund J (2021) Mercury in fossil leaves as a proxy for tracking Large Igneous Province volcanism. BSc thesis, Uppsala University, Uppsala, 18 pp. Published thesis <https://www.diva-portal.org/smash/get/diva2:1574588/FULLTEXT01.pdf>.
- Nesbitt HW and Young GM (1982) Early Proterozoic climates and plate motions inferred from major element chemistry of lutites. *Nature* **299**, 715–717.
- Newton RJ, Reeves EP, Kafousia N, Wignall PB, Bottrell SH and Sha J-G (2011) Low marine sulfate concentrations and the isolation of the European epicontinental sea during the Early Jurassic. *Geology* **39**, 7–10.
- Nie Y, Fu X, Liang J, Wei H, Chen Z, Lin F, Zeng S, Wu Y, Zou Y and Mansour A (2023) The Toarcian Oceanic Anoxic Event in a shelf environment (Eastern Tethys): implications for weathering and redox conditions. *Sedimentary Geology* **455**, 106476.
- Nielsen SG, Goff M, Hesselbo SP, Jenkyns HC, LaRowe DE and Lee CTA (2011) Thallium isotopes in early diagenetic pyrite – A paleoredox proxy? *Geochimica et Cosmochimica Acta* **75**, 6690–6704.
- Nielsen SG, Rehkämper M and Prytulak J (2017) Investigation and application of thallium isotope fractionation. *Reviews in Mineralogy and Geochemistry* **82**, 759–798.
- Nikitenko BL and Mickey MB (2004) Foraminifera and ostracodes across the Pliensbachian–Toarcian boundary in the Arctic Realm (stratigraphy, palaeobiogeography and biofacies). In *The Palynology and Micropalaeontology of Boundaries* (eds AB Beaudoin and MJH Head). Geological Society London Special Publications **230**, 137–174.
- Nordt L, Breecker D and White J (2022) Jurassic greenhouse ice-sheet fluctuations sensitive to atmospheric CO₂ dynamics. *Nature Geoscience* **15**, 54–59.
- O'Brien NR (1990) Significance of lamination in Toarcian (Lower Jurassic) shales from Yorkshire, Great Britain. *Sedimentary Geology* **67**, 25–34.
- Oliveira LCV, Rodriguez R, Duarte LV and Lemos VB (2006) Avaliação do potencial gerador de petróleo e interpretação paleoambiental com base em biomarcadores e isótopos estáveis de carbono da seção Pliensbaquiano – Toarciano inferior (Jurássico Inferior) da região de Peniche (Bacia Lusitânica, Portugal). *Boletim de Geociências da Petrobras, Rio de Janeiro* **14**, 207–234.
- Ostrander CM, Owens JD and Nielsen SG (2017) Constraining the rate of oceanic deoxygenation leading up to a Cretaceous Oceanic Anoxic Event (OAE-2: ~94 Ma). *Science Advances* **3**, e1701020.
- Otto-Bliensner BL, Brady EC and Shields C (2002) Late Cretaceous ocean: coupled simulations with the National Center for Atmospheric Research climate system model. *Journal of Geophysical Research - Atmospheres* **107**, 4019.
- Owens JD (2019) *Application of Thallium Isotopes Tracking Marine Oxygenation Through Manganese Oxide Burial*. Elements in Geochemical Tracers in Earth System Science Cambridge: Cambridge University Press, 21 pp.
- Owens JD, Gill BC, Jenkyns HC, Bates SM, Severmann S, Kuypers MMM, Woodfine RG and Lyons TW (2013) Sulfur isotopes track the global extent and dynamics of euxinia during Cretaceous Oceanic Anoxic Event 2. *Proceedings of the National Academy of Sciences* **110**, 18407–18412.
- Owens JD, Lyons TW and Lowery CM (2018) Quantifying the missing sink for global organic carbon burial during a Cretaceous oceanic anoxic event. *Earth and Planetary Science Letters* **499**, 83–94.
- Owens JD, Nielsen SG, Horner TJ, Ostrander CM and Peterson LC (2017) Thallium-isotopic compositions of euxinic sediments as a proxy for global manganese-oxide burial. *Geochimica et Cosmochimica Acta* **213**, 291–307.
- Owens JD, Reinhard CT, Rohrsen M, Love GD and Lyons TW (2016) Empirical links between trace metal cycling and marine microbial ecology during a large perturbation to Earth's carbon cycle. *Earth and Planetary Science Letters* **449**, 407–417.
- Oxburgh R (2001) Residence time of osmium in the oceans. *Geochemistry, Geophysics, Geosystems* **2**, 2000GC000104.
- Page KN (2017) From Opper to Callomon (and beyond): building a high resolution ammonite-based biochronology for the Jurassic System. *Lethaia* **50**, 336–355.
- Pálffy J and Smith PL (2000) Synchrony between Early Jurassic extinction, oceanic anoxic event, and the Karoo–Ferrar flood basalt volcanism. *Geology* **28**, 747–750.
- Pancost RD, Crawford N, Magness S, Turner A, Jenkyns HC and Maxwell JR (2004) Further evidence for the development of photic-zone euxinic conditions during Mesozoic oceanic anoxic events. *Journal of the Geological Society* **161**, 353–364.
- Pankhurst RJ, Riley TR, Fanning CM and Kelley SP (2000) Episodic silicic volcanism in Patagonia and the Antarctic Peninsula: chronology of magmatism associated with the break-up of Gondwana. *Journal of Petrology* **41**, 605–625.
- Papadomanolaki NM, Lenstra WK, Wolthers M and Slomp CP (2022) Enhanced phosphorus recycling during past oceanic anoxia amplified by low rates of apatite authigenesis. *Science Advances* **8**, 1–12.
- Parkinson DN (1996) Gamma-ray spectrometry as a tool for stratigraphical interpretation: examples from the western European Lower Jurassic. In *Sequence Stratigraphy in British Geology* (eds SP Hesselbo and DN Parkinson). Geological Society Special Publication **103**, 231–255.
- Paul KM, van Helmond NAGM, Slomp CP, Jokinen SA, Virtasalo JJ, Filipsson HL and Jilbert T (2023) Sedimentary molybdenum and uranium: improving proxies for deoxygenation in coastal depositional environments. *Chemical Geology* **615**, 1–18.
- Paytan A, Kastner M, Campbell D and Thiemens MH (2004) Seawater sulfur isotope fluctuations in the Cretaceous. *Science* **304**, 1663–1665.
- Paytan A, Yao W and Gray ET (2020) Sulfur isotope stratigraphy. In *The Geologic Time Scale 2020* (eds F Gradstein, JG Ogg and G Ogg). **1**, pp. 259–278. Amsterdam: Elsevier.
- Pearce CR, Cohen AS, Coe AL and Burton KW (2008) Molybdenum isotope evidence for global ocean anoxia coupled with perturbations to the carbon cycle during the Early Jurassic. *Geology* **36**, 231–234.
- Percival LME, Bergquist BA, Mather TA and Sanei H (2021) Sedimentary mercury enrichments as a tracer of Large Igneous Province volcanism. In *Large Igneous Provinces: A Driver of Global Environmental and Biotic Changes* (eds RE Ernst, AJ Dickson and A Bekker), pp. 247–262. Geophysical Monographs 255.
- Percival LME, Cohen AS, Davies MK, Dickson AJ, Hesselbo SP, Jenkyns HC, Leng MJ, Mather TA, Storm MS and Xu W (2016) Osmium isotope evidence for two pulses of increased continental weathering linked to Early Jurassic volcanism and climate change. *Geology* **44**, 759–762.
- Percival LME, Witt MLI, Mather TA, Hermoso M, Jenkyns HC, Hesselbo SP, Al-Suwaidi AH, Storm MS, Xu W and Ruhl M (2015) Globally enhanced mercury deposition during the end-Pliensbachian extinction and Toarcian OAE: a link to the Karoo–Ferrar Large Igneous Province. *Earth and Planetary Science Letters* **428**, 267–280.
- Peti L and Thibault N (2017) Abundance and size changes in the calcareous nannofossil *Schizosphaerella* – Relation to sea-level, the carbonate factory and palaeoenvironmental change from the Sinemurian to earliest Toarcian of the Paris Basin. *Palaeogeography, Palaeoclimatology, Palaeoecology* **485**, 271–282.

- Peti L, Thibault N, Clemence ME, Korte C, Dommergues JL, Bougeault C, Pellenard P, Jelby ME and Ullmann CV (2017) Sinemurian–Pliensbachian calcareous nannofossil biostratigraphy and organic carbon isotope stratigraphy in the Paris Basin: calibration to the ammonite biozonation of NW Europe. *Palaeogeography, Palaeoclimatology, Palaeoecology* **468**, 142–161.
- Peti L, Thibault N, Korte C, Ullmann CV, Cachão M, Fibæk M (2021) Environmental drivers of size changes in lower Jurassic *Schizosphaerella* spp. *Marine Micropaleontology* **168**, 102053.
- Peucker-Ehrenbrink B and Ravizza G (2002) The marine osmium isotope record. *Terra Nova* **12**, 205–219.
- Peucker-Ehrenbrink B and Ravizza GE (2020) Osmium isotope stratigraphy. In *The Geologic Time Scale 2020* (eds F Gradstein, JG Ogg and G Ogg). pp. 239–257. Amsterdam: Elsevier.
- Phillips J (1829) *Illustrations of the geology of Yorkshire or a description of the strata and organic remains of the Yorkshire coast: accompanied by a geological map, sections and plates of the fossil plants and animals*. York: J. Phillips, 192 pp.
- Piazza V, Ullmann CV and Aberhan M (2020) Ocean warming affected faunal dynamics of benthic invertebrate assemblages across the Toarcian Oceanic Anoxic Event in the Iberian Basin (Spain). *PLoS One* **15**, 1–27.
- Piper DZ and Calvert SE (2009) A marine biogeochemical perspective on black shale deposition. *Earth-Science Reviews* **95**, 63–96.
- Poulsen CJ, Barron EJ, Arthur MA and Peterson WH (2001) Response of the mid-Cretaceous global oceanic circulation to tectonic and CO₂ forcings. *Paleoceanography* **16**, 576–592.
- Powell JH (1984) Lithostratigraphical nomenclature of the Lias Group in the Yorkshire Basin. *Proceedings of the Yorkshire Geological Society* **45**, 51–57.
- Powell JH (2010) Jurassic sedimentation in the Cleveland Basin: a review. *Proceedings of the Yorkshire Geological Society* **58**, 21–72.
- Pye K (1985) Electron microscope analysis of zoned dolomite rhombs in the Jet Rock Formation (Lower Toarcian) of the Whitby area, U.K. *Geological Magazine* **122**, 279–286.
- Pye K and Krinsley DH (1986) Microfabric, mineralogy and early diagenetic history of the Whitby Mudstone Formation (Toarcian), Cleveland Basin, U.K. *Geological Magazine* **123**, 191–203.
- Quinby-Hunt MS and Wilde P (1994) Thermodynamic zonation in the black shale facies based on iron–manganese–vanadium content. *Chemical Geology* **113**, 297–317.
- Rahman MW, Rimmer SM and Rowe HD (2018) The impact of rapid heating by intrusion on the geochemistry and petrography of coals and organic-rich shales in the Illinois Basin. *International Journal of Coal Geology* **187**, 45–53.
- Raiswell R (1988) Chemical model for the origin of minor limestone–shale cycles by anaerobic methane oxidation. *Geology* **16**, 641–644.
- Raiswell R and Berner RA (1985) Pyrite formation in euxinic and semi-euxinic sediments. *American Journal of Science* **285**, 710–724.
- Raiswell R, Bottrell SH, Al-Biatty HJ and Tan MM (1993) The influence of bottom water oxygenation and reactive iron content on sulfur incorporation into bitumens from Jurassic marine shales. *American Journal of Science* **293**, 569–596.
- Raiswell R, Buckley F, Berner RA and Anderson TF (1988) Degree of pyritization of iron as a paleoenvironmental indicator of bottom-water oxygenation. *Journal of Sedimentary Petrology* **58**, 812–819.
- Raiswell R and Canfield DE (1998) Sources of iron for pyrite formation in marine sediments. *American Journal of Science* **298**, 219–245.
- Raiswell R, Hardisty DS, Lyons TW, Canfield DE, Owens JD, Planavsky NJ, Poulton SW and Reinhard CT (2018) The iron paleoredox proxies: a guide to the pitfalls, problems and proper practice. *American Journal of Science* **318**, 491–526.
- Raiswell R (1987) Non-steady state microbiological diagenesis and the origin of concretions and nodular limestones. In *Diagenesis of Sedimentary Sequences* (ed JD Marshall), pp. 41–54. Geological Society London, Special Publications 36.
- Raiswell R, Newton R and Wignall PB (2001) An indicator of water-column anoxia: resolution of biofacies variations in the Kimmeridge Clay (Upper Jurassic, U.K.). *Journal of Sedimentary Research* **71**, 286–294.
- Raucsik B and Varga A (2008) Climato-environmental controls on clay mineralogy of the Hettangian–Bajocian successions of the Mecsek Mountains, Hungary: an evidence for extreme continental weathering during the early Toarcian oceanic anoxic event. *Palaeogeography, Palaeoclimatology, Palaeoecology* **265**, 1–13.
- Raup DM and Sepkoski JJ (1984) Periodicity of extinctions in the geologic past. *Proceedings of the National Academy of Science USA* **81**, 801–805.
- Rawson PF, Greensmith JT and Shalaby SE (1983) Coarsening-upwards cycles in the uppermost Staithe and Cleveland Ironstone Formations (Lower Jurassic) of the Yorkshire coast, England. *Proceedings of the Geologists' Association* **94**, 91–93.
- Rawson PF and Wright JK (1992) *The Yorkshire Coast*. Geologists' Association Field Guide London: Geologists' Association, 120 pp.
- Rawson PF and Wright JK (2000) *The Yorkshire Coast*. Geologists' Association Guides 34, London: Geologists' Association, 130 pp.
- Rawson PF and Wright JK (2018) *Geology of the Yorkshire Coast*. Geologists' Association Guides 34, London: Geologists' Association, 178 pp.
- Rawson PF and Wright JK (1995) Jurassic of the Cleveland Basin, North Yorkshire. In *Field Geology of the British Jurassic* (ed PD Taylor), pp. 173–208. Bath: The Geological Society, London.
- Redfield AC, Ketchum BH and Richards FA (1963) The influence of organisms on the composition of seawater. In *The Composition of Seawater: Comparative and Descriptive Oceanography. The Sea: Ideas and Observations on Progress in the Study of the Seas*, 2 (ed MN Hill), pp. 26–77. New York: Interscience Publishers.
- Reershemius T and Planavsky NJ (2021) What controls the duration and intensity of ocean anoxic events in the Paleozoic and the Mesozoic? *Earth-Science Reviews* **221**, 103787.
- Rees CE, Jenkins WJ and Monster J (1978) The sulphur isotopic composition of ocean water sulphate. *Geochimica et Cosmochimica Acta* **42**, 377–381.
- Reinhard CT, Planavsky NJ, Robbins LJ, Partin CA, Gill BC, Lalonde SV, Bekker A, Konhauser KO, Lyons TW (2013) Proterozoic ocean redox and biogeochemical stasis. *Proceedings of the National Academy of Sciences* **110**, 5357–5362.
- Remirez MN and Algeo TJ (2020a) Carbon-cycle changes during the Toarcian (Early Jurassic) and implications for regional versus global drivers of the Toarcian oceanic anoxic event. *Earth-Science Reviews* **209**, 103283.
- Remirez MN and Algeo TJ (2020b) Paleosalinity determination in ancient epicontinental seas: a case study of the T-OAE in the Cleveland Basin (UK). *Earth-Science Reviews* **201**, 1–15.
- Reolid M, Emanuela M, Nieto LM and Rodríguez-Tovar FJ (2014) The early Toarcian Oceanic Anoxic Event in the External Subbetic (Southiberian Palaeomargin, westernmost Tethys): geochemistry, nannofossils and ichnology. *Palaeogeography, Palaeoclimatology, Palaeoecology* **411**, 79–94.
- Reolid M, Mattioli E, Duarte LV and Marok A (2020) The Toarcian Oceanic Anoxic Event and the Jenkyns Event (IGCP-655 final report). *Episodes* **43**, 1–12.
- Reolid M, Mattioli E, Duarte LV and Ruebsam W (2021) The Toarcian Oceanic Anoxic Event: Where do we stand? In *Carbon Cycle and Ecosystem Response to the Jenkyns Event in the Early Toarcian (Jurassic)* (eds M Reolid, E Mattioli, LV Duarte and W Ruebsam), pp. 1–11. Geological Society London, Special Publications 514.
- Richey JD, Nordt L, White JD and Breecker DO (2023) ISOORG23: an updated compilation of stable carbon isotope data of terrestrial organic materials for the Cenozoic and Mesozoic. *Earth-Science Reviews* **241**, 104439.
- Rickard D (2019) Sedimentary pyrite framboid size-frequency distributions: a meta-analysis. *Palaeogeography, Palaeoclimatology, Palaeoecology* **522**, 62–75.
- Riegraf W (1985) Microfauna, Biostratigraphie und Fazies im Unteren Toarcium Südwestdeutschlands und Vergleiche mit benachbarten Gebieten. *Tübinger Mikropaläontologische Mitteilungen* **3**, 1–232.
- Riegraf W (1982) The bituminous Lower Toarcian at the Truc-de-Balduc near Mende (Département de la Lozère, S-France). In *Cyclic and Event Stratification* (eds S Einsele and A Seilacher), pp. 506–511. New York: Springer.
- Röhl H-J, Schmid-Röhl A, Oschmann W, Frimmel A and Schwark L (2001) The Posidonia Shale (Lower Toarcian) of SW-Germany: an oxygen-depleted ecosystem controlled by sea level and palaeoclimate. *Palaeogeography, Palaeoclimatology, Palaeoecology* **165**, 27–52.

- Rosales I, Barnolas A, Goy A, Sevillano A, Armendáriz M and López-García JM (2018) Isotope records (C–O–Sr) of late Pliensbachian–early Toarcian environmental perturbations in the westernmost Tethys (Majorca Island, Spain). *Palaeogeography, Palaeoclimatology, Palaeoecology* **497**, 168–185.
- Rosales I, Robles S and Quesada S (2004) Elemental and oxygen isotope composition of early Jurassic belemnites: salinity vs. temperature signals. *Journal of Sedimentary Research* **74**, 342–354.
- Rudnick RL and Gao S (2014) Composition of the continental crust. In *Treatise on Geochemistry* (2nd Edn) (eds HD Holland and KK Turekian). **4**, pp. 1–51. Amsterdam: Elsevier.
- Ruebsam W and Al-Husseini M (2020) Calibrating the Early Toarcian (Early Jurassic) with stratigraphic black holes (SBH). *Gondwana Research* **82**, 317–336.
- Ruebsam W, Mattioli E and Schwark L (2022) Molecular fossils and calcareous nanofossils reveal recurrent phytoplanktonic events in the early Toarcian. *Global and Planetary Change* **212**, 103812.
- Ruebsam W, Mayer B and Schwark L (2019) Cryosphere carbon dynamics control early Toarcian global warming and sea level evolution. *Global and Planetary Change* **172**, 440–453.
- Ruebsam W, Muller T, Kovacs J, Palfy J and Schwark L (2018) Environmental response to the early Toarcian carbon cycle and climate perturbations in the northeastern part of the West Tethys shelf. *Gondwana Research* **59**, 144–158.
- Ruebsam W, Munzberger P and Schwark L (2014) Chronology of the Early Toarcian environmental crisis in the Lorraine Sub-Basin (NE Paris Basin). *Earth and Planetary Science Letters* **404**, 273–282.
- Ruebsam W, Pienkowski G and Schwark L (2020a) Toarcian climate and carbon cycle perturbations – its impact on sea-level changes, enhanced mobilization and oxidation of fossil organic matter. *Earth and Planetary Science Letters* **546**, 116417.
- Ruebsam W, Reolid M, Marok A and Schwark L (2020b) Drivers of benthic extinction during the early Toarcian (Early Jurassic) at the northern Gondwana paleomargin: implications for paleoceanographic conditions. *Earth-Science Reviews* **203**, 103117.
- Ruebsam W, Reolid M, Sabatino N, Masetti D and Schwark L (2020c) Molecular paleothermometry of the early Toarcian climate perturbation. *Global and Planetary Change* **195**, 103351.
- Ruebsam W, Reolid M and Schwark L (2020d) $\delta^{13}\text{C}$ of terrestrial vegetation records Toarcian CO_2 and climate gradients. *Scientific Reports* **10**, 117.
- Ruebsam W, Schmid-Röhl A and Al-Husseini M (2023) Astronomical timescale for the early Toarcian (Early Jurassic) Posidonia Shale and global environmental changes. *Palaeogeography, Palaeoclimatology, Palaeoecology* **623**, 111619.
- Ruebsam W and Schwark L (2024) Disparity between Toarcian Oceanic Anoxic Event and Toarcian carbon isotope excursion. *International Journal of Earth Sciences* <https://doi.org/10.1007/s00531-024-02408-8>.
- Ruebsam W and Schwark L (2021) Impact of a northern-hemispherical cryosphere on late Pliensbachian–early Toarcian climate and environment evolution. In *Carbon Cycle and Ecosystem Response to the Jenkyns Event in the Early Toarcian (Jurassic)* (eds M Reolid, LV Duarte, E Mattioli and W Ruebsam), pp. 359–385. Geological Society London, Special Publications 514.
- Ruhl M, Hesselbo SP, Jenkyns HC, Xu W, Silva RL, Matthews KJ, Mather TA, Mac Niocaill C and Riding JB (2022) Reduced plate motion controlled timing of Early Jurassic Karoo–Ferrar large igneous province volcanism. *Science Advances* **8**, eabo0866.
- Ruvalcaba Baroni I, Palastanga V and Stomp CP (2020) Enhanced organic carbon burial in sediments of oxygen minimum zones upon ocean deoxygenation. *Frontiers in Marine Science* **6**, 1–15.
- Ruvalcaba Baroni I, Pohl A, van Helmond N, Papadomanolaki NM, Coe AL, Cohen AS, van de Schootbrugge B, Donnadiou Y and Slomp CP (2018) Ocean circulation in the Toarcian (Early Jurassic): a key control on deoxygenation and carbon burial on the European shelf. *Paleoceanography and Paleoclimatology* **33**, 994–1012.
- Sælen G, Doyle P and Talbot MR (1996) Stable-isotope analyses of belemnite rostra from the Whitby Mudstone Fm, England: surface water conditions during deposition of a marine black shale. *Palaaios* **11**, 97–117.
- Sælen G, Tyson RV, Talbot MR and Telnaes N (1998) Evidence of recycling of isotopically light CO_2 (aq) in stratified black shale basins: contrasts between the Whitby Mudstone and Kimmeridge Clay formations, United Kingdom. *Geology* **26**, 747–750.
- Sælen G, Tyson RV, Telnaes N and Talbot MR (2000) Contrasting watermass conditions during deposition of the Whitby Mudstone (Lower Jurassic) and Kimmeridge Clay (Upper Jurassic) formations, UK. *Palaeogeography, Palaeoclimatology, Palaeoecology* **163**, 163–196.
- Salem N-E (2013) Geochemical characterisation of the Pliensbachian–Toarcian boundary during the onset of the Toarcian Oceanic Anoxic Event, North Yorkshire, UK. PhD thesis, Newcastle University, Newcastle upon Tyne, 276 pp. Published thesis <https://ethos.bl.uk/OrderDetails.do?uin=uk.bl.ethos.618173>.
- Schieber J, Miclaus C, Seserman A, Liu B and Teng J (2019) When a mudstone was actually a “sand”: results of a sedimentological investigation of the bituminous marl formation (Oligocene), Eastern Carpathians of Romania. *Sedimentary Geology* **384**, 12–28.
- Schlanger SO, Arthur MA, Jenkyns HC and Scholle PA (1987) The Cenomanian–Turonian Oceanic Anoxic event, I. Stratigraphy and distribution of organic carbon-rich beds and the marine $\delta^{13}\text{C}$ excursion. In *Marine Petroleum Source Rocks* (eds J Brooks and AJ Fleet), pp. 371–399. Geological Society London, Special Publications 26.
- Schlanger SO and Jenkyns HC (1976) Cretaceous oceanic anoxic events: causes and consequences. *Geologie en Mijnbouw* **55**, 179–184.
- Schmitz MD, Singer BS and Rooney AD (2020) Radioisotope geochronology. In *The Geologic Time Scale 2020* (eds F Gradstein, JG Ogg and G Ogg). **1**, pp. 193–209. Amsterdam: Elsevier.
- Schnyder J, Pons D, Yans J, Tramoy R and Abdulanova S (2017) Integrated stratigraphy of a continental Pliensbachian–Toarcian Boundary (Lower Jurassic) section at Taskomirsay, Leontiev Graben, southwest Kazakhstan. In *Geological Evolution of Central Asian Basins and the Western Tien Shan Range* (eds M-F Brunet, T McCann and ER Sobel), pp. 337–356. Geological Society London, Special Publications 427.
- Scholle PA and Arthur MA (1980) Carbon isotope fluctuation in Cretaceous pelagic limestones: potential stratigraphic and petroleum exploration tool. *American Association of Petroleum Geologists Bulletin* **64**, 67–87.
- Scholz F (2018) Identifying oxygen minimum zone-type biogeochemical cycling in Earth history using inorganic geochemical proxies. *Earth-Science Reviews* **184**, 29–45.
- Scholz F, Siebert C, Dale AW and Frank M (2017) Intense molybdenum accumulation in sediments underneath a nitrogenous water column and implications for the reconstruction of paleo-redox conditions based on molybdenum isotopes. *Geochimica et Cosmochimica Acta* **213**, 400–417.
- Schouten S, Van Kaam-Peters HME, Rijpstra WIC, Schoell M and Sinninghe Damsté JSS (2000) Effects of an oceanic anoxic event on the stable carbon isotopic composition of early Toarcian carbon. *American Journal of Science* **300**, 1–22.
- Schwark L and Frimmel A (2004) Chemostratigraphy of the Posidonia Black Shale, SW-Germany II. Assessment of extent and persistence of photic-zone anoxia using aryl isoprenoid distributions. *Chemical Geology* **206**, 231–248.
- Scott C and Lyons TW (2012) Contrasting molybdenum cycling and isotopic properties in euxinic versus non-euxinic sediments and sedimentary rocks: refining the paleoproxies. *Chemical Geology* **324–325**, 19–27.
- Sellwood BW and Sladen CP (1981) Mesozoic and Tertiary argillaceous units: distribution and composition. *Quarterly Journal of Engineering Geology* **14**, 263–275.
- Shalaby SE (1980) *The middle Liassic sedimentary rocks of the coastal zone of northwest Yorkshire: their petrology and sedimentation*. Unpublished PhD thesis, Queen Mary, University of London, 420 pp.
- Sheen AI, Kendall B, Reinhard CT, Creaser RA, Lyons TW, Bekker A, Poulton SW and Anbar AD (2018) A model for the oceanic mass balance of rhenium and implications for the extent of Proterozoic ocean anoxia. *Geochimica et Cosmochimica Acta* **227**, 75–95.
- Silva RL, Duarte LV, Comas-Rengifo MJ, Mendonça Filho JG and Azerêdo AC (2011) Update of the carbon and oxygen isotopic records of the Early–Late Pliensbachian (Early Jurassic, ~187 Ma): insights from the organic-rich hemipelagic series of the Lusitanian Basin (Portugal). *Chemical Geology* **283**, 177–184.

- Simms MJ, Chidlaw N, Morton N and Page KN** (2004a) *British Lower Jurassic Stratigraphy*. The Geological Conservation Review Series 30, Peterborough: Joint Nature Conservation Committee, 458 pp.
- Simms MJ, Chidlaw N, Page KN and Morton N** (2004b) Chapter 6 The Cleveland Basin. In *British Lower Jurassic Stratigraphy* (ed R Gallois). Geological Conservation Review Series 30, pp. 237–304. Peterborough: Joint Nature Conservation Committee.
- Singer A** (1984) The paleoclimatic interpretation of clay minerals in sediments – a review. *Earth-Science Reviews* **21**, 251–293.
- Sinninghe Damsté JSS, Kenig F, Koopmans MP, Köster J, Schouten S, Hayes JM and de Leeuw JW** (1995) Evidence for gammacerane as an indicator of water column stratification. *Geochimica et Cosmochimica Acta* **59**, 1895–1900.
- Slater SM, Bown P, Twitchett RJ, Danise S and Vajda V** (2022) Global record of “ghost” nannofossils reveals plankton resilience to high CO₂ and warming. *Science* **376**, 853–856.
- Slater SM, Twitchett RJ, Danise S and Vajda V** (2019) Substantial vegetation response to Early Jurassic global warming with impacts on oceanic anoxia. *Nature Geoscience* **12**, 462–467.
- Slopp CP and Van Cappellen P** (2007) The global marine phosphorus cycle: sensitivity to oceanic circulation. *Biogeosciences* **4**, 155–171.
- Song J, Littke R and Weniger P** (2017) Organic geochemistry of the Lower Toarcian Posidonia Shale in NW Europe. *Organic Geochemistry* **106**, 76–92.
- Song J, Littke R, Weniger P, Ostertag-Henning C and Nelskamp S** (2015) Shale oil potential and thermal maturity of the Lower Toarcian Posidonia Shale in NW Europe. *International Journal of Coal Geology* **150–151**, 127–153.
- Spirakis CS** (1996) The roles of organic matter in the formation of uranium deposits in sedimentary rocks. *Ore Geology Reviews* **11**, 53–69.
- Storm MS, Hesselbo SP, Jenkyns HC, Ruhl M, Ullmann CV, Xu W, Leng MJ, Riding JB and Gorbanenko O** (2020) Orbital pacing and secular evolution of the Early Jurassic carbon cycle. *Proceedings of the National Academy of Sciences* **117**, 3974–3982.
- Suan G, Mattioli E, Pittet B, Lecuyer C, Sucheras-Marx B, Duarte LV, Philippe M, Reggiani L and Martineau F** (2010) Secular environmental precursors to Early Toarcian (Jurassic) extreme climate changes. *Earth and Planetary Science Letters* **290**, 448–458.
- Suan G, Mattioli E, Pittet B, Mailliot S and Lecuyer C** (2008a) Evidence for major environmental perturbation prior to and during the Toarcian (Early Jurassic) oceanic anoxic event from the Lusitanian Basin, Portugal. *Paleoceanography* **23**, PA1202.
- Suan G, Nikitenko BL, Rogov MA, Baudin F, Spangenberg JE, Knyazev VG, Glinkikh LA, Goryacheva AA, Adatte T, Riding JB, Follmi KB, Pittet B, Mattioli E and Lecuyer C** (2011) Polar record of Early Jurassic massive carbon injection. *Earth and Planetary Science Letters* **312**, 102–113.
- Suan G, Pittet B, Bour I, Mattioli E, Duarte LV and Mailliot S** (2008b) Duration of the Early Toarcian carbon isotope excursion deduced from spectral analysis: consequence for its possible causes. *Earth and Planetary Science Letters* **267**, 666–679.
- Suan G, Schlogl J and Mattioli E** (2016) Bio- and chemostratigraphy of the Toarcian organic-rich deposits of some key successions of the Alpine Tethys. *Newsletters on Stratigraphy* **49**, 401–419.
- Suan G, van de Schootbrugge B, Adatte T, Fiebig J and Oschmann W** (2015) Calibrating the magnitude of the Toarcian carbon cycle perturbation. *Paleoceanography* **30**, 495–509.
- Svensen H, Planke S, Chevillier L, Malthes-Sørensen A, Corfu F and Jamtveit B** (2007) Hydrothermal venting of greenhouse gases triggering Early Jurassic global warming. *Earth and Planetary Science Letters* **256**, 554–566.
- Swanson VE** (1961) Geology and geochemistry of uranium in marine black shales A review. *USGS Professional Paper 356-C*, 67–112.
- Sweere TC, Dickson AJ, Jenkyns HC, Porcelli D, Ruhl M, Murphy MJ, Idiz E, van der Boorn SHJM, Eldrett JS and Henderson GM** (2020) Controls on the Cd-isotope composition of Upper Cretaceous (Cenomanian–Turonian) organic-rich mudrocks from south Texas (Eagle Ford Group). *Geochimica et Cosmochimica Acta* **287**, 251–262.
- Sweere TC, van den Boorn S, Dickson AJ and Reichart GJ** (2016) Definition of new trace-metal proxies for the controls on organic matter enrichment in marine sediments based on Mn, Co, Mo and Cd concentrations. *Chemical Geology* **441**, 235–245.
- Tate R and Blake JF** (1876) *The Yorkshire Lias*. London: John Van Voorst, 475 pp.
- Taylor SR and McLennan SM** (2001) Chemical composition and element distribution in the Earth’s crust (3rd Edn). In *Encyclopedia of Physical Science and Technology* (ed RA Meyers), pp. 697–719. San Diego: Academic Press.
- Them TR II, Gill BC, Caruthers AH, Gerhardt AM, Gröcke DR, Lyons TW, Marroquin SM, Nielsen SG, Alexandre JPT and Owens JD** (2018) Thallium isotopes reveal protracted anoxia during the Toarcian (Early Jurassic) associated with volcanism, carbon burial, and mass extinction. *Proceedings of the National Academy of Sciences of the United States of America* **115**, 6596–6601.
- Them TR II, Gill BC, Caruthers AH, Gröcke DR, Tulsy ET, Martindale RC, Poulton TP and Smith PL** (2017a) High-resolution carbon isotope records of the Toarcian Oceanic Anoxic Event (Early Jurassic) from North America and implications for the global drivers of the Toarcian carbon cycle. *Earth and Planetary Science Letters* **459**, 118–126.
- Them TR II, Gill BC, Selby D, Gröcke DR, Friedman RM and Owens JD** (2017b) Evidence for rapid weathering response to climatic warming during the Toarcian Oceanic Anoxic Event. *Scientific Reports* **7**, 5003.
- Them TR II, Jagoe CH, Caruthers AH, Gill BC, Grasby SE, Gröcke DR, Yin R and Owens JD** (2019) Terrestrial sources as the primary delivery mechanism of mercury to the oceans across the Toarcian Oceanic Anoxic Event (Early Jurassic). *Earth and Planetary Science Letters* **507**, 62–72.
- Them TR II, Owens JD, Marroquin SM, Caruthers AH, Trabuco-Alexandre JP and Gill BC** (2022) Reduced marine molybdenum inventory related to enhanced organic carbon burial and an expansion of reducing environments in the Toarcian (Early Jurassic) oceans. *AGU Advances* **3**, 1–20.
- Thibault N, Ruhl M, Ullmann CV, Korte C, Kemp DB, Gröcke DR and Hesselbo SP** (2018) The wider context of the Lower Jurassic Toarcian oceanic anoxic event in Yorkshire coastal outcrops, UK. *Proceedings of the Geologists’ Association* **129**, 372–391.
- Trabuco-Alexandre J, Gröcke DR, Atar E, Herringshaw L and Jarvis I** (2022) A new subsurface record of the Pliensbachian–Toarcian of Yorkshire. *Proceedings of the Yorkshire Geological Society* **64**, 1–12.
- Trabuco-Alexandre J** (2015) More gaps than shale: Erosion of mud and its effect on preserved geochemical and palaeobiological signals. In *Strata and Time: Probing the Gaps in Our Understanding* (eds DG Smith, RJ Bailey, PM Burgess and AJ Fraser), pp. 251–270. Geological Society London, Special Publications 404.
- Trabuco-Alexandre J, Tuenter E, Henstra GA, van der Zwan KJ, van de Wal RSW, Dijkstra HA and de Boer PL** (2010) The mid-Cretaceous North Atlantic nutrient trap: black shales and OAEs. *Paleoceanography* **25**, PA4201.
- Trabuco-Alexandre J, van Gilst RI, Rodríguez-López JP and de Boer PL** (2011) The sedimentary expression of oceanic anoxic event 1b in the North Atlantic. *Sedimentology* **58**, 1217–1246.
- Tribouillard N** (2020) Arsenic in marine sediments: how robust a redox proxy? *Palaeoecology, Palaeoclimatology, Palaeoecology* **550**, 1–14.
- Tribouillard N** (2021) Conjugated enrichments in arsenic and antimony in marine deposits used as paleoenvironmental proxies: preliminary results. *BSGF Earth Sciences Bulletin* **192**, 39.
- Tribouillard N, Algeo TJ, Baudin F and Riboulleau A** (2012) Analysis of marine environmental conditions based on molybdenum–uranium covariation – applications to Mesozoic paleoceanography. *Chemical Geology* **324**, 46–58.
- Tribouillard N, Algeo TJ, Lyons T and Riboulleau A** (2006) Trace metals as paleoredox and paleoproductivity proxies: an update. *Chemical Geology* **232**, 12–32.
- Tucker ME** (2011) *Sedimentary Rocks in the Field* (4th Edn). The Geological Field Guide Series. Chichester: Wiley-Blackwell, 275 pp.
- Turgeon S and Brumsack HJ** (2006) Anoxic vs dysoxic events reflected in sediment geochemistry during the Cenomanian–Turonian Boundary Event (Cretaceous) in the Umbria–Marche Basin of central Italy. *Chemical Geology* **234**, 321–339.
- Tyson RV** (2005) The “productivity versus preservation” controversy: Cause, flaws, and resolution. In *The Deposition of Organic-Carbon-Rich Sediments:*

- Models, Mechanisms, and Consequences* (ed NB Harris). SEPM Special Publication 82, 17–33.
- Tyson RV** (1995) Bulk geochemical characterization and classification of organic matter: stable carbon isotopes ($\delta^{13}\text{C}$). In *Sedimentary Organic Matter. Organic Facies and Palynofacies* (ed RV Tyson). pp. 395–416. Dordrecht: Springer.
- Ullmann CV, Boyle R, Duarte L, Hesselbo S, Kasemann SA, Klein T, Lenton TM, Piazza V and Aberhan M** (2020) Warm afterglow from the Toarcian Oceanic Anoxic Event drives the success of deep-adapted brachiopods. *Scientific Reports* 10, 6549.
- Ullmann CV, Frei R, Korte C and Hesselbo SP** (2015) Chemical and isotopic architecture of the belemnite rostrum. *Geochimica et Cosmochimica Acta* 159, 231–243.
- Ullmann CV, Szűcs D, Jiang M, Hudson AJL and Hesselbo SP** (2022) Geochemistry of macrofossil, bulk rock and secondary calcite in the Early Jurassic strata of the Llanbedr (Mochras Farm) drill core, Cardigan Bay Basin, Wales, UK. *Journal of the Geological Society* 179, jgs2021–2018.
- Ullmann CV, Thibault N, Ruhl M, Hesselbo SP and Korte C** (2014) Effect of a Jurassic oceanic anoxic event on belemnite ecology and evolution. *Proceedings of the National Academy of Sciences of the United States of America* 111, 10073–10076.
- Vaes B, van Hinsbergen DJJ, van de Lagemaat SHA, van der Wiel E, Lom N, Advokaat EL, Boschman LM, Gallo LC, Greve A, Guilmette C, Li S, Lippert PC, Montheil L, Qayyum A and Langereis CG** (2023) A global apparent polar wander path for the last 320 Ma calculated from site-level paleomagnetic data. *Earth-Science Reviews* 245, 104547.
- van Acken D, Tütken T, Daly JS, Schmid-Röhl A and Orr PJ** (2019) Rhenium–osmium geochronology of the Toarcian Posidonia Shale, SW Germany. *Palaeogeography, Palaeoclimatology, Palaeoecology* 534, 1–12.
- Van Breugel Y, Baas M, Schouten S, Mattioli E and Sinnighe Damsté JSS** (2006) Isorenieratane record in black shales from the Paris Basin, France: constraints on recycling of respired CO_2 as a mechanism for negative carbon isotope shifts during the Toarcian oceanic anoxic event. *Paleoceanography* 21, 1–8.
- Van Buchem FSP and Knox RWOB** (1998) Lower and Middle Liassic depositional sequences of Yorkshire (U.K.). In *Mesozoic and Cenozoic Sequence Stratigraphy of European Basins* (eds P-Cd Graciansky, J Hardenbol, T Jacquin and PR Vail). SEPM, Special Publication 60, 545–559.
- Van Cappellen P and Ingall ED** (1994) Benthic phosphorus regeneration, net primary production, and ocean anoxia – a model of the coupled marine biogeochemical cycles of carbon and phosphorus. *Paleoceanography* 9, 677–692.
- van de Schootbrugge B, Houben AJP, Ercan FEZ, Verreussel R, Kerstholt S, Janssen NMM, Nikitenko B and Suan G** (2020) Enhanced Arctic–Tethys connectivity ended the Toarcian Oceanic Anoxic Event in NW Europe. *Geological Magazine* 157, 1593–1611.
- van de Schootbrugge B, McArthur JM, Bailey TR, Rosenthal Y, Wright JD and Miller KG** (2005) Toarcian oceanic anoxic event: an assessment of global causes using belemnite C isotope records. *Paleoceanography* 20, PA3008.
- van Hinsbergen DJJ, de Groot LV, van Schaik SJ, Spakman W, Bijl PK, Sluijs A, Langereis CG, Brinkhuis H** (2015) A paleolatitude calculator for paleoclimate studies. *PLoS ONE* 10, 1–21.
- van Hulten M, Middag R, Dutay J-C, De Baar H, Roy-Barman M, Gehlen M, Tagliabue A and Sterl A** (2017) Manganese in the west Atlantic Ocean in the context of the first global ocean circulation model of manganese. *Biogeosciences* 14, 1123–1152.
- Vasseur R, Lathuilière B, Lazár I, Martindale RC, Bodin S and Durllet C** (2021) Major coral extinctions during the early Toarcian global warming event. *Global and Planetary Change* 207, 103647.
- Vine JD and Tourtelot EB** (1970) Geochemistry of black shale deposits – a summary report. *Economic Geology* 65, 253–272.
- Visentin S and Erba E** (2021) High-resolution calcareous nannofossil biostratigraphy across the Toarcian Oceanic Anoxic Event in northern Italy: clues from the Sogno and Gajum cores (Lombardy Basin, Southern Alps). *Rivista Italiana di Paleontologia e Stratigrafia* 127, 539–556.
- Von Eynatten H, Barceló-Vidal C and Pawlowsky-Glahn V** (2003) Modelling compositional change: the example of chemical weathering of granitoid rocks. *Mathematical Geology* 35, 231–251.
- Wadley MR, Stevens DP, Jickells TD, Hughes C, Chance R, Hepach H, Tinerl L and Carpenter LJ** (2020) A global model for iodine speciation in the upper ocean. *Global Biogeochemical Cycles* 34, e2019GB006467.
- Walker RG and Plint AG** (1992) Wave- and storm-dominated shallow marine systems. In *Facies Models: Response to Sea Level Change* (eds RG Walker and NP James). GeoText 1, pp. 219–238. St John's, Newfoundland: Geological Association of Canada.
- Wang Y** (2022) Anomalous weathering records in the Cleveland Basin (Yorkshire, UK) during the T-OAE global warming. *Terra Nova* 35, 153–166.
- Wang Y, Lu W, Costa KM and Nielsen SG** (2022) Beyond anoxia: exploring sedimentary thallium isotopes in paleo-redox reconstructions from a new core top collection. *Geochimica et Cosmochimica Acta* 333, 347–361.
- Wang Y, Ossa FO, Spangenberg JE and Schoenberg R** (2021) Restricted oxygen-deficient basins on the northern European epicontinental shelf across the Toarcian carbon isotope excursion interval. *Paleoceanography and Paleoclimatology* 36, e2020PA004207.
- Wang Y, Ossa FO, Wille M, Schurr S, Saussele M-E, Schmid-Röhl A and Schoenberg R** (2020) Evidence for local carbon-cycle perturbations superimposed on the Toarcian carbon isotope excursion. *Geobiology* 18, 682–709.
- Ware B, Jourdan F and Timms NE** (2023) The Ferrar Continental Flood Basalt: a ~1.6 Ma long duration evidenced by high-precision $^{40}\text{Ar}/^{39}\text{Ar}$ ages suggest a potential role in the Pliensbachian–Toarcian extinction event. *Earth and Planetary Science Letters* 622, 118369.
- Whitehead TH, Anderson W, Wilson V and Wray DA** (1952) Liassic iron ores of the Cleveland district. In *The Liassic Ironstones*. Memoirs of the Geological Survey of Great Britain. The Mesozoic Ironstones of England. pp. 35–67. London: HMSO.
- Wignall PB and Bond DPG** (2008) The end-Triassic and Early Jurassic mass extinction records in the British Isles. *Proceedings of the Geologists' Association* 119, 73–84.
- Wignall PB and Newton R** (1998) Pyrite framboid diameter as a measure of oxygen deficiency in ancient mudrocks. *American Journal of Science* 298, 537–552.
- Wignall PB, Newton RJ and Little CTS** (2005) The timing of paleoenvironmental change and cause-and-effect relationships during the Early Jurassic mass extinction in Europe. *American Journal of Science* 305, 1014–1032.
- Wilkin RT, Barnes HL and Brantley SL** (1996) The size distribution of framboidal pyrite in modern sediments: an indicator of redox conditions. *Geochimica et Cosmochimica Acta* 60, 3897–3912.
- Wilkinson GM, Besterman A, Buelo C, Gephart J and Pace ML** (2018) A synthesis of modern organic carbon accumulation rates in coastal and aquatic inland ecosystems. *Scientific Reports* 8, 15736.
- Woodfine RG, Jenkyns HC, Sarti M, Baroncini F and Violante C** (2008) The response of two Tethyan carbonate platforms to the early Toarcian (Jurassic) oceanic anoxic event: environmental change and differential subsidence. *Sedimentology* 55, 1011–1028.
- Worden RH, Utley JEP, Butcher AR, Griffiths J, Wooldridge LJ and Lawan AY** (2020) Improved imaging and analysis of chlorite in reservoirs and modern day analogues: New insights for reservoir quality and provenance. In *Application of Analytical Techniques to Petroleum Systems* (eds P Dowey, M Osborne and H Volk). Geological Society London, Special Publications 484, 189–204.
- Wright JK** (2022) The Market Weighton High in the 21st century – new understanding of a long-standing problem. *Proceedings of the Yorkshire Geological Society* 64, pygs2021–2008.
- Wu F, Owens JD, Huang T, Sarafian A, Huang K-F, Sen IS, Horner TJ, Blusztajn J, Mprton P and Nielsen SG** (2019) Vanadium isotope composition of seawater. *Geochimica et Cosmochimica Acta* 244, 403–415.
- Xia G and Mansour A** (2022) Paleoenvironmental changes during the early Toarcian Oceanic Anoxic Event: insights into organic carbon distribution and controlling mechanisms in the eastern Tethys. *Journal of Asian Earth Sciences* 237, 105344.
- Xu WM, Ruhl M, Jenkyns HC, Hesselbo SP, Riding JB, Selby D, Naafs BDA, Weijers JH, Pancost RD, Tegelaar E and Idiz EF** (2017) Carbon

- sequestration in an expanded lake system during the Toarcian oceanic anoxic event. *Nature Geoscience* **10**, 129–134.
- Xu WM, Ruhl M, Jenkyns HC, Leng MJ, Huggett JM, Minisini D, Ullmann CV, Riding JB, Weijers JWH, Storm MS, Percival LME, Tosca NJ, Idiz EF, Tegelaar EW and Hesselbo SP** (2018) Evolution of the Toarcian (Early Jurassic) carbon-cycle and global climatic controls on local sedimentary processes (Cardigan Bay Basin, UK). *Earth and Planetary Science Letters* **484**, 396–411.
- Xu WM, Weijers JWH, Ruhl M, Idiz EF, Jenkyns HC, Riding JB, Gorbanenko O and Hesselbo SP** (2021) Molecular and petrographical evidence for lacustrine environmental and biotic change in the palaeo-Sichuan mega-lake (China) during the Toarcian Oceanic Anoxic Event. In *Carbon Cycle and Ecosystem Response to the Jenkyns Event in the Early Toarcian (Jurassic)* (eds M Reolid, LV Duarte, E Mattioli and W Ruebsam). Geological Society London, Special Publications 514, 335–357.
- Yan Q, Li X, Kemp DB, Guo J, Zhang Z and Hu Y** (2023) Elevated atmospheric CO₂ drove an increase in tropical cyclone intensity during the early Toarcian hyperthermal. *PNAS* **120**, e2301018120.
- Yang T, Shen Y, Qin YJ, Jin JS, Zhang Y, Tong G and Liu J** (2021) Distribution of radioactive elements (Th, U) and formation mechanism of the bottom of the Lopingian (Late Permian) coal-bearing series in western Guizhou, SW China. *Journal of Petroleum Science and Engineering* **205**, 108779.
- Yano M, Yasukawa K, Nakamura K, Ikehara M and Kato Y** (2020) Geochemical features of redox-sensitive trace metals in sediments under oxygen-depleted marine environments. *Minerals* **10**, 1–20.
- Young GAM and Bird J** (1822) *A Geological Survey of the Yorkshire Coast: Describing the Strata and Fossils occurring between the Humber and the Tees, from the German Ocean to the Plain of York*. Whitby: George Clark, 332 pp.
- Young TP, Aggett JR and Howard AS** (1990) The Cleveland Ironstone Formation. In *Jurassic and Ordovician Ooidal Ironstones* (ed TP Young). pp. 1–31. Nottingham: British Sedimentological Research Group.
- Zakharov VA, Shurygin BN, Il'ina VI and Nikitenko BL** (2006) Pliensbachian–Toarcian biotic turnover in north Siberia and the Arctic region. *Stratigraphy and Geological Correlation* **14**, 399–417.
- Zhai R, Zeng Z, Zhang R and Yao W** (2023) The response of nitrogen and sulfur cycles to ocean deoxygenation across the Cenomanian–Turonian boundary. *Global and Planetary Change* **227**, 104182.
- Zhang F, Lenton TM, del Rey A, Romaniello SJ, Chen X, Planavsky NJ, Clarkson MO, Dahl TW, Lau KV, Wang W, Li Z, Zhao M, Isson T, Algeo TJ and Anbar AD** (2020) Uranium isotopes in marine carbonates as a global ocean paleoredox proxy: a critical review. *Geochimica et Cosmochimica Acta* **287**, 27–49.
- Zhang R, Kemp DB, Thibault N, Jelby ME, Li M, Huang C, Sui Y, Wang Z, Liu D and Jia S** (2023) Astrochronology and sedimentary noise modeling of Pliensbachian (Early Jurassic) sea-level changes, Paris Basin, France. *Earth and Planetary Science Letters* **614**, 118199.
- Zhou XL, Jenkyns HC, Owens JD, Junium CK, Zheng XY, Sageman BB, Hardisty DS, Lyons TW, Ridgwell A and Lu ZL** (2015) Upper ocean oxygenation dynamics from I/Ca ratios during the Cenomanian–Turonian OAE 2. *Paleoceanography* **30**, 510–526.
- Zhu Y, La Croix A, Kemp DB, Shen J, Huang C, Hua X, Li Y and Wei M** (2024) Are sulfides the primary host of sedimentary Hg? A case study from the Lower Jurassic of the Surat Basin (Australia). *Chemical Geology* **652**, 122028.